July 2019

EVALUATION OF THE EFFECT OF BOTTOM BAR SPLICE LOCATION ON PERFORMANCE OF BEAMS IN REINFORCED CONCRETE PERIMETER FRAMES

Jorge Rivera Cruz

EVALUATION OF THE EFFECT OF BOTTOM BAR SPLICE LOCATION ON PERFORMANCE OF BEAMS IN REINFORCED CONCRETE PERIMETER FRAMES

A Dissertation Presented

by

Jorge A. Rivera Cruz

Submitted to the Graduate School of the
University of Massachusetts Amherst in partial fulfillment
of the requirements for the degree of

DOCTOR OF PHILOSOPHY

May 2019

Civil and Environmental Engineering

EVALUATION OF THE EFFECT OF BOTTOM BAR SPLICE LOCATION ON PERFORMANCE OF BEAMS IN REINFORCED CONCRETE PERIMETER FRAMES

A Dissertation Presented

by

Jorge A. Rivera Cruz

Approved as to style and content by:

_____

Sergio F. Breña, Chairperson

_____

Simos Gerasimidis, Member

_____

Peggi L. Clouston, Member

_____

Richard N. Palmer, Department Head
Civil and Environmental Engineering

DEDICATION

To my parents, thanks to the values they have taught me since I was a child, today I am a good human being.

ACKNOWLEDGMENTS

First of all, I thank to God for giving the tools to complete my Ph.D. journey. I owe it all to Him.

I would like to express my gratitude to my mentor and advisor Professor Sergio F. Breña for guided me thought my doctoral degree, a great human being. His advice and comments were a vital part of my success. I would also like to extend my gratitude to my committee members; Prof. Simos Gerasimidis and Prof. Peggi L. Clouston for their valuable comments, questions and suggestions about my research.

I would like to express my gratitude to the Concrete Reinforced Steel Institute (CRSI) and the Northeast Alliance for Graduate Education and the Professoriate (NEAGEP) for supporting this research.

Last but not least, I would like to thank my UMass fellow Joan M. Rodriguez Suarez for all her help. She became more than a friend for me during my Ph.D. Without her, this journey would not have been completed.

ABSTRACT

EVALUATION OF THE EFFECT OF BOTTOM BAR SPLICE LOCATION ON PERFORMANCE OF BEAMS IN REINFORCED CONCRETE PERIMETER FRAMES

MAY 2019

JORGE A. RIVERA CRUZ, B.S. IN CIVIL ENGINEERING, UNIVERSITY OF PUERTO RICO, MAYAGUEZ CAMPUS

M.E. IN CIVIL ENGINEERING, UNIVERSITY OF PUERTO RICO, MAYAGUEZ CAMPUS

Ph.D., UNIVERSITY OF MASSACHUSETTS AMHERST

Directed by: Professor Sergio F. Breña

The American Concrete Institute (ACI) *Building Code Requirements for Structural Concrete and Commentary* (ACI 318-14) indirectly accounts for resistance to progressive collapse by providing requirements for structural integrity in concrete structures. *ACI 318-14* structural integrity requirements are intended to provide alternate load paths so that progressive collapse is avoided in the event of the unintended loss of an interior support.

ACI 318-14 §9.7.7.5 requires that splices of structural integrity reinforcement be designed as Class B splices near mid-span for top reinforcement and near the support for bottom reinforcement. However, *ACI 318-14* does not provide a clear definition for the support region where bottom reinforcement splices should be located. In addition, bottom reinforcing bar splices at the face of the support or inside the beam-column joint have the

potential for generating congestion and introducing difficulties during construction. Therefore, relocating the splice location outside the joint may improve constructability but it is not clear if this practice will affect the behavior and the load redistribution capacity of the system.

The research presented in this dissertation is intended to evaluate the effect of splice location of structural integrity reinforcement on the performance of beams in perimeter frames after loss of an interior or an exterior column in a hypothetical reinforced concrete frame building. The ten-story reinforced concrete building prototype was designed for a low seismic design category following the requirements of the *ACI 318-14* Code, excepting Chapter 18. The study includes laboratory testing of three full-scale sub-assemblages of a ten-story reinforced concrete building prototype that simulate the loss of an interior column for the purpose of investigating the effect of bottom lap splice location. The two-span laboratory specimen contains a center column stub where the existing building column was removed to simulate loss of an interior support from an extreme event. The test specimens achieved similar maximum applied force values in the three experiments. After reaching the maximum force, a sudden decrease in the applied force occurred because of shear failure at the exterior end of one of the beams. This failure was generated by loss of aggregate interlock in the concrete after development of the critical diagonal crack. Premature failure of the beam limited the development of catenary action that has been reported to develop at large displacements by other researchers in laboratory experiments of similar specimens, but where seismic design details have been employed. Rotations just prior to the shear failure were similar for the north and south beams in the exterior plastic hinge regions for all specimens.

Three-dimensional structural models were built and analyzed using a commercially available structural analysis program (SAP 2000) to investigate the progressive collapse behavior of the ten story prototype concrete building after non-simultaneous removal of an interior and a corner column. The plastic collapse mechanism was captured by assigning nonlinear hinges at critical moment sections of beams and columns using a lumped plasticity approach. Hinges were also assigned at different locations along elements to capture the possibility of hinge formation away from ends of elements after moment redistribution occurred. The moment–curvature relationship of a beam plastic hinge was constructed analytically and subsequently calibrated using the experimental results of Specimen 3. Based on the *GSA 2016 Guidelines* and the performance on the plastic hinges, the interior perimeter column removal condition met the requirements of prevention for progressive collapse. In contrast, a corner perimeter column removal did not meet the requirements to prevent generating progressive collapse according to the *GSA 2016 Guidelines*. The research highlights the importance of proper reinforcing detailing of reinforced concrete frames to provide progressive collapse resistance, and the importance of three-dimensional modeling to evaluate moment redistribution of reinforced concrete perimeter frames after loss of supports.

TABLE OF CONTENTS

Page

LIST OF TABLES

Page

LIST OF FIGURES

Page

CHAPTER 1

INTRODUCTION

1.1 Background

Progressive collapse remains among the most challenging events in structural engineering to predict due to the uncertainty of the factors that initiate it, for example, a gas explosion, a vehicular impact, or a fire (Mohamed 2006). The American Society of Civil Engineering (ASCE) defines progressive collapse as "the spread of an initial local failure from element to element, eventually resulting in the collapse of an entire structure or a disproportionately large part of it" (ASCE 7-10).

Current building codes and guidelines developed to prevent progressive collapse of structures have included requirements to ensure the existence of an alternate load path and adequate redundancy to mitigate the effects of progressive collapse. *ASCE 7-10* defines two general approaches for preventing progressive collapse: direct and indirect design. Direct design makes available alternate load paths for loads in elements that might fail. In indirect design, resistance to progressive collapse is enabled implicitly by incorporating continuity and ductility in the design.

The American Concrete Institute (ACI) *Building Code Requirements for Structural Concrete and Commentary* (ACI 318-14) indirectly accounts for resistance to progressive collapse by providing requirements for structural integrity in concrete structures. *ACI 318-14* structural integrity requirements provide redundant load paths so

that progressive collapse is avoided in the event of the unintended loss of an interior support.

Figure 1.1 shows the partial collapse of the Alfred P. Murrah Federal Building in Oklahoma in 1995 that resulted from a detonation. A large truck bomb was detonated about 10 feet away from the first story of the building killing 167 people and injuring 782 (Hinman 1997). The FEMA Building Performance Investigation Team reported that only three columns were directly affected by the blast. Another highly studied case of progressive collapse is the major collapse of the Ronan Point apartment building in England in 1968, as shown in Figure 1.2. The major collapse was caused by a gas explosion in an apartment on the 18th floor. The explosive impact resulted in the loss of nearby exterior walls and the collapse of the slab. This additional weight caused the collapse of the slabs and walls below in that corner of the building (Nair 2006). These cases provide a clear example of the lack of structural integrity as a problem in a progressive collapse scenario. Owing to these events, present design codes and guidelines have included recommendations to mitigate progressive collapse in structures. Moreover, many academic researchers have carried out experimental and analytical studies to investigate the behavior of structures under progressive collapse.

Figure 1.1: Partial collapse of the Alfred P. Murrah Federal Building (www.fbi.gov)

Figure 1.2: Partial collapse of the Ronan Point apartment building (Pearson & Delatte 2005)

1.2 Motivation of this Research

As mentioned in Section 1.1, the approach that ACI follows to mitigate the likelihood of progressive collapse in reinforced concrete structures is to incorporate details that promote the creation of alternate load paths in the case of loss of key structural members such as columns located in the perimeter of a building. To achieve this, beams in perimeter frames must be provided with continuous top and bottom reinforcement (structural integrity reinforcement). Reinforcement may be deemed continuous if spliced in selected regions along the span following the requirements of Class B splices. A Class B splice is defined in *ACI 318-14* as an overlapping length equal to 1.3 times the development length of the bars being spliced. *ACI 318-14 §*9.7.7.5 requires that splices of structural integrity reinforcement be designed as Class B splices near mid-span for top reinforcement and near the support for bottom reinforcement as shown in Figure 1.3. However, *ACI 318-14* does not provide a clear definition for what constitutes the support region where bottom reinforcement splices should be located. In addition, bottom reinforcing bar splices at the face of the support or inside the beam-column joint have the potential for generating congestion and introducing difficulties during construction. Therefore, relocating the splice location outside the joint may improve constructability but it is not clear if this practice will affect the behavior and the load redistribution capacity of the system.

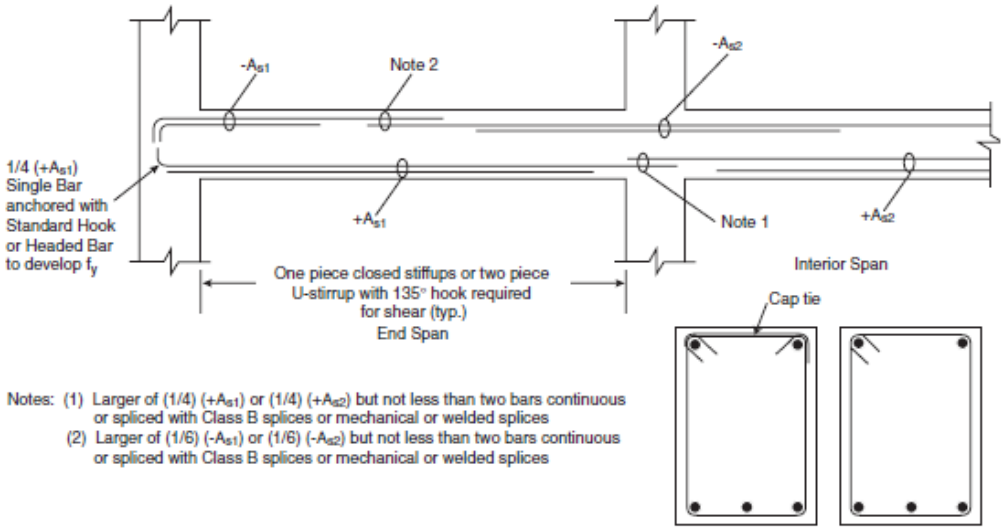

Figure 1.3: Structural integrity details for beams along the perimeter of the structure (*ACI 318-14*)

Recent results from laboratory experiments show that the major mechanisms to prevent progressive collapse in reinforced concrete frame buildings are the formation of either a Vierendeel action or catenary action after loss of a support. Sasani and Sagiroglu (2008) evaluated the progressive collapse resistance of a six-story reinforced concrete frame building. The investigators found the development of Vierendeel frame action as a major mechanism for the redistribution of the loads. This action changed the direction of the bending moments in the damaged beam-column joint generating tension in bottom beam reinforcement. Lew et al. (2014) tested two reinforced concrete frame sub-assemblages under a progressive collapse scenario. The experiment results showed that the failure mechanism was governed by catenary action in the beam, which eventually led to fracture of the bottom reinforcing bars near the damaged beam-column joint. Relocating the splice location outside the joint might avoid reinforcing bar fracture at the beam-column joint by moving the critical flexural crack away from the column face.

1.3 Research Objective

The objective of this research project is to evaluate the effect of splice location of structural integrity reinforcement on the performance of beams in perimeter frames after loss of an interior support in reinforced concrete frame buildings. Analytical and experimental phases are included to better understand the effect of splice location on redistribution capacity of the beam. The study aims also at evaluating current detailing practices to promote adequate structural integrity performance.

1.4 Scope

This study will focus on the behavior of a ten-story reinforced concrete frame structure after the loss an interior column in a perimeter of the first floor. The selected structure will be the same as the one studied by Lew et al. (2014) to allow comparison with the results from that study. The main difference is that Lew et al. detailed their laboratory specimens to be consistent with structures located in high or moderate seismic zones, and their correspondingly high seismic design categories (SDC) (SDC C or SDC D). The research presented in this dissertation focuses on detailing of structures in an area of low seismicity, with detailing consistent of a SDC A. This is a major departure from the previous studies that will be summarized in Chapter 2, because most researchers have focused on structures containing details of high seismic regions.

The dissertation is organized as follows. Chapter 2 summarizes relevant provisions for progressive collapse resistance that exist in present design codes and guidelines. Also, a literature review on past research studies are provided in this chapter.

The description of the ten-story prototype reinforced concrete frame building used in this study is presented in Chapter 3, including the structural analysis and design. The prototype details are based on the *ACI 318-14* requirements for a non-seismic zone.

Chapter 4 describes the laboratory tests designed to study the collapse behavior of full-scale sub-assemblages based on the prototype building discussed in Chapter 3. These laboratory specimens represent two interior spans of a beam in the perimeter of the first story where an intermediate column has been lost. The bottom reinforcement of the beams in the laboratory specimens was spliced at different locations, in reference to the face of the center support. The experimental behavior and test results of the laboratory specimens are discussed in Chapter 5 and 6, including crack patterns at representative load steps and measurements taken by the internal and external array of instruments described in Chapter 4.

An analytical procedure was developed using a commercially available structural analysis program to investigate the progressive collapse mechanism after column removal scenario of the prototype building described in Chapter 3. The results of the analytical simulations are presented in Chapter 7. Finally, Chapter 8 presents a summary and conclusions of this research project.

CHAPTER 2

LITERATURE REVIEW

2.1 Introduction

Owing the progressive collapse events discussed in Chapter 1, present codes have included recommendations to mitigate progressive collapse in reinforced concrete frame structures. This chapter summarizes the recommendations included in present design codes and guidelines and presents key results of researchers that have addressed this topic.

Several academic researchers have carried out experimental and analytical studies to investigate the behavior of reinforced concrete frame structures under progressive collapse. Therefore, literature review on past studies is provided in this chapter.

2.2 Building Codes and Guidelines

Current building codes and guidelines developed to prevent progressive collapse of structures have included requirements to ensure the existence of an alternate load path and adequate redundancy to mitigate the effects of progressive collapse. This section summarizes relevant provisions for progressive collapse resistance that exist in present design codes and guidelines.

2.2.1 ASCE 7-10

The American Society of Civil Engineers *Minimum Design Loads for Buildings and Other Structures Standard* (ASCE 7-10) defines two general approaches for preventing progressive collapse: direct and indirect design.

The indirect design approach involves providing ties within the structural system as an alternate load mechanism after failure of a structural member. In this approach, ties capable to resist a minimum level of load are provided to enhance continuity, ductility, and to allow development of alternate load paths. Ties can be provided by the existing structural elements that are used to transfer the loads from the damaged portion of the structure to the undamaged portion. Different structural elements can be used to provide the required tie strength; for example, horizontal tie strength can be provided by a series of beams connected to a column. Vertical ties can be provided by the continuity of the columns.

The direct design approach involves explicit consideration of resistance to progressive collapse during the design process using the alternate path method or specific local resistance method. The alternate path method requires the structure to redistribute the load after loss of a primary member while remaining stable. After loss of an element, the capacity of the damaged structure is evaluated using the following gravity load combination:

$$(0.9\ or\ 1.2)D + 0.5L + 0.2(L_r\ or\ S\ or\ R) \qquad 2.1$$

where *D*, *L*, L_r, *S* and *R* are dead, live, roof live, snow and rain load effects in accordance with *ASCE 7-10*. A 0.9 load factor for dead loads is used when effects from dead loads counteract effects from live loads; otherwise, the load factor for dead load is 1.2. In the specific local resistance method, the design requires designing key primary structural elements against a specific extreme event such as blast load. To evaluate the capacity of the key primary structural elements to withstand the effect of an extreme load, the following gravity load combination is considered:

$$(0.9\ or\ 1.2)D + 1.0A_k + 0.5L + 0.2S \qquad 2.2$$

where A_k is the load effect resulting from the extreme event. The uncertainty in the extreme event is captured as part of the calculation of A_k so a load factor of 1.0 is used in Eq. 2.2 (Mohamed 2006).

2.2.2 GSA 2016 Guidelines

The General Services Administration published in 2016 the *Alternate Path Analysis and Design Guidelines for Progressive Collapse Resistance* (GSA 2016 Guidelines). The main aim of these guidelines is to reduce the potential for progressive collapse in new and renovated federal buildings. Similar to *ASCE 7-10*, this document uses the alternate path method for progressive collapse resistance.

When using the *GSA 2016 Guidelines*, a building structure is required to be analyzed and evaluated after a column is removed. Three analysis procedures are allowed: linear static, nonlinear static and nonlinear dynamic. If a static analysis procedure is used the structure is required to be analyzed under the gravity load

combination of Eq. 2.3 acting on those bays immediately adjacent to the removed column and on all floors above the removed column:

$$G_N = \Omega_N[1.2D + (0.5L \; or \; 0.2S)] \quad 2.3$$

where Ω_N is the dynamic increase factor, D is the dead load effect, L is the live load effect and S the snow load effect. The bays located away from the removed column are analyzed using the gravity load combination given in Eq. 2.4:

$$G = 1.2D + (0.5L \; or \; 0.2S) \quad 2.4$$

When a dynamic analysis procedure is used the structure is required to be analyzed using the gravity load effects determined from Equation 2.4 applied on all bays, including those located far from the location of column removal. A three-dimensional analysis is required when these procedures are used.

For analysis using the linear static procedures the demand-capacity ratio of each component is computed to compare with threshold values based on the type of component. The demand-capacity ratio values are calculated with the following formula:

$$DCR = Q_{UD}/(\phi Q_{CE}) \quad 2.5$$

where Q_{UD} is the maximum load effect such as bending moment, shear force, and axial force determined in the component from a linear analysis; Q_{CE} is the expected strength of the component and ϕ is the strength reduction factor. The guidelines allow increase the design material strengths by 1.25 to determine the expected material strengths.

2.2.3 ACI 318-14

The American Concrete Institute (ACI) *Building Code Requirements for Structural Concrete and Commentary (*ACI 318-14*)* indirectly accounts for resistance to progressive collapse by providing requirements for structural integrity in concrete structures. *ACI 318-14* structural integrity requirements are intended to provide alternate load paths so that progressive collapse is avoided in the event of the unintended loss of an interior support

ACI 318-14 §9.7.7.1 gives requirements for structural integrity reinforcement for beams along the perimeter of concrete structures. The section stipulates that at least one-quarter of the bottom longitudinal reinforcement shall be continuous, with a minimum of two bars. Furthermore, at least one-sixth of the top reinforcement required at the critical section must be continuous, again with at least two bars needed to satisfy this requirement. The longitudinal structural integrity reinforcement must be enclosed by closed stirrups in satisfying section 9.7.7.1.

Longitudinal structural integrity reinforcement is required to pass through the region bounded by the longitudinal reinforcement of the columns and anchored at non-continuous supports by sections 9.7.7.3 and 9.7.7.4, respectively. *ACI 318-14* §9.7.7.5 requires that splices of structural integrity reinforcement be designed as Class B splices near mid-span for top reinforcement and near the support for bottom reinforcement. Figure 2.1 shows typical structural integrity details for beams located on perimeter frames of a building structure. The figure also illustrates the details that are acceptable to consider a stirrup to be closed.

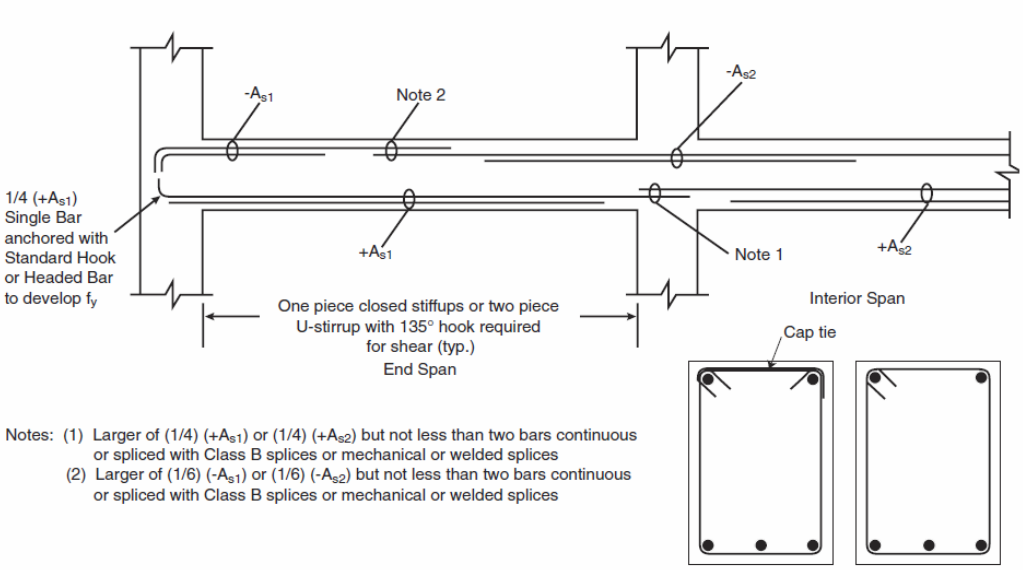

Figure 2.1: Structural integrity details for beams along the perimeter of the structure (*ACI 318-14*)

2.3 Previous Research Studies

Several academic researchers have carried out experimental and analytical studies to investigate the behavior of reinforced concrete frame structures under progressive collapse. The analytical studies have focused on column removal procedures following the alternate path method described in the previous section. The experimental studies have focused on full and scaled frame tests that simulate the loss of an interior column. The following sections discuss key findings of relevant analytical and experimental studies.

2.3.1 Tsai and Lin (2008)

Tsai and Lin (2008) studied the behavior of an eleven-story reinforced concrete frame building designed following the Taiwan seismic design code to estimate its resistance against progressive collapse. Using SAP2000 software (SAP2000 Version 17.0), four column-removal scenarios were investigated using linear static,

nonlinear static and nonlinear dynamic analysis. The four column-removal scenarios were designated as Case 1B, Case 2A, Case 1A, and Case 2B that correspond to first story column locations shown in Figure 2.2.

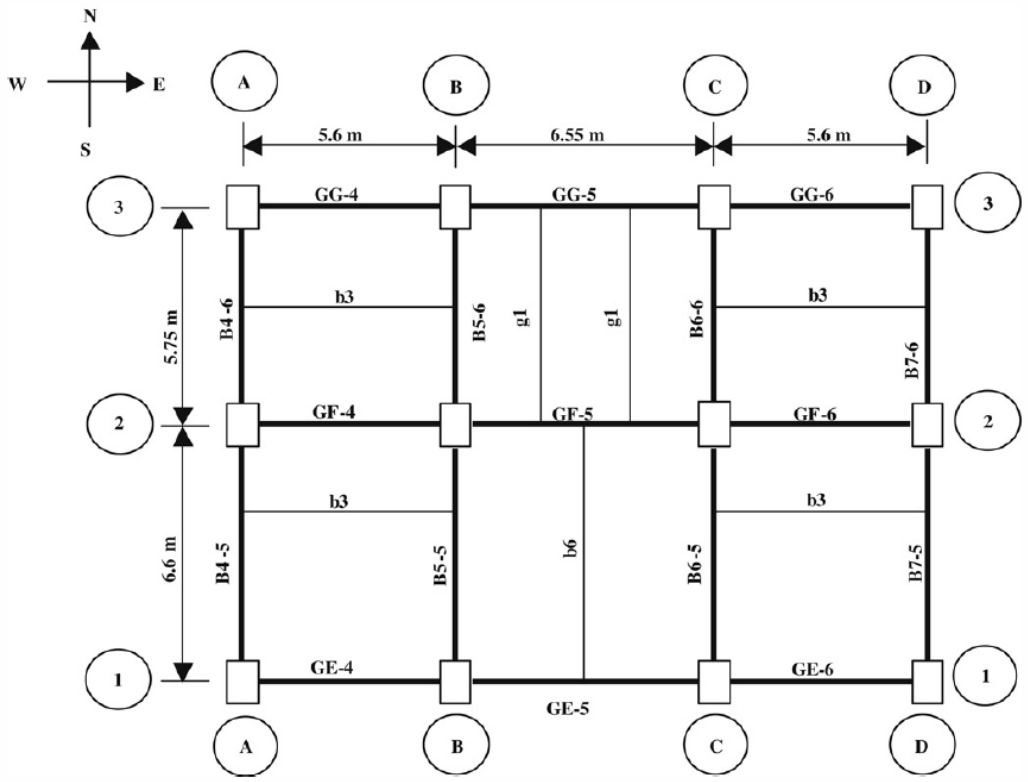

Figure 2.2: Plan view of the building (Tsai and Lin 2008)

Based on the *NEHRP Guidelines for the Seismic Rehabilitation of Buildings* (FEMA 273), the nonlinear moment-rotation response of the beams was simulated by assigning plastic hinges to each end of beam elements. The researchers used the *Progressive Collapse Analysis and Design Guidelines for New Federal Office Buildings and Major Modernization Projects* (GSA 2003 Guidelines), to determine the load combinations and acceptance criteria to use in their analyses when column removal scenarios were investigated.

According to the *GSA 2003 Guidelines* linear static analysis approach, all the elements satisfied the strength acceptance criteria. Based on this, the researchers concluded that the building has a low potential for progressive collapse. Nonlinear results demonstrated that the building meets the loading requirement of the *GSA 2003 Guidelines*. Based on an assumed plastic mechanism forming in beams, the maximum loading capacity was equal to $1.25P_{st}$, $1.62P_{st}$, $1.39P_{st}$, and $1.39P_{st}$ for Case 1B, 2A, 1A, and 2B respectively. To obtain the maximum load capacity using results from a nonlinear dynamic analysis, the peak displacement response of each time history was collected to construct the load-displacement envelope. The maximum loading capacity for the four cases was equal to $2.15P_{dy}$, $2.75P_{dy}$, $2.4P_{dy}$, and $2.4P_{dy}$ for Case 1B, 2A, 1A, and 2B respectively. P_{st} and P_{dy} are the gravity load combinations for static and dynamic analyses, respectively.

The dynamic amplification factor is defined as the ratio of the dynamic displacement response to static displacement response under an equal applied load. Based on this, the authors also concluded that nonlinear static analysis is a conservative method for estimating the resisting capacity of this structure. Nonlinear dynamic analysis is thought to be a more accurate method to analyze progressive collapse of structures. A major drawback, however, is that it is more computationally demanding than static procedures and for this reason has not been used extensively in practice. Therefore, the researchers proposed a more efficient method by using a capacity curve to simulate the nonlinear dynamic analysis results. The area under the nonlinear static load-displacement curve represents the absorbed energy of the building. The capacity curve was obtained by dividing the accumulated area under the nonlinear static curve by the maximum

displacement. Figure 2.3 shows the capacity curve, compared with the nonlinear static and dynamic curves. It can be seen that, for the case examined by Tsai and Lin, the approach based on the capacity curve compares favorably with the nonlinear dynamic analysis procedure, while the nonlinear static analysis procedure overestimates the collapse load.

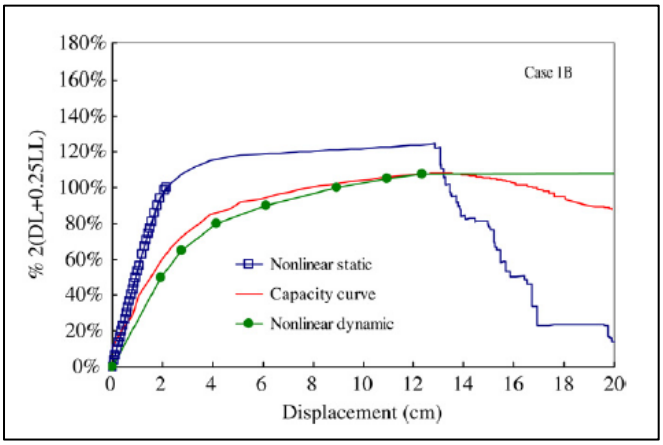

Figure 2.3: Capacity curve, and the nonlinear static and dynamic curves (Tsai and Lin 2008)

2.3.2 Yi, He, Xiao, and Kunnath (2008)

Yi et al. (2008) tested a four bay, three-story 0.33-scale sub-assemblage to investigate the progressive collapse mechanism of a reinforced concrete frame after the loss of a column in the first floor. The sub-assemblage represents the lower three stories of a frame in the perimeter of a prototype building selected by the research group. The experiment was conducted under displacement control to simulate the loss of the column of the selected building. Yi et al. (2008) selected a four-bay, eight-story reinforced concrete frame structure as a prototype and designed it according to the concrete design code in China, which has similar requirements to *ACI 318-02* but with load and resistance factors that are slightly different.

The researchers divided the force-displacement response of the sub-assemblage corresponding to a middle column removal scenario into three stages: (1) elastic, (2) formation of plastic hinge mechanism, and (3) formation of catenary action in beam, as shown in Figure 2.4. The failure of the sub-structure was governed by rupture of the bottom steel bars of the first floor beam near the middle column.

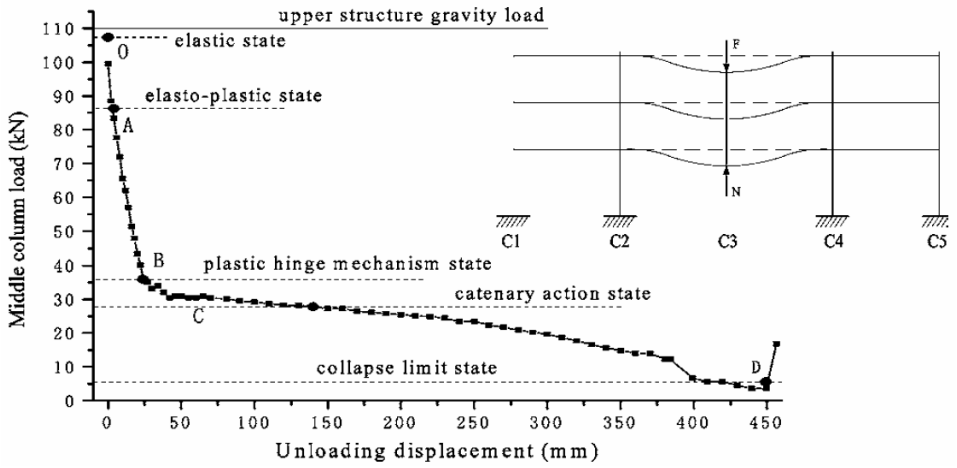

Figure 2.4: Load-displacement stages defined by Yi, He, Xiao and Kunnath (2008) for progressive collapse analysis of 2D frame

The experiment only considered the capacities of beams in the three lower floors, so the researchers claimed that it was a conservative representation of the building. Moreover, neither the capacity of the beams in the transverse direction nor the capacity of the slab were considered. Based on these assumptions and the obtained experimental results, the authors concluded that for this particular configuration the prototype structure would not collapse under its own weight after failure of one interior column in the perimeter of the first floor.

According to the authors, the static method reliably captured the behavior of their structure in a progressive collapse event. However, the researchers also concluded that a dynamic analysis should be used to obtain more accurate results.

2.3.3 Sasani and Sagiroglu (2008)

Sasani and Sagiroglu (2008) carried out a field investigation on the behavior of a six-story nonductile reinforced concrete building after failure of two columns in the first-floor corner of the building. Failure of the corner columns was generated by the simultaneous detonation of the columns during partial demolition of the building. Figure 2.5 shows the structure used in their study.

Figure 2.5: Six-story building tested by Sasani and Sagiroglu (2008)

The test results indicated that progressive collapse would not be generated after removal of corner columns in this building, even though the reinforcing details were considered non-ductile. Since the structure does not meet the integrity requirements of

the *ACI 318-14*, Sasani and Sagiroglu concluded that the structure was able to withstand the column damage and not generate progressive collapse due the three-dimensional response and redundancy of the structure. The results from this test highlight the importance of including the contribution of structural elements in the out-of-plane direction of the perimeter frame. The mechanism indentified that allowed the redistribution of loads after column removal was the bidirectional vierendeel action of the transverse and longitudinal frames.

The field test results also showed that the direction of bending moments in the beams changed in the vicinity of the joints above the detonated columns. Sasani and Sagiroglu concluded that in order for the beam bottom reinforcement to be fully effective and develop stresses up to ultimate at the face of a removed column, the reinforcement should be well anchored into the joint.

2.3.4 Qian and Li (2012a, 2012b)

Qian and Li (2012a) investigated the progressive collapse resistance of different reinforced concrete frame structures. The researchers investigated the behavior of a two-dimensional eight-story reinforced concrete frame structure after loss of a corner column in the first story. The study entailed testing four full-scale interior beam-column sub-assemblages based on the geometry of the 8-story reinforced concrete frame structure as shown in Figure 2.6. Each sub-assemblage was designed using different non-seismic details. The variables in the test specimens included longitudinal reinforcement ratios and spacing of the transverse reinforcement. Loads were applied to the laboratory specimens

using displacement control. The researchers also used finite element analysis to validate the laboratory results.

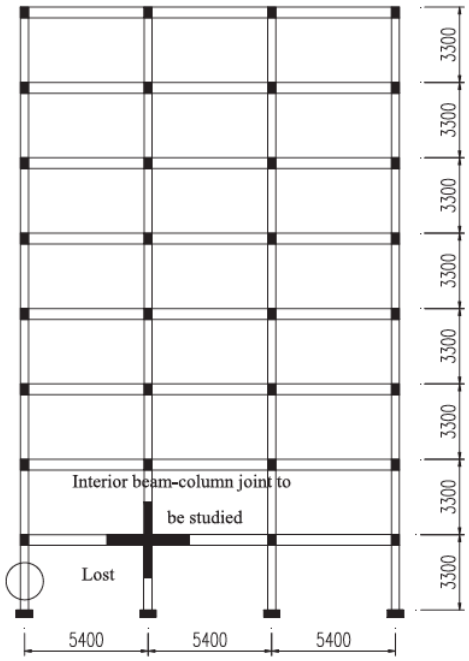

Figure 2.6: Sketch of the eight-story reinforced concrete framed structure (in mm) investigated by Qian and Li (2012a)

The laboratory results showed that the failure mechanism was controlled by the formation of a plastic hinge in the left beam near the column face. Also, increment of the longitudinal and transverse reinforcement ratios of the non-seismic detailing increased the load-carrying capacity and the displacement response of reinforced concrete frames in resisting progressive collapse caused by the loss of an exterior column. Finally, the finite element simulations compared well with the load-displacement response measured in the laboratory as shown in Figure 2.7.

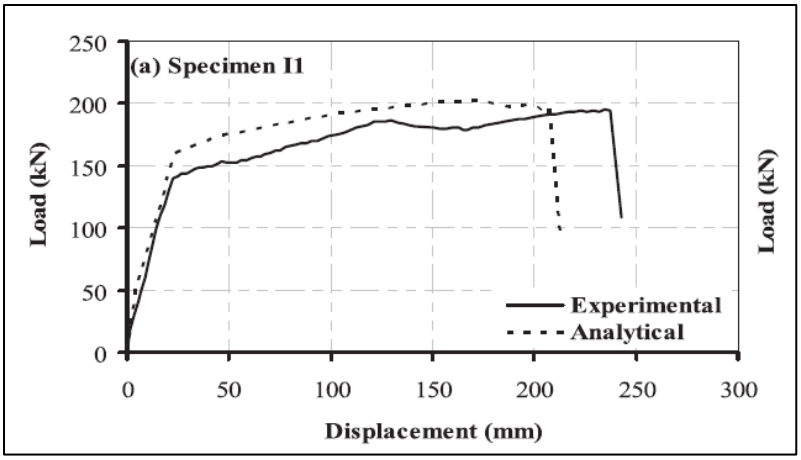

Figure 2.7: Analytical and experimental load displacement results (Qian and Li 2012a)

Subsequently, Qian and Li (2012b) performed a series of push-down tests to study the slab effect on reinforced concrete frame structures after loss of a column). Six specimens, three with slab and three without the slab, were tested under monotonic loading. Two specimens with slab and two without slab were designed for a non-seismic zone according to provisions of Singapore Standard CP 65, and one specimen with slab and one without slab were designed for a seismic zone based in the *ACI 318-08*.

The experimental results showed that the presence of a reinforced concrete slab increased the the ultimate load-carrying capacity of the specimens to resist progressive collapse by 40 to 63%. Similarly, the seismic detailing increased the ultimate load-carrying capacity of the specimens to resist progressive collapse by approximately 62%. Failure occurred by fracture of the top reinforcing bars near the fixed end on the beam-column specimens, and shear diagonal cracks in the slab of the specimens with slabs. Only the specimens designed with seismic details reached the required load specified by *GSA 2003 Guidelines* to resist progressive collapse.

2.3.5 Dat and Hai (2013)

Dat and Hai (2013) studied the effect of membrane action on the progressive collapse behavior of a beam-slab substructure when subjected to a penultimate-internal column loss. Sixteen 0.5-scale sub-assemblages of a prototype nine-story reinforced concrete frame building were analyzed applying distributed load on the slab using the non-linear finite element software DIANA (TNO DIANA BV), and validated using previous experimental data. The effect of several parameters was studied, including the rotational restraint of the slab around the perimeter, top reinforcement and presence of interior beams. The main variables in all specimens were the slab top and bottom reinforcement ratios. Figures 2.8 and 2.9 show the details of the substructure.

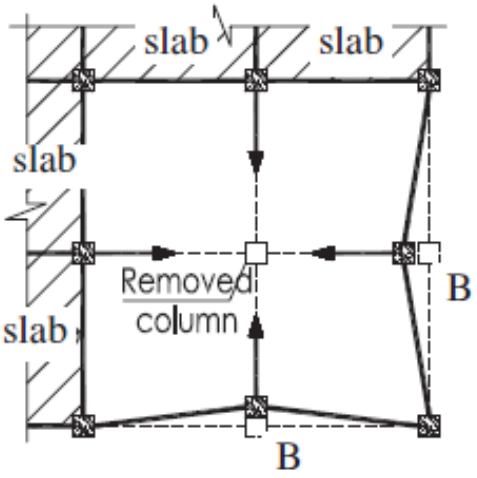

Figure 2.8: Details of the substructure investigated by Dat and Hai (2013)

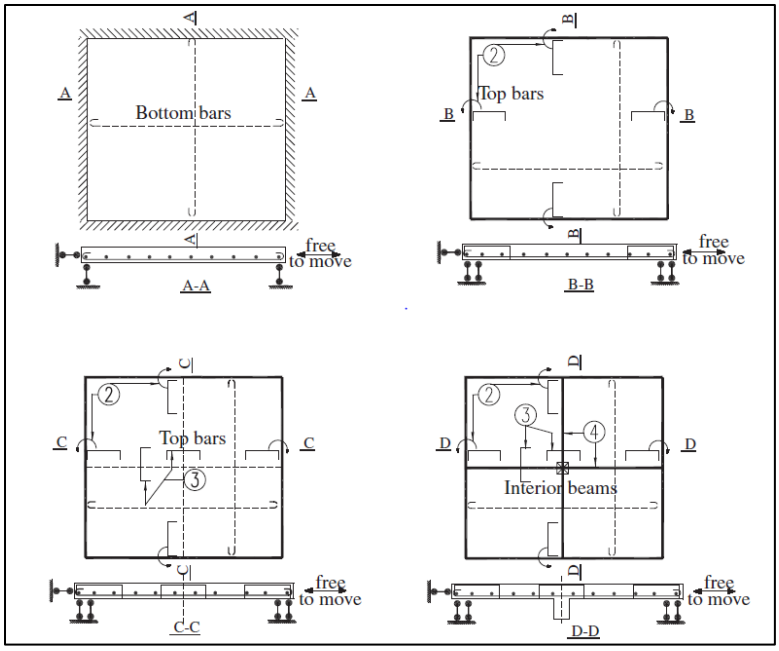

Figure 2.9: Slab Models used by Dat and Hai (2013)

The researchers concluded that the membrane behavior of the affected slabs, consisting of a peripheral compressive ring of concrete supporting tensile membrane action in the central region, represents an important line of defense against progressive collapse. The load-carrying capacity of beam-slab substructures can be increased by rotational restraint of the slab, top reinforcement content in the slab and interior beams. As shown in Figure 2.10, the collapse mechanism that controlled the simply supported slab model was the tensile membrane action. The load-carrying capacity of the rotationally restrained slab increased due the contribution of slab negative moment along the edge perimeter. The rotationally restrained beam-slab models increased the load-carrying capacity due the contributions of slab and beam negative moment, and catenary action developed in the beams.

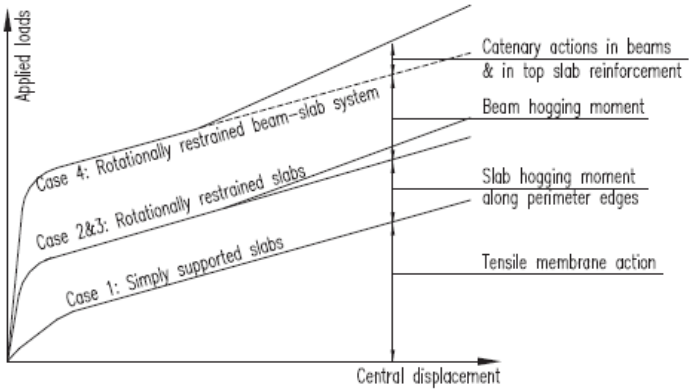

Figure 2.10: Load carrying capacity of the models investigated by Dat and Hai (2013)

2.3.6 Yu and Tan (2013, 2014)

Yu and Tan (2013) investigated the progressive collapse resistance of different reinforced concrete frame structures. Two 0.5-scale beam-column sub-assemblages of a five-story reinforced concrete frame structure were tested under a middle column removal scenario to simulate progressive collapse. The specimens consisted of a two-span beam, a middle joint that simulated the column removal position and two end columns of 900 mm length. The tests were conducted by applying a point load at the top of the middle joint using displacement control until the specimens failed. The prototype had a ground story height of 4 m and a typical story height of 3 m. The typical span length in both directions was 6 m. The prototype dimensions were used to complete two different designs: one for seismic zone and the second for a non-seismic zone based on *ACI 318-05*. The main differences in the designs were the longitudinal and transverse reinforcement ratios in beams. For seismic design, the prototype was designed as a special moment-resisting frame with a base shear coefficient of 0.034. The top, bottom and transverse reinforcement ratios in the beams were 0.90%, 0.49% and 0.0075% respectively. On the other hand, the top, bottom and transverse reinforcement ratios for

the prototype designed for a non-seismic zone were 0.73%, 0.49% and 0.0037% respectively. In addition, a macromodel-based finite element model of the specimens using the non-linear finite element software Engineer's Studio (Forum8) was proposed to simulate the structural response of the specimens using fiber elements for the beams, columns and joint.

Yu and Tan concluded that the laboratory specimens developed three distinct load carrying mechanisms at progressively increased displacements: (1) flexural mechanism governed by the bending strength of the beam at critical (end) sections, (2) compressive arch action developed after plastic hinges form at the beam ends near the middle column, and (3) catenary action when the axial force in the beam changed from compressive (arch) to tensile. Due the advantage of seismic detailing in shear resistance was not fully exposed, seismic detailing did not increase the load-carrying capacity. Failure occurred at the beam ends after significant widening of cracks in the concrete and bottom longitudinal reinforcing bar fracture. Finally, compared to an analytical model constructed using frame elements connected using rigid joints; the proposed finite element model was more accurate.

Yu and Tan (2014) tested four specimens under a column removal scenario to investigate the effect of special detailing techniques in the catenary capacity of the beams. The special detailing techniques recommended by the authors consisted of: (1) adding a reinforcement layer at mid-height of beam sections; (2) partially debonding bottom-reinforcing bars in the joint region, and (3) constructing partial hinges located one beam depth from the closest joint face to develop a "strong column weak beam mechanism". The partial hinges were built by bending one of the top bars down and

bending one bottom bar was up. The two bent bars were leveled off at the bottom and top reinforcement layer respectively at the end of the partial hinge region. Two top reinforcing bars were stopped at 1000 mm from the face of the column. The bottom reinforcing bars were continuous along the beam. The design of the prototype building and the sub-assemblage specimens was the same as in Yu and Tan (2013) designed for non-seismic zone, but with different reinforcement ratios. The top, bottom and transverse reinforcement ratios in the beam were 1.24%, 0.82% and 0.0075% respectively. In addiction of this specimen, three specimens were designed with the explained special detailing techniques.

The experimental results also exhibited the different load-carrying mechanisms reported in Yu and Tan (2013) at different values of center displacement. All the special detailing techniques used in the specimens resulted in increased deformation capacity and catenary capacity of the beams. The presence of an additional reinforcement layer at mid-height of beam sections increased the ultimate load-carrying capacity by 112%. The partially debonding and the plastic hinges special detailing techniques sections increased the ultimate load-carrying capacity by 79% and 127%, respectively. In addition, the deformation capacities of the three specimens with special detailing increased by 19%, 14% and 21% for the special detailing techniques 1, 2 and 3 respectively.

Yu and Tan (2014) concluded that the additional reinforcement layer and the deboning bottom reinforcing bars in the middle joint technique increased the rotation capacity at the beam-column connections. The partial hinges increased the rotation capacity of the connections and shortened the effective lengths of beam segments in rigid rotation. Given that the first two techniques require additional reinforcing bars, the

authors recommended the partial hinges technique as a more economical alternative to improve the displacement capacity and be able to the large-displacement mechanisms needed to prevent progressive collapse.

2.3.7 Lew, Bao, Pujol, and Sozen (2014)

The selected prototype structure in the research project is the same as the one used in this study to allow comparison with the results. The main difference is that Lew et al. (2014) detailed their laboratory specimens to be consistent with structures located in high or moderate seismic zones, and their correspondingly high seismic design categories (SDC) (SDC C or SDC D). The research presented in this dissertation focuses on detailing of structures in an area of low seismicity, with detailing consistent of a SDC A.

Lew et al. (2014) tested two full-scale reinforced concrete beam-column sub-assemblages under a column removal scenario to investigate the behavior and failure modes in a progressive collapse scenario. A 10-story prototype reinforced concrete frame building was used as the building prototype for their tests. The ground story of the prototype was 15 ft high; upper stories were 12 ft tall. The spans length for the longitudinal and transverse direction was 20 ft and 30 ft respectively. The first prototype was designed for Seismic Design Category C, and the other for Seismic Design Category D, according to the *ACI 318-02* Code.

A sub-assemblage based on the prototype building geometry was constructed in the laboratory to represent two 20-ft spans of the exterior moment-resisting frames in the first floor where an intermediate support was eliminated. To simulate the column removal

scenario, monotonic vertical displacement was applied to the center of the laboratory specimen at the position of column removal.

From the observed specimen behavior, the investigators divided the load transfer characteristics into three stages that occurred during the tests: (1) arching action caused by the additional capacity provided by horizontal restraint coming from a floor slab; (2) plastic hinge formation governed by yielding of the reinforcing bars and concrete crushing; (3) and catenary action due to the development of tensile axial force in the longitudinal reinforcement in the beams. These mechanisms developed at successively larger center column displacement applied during the tests. Figure 2.11 illustrates the load transfer characteristics in these three stages. Failure of the specimens occurred when bottom reinforcing bars fractured at the location of a principal crack that formed close to the central column. The experiment results showed that the beam chord rotation capacities of the specimens were seven to eight times larger than those given in the *Seismic Rehabilitation of Existing Buildings Standard* (ASCE 41-06).

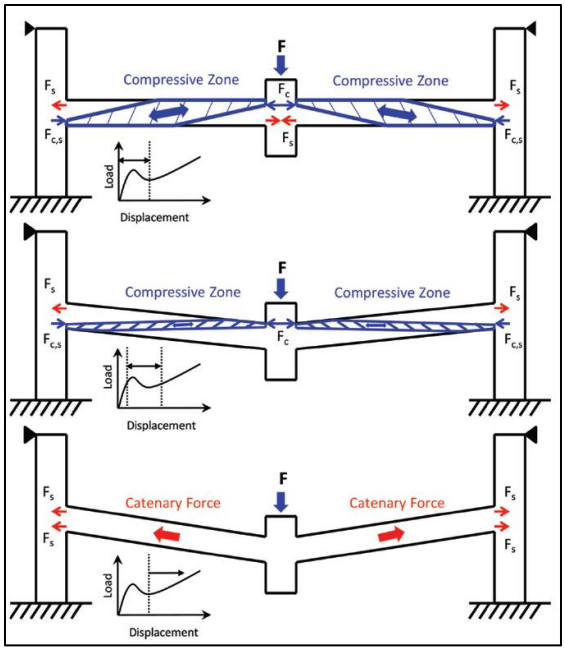

Figure 2.11: Specimens behavior described by Lew et al. (2014)

2.3.8 Alogla, Weekes, and Augusthus-Nelson (2016)

In this study, four 0.5-scale reinforced concrete beam column sub-assemblages of a multi-story building were studied under a column removal to investigate the progressive collapse behavior of reinforced concrete frame structures. The geometry of the sub-assemblages is similar to those that Yu and Tan (2013, 2014) tested. Through this study the investigators proposed a new mitigation scheme to increase the catenary action resistance against progressive collapse. The new mitigation scheme consists of adding two additional longitudinal bars at different elevations of the beam section. The test specimens represent part of a multi-story, multi-bay frame building designed in non-seismic zones according to the *ACI 318-05*.

The experimental results showed that the behavior of the specimens could be divided into three stages: (1) flexural, (2) compressive arch action, and (3) catenary action. At the beginning of the test, flexure was the dominant mechanism. Compressive

arch action began when cracks developed at the beam-column joint interfaces. Finally, once the cracks were developed throughout the beam length and passed completely through the beam section, the behavior was dominated by catenary action. Figure 2.12 shows load-deflection curves where the three behavior stages are marked. The load-carrying capacity of specimens containing the new reinforcing scheme proposed by the investigators was 5 to 12% larger in the compressive arch action stage and 52 to 109% larger during catenary action compared with the specimen with a standard reinforcing pattern.

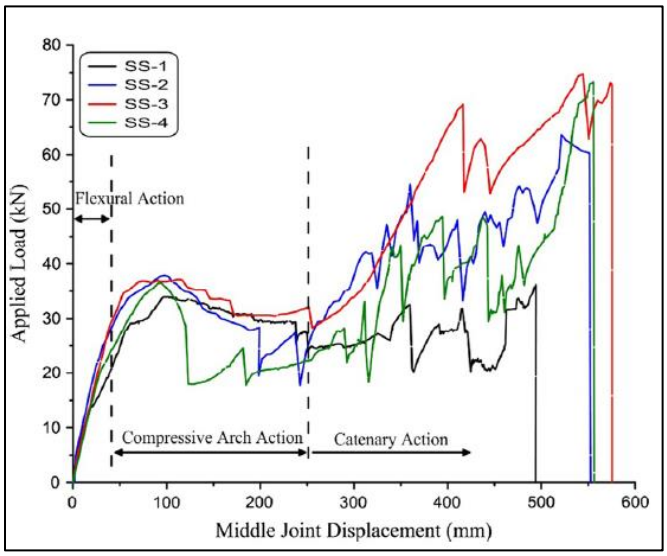

Figure 2.12: Three stages described by Alogla Weekes and Augusthus-Nelson (2016)

2.3.9 Ren, Li, Lu, Guan, and Zhou (2016)

The main objective of this study was to investigate the resisting mechanisms contributing to progressive collapse resistance in reinforced concrete frame structures taking in consideration the influence of the slab. Seven 0.33-scale reinforced concrete beam-slab sub-assemblages of a six-story reinforced concrete frame building designed in accordance with the Chinese building codes were tested under a middle column removal

scenario. The first story was 4.2 m high, and the remaining stories were 3.6 m high. The span length in both directions was 6 m. Also, the floor system was composed of beams and slabs. Several parameters were considered, including beam height, slab thickness, and the peak ground acceleration in the seismic design.

The researchers found two main resisting mechanisms: a flexural mechanism at displacements smaller than 6.6% of the beam span length, and catenary action at displacements larger than 6.6% of the beam span length. The slab increased both load carrying resisting mechanisms. Increases in beam height and slab thickness resulted in an increase only in the load carrying capacity during development of the flexural mechanism. In contrast to previous studies, increase the peak ground acceleration in the seismic design did not make a significant difference in the catenary mechanism.

2.3.10 Khorsandnia, Valipour, Foster, and Amin (2017)

Khorsandnia et al. (2017) tested two 0.4-scale reinforced concrete frames having three bays and two stories to investigate the development of catenary action after interior column removal. To simulate this scenario, load was applied at the top of the missing column using displacement control. Also, the effect of use a reduce number of beam stirrups with steel fibers in the concrete throughout the frame was investigated.

The laboratory results showed that the beams developed minimum tensile catenary action as shown in Figure 2.13. The frames were tested without taking into account the restraint provided by floor slabs present in real buildings. Because of this, the researchers noted the results may have been influenced by not having the horizontal restraint.

This restraint allows development of membrane action, which has been found to increase the load carrying capacity by the catenary action. The replacement of stirrups with steel fibers in the concrete did not affect the resisting mechanisms as shown in Figure 2.13, where the frame with conventional stirrups are designated as CRC, and the frame with steel fiber reinforced concrete is designated as SFRC.

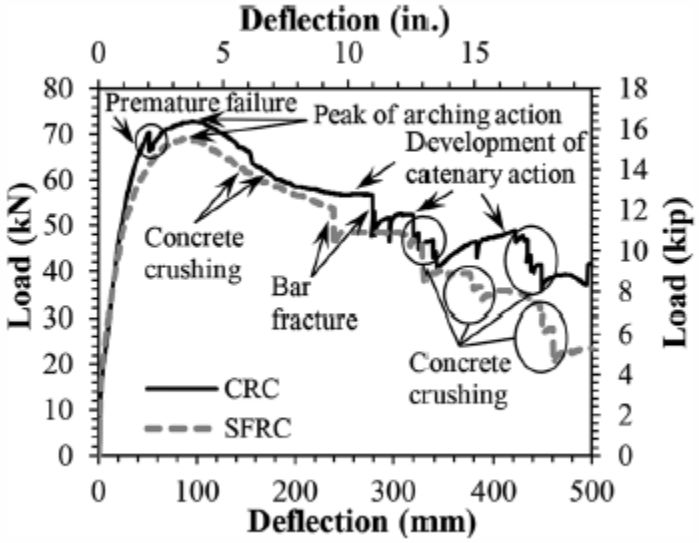

Figure 2.13: Load versus vertical deflection at top of the removed column (Khorsandnia, Valipour, Foster, & Amin 2017)

2.4 Summary and Conclusions

Based on the literature review presented in this chapter, it can be seen that most of the research groups have focused on testing scaled sub-assemblages and of buildings containing seismic details. These sub-assemblages have been investigated under loading resembling progressive collapse scenarios. The research proposed seeks to investigate the structural integrity of buildings designed for a non-seismic zone. Non-seismic detailing of beams in perimeter frames is specifically different from seismic detailing in two major areas: (1) the spacing of transverse reinforcement at beam ends is larger; and (2) bottom

longitudinal bar splices are typically located near beam ends whereas they would occur near midspan for seismic detailing. The effect of splice location of bottom longitudinal reinforcement on the performance of beams in perimeter frames after loss of an interior support is an important variable that should be evaluated. The effect of increased spacing of transverse reinforcement will be included in the design of the prototype building since a non-seismic region will be chosen for design. This research project includes laboratory testing of full-scale beam-column sub-assemblages of a ten-story reinforced concrete frame building prototype identical to the one chosen by Lew et al. (2014) to allow for direct comparison with past research. Moreover, analytical simulations of the prototype building and the sub-assemblages will be carried out and validated with the experimental results.

CHAPTER 3

PROTOTYPE BUILDING DESIGN

3.1 Introduction

This chapter describes the analysis and design procedure used in the ten-story prototype reinforced concrete frame building from which the laboratory specimens were modeled. The structural analysis of the prototype building was based on the *International Building Code 2015* (IBC 2015) which refers to *ASCE 7-10* to define loading in the prototype building. In order to evaluate the effect of splice location of structural integrity reinforcement of beams along the perimeter of the structure after loss of an interior support, the first story of the exterior frame labeled as 1 in Figure 3.1 was designed for a low seismic design category so that the non-seismic provisions of *ACI 318-14* would apply (*ACI 318-14*, Chapter 18 was not followed for design of the prototype). As indicated in Chapter 2 – Literature Review, most of the research studies conducted to date on progressive collapse of reinforced concrete buildings have concentrated on elements containing seismic details and none have studied the effect of splice location of structural integrity reinforcement so the motivation for choosing this design is to investigate the structural integrity in buildings designed for a non-seismic zone.

3.2 Description

Lew et al. (2014) developed the overall configuration and dimensions of two ten-story prototype reinforced concrete buildings for office occupancy to design laboratory specimens in a research program intended to evaluate the progressive collapse resistance

of reinforced concrete frames. Each of the two prototypes buildings was designed in different seismic design regions to evaluate the effect of detailing corresponding to special and intermediate moment-resisting frames. For comparison with the laboratory results reported by Lew et al. (2014), the same configuration was chosen for the prototype building in this research with plan dimensions equal to 100 ft × 150 ft. In contrast with the prototypes buildings designed by Lew et al., the prototype building was designed for a location in Houston, TX, resulting in a prototype building with a low seismic design category (SDC A). Therefore, the lateral-force resisting system design was governed by wind effects and was composed of ordinary moment frames. Figures 3.1 and 3.2 show the plan layout and exterior frame elevation along column line 1 of the prototype building, respectively. The beams and the columns have the same dimensions at all story levels.

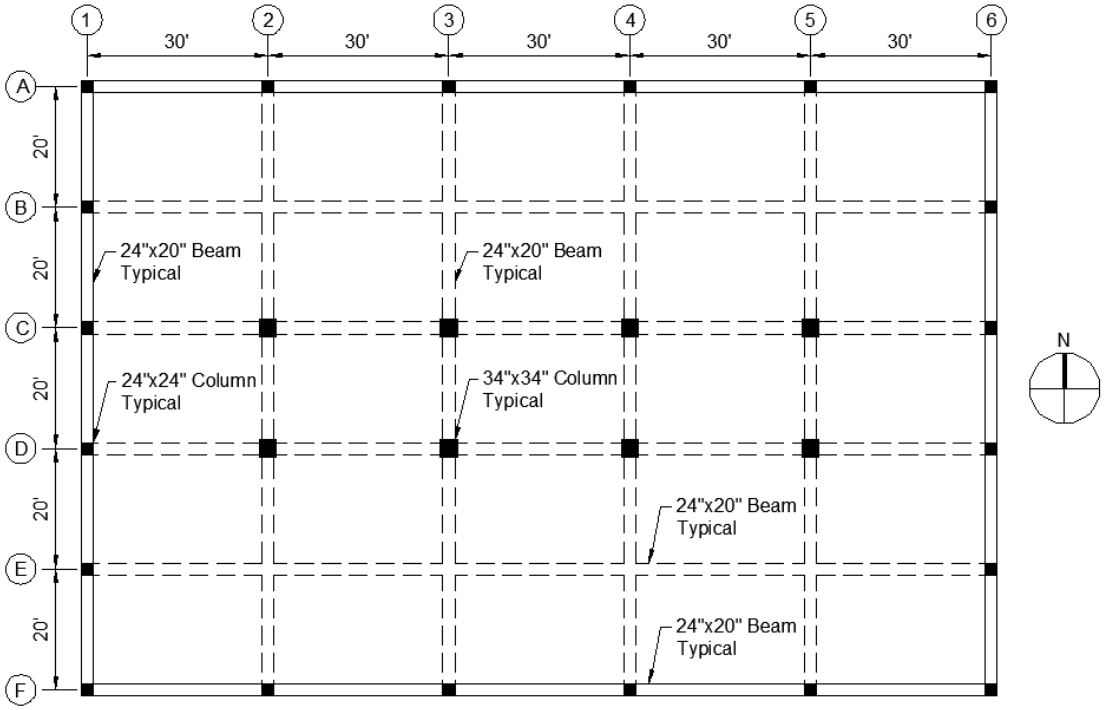

Figure 3.1: Plan layout of the prototype building (Lew et al. 2014)

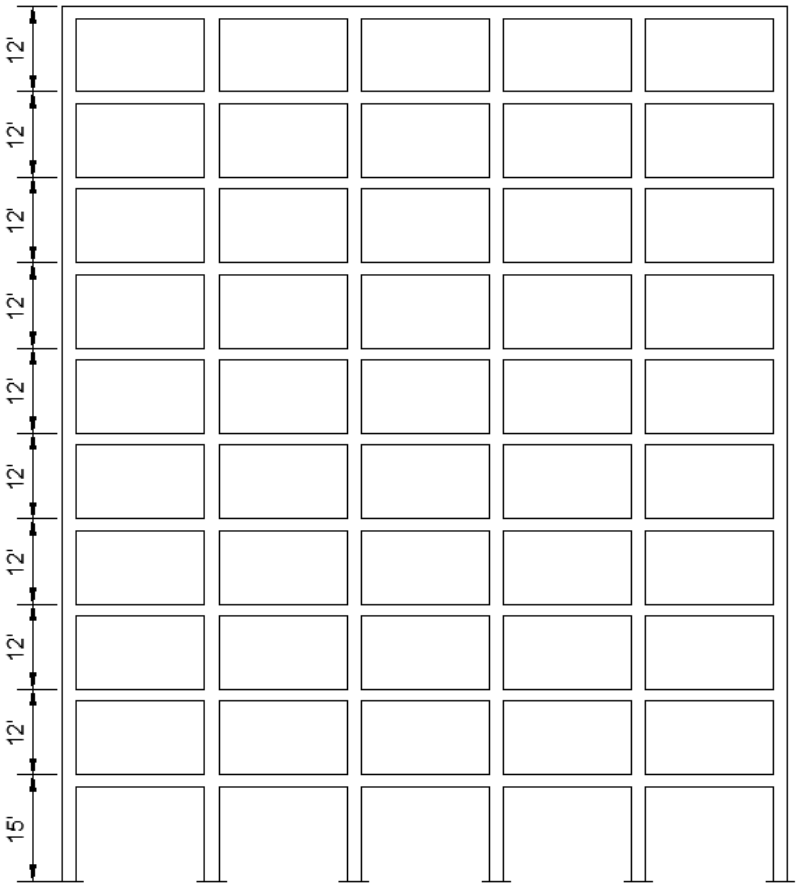

Figure 3.2: Elevation view of prototype building along column line 1 (Lew et al. 2014)

3.3 Structural Analysis

Loads on the prototype building were determined using the *IBC 2015*, which refers to *ASCE 7-10* for wind and seismic loads. *ASCE 7-10* was also used to calculate dead and live loads.

3.3.1 Load Combinations

Consistent with Chapter 2 of *ASCE 7-10*, the following load combinations were used for design of the prototype building.

$$U = 1.4D \quad (3.1)$$

$$U = 1.2D + 1.6L \quad (3.2)$$

$$U = 1.2D + 0.5W \quad (3.3)$$

$$U = 1.2D + 1.0W + 1.0L \quad (3.4)$$

$$U = 1.2D + 1.0E + 1.0L \quad (3.5)$$

$$U = 0.9D + 1.0W \quad (3.6)$$

$$U = 0.9D + 1.0E \quad (3.7)$$

where:

U= factored load effect

D = dead load effect,

E = earthquake load effect,

L = live load effect, and

W = wind load effect.

3.3.2 Dead and Live Loads

Dead and live loads analysis was based on specifications in *ASCE 7-10*. Superimposed dead loads were determined according Chapter 3 of *ASCE 7-10.* Furthermore, live loads were determined according Chapter 4 of *ASCE 7-10*. Table 3.1 shows the loads values. Floor live load of 100 psf was chosen for consistency with Lew et al. (2014).

Table 3.1: Superimposed gravity loads

Load	Uniform Load (psf)
floor superimposed dead load	30
roof superimposed dead load	10
floor live load	100
roof live load	20

3.3.3 Wind Loads

Wind loads were computed using *ASCE 7-10*. The prototype building met all requirements for the Directional Procedure described in Chapter 27 of *ASCE 7-10*. Table 3.2 shows the concentrated lateral force applied at each floor and the resultant force generated by the wind loads. The details of the procedure to determine the wind loads are given in Appendix A.

Table 3.2: Wind loads values

Floor	Concentrated Wind Force (kip)	
	E-W	N-S
roof	26	42
9	51	83
8	50	82
7	49	80
6	48	78
5	46	76
4	45	74
3	43	71
2	41	68
1	42	71
∑	441	725

3.3.4 Seismic Loads

Seismic load analysis met the requirements of *ASCE 7-10*. The seismic analysis method followed the Equivalent Lateral Force Procedure described in Chapter 12 of *ASCE 7-10*. Table 3.3 lists the concentrated seismic force at each floor and the seismic base shear generated by the seismic loads. The details of the procedure to determine the seismic loads are given in Appendix A.

Table 3.3: Seismic loads values

Floor	Concentrated Seismic Force (kip)
10	48
9	47
8	40
7	34
6	28
5	22
4	16
3	11
2	7
1	3
∑ (Seismic Base Shear)	255

3.4 Frame Design

The prototype building was analyzed using a structural analysis commercial package SAP2000 (SAP2000 Version 17.0). The SAP2000 model simulates the three-dimensional prototype building assuming fixed-base connections to the foundation as shown in Figure 3.3. The nominal properties of the materials that were used in the analysis are listed in Table 3.4. Moment of inertia of the beams and columns was reduced to one-half to account for cracked section properties. Also, the weight of a 7.5 in. thick concrete slab was taken into account and applied to the beams according to their tributary area. Although the slab thickness was not designed, it met the minimum thickness requirement of Chapter 8 in the *ACI 318-14* Code for a two-way slab with beams spanning between the supports on all sides. The first floor of the exterior frame along column line 1 (Figure 3.1) of the prototype building was designed following the non-seismic requirements of the *ACI 318-14* Code (Chapter 18 was excluded). The design was controlled by the load combinations of gravity and wind loads. Figure 3.4 shows

typical exterior and interior beam span of the exterior frame on the first floor including the design loads. The design loads values are summarized in Table 3.5.

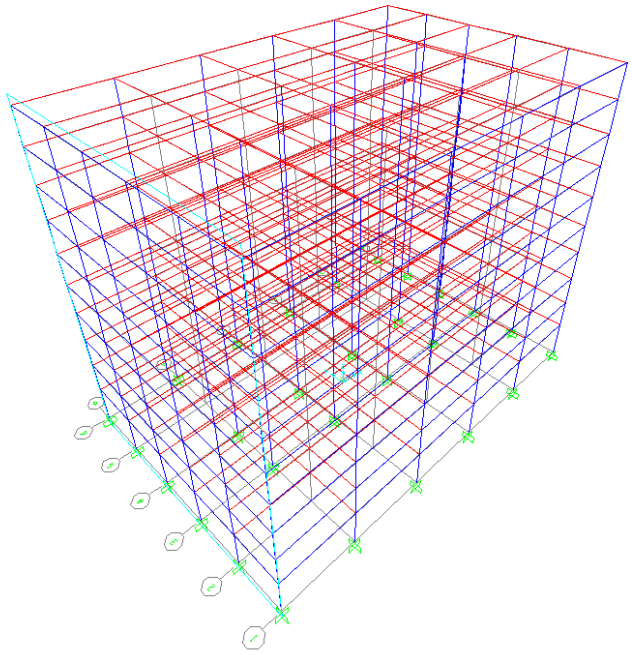

Figure 3.3: Sap2000 model of the prototype building

Table 3.4: Nominal properties of the material used in the analysis

Property	Value
normal weight concrete (lb/ft^3)	150
concrete nominal compressive strength (psi)	4000
reinforcing bars yield strength (ksi)	60

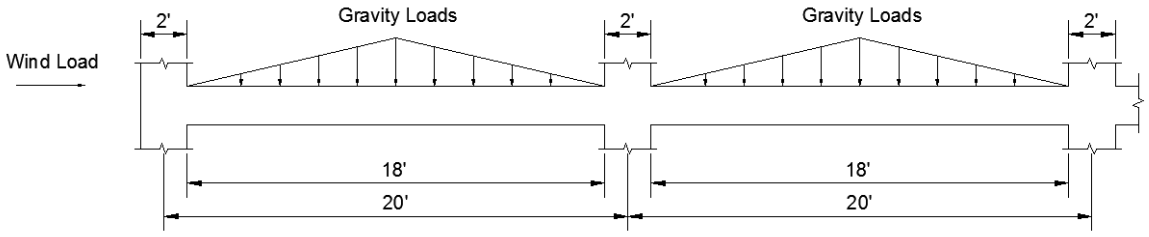

Figure 3.4: Typical exterior and interior beam span of the exterior frame on the first floor including the design loads

Table 3.5: Design loads values

Load	Value
superimposed dead load (plf)	300
live load (plf)	1000
wind load (kip)	71

3.4.1 Beam Design

Following Chapter 9 and 22 of the *ACI 318-14* Code, Table 3.6 shows the flexural design for critical sections in a typical exterior and interior beam of exterior frame 1 on the first floor. Furthermore, Table 3.7 shows the shear and torsion design according Chapter 9 and 22 of the *ACI 318-14*. The reinforcement details meet the requirements of Chapter 25 of the *ACI 318-14*. Also, the reinforcement details meet the provisions for structural integrity contained in *ACI 318-14 §*9.7.7. Figures 3.5 and 3.6 show the reinforcement details for the typical exterior and interior beam of exterior frame 1 on the first floor. Detailed design calculations are presented in Appendix B.

Table 3.6: Summary of flexural reinforcement needed at critical section for typical exterior and interior beam of exterior frame 1 on the first floor

Location		M_u (k-ft)	A_s Required (in^2)	Reinforcement	ϕM_n (k-ft)
Exterior span	midspan	56.2	1.41	4-No. 6	134.5
	face of the support	-159.4	2.11	4-No. 7	-180.2
	face of the support	88.6	1.41	4-No. 6	134.5
Interior span	midspan	44.7	1.41	4-No. 6	134.5
	face of the support	-145.9	1.92	4-No. 7	-180.2
	face of the support	71.6	1.41	4-No. 6	134.5

Table 3.7: Summary of shear and torsion design for typical exterior and interior beam of exterior frame 1 on the first floor

Location	V_u (k)	T_u(k-ft)	Transverse Reinforcement
Exterior Span	25.3	81.2	No. 4 @ 8”
Interior Span	29.9	81.2	No. 4 @ 8”

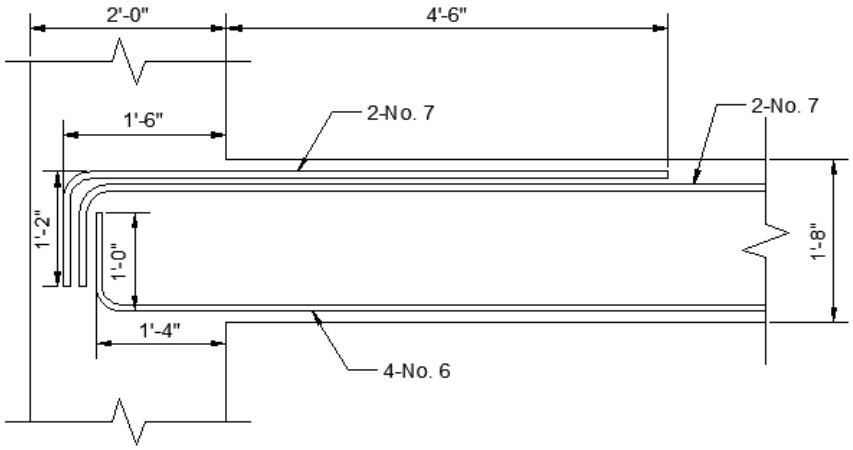

a)

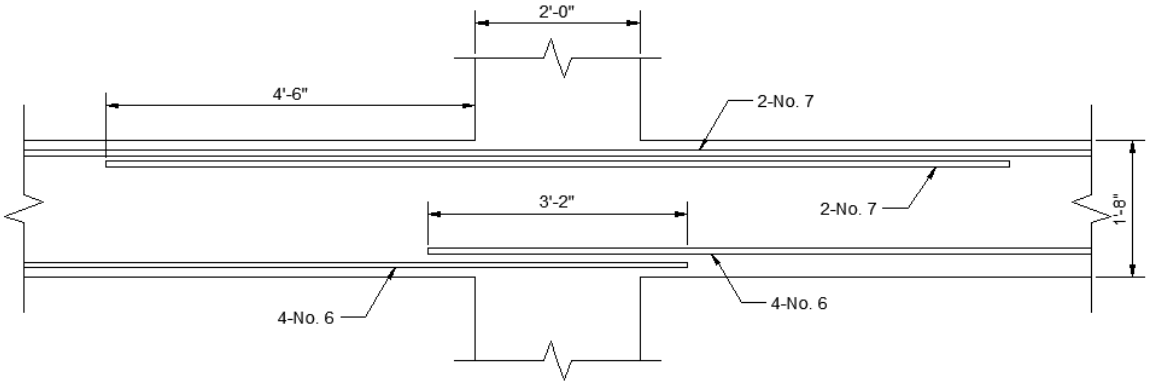

b)

Figure 3.5: Details of flexural reinforcement a) anchorage at exterior column and b) at interior column (note: stirrups are excluded for clarity)

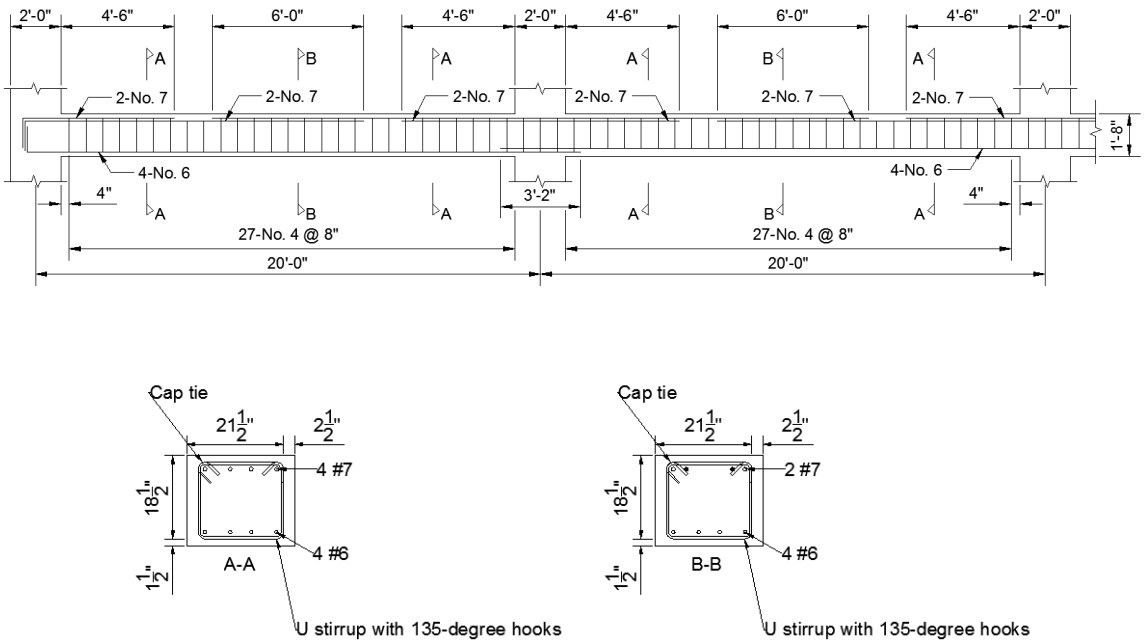

Figure 3.6: Reinforcement details for typical exterior and first interior beam of the first floor beam of frame 1

3.4.2 Column Design

Figure 3.7 shows the interaction diagrams with the factored loads for typical corner and interior column of exterior frame 1 on the first floor. Reinforcement details for the columns are shown in Figure 3.8 and 3.9. The design was based on Chapters 10, 22 and 25 of the *ACI 318-14*. The design calculations are presented in Appendix B.

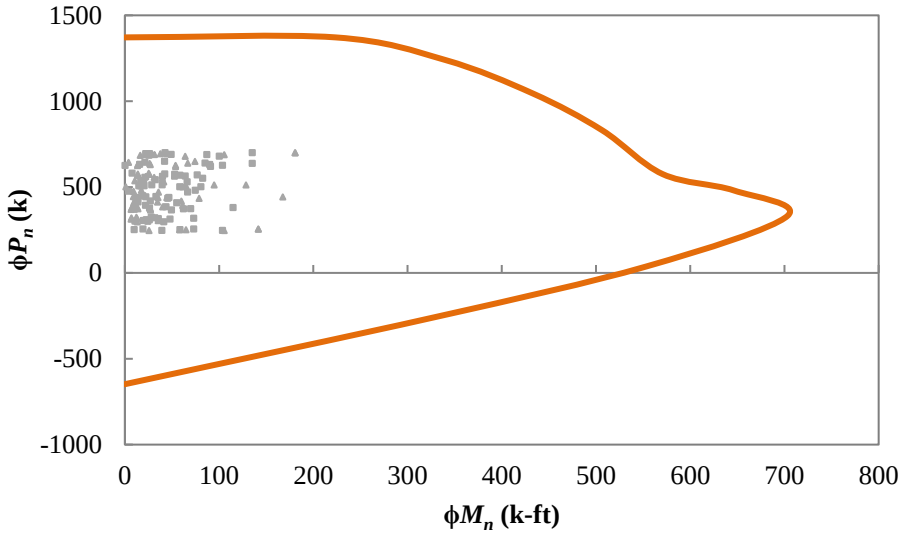

a)

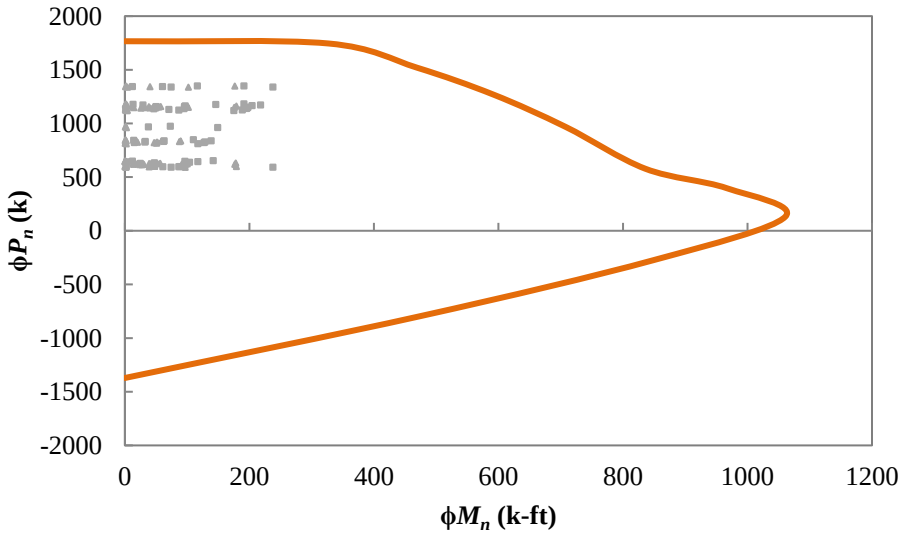

b)

Figure 3.7: Interaction diagram for (a) corner column and (b) interior column of exterior frame 1 on the first floor (grey squares represent values from different load combinations)

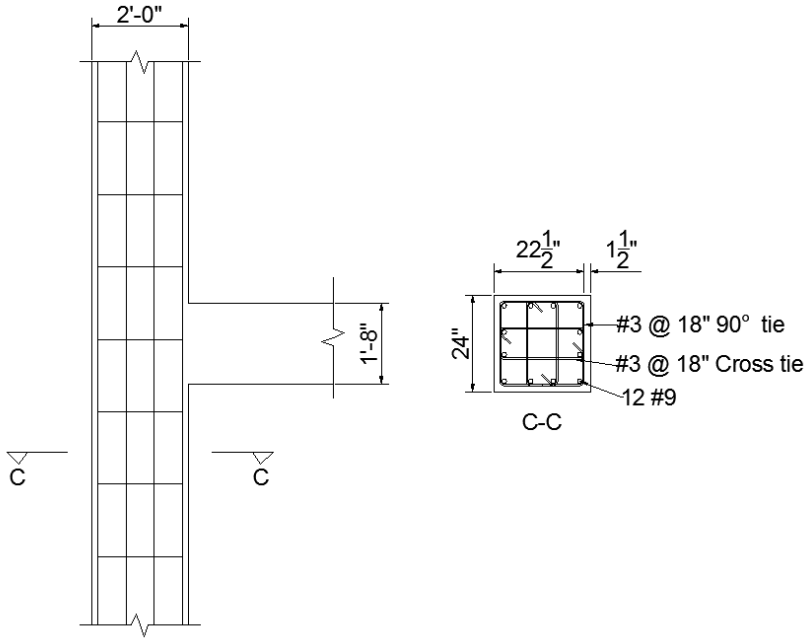

Figure 3.8: Reinforcement details for corner column of exterior frame 1 on the first floor

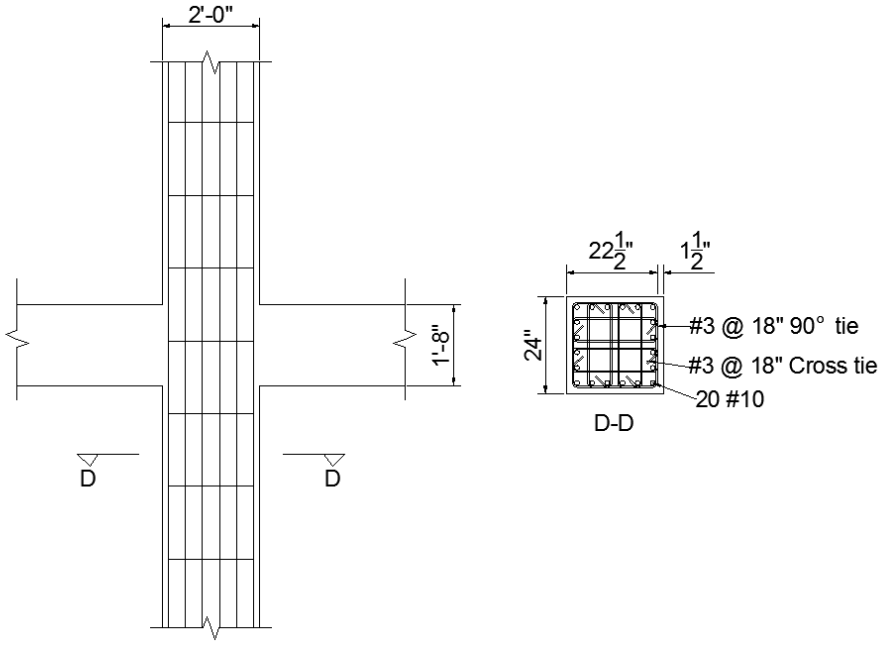

Figure 3.9: Reinforcement details for interior column of exterior frame 1 on the first floor

3.5 Summary

The procedures for the structural analysis used in prototype building from which the laboratory specimens were modeled were presented in this chapter. The structural analysis of the prototype building was based on the *IBC 2015* which refers to *ASCE 7-10* to define loading in the prototype building. In order to evaluate the effect of splice location of structural integrity reinforcement of beams along the perimeter of the structure after loss of an interior support, the first story of the exterior frame along column line 1 was designed for a low seismic design category. The design met the requirements of the *ACI 318-14* Code, excepting Chapter 18. Because the design is typical for all spans, two interior spans of the exterior frame 1 on the first story were chosen as specimens to capture the behavior of the beam after loss of an interior column in the prototype building. The laboratory specimens represent the full-scale portion of the prototype building. The description of the laboratory specimens is presented in Chapter 4.

CHAPTER 4

DESCRIPTION OF LABORATORY SPECIMENS

4.1 Introduction

This chapter discusses the laboratory tests designed to study the collapse behavior of a sub-assemblage based on the prototype building discussed in Chapter 3. The laboratory specimens represent a full-scale portion of the ten-story reinforced concrete frame building prototype. The sub-assemblage was chosen to capture the behavior of the beam along a perimeter after loss of an interior column. This chapter presents the laboratory specimen geometry, its design details and the boundary conditions selected. The laboratory setup; specimen instrumentation and it purpose; and the testing protocol employed is also discussed.

4.2 Specimen Description

The test specimens represent full-scale beam-column sub-assemblages of a first story frame in the perimeter of the prototype. These laboratory specimens represent two interior spans of a beam in the perimeter of the first story where an intermediate column has been lost. Figures 4.1 and 4.2 show the specimen location.

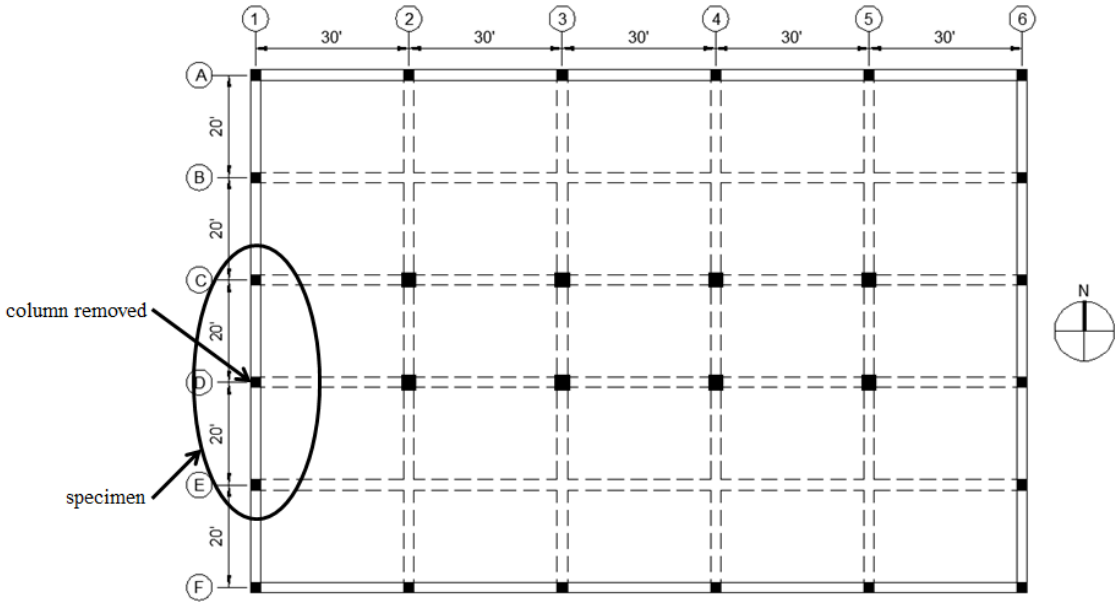

Figure 4.1: Plan layout of the specimen location

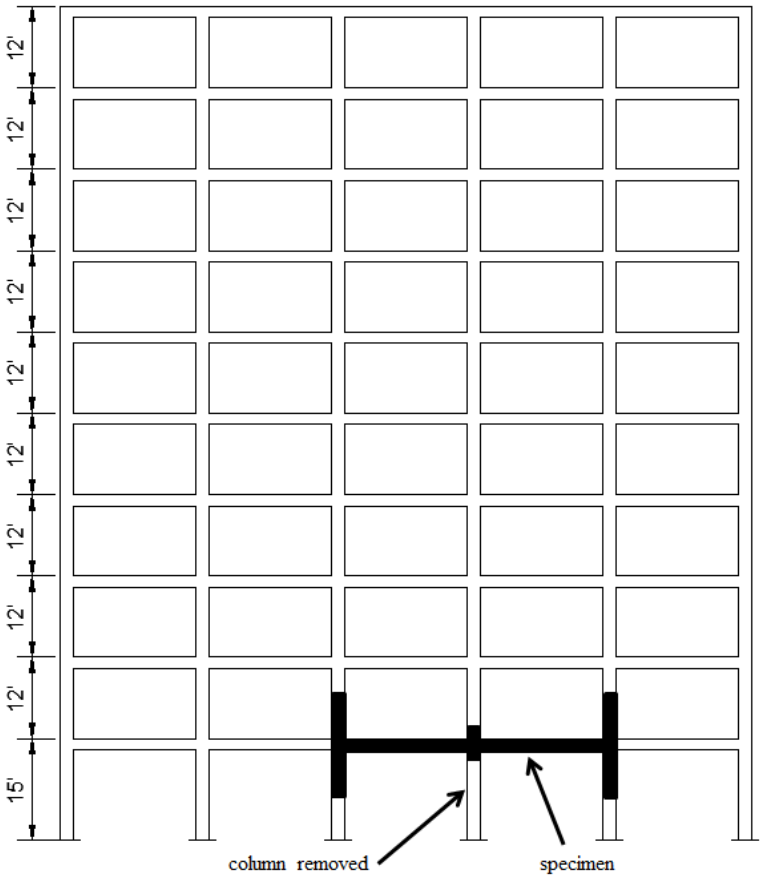

Figure 4.2: Elevation view of the specimen location

4.3 Specimen Design and Construction

4.3.1 Design

The laboratory specimens were designed using the prototype reinforcement in accordance with *ACI 318-14*, described in Chapter 3. Exterior columns were constructed up to mid-height at the approximate location of the point of inflection for lateral loading.

The longitudinal reinforcing bar details designed for the prototype were varied in each of the three specimens. *ACI 318-14* requires that longitudinal reinforcement in beams of perimeter frames be continuous. Continuity of reinforcement may be achieved by providing Class B splices near the end of the beams for bottom bars and near midspan for top bars. Given that beam-column joints typically have congestion of reinforcement, the effect of moving splices of bottom bars into the beam span was the primary experimental variable included in the testing program. The bottom reinforcement of the beams in the laboratory specimens was spliced at different locations, in reference to the face of the center support, as show in Table 4.1. The geometry and reinforcement details, including the bar splice location of the specimens (bottom reinforcement splices zone is enclosed within dash lines), are shown in Figure 4.3.

Table 4.1: Slice location of the specimens

Specimen	Splice Location[a]
1	support
2	2d
3	d

[a]d is the effective depth of the beam

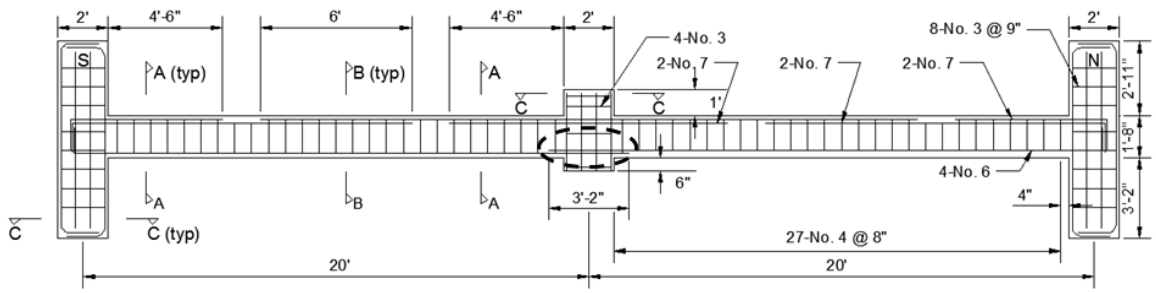

a)

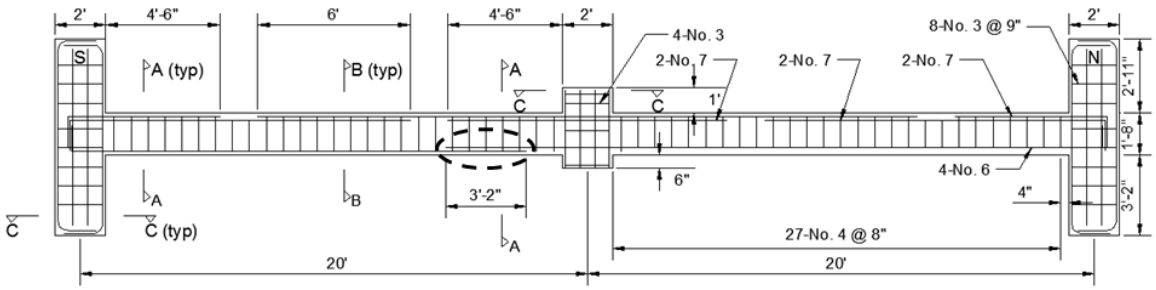

b)

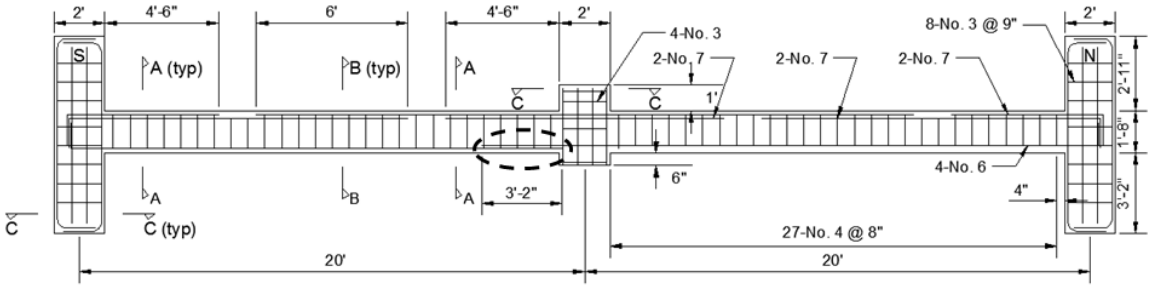

c)

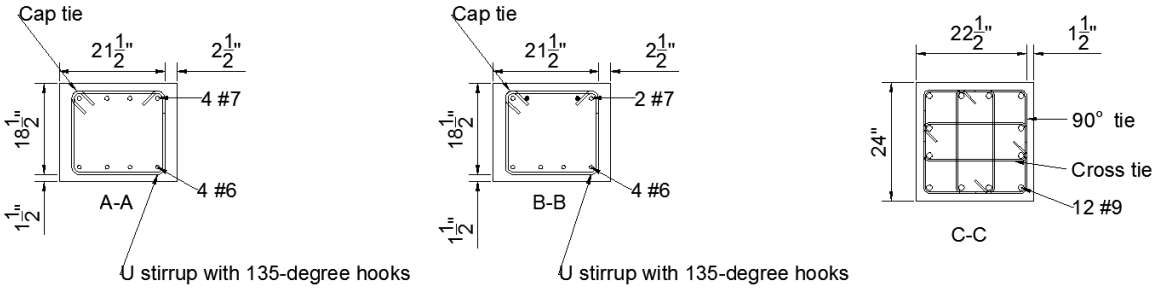

d)

Figure 4.3: Geometry and reinforcement details of a) Specimen 1, b) Specimen 2, c) Specimen 3 and d) beam and column cross sections

4.3.2 Construction

The fabrication and concrete casting of laboratory specimens were carried out in a horizontal position. The fabrication process started by tying the column cages. The column cages and the longitudinal reinforcing bars of the beams were set into part of the assembled formwork. Then, the longitudinal reinforcing bars and the stirrups of the beams were tied. Figure 4.4 shows details of the specimen construction process. The other side of the formwork was placed after the reinforcing cage was tied and reinforcing bars were instrumented using strain gauges (see Section 4.4.2.3). As show in Figure 4.5, PVC tubes were passed through the exterior column cages to accommodate high strength threaded rods to post-tension columns onto the supporting steel bases. Finally, the laboratory specimens were cast using concrete supplied from a ready mix plant. Figure 4.6 shows the finished Specimen 1 in the horizontal position. In order to place the specimens in the testing rig, the specimens were lifted and rotated using a bridge crane.

a)

b)

Figure 4.4: Reinforcing bar cage of a) columns and b) beams

Figure 4.5: PVC tubes passed through the exterior column cages

Figure 4.6: Finished Specimen 1

4.4 Test Setup

4.4.1 Model and Test Procedure

Schematic drawings of the test setup are shown in Figure 4.7 and 4.8, and Figure 4.9 shows a picture of Specimen 1 positioned in the testing rig. In order to simulate the points of contraflexure at column mid-height, pin connections were used in the top and bottom of the columns. Horizontal movement at the top of the columns was restrained by providing in-plane bracing of the specimen using a diagonal W8X35 steel brace fixed to the laboratory strong floor at each end. These braces were connected to the laboratory specimen using a pin connection to allow rotation of the column at the top point of contraflexure (Figure 4.10a). The columns were supported on thick plates with pin connections at their bottom to provide horizontal and vertical restraint (Figure 4.10b).

Four 1-in. diameter high strength threaded rods were passed through PVC pipes embedded into the end columns during casting to apply a post-tensioning force. The post-tensioning force was intended to simulate a fraction of the axial force in the prototype columns, and more importantly to secure the columns against the pinned base plates. Two steel lateral supports were used along the specimen length at beam mid-span to restrain the out-of-plane movement of the laboratory specimens during testing. The lateral supports consisted of two W12X16 steel columns supported by a W12X72 steel beam anchored to the laboratory strong floor as shown in Figure 4.11.

Load was applied by force control until specimen failure. The force was applied through the stub cast in the middle of the specimen representing the location of the removed interior column. The loading beam was a stiff built-up section consisting of two

MC18x58 channels connected using top and bottom plates at three different locations along the beam. Two 60 ton capacity hydraulic jacks were placed on the top of the beam to apply load through two 1 in. diameter threaded rods connected to the ends of the beam. These rods were fixed in the bottom part to the floor by means of anchor blocks (see Fig. 4.8). The details of the steel elements used in the test setup are presented in Appendix C.

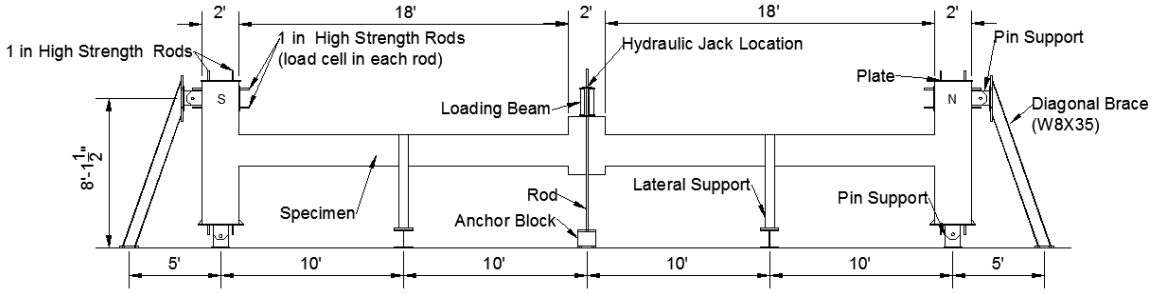

Figure 4.7: Test setup details

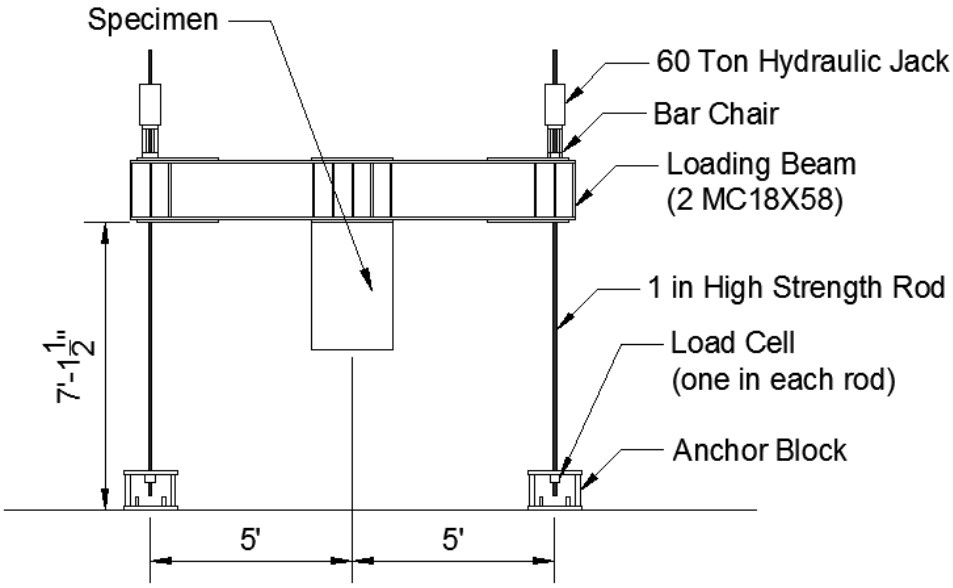

a)

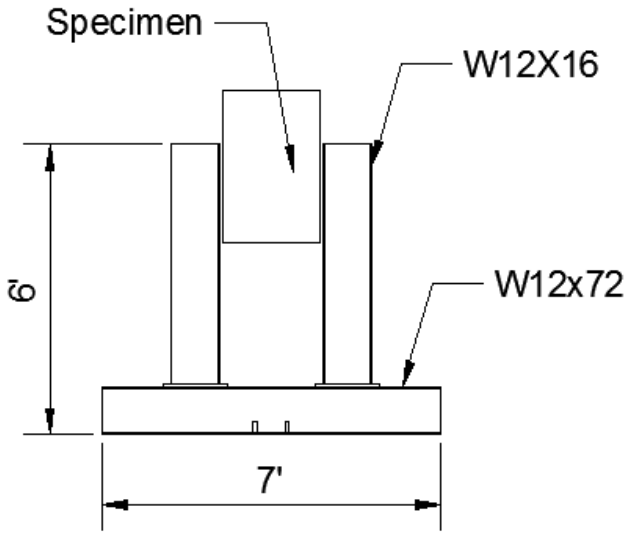

b)

Figure 4.8: Cross sectional view of the test setup taken a) at the loading beam and b) at the lateral support

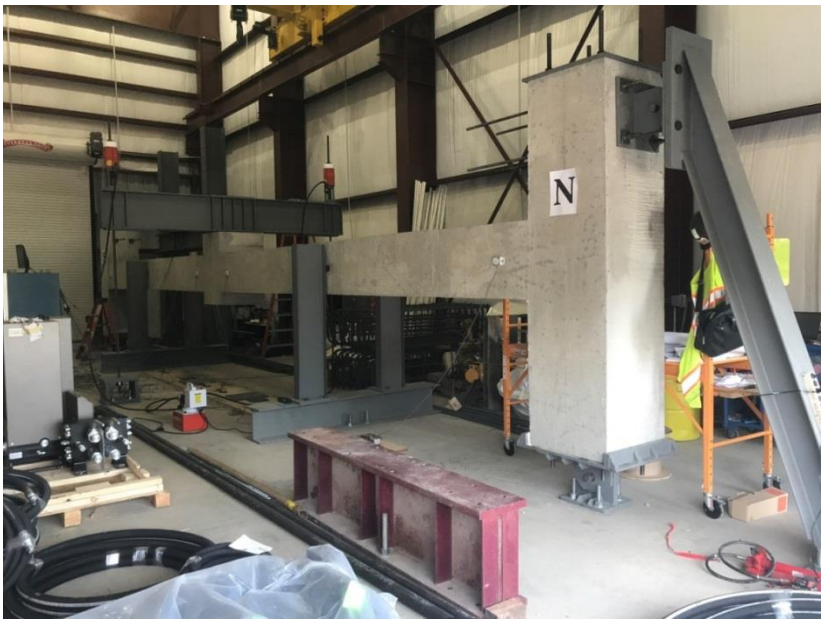

Figure 4.9: Specimen 1 in testing rig

a) b)

Figure 4.10: Typical pin connection at a) the top of the column and, b) column base

Figure 4.11: Typical lateral support along the specimen length at beam mid-span

4.4.2 Instrumentation

Specimen instrumentation consisted of external and internal elements including: 6 load cells, 2 located in the area where the force was applied and 4 located in the horizontal support to measure the reaction force; 7 linear displacement transducers located along the beams to measure vertical displacements; 4 inclinometers located at each end of each beam to measure rotation; and 20 strain gauges placed in reinforcing bars at bottom and top splices to measure the strains along the splices during loading. Figures 4.12 and 4.13 present the external and internal instrumentation, respectively. Also, Table 4.2 summarized the external instrumentation used.

4.4.2.1 Load Cells

Two load cells with a capacity of 100 kip each were placed in the threaded rods located in the double channel beam member. These load cells are designated as W-LC and E-LC in Figure 4.12. Also, four load cells with capacity of 50 kip each were placed in the threaded rods located in the south horizontal support to measure the horizontal force generated during the test. The designation for these load cells are TL-LC, TR-LC, BL-LC and BR-LC (BR-LC was used only in the Specimen 1 test).

4.4.2.2 Linear Displacement Transducers and Inclinometers

Seven linear displacement transducers with a capacity of up to 20 in. were attached to beam mid-height and referenced to the laboratory strong floor along the specimen to measure vertical displacements and determine the deformed shape of the beams during testing. The linear displacement transducers are designated as SS-LDT,

SC-LDT, SN-LDT, CC-LDT, NS-LDT, NC-LDT and NN-LDT in Figure 4.12 (CC-LDT was used only in the Specimen 2 and 3 tests). Also, four inclinometers with a capacity of 30 degrees were attached at mid-height of each beam end to measure the rotation of the beam during testing. The inclinometers are designated as SS-INC, SN-INC, NS-INC and NN-INC in Figure 4.12.

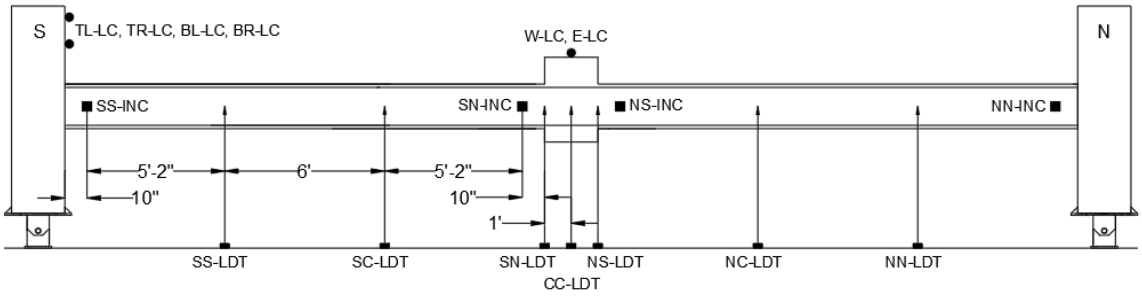

Figure 4.12: External instrumentation system details

Table 4.2: Summary of external instrumentation

Label	Instrument Type	Capacity	Location
TL-LC	load cell	50 kip	south horizontal support
TR-LC	load cell	50 kip	south horizontal support
BL-LC	load cell	50 kip	south horizontal support
BR-LC	load cell	50 kip	south horizontal support
W-LC	load cell	100 kip	anchor block, west side
E-LC	load cell	100 kip	anchor block, east side
SS-LDT	displacement transducer	10 in.	south side, south beam
SC-LDT	displacement transducer	10 in.	midspan, south beam
SN-LDT	displacement transducer	10 in.	north side, south beam
CC-LDT	displacement transducer	20 in.	center, center column
NS-LDT	displacement transducer	20 in.	south side, north beam
NC-LDT	displacement transducer	10 in.	midspan, north beam
NN-LDT	displacement transducer	5 in.	north side, north beam
SS-INC	inclinometer	30°	south beam end, south beam
SN-INC	inclinometer	30°	north beam end, south beam
NS-INC	inclinometer	30°	south beam end, north beam
NN-INC	inclinometer	30°	north beam end, north beam

4.4.2.3 Strain Gauges

To measure strains along the splice regions throughout the test, twenty strain gauges were attached in the bottom and top reinforcing bar splice zones. Thirteen strain gauges were used in the bottom splice zone and seven were used in the top splice zone. Figure 4.13 shows the details of the strain gauges instrumentation. Only a fraction of the total bars within a splice region were instrumented: 2 out of the 4 splices in bottom bar splices, and 1 out of 2 splices in top bar splices. Table 4.1 shows the locations of the bottom bar splice zones for the four specimens. The location is measured from the column centerline to the center of the splice. Also, Figures 4.14 show the layout of strain gauges for bottom splice and top splice zones, respectively. In the bottom splice zone, the labels B1 through B4 identify bars that come from the north beam and terminate at the end of the splice, and labels B1' through B4' identify south beam bars that begin at the splice. The instrumented sections within the splice are identified as CS, CC, or CN to indicate section at the center column stub (C) and the location relative to the center of the splice (S, C, or N for south, center, or north, respectively). Similar nomenclature was used in the top splice zone.

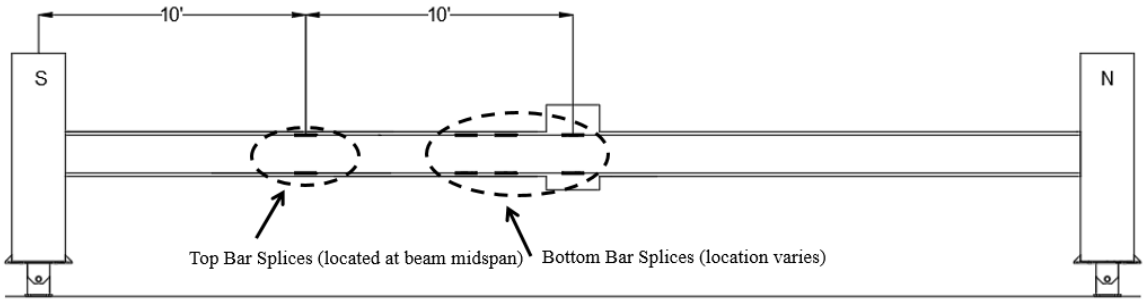

Figure 4.13: Location of section instrumented using strain gauges

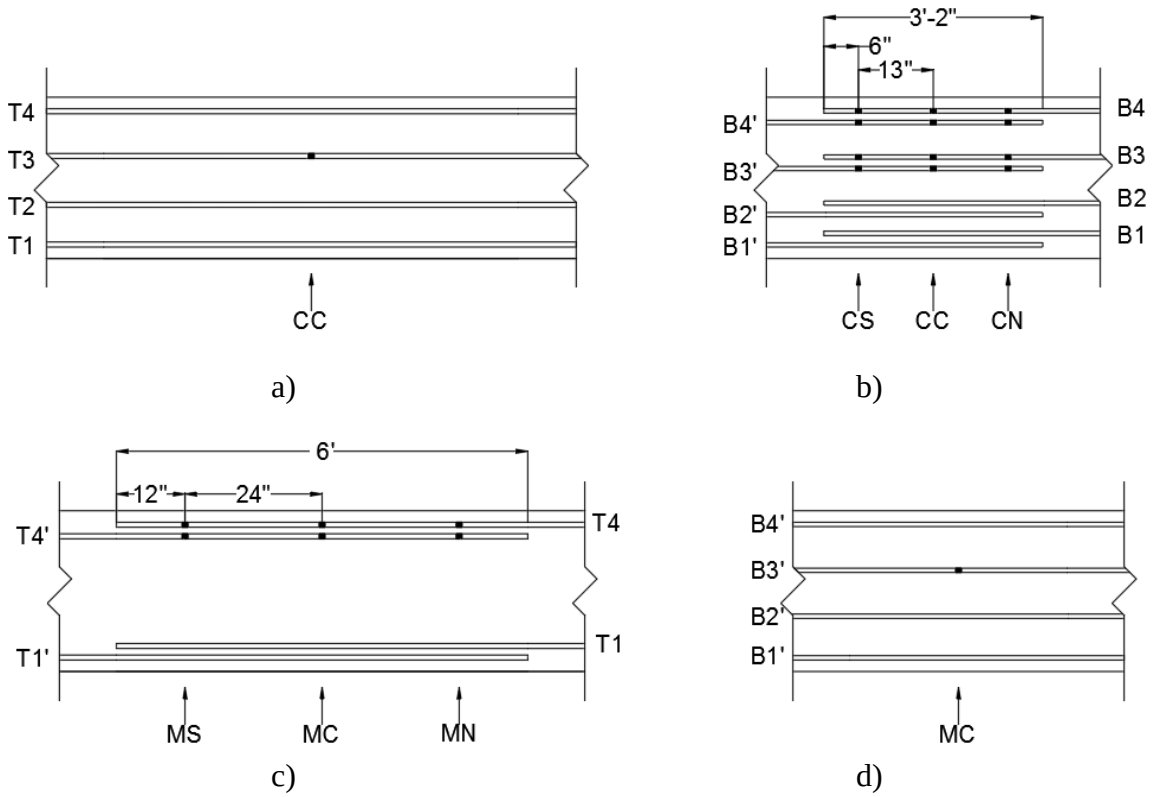

Figure 4.14: Plan view of strain gauges on reinforcing bars in the bottom splice zone for a) top bars and b) bottom bars and, top splice zone for c) the top bars and d) bottom bars

4.5 Summary

The procedure for design and construction of the laboratory specimens were presented in this chapter. The laboratory specimens represent a full-scale portion of the ten-story reinforced concrete frame prototype building discussed in Chapter 3. The laboratory setup; specimen instrumentation and its purpose; and the testing protocol employed was also discussed. The behavior and test results of the laboratory specimens described in this chapter are presented in Chapter 5.

CHAPTER 5

LABORATORY TEST RESULTS

5.1 Introduction

This chapter presents the observed behavior and test results of the laboratory specimens described in Chapter 4. The observed response is first described followed by a presentation of the measured response from the instrumentation. The test results that are presented include crack patterns at selected load steps and measurements from the internal and external array of instruments described in Chapter 4.

5.2 Specimen 1

5.2.1 Observed Response

Because the specimen was cast in the horizontal position, narrow cracks near the lifting points were generated during handling and placement of specimen in the test apparatus. In addition, narrow flexural cracks developed in the bottom part of the beams near the center column stub due to self-weight. The maximum width of the cracks measured after positioning the specimen in the test setup was 0.005 in. The weight of the double-channel beam used to transfer the load to the specimen increased the width of the cracks near the center column to 0.008 in. The estimated deflection caused by self-weight of the concrete beam and the weight of the double-channel loading beam was 0.5 in. For this estimation, moment of inertia of the beams was reduced to 20% to account for cracked section properties. This value was used to be consistent with the analytical model

described in Chapter 6. Figure 5.1 shows the crack pattern that formed after placement of Specimen 1 in the test apparatus.

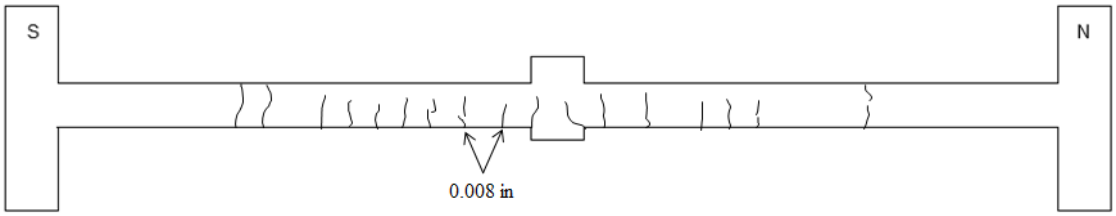

Figure 5.1: Crack pattern of Specimen 1 formed by the self-weight of the specimen during handling and positioning, and by weight of loading beam (crack widths not indicated are smaller than 0.008 in.)

The test was conducted by applying a vertical force on the center column using force control. At 32 kip of applied force and a 1.4 in. vertical displacement of the center column (vertical displacements were measured after the specimen was in position so they do not include the estimated vertical deflection that occurred after the specimen placement), flexural cracks developed at the top of the beams near the exterior columns, and at the bottom of the beams near the center column. The maximum width of these newly formed cracks was 0.008 in. One of the existing dead load cracks near the center column on the south beam widened to 0.060 in., as shown in Figure 5.2. Figure 5.3 illustrates the crack pattern that the specimen exhibited at this force level.

Figure 5.2: Critical flexural crack near the center column (Specimen 1)

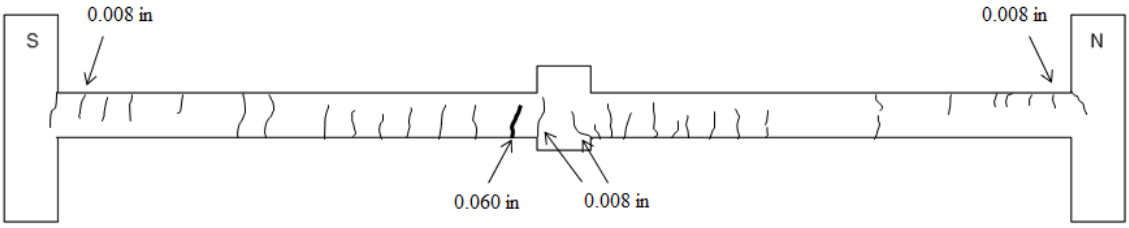

Figure 5.3: Crack pattern of Specimen 1: Force = 32 kip; center displacement = 1.4 in.

As the applied force reached the maximum applied value of 52 kip (center column vertical displacement of 4.9 in.), diagonal tension cracks appeared at the beam ends near the exterior columns. The maximum width of these observed cracks was 0.080 in. Figure 5.4 shows the diagonal tension cracks near the south column. The critical flexural crack near the center column increased to a width of 0.25 in. Also, initiation of concrete crushing was observed at the top of the beams meeting at the center column. Figure 5.5 shows the crack pattern for this force level.

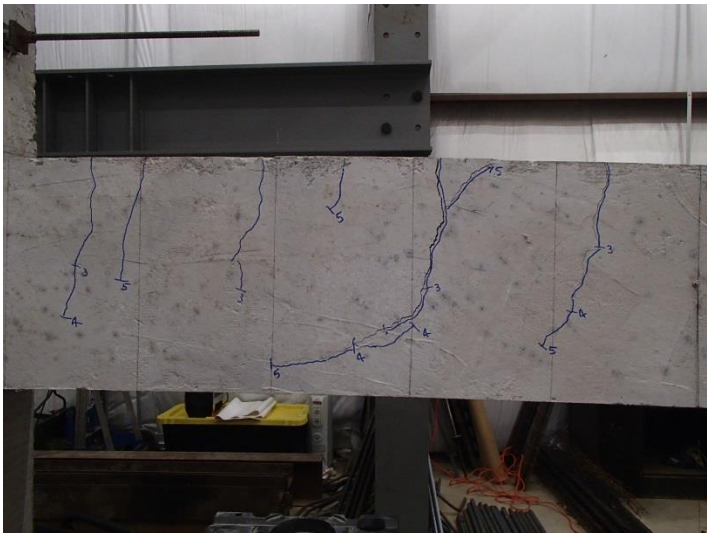

Figure 5.4: Diagonal tension cracks near the south column (Specimen 1)

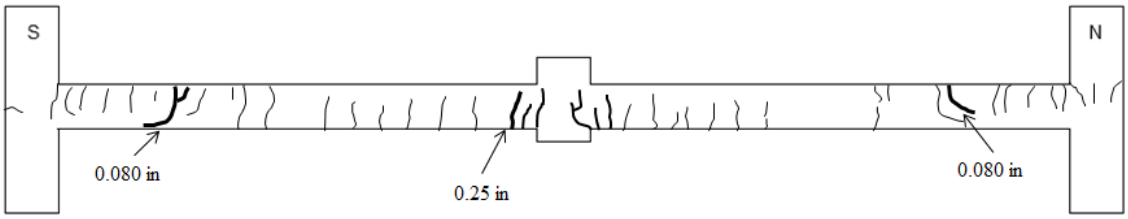

Figure 5.5: Crack pattern of Specimen 1: Force = 52 kip; center displacement = 4.9 in.

At this point in the testing, loading proceeded without an increase in the applied force. Instead, the force in the specimen dropped at increased center displacement. Concrete splitting occurred at the end of the top reinforcing bars that were hooked (anchored) into the north column at an applied force of 48 kip corresponding to a 9.5 in. center column vertical displacement. Widening of the diagonal tension crack that formed from the section where part of the top reinforcing bars were cut into the beam span near the north column occurred at an applied force equal to 43 kip of (13.9 in. center column vertical displacement). Widening of this diagonal tension crack triggered loss of aggregate interlock causing the applied force to decrease suddenly to 28 kip. Attempts were made to continue loading the specimen but the applied force did not increase

further, and concrete spalling near the diagonal tension crack was observed at a 16.3 in. center column vertical displacement. Near full-depth diagonal tension cracks were observed at the beam near the north column with a maximum width of 0.5 in and accompanied by concrete spalling. Crushing of the concrete at the bottom of the beams occurred near the exterior columns. One flexural crack near the center column increased in width to 1 in. For safety, the test was stopped at this point because the beam started to deflect laterally and came in contact with the lateral supports. Figures 5.6 and 5.7 show the condition of Specimen 1 at the end of the test after the loading beam was removed. Also, Figure 5.8 shows the final crack pattern.

Figure 5.6: Specimen 1 condition at the end of testing after removal of force

a)

b)

c)

Figure 5.7: Specimen 1 condition at the end of the test a) near the south column, b) near the north column and c) at the center column

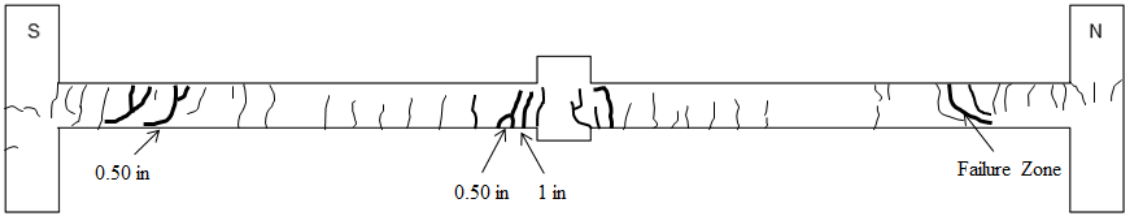

Figure 5.8: Crack pattern of Specimen 1 at the end of the test: Force = 28 kip; center displacement = 16.3 in.

5.2.2 Measured Force-Displacement Response

Figure 5.9 shows the applied force versus the vertical displacement measured at the center column. The applied force was determined by adding the measured values from the two load cells designated as W-LC and E-LC. The vertical displacement of the center column was measured using a linear displacement transducer referenced to the beam axis at the north face of the column stub (NS-LDT). Figure 5.9 shows that the specimen was unloaded when the vertical displacement of the center column reached approximately 1.4 in. to verify the hydraulic system because pressure was being lost during the load holds necessary to measure cracks and take pictures.

Based on the moment-curvature relationships of the reinforced concrete beam sections using measured properties of the materials, and the bending moment generated by the applied force, the longitudinal reinforcement reached yield on both faces of the center column at 33 kip corresponding to a 1.5 in. center column vertical displacement (point A in Figure 5.9). Similarly, the longitudinal reinforcement near the exterior column was calculated to reach yield at 38 kip, corresponding to a 1.8 in. center column vertical displacement (point B in Figure 5.9). A slight reduction in slope in the load-displacement plot is indicative of the loss in stiffness associated with yielding. These forces were calculated using a plastic analysis of the specimen and take into account the self-weight of the concrete beam and the weight of the double-channel loading beam. This analysis is described in Chapter 6.

The peak applied force was 52 kip (point C in Figure 5.9). At an applied force equal to 43 kip (point D in Figure 5.9), widening of the critical diagonal tension crack in the beam near the north column occurred causing the applied force to decrease suddenly to 28 kip (point E in Figure 5.9). Attempts were made to continue loading the specimen but the applied force did not increase further and the specimen was fully unloaded (point F in Figure 5.9).

Figure 5.10 shows the horizontal reaction measured at the top of the south column plotted against the vertical displacement of the center column. The horizontal reaction was measured using the load cells designated as TL-LC, TR-LC, BL-LC and BR-LC positioned on the rods connecting the column to the steel brace. As the vertical displacement of the center column reached the value of 6.39 in., the horizontal reaction increased to 3.7 kip. The horizontal reaction remained constant until the applied load

decreased suddenly. In the plot, positive values of the horizontal reaction represent inward restraint in the top of the south column. Inward restraint generated tension force in the diagonal brace.

Figure 5.11 shows the deformed shapes constructed using displacement measurements taken along the beams at maximum force, after the critical diagonal tension crack widened and at the end of the test. Due to the formation of plastic hinges in the beams near the exterior columns and center column after the maximum force, the vertical displacement increased and concentrated in the center column. The linear displacement transducer designated as SN-LDT malfunctioned so this point is not included in the plot.

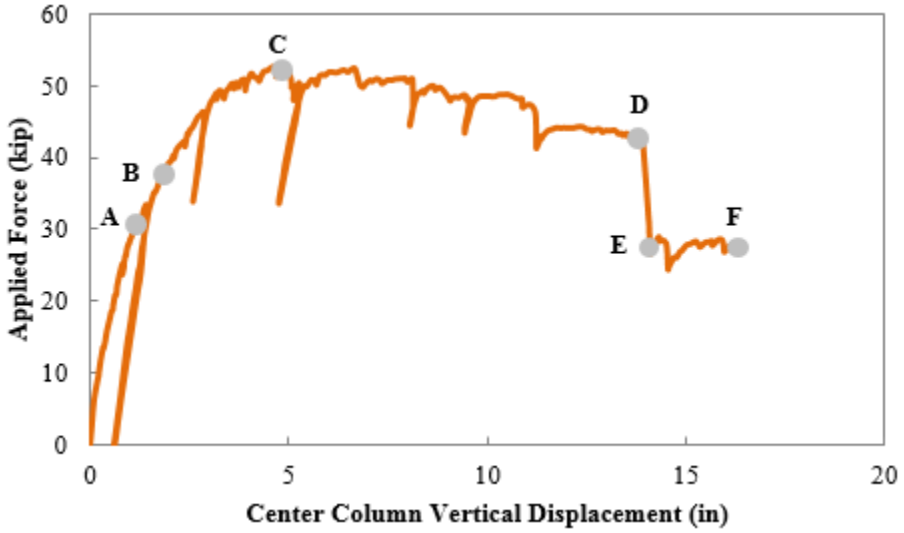

Figure 5.9: Force versus displacement of the center column (Specimen 1)

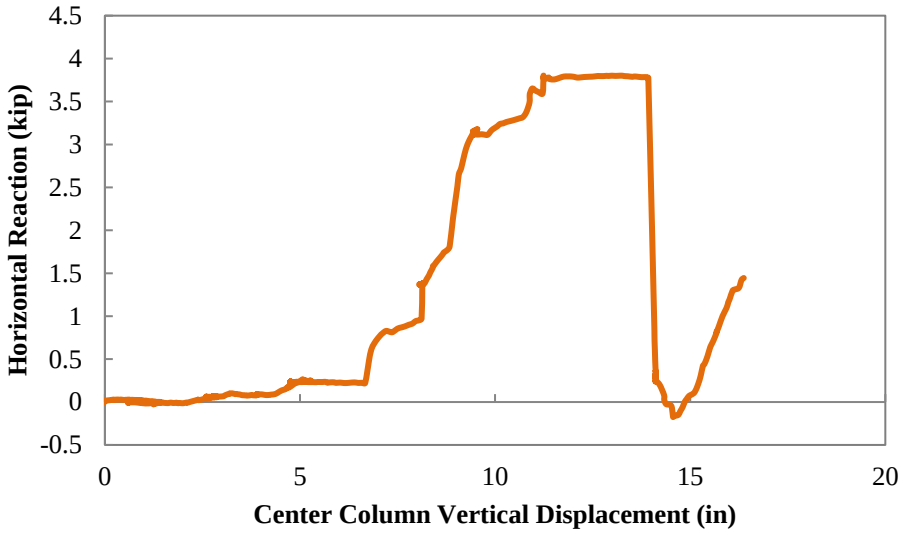

Figure 5.10: Horizontal reaction in the top of the south column versus vertical displacement of the center column (Specimen 1)

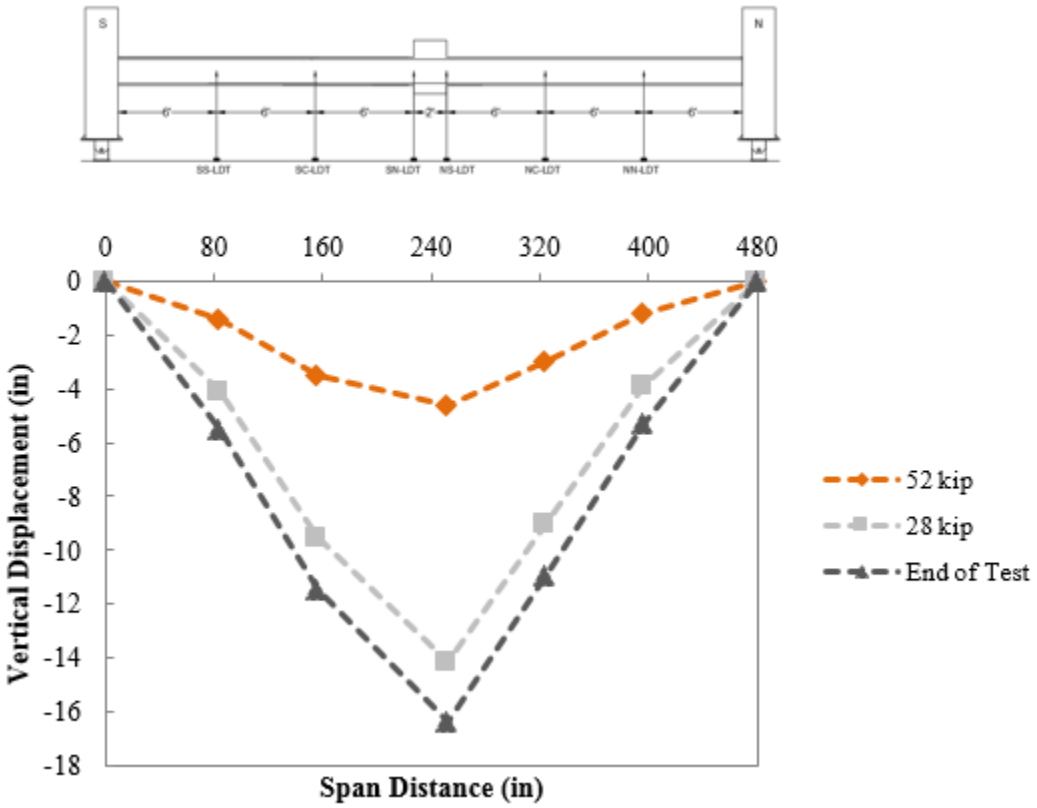

Figure 5.11: Deformed shape of the beams at peak, after widening of the critical diagonal tension crack and at the end of the test (Specimen 1)

5.2.3 Measured Rotation Response

Figure 5.12 shows the applied force versus the rotations measured using the inclinometers positioned at both ends of the beam (NN-INC and NS-INC) in the north span. The instruments were positioned at beam mid-height and centered at a distance of 10 in. from the face of the column and column stub, respectively. These locations were chosen because they approximately represent the center of plastic hinges that typically form at ends of beam-column connections. The NN-INC inclinometer was used to measure the rotation in the beam end near the north column, and the NS-INC inclinometer was used to measure the rotation in the beam end near the center column. The measured rotations near both beam ends were similar until the force reached approximately 32 kip. At this force level, one flexural crack near the center column widened to approximately 0.060 in., resulting in a significant reduction in section flexural stiffness. After this reduction in section stiffness, rotations concentrated near the center column stub instead of the north end of the beam. The measured rotations just prior to widening of the critical diagonal tension crack were 0.112 rad for the beam end near the center column, and 0.029 rad for the beam end near the north column. As shown in Figure 5.13, the measured rotations just prior to widening of the critical crack were 0.130 rad for the beam end near the center column (SN-INC) in the south span. The inclinometer designated as SS-INC malfunctioned so the plot of this instrument is not given here.

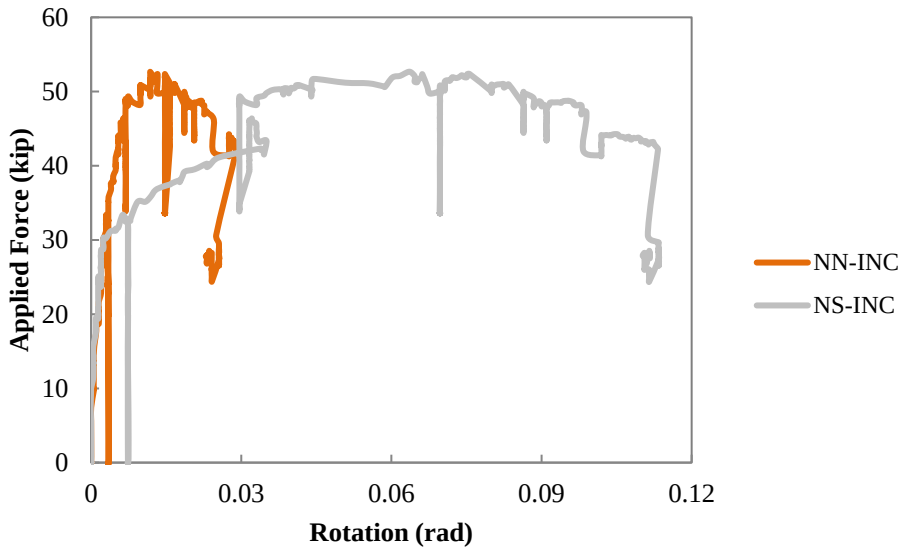

Figure 5.12: Force versus rotations at the beam end for the beam on the north span (Specimen 1)

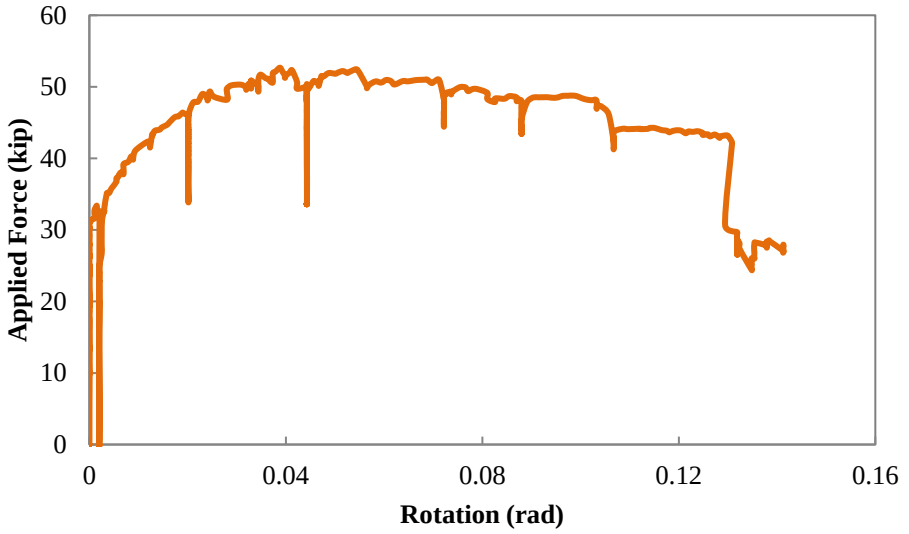

Figure 5.13: Force versus rotation at the beam end near the center column for the beam on the south span (Specimen 1)

5.2.4 Measured Strain Response

Figure 5.14 shows the location of strain gauges placed on the bottom reinforcing bar splice zone near the beam-column stub connection, and on the top reinforcing bars in the splice zone near beam midspan (south span). The bottom splice zone was centered

within the center column stub in this specimen, and the top splice zone is located at midspan 10 ft from the centerline of south column. These details are in compliance with the requirements of integrity reinforcement in *ACI 318-14* §9.7.7.5. Since the location of bottom bar splice region is not clearly specified in *ACI 318-14*, each specimen had a different location for the center of the bottom splice as indicated in Section 4.3.1. Only the splice zones located in the south beam (bottom and top) were instrumented using strain gauges. The bottom splice location was shifted into the south span beam in subsequent specimens, so it was important to position instrumentation in the top splice as well for consistency with Specimen 1. Thirteen strain gauges were used in the bottom splice and seven were used in the top splice. The layout of strain gauges for bottom splice and top splice zones are presented in Figure 4.14. In Specimen 1, the strain gauge attached in the reinforcing bar B3' at the MC section malfunctioned so data for this instrument are not presented nor discussed.

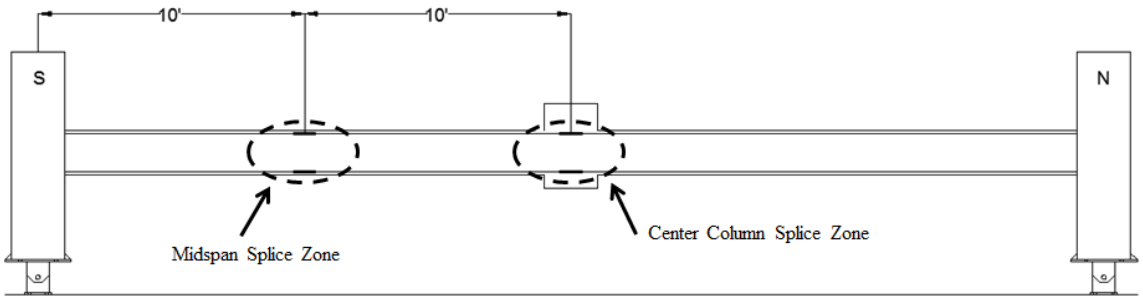

Figure 5.14: Location of sections instrumented using strain gauges (Specimen 1)

Figure 5.15 shows a plot of applied force versus strain for the bottom reinforcing bars B3' and B3 at the center column splice zone. In section CS, tensile strains in both reinforcing bars were similar until the force reached approximately 24 kip. At this force level, reinforcing bar B3' developed strains larger than those for reinforcing bar B3. The

small strains recorded in bar B3 at higher forces occurred due to the proximity of the instrument to the reinforcing bar B3 edge at the end of the splice region. It is likely that bar may slip may have occurred at higher forces so high strains did not develop. Furthermore, the critical flexural crack that formed at a lower force near the face column stub widened to approximately 0.060 in. at approximately 32 kip, causing strains in reinforcing bar B3 at this section to decrease and go into compression. The measured strain in reinforcing bar B3' exceeded the expected yield strain (0.0025) in section CS at applied force of about 52 kip. Section CC is located halfway along the splice located at the center column stub. As expected, similar tensile strains in both reinforcing bars were measured. Yielding of the reinforcing bars in section CC was not reached according to the measured readings. In section CN, tensile strains in both reinforcing bars were similar until the force reached approximately 24 kip. At this force level, reinforcing bar B3 developed strains larger than those for reinforcing bar B3'. Similar to section CS, the small strains recorded in bar B3' at higher forces occurred due to the proximity of the instrument to the reinforcing bar B3' edge at the end of the splice region. The measured strain in reinforcing bar B3 exceeded the expected yield strain (0.0025) in section CN at applied force of about 52 kip. The maximum measured strain at the splice was 0.035 in the bar B3' in section CS. Similar strain variation was observed in bars B4 and B4' and is presented in Appendix D.

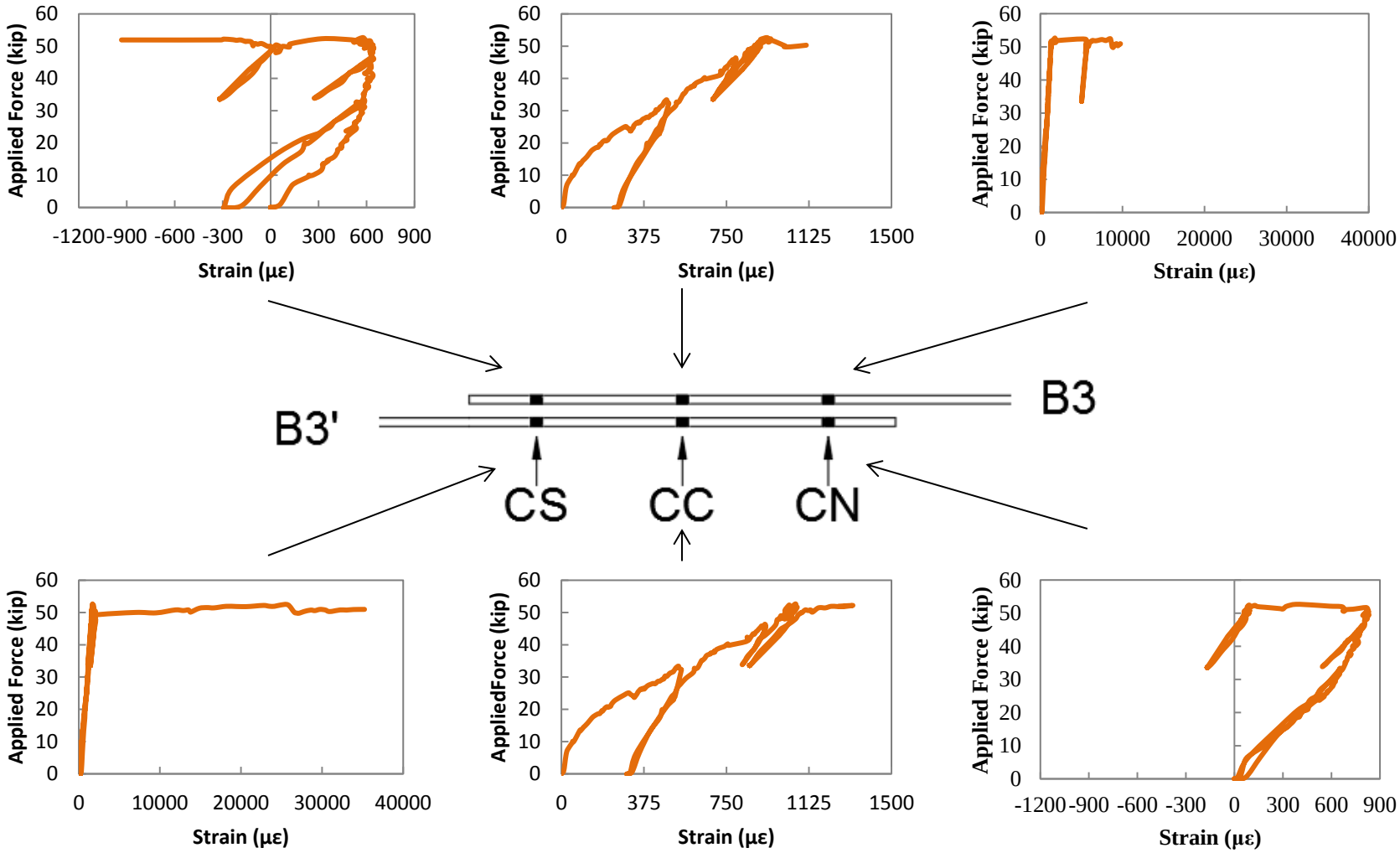

Figure 5.15: Force-strain response of bottom reinforcing bars at center column splice zone (Specimen 1)

Figure 5.16 shows a plot of applied force versus strain for the top reinforcing bars T4’ and T4 at the midspan splice zone. In section MS, tensile strains in both reinforcing bars were similar until the force reached approximately 50 kip. At this force level, reinforcing bar T4’ developed strains larger than those for reinforcing bar T4. Similar to the measured strains in reinforcing bar B3 at the center column splice, lower strains in bar T4 were likely caused because of the proximity of the strain gauge to the end of the bar within the splice region. It is likely that the bar may have slip preventing high strains to develop. Yielding of the reinforcing bars in section MS was not observed since the section was located in a region of low moment. Section MC is located halfway along the splice at beam midspan, so similar strains in both reinforcing bars was measured. The strains in this section were in tension initially and gradually changed to compression after the applied peak force, which indicate a change in the location of the point of inflection for moment at this section. The yielding of the reinforcing bars section MC was not observed. Due the measured strains in section MN were low (less than 0.00023), strains in both reinforcing bars were similar during the test. The maximum measured strain at the splice was 0.001 in the bar T4’ in section MS.

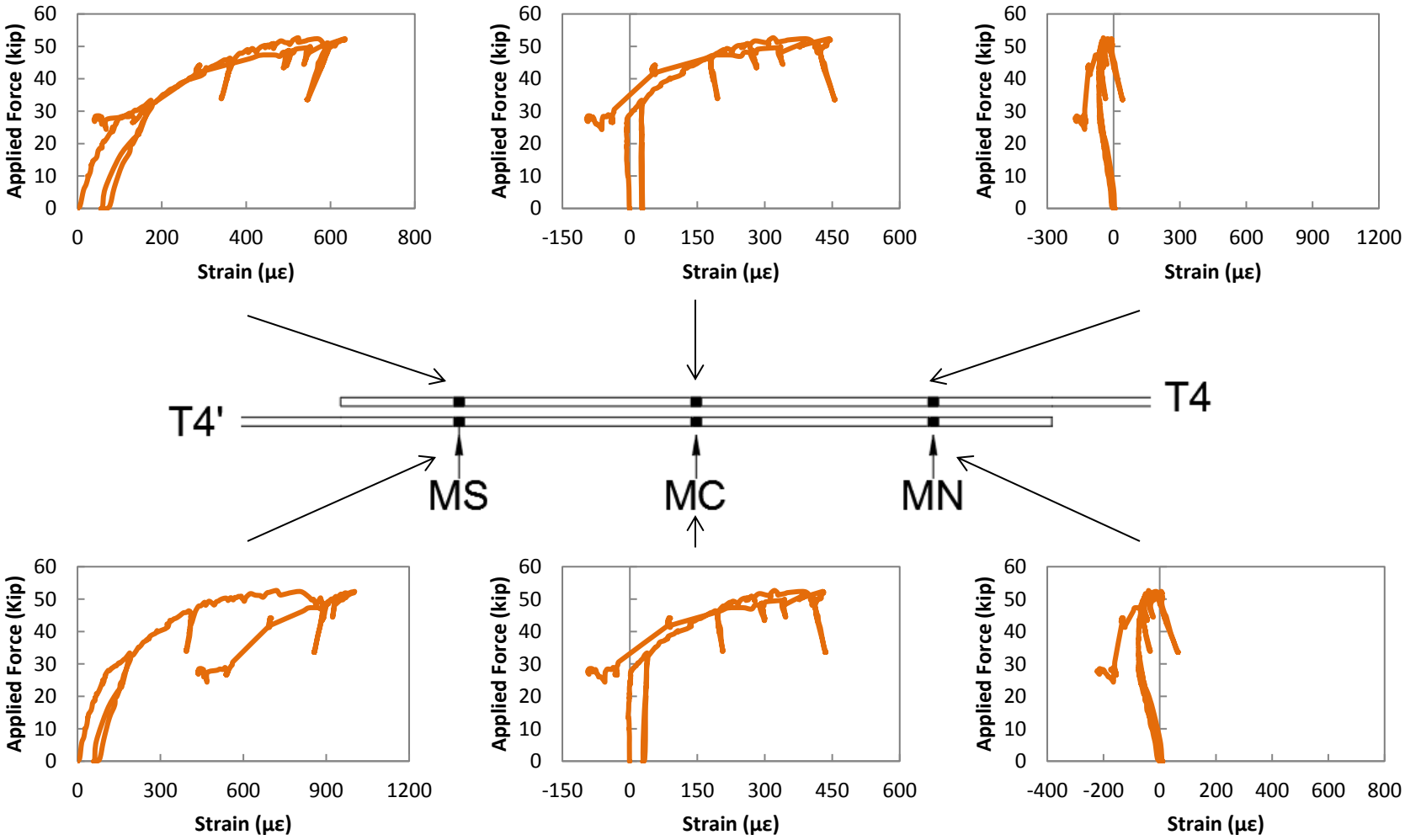

Figure 5.16: Force-strain response of top reinforcing bars at midspan splice zone (Specimen 1)

Figure 5.17 shows the strain variation at 52 kip of the bottom reinforcing bars B3' and B3 in the bottom splice and summarizes the effect of the development length in the strains. Similarly, Figure 5.18 shows the strain variation of the bottom reinforcing bars B4' and B4. In the plots, section CS represents bar cutoff section for reinforcing bars B3 and B4; and section CN represents bar cutoff section for reinforcing bars B3' and B4'.

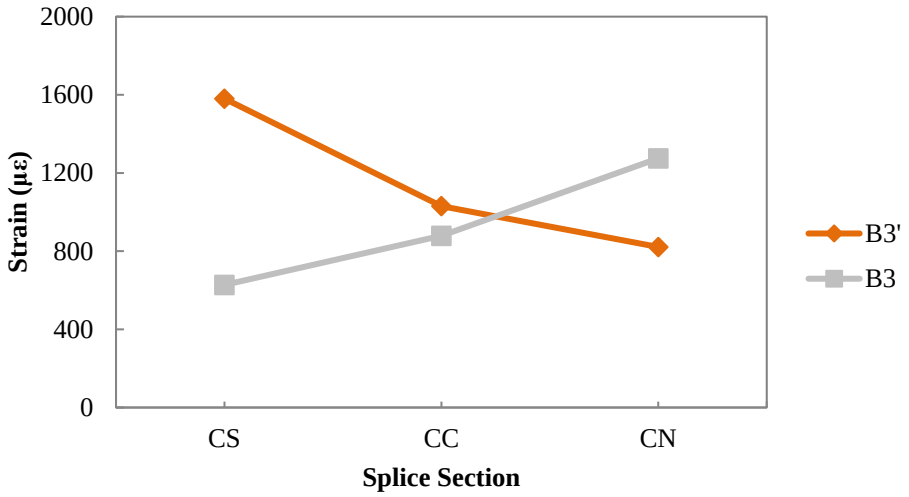

Figure 5.17: Strain variation of bottom reinforcing bars B3' and B3 in the bottom splice at 52 kip (Specimen 1)

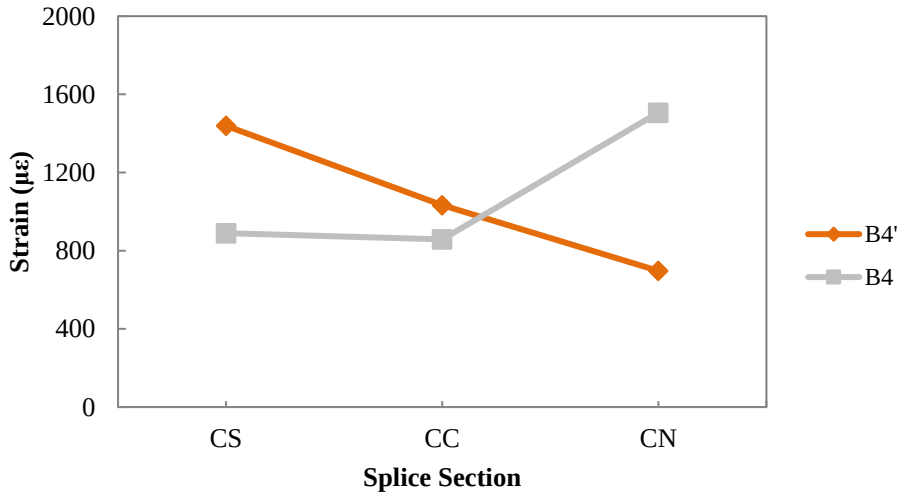

Figure 5.18: Strain variation of bottom reinforcing bars B4' and B4 in the bottom splice at 52 kip (Specimen 1)

5.3 Specimen 2

5.3.1 Observed Response

Due to self-weight, narrow flexural cracks developed in the bottom part of the beams near the center column stub. The maximum width of the cracks measured after positioning the specimen in the test setup was 0.005 in. The weight of the double-channel beam used to transfer the load to the specimen increased the width of the cracks near the center column to 0.008 in. The measured deflection caused by self-weight of the concrete beam and the weight of the double-channel loading beam was 0.625 in. Figure 5.19 shows the crack pattern that formed after placement of Specimen 2 in the test apparatus.

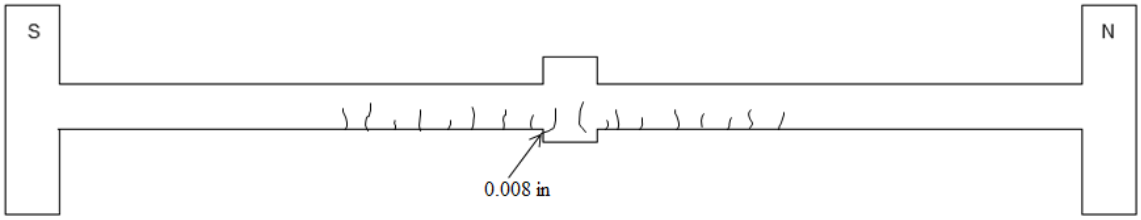

Figure 5:19: Crack pattern of Specimen 2 formed by the self-weight of the specimen during handling and positioning, and by weight of loading beam (Crack widths not indicated are smaller than 0.008 in.)

At 32 kip of applied force and a 1.0 in. vertical displacement of the center column, flexural cracks developed at the top of the beams near the exterior columns, and at the bottom of the beams near the center column. The maximum width of these newly formed cracks was 0.006 in. Three existing dead load cracks near the center column widened to 0.060 in., as shown in Figure 5.20. Figure 5.21 illustrates the crack pattern that the specimen exhibited at this force level.

Figure 5.20: Critical flexural cracks near the center column (Specimen 2)

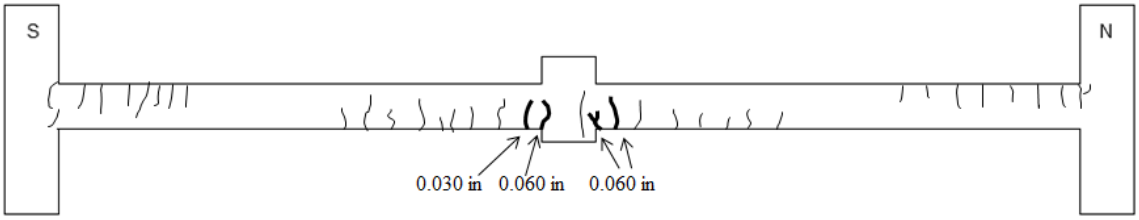

Figure 5.21: Crack pattern of Specimen 2: Force = 32 kip; center displacement = 1.0 in.

As the applied force reached the maximum applied value of 50 kip (center column vertical displacement of 6.4 in.), diagonal tension cracks appeared at the beam ends at near the exterior columns. The maximum width of these observed cracks was 0.25 in. The critical flexural crack near the center column increased to a width of 0.25 in. Also, initiation of concrete crushing was observed at the top of the beams meeting at the center column. Shear and flexural cracks appeared at the joint and the exterior face of the exterior columns respectively. Figure 5.22 shows the cracks near the south column. Also, Figure 5.23 shows the crack pattern for this force level.

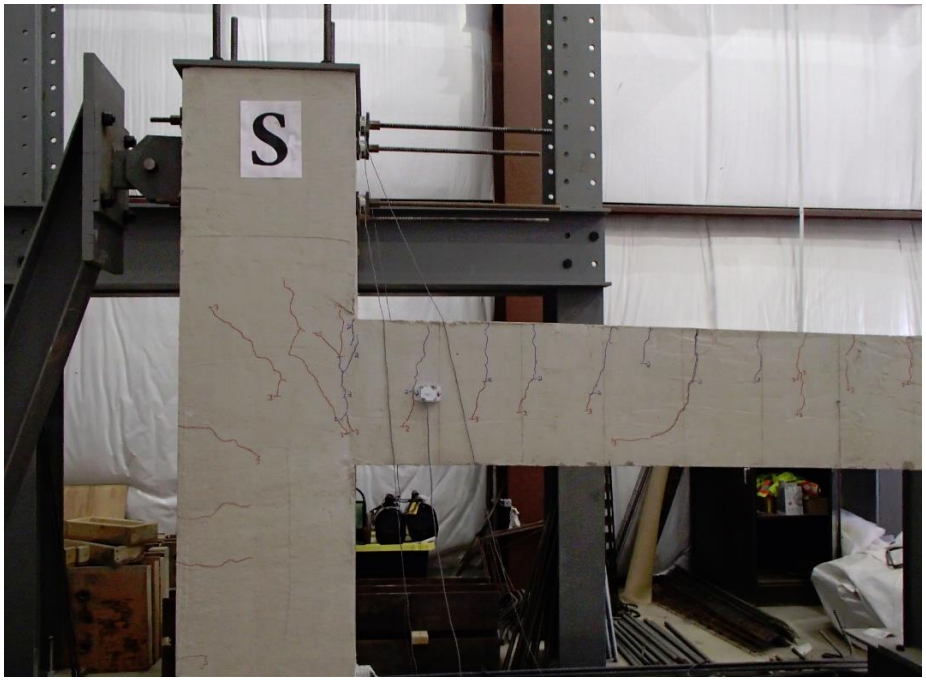

Figure 5.22: Cracks near the south column (Specimen 2)

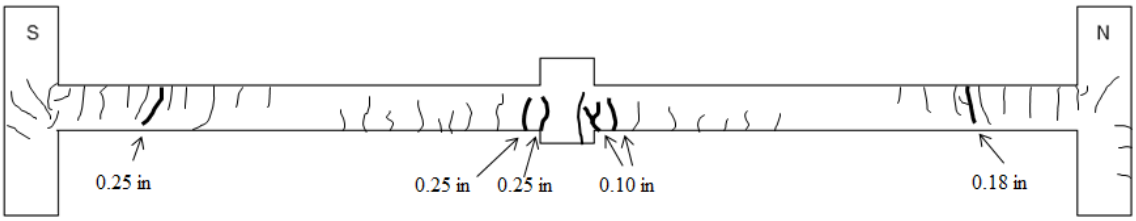

Figure 5.23: Crack pattern of Specimen 2: Force = 50 kip; center displacement = 6.4 in.

At this point in the testing, loading proceeded without an increase in the applied force. Instead, the force in the specimen dropped at increased center displacement. Widening of the critical diagonal tension crack in the beam near the south column occurred at an applied force equal to 40 kip of (15.8 in. center column vertical displacement). The widening of this diagonal tension crack may have generated loss of aggregate interlock causing the applied force to decrease suddenly to 26 kip. At a center column vertical displacement of about 18 in., the applied force started to increase again until it reached 35 kip (27.9 in. center column vertical displacement). At this applied

force, full-depth diagonal tension cracks were observed at the beam near the south column with a maximum width of 2 in. and accompanied by concrete spalling. Crushing of the concrete at the bottom of the beams occurred near the exterior columns. One flexural crack near the center column increased in width to 0.75 in. For safety, the test was stopped at this point. Figures 5.24 and 5.25 show the condition of Specimen 2 at the end of the test after the loading beam was removed. Also, Figure 5.26 shows the final crack pattern.

Figure 5.24: Specimen 2 condition at the end of testing after removal of force

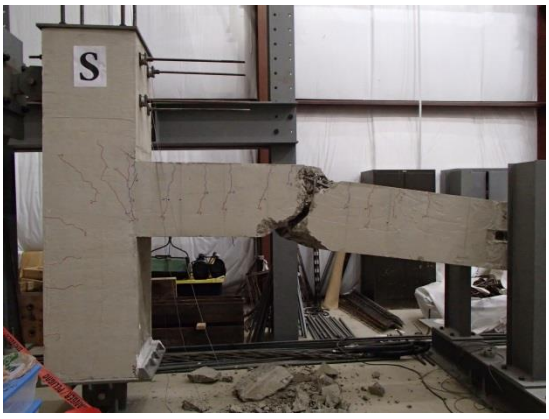

a)

b)

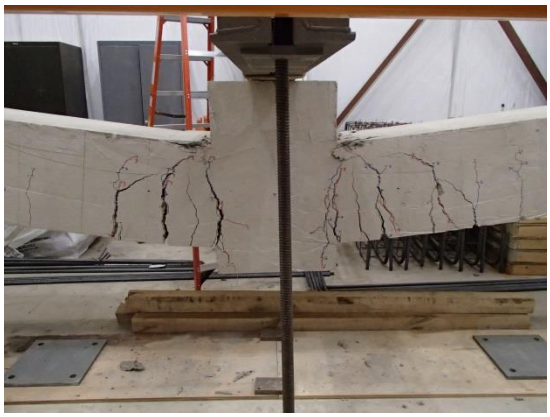

c)

Figure 5.25: Specimen 2 condition at the end of the test a) near the south column, b) near the north column and c) at the center column

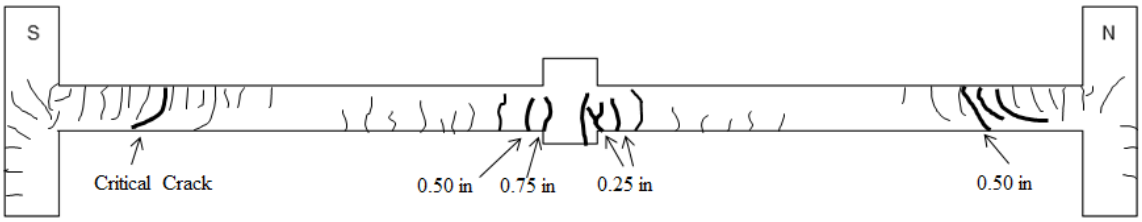

Figure 5.26: Crack pattern of Specimen 2 at the end of the test: Force= 35 kip; center displacement = 27.9 in.

5.3.2 Measured Force-Displacement Response

Figure 5.27 shows the applied force versus the vertical displacement measured at the center column. The applied force was measured using the load cells designated as W-LC and E-LC. The vertical displacement of the center column was measured using a linear displacement transducer referenced to the beam axis at the column stub (CC-LDT). As shown in Figure 5.27, the force in the specimen decreased slightly during holds that were taken a few times during the test to measure cracks and take pictures.

The longitudinal reinforcement reached the yield strength on both sides of the center column at 33 kip corresponding to a 1.0 in. center column vertical displacement (point A in Figure 5.27). Similarly, the longitudinal reinforcement reached the yield strength near the exterior column at 39 kip corresponding to a 1.5 in. center column vertical displacement (point B in Figure 5.27)

The peak applied force was 50 kip (point C in Figure 5.27). At an applied force equal to 40 kip (point D in Figure 5.27), widening of the critical diagonal tension crack in the beam near the south column occurred causing the applied force decrease suddenly to 26 kip (point E in Figure 5.27). At a center column vertical displacement of about 18 in., the applied force started to increase again until it reached 35 kip (point F in Figure 5.27). Subsequent to this stage the specimen was fully unloaded.

Due channel limitations of the data acquisition system used in the test, only three of the four threaded rods located in the south horizontal support were instrumented to measure the horizontal reaction generated during the test. Figure 5.28 shows the horizontal force measured in three of the four rods located near the top of the south column plotted against the vertical displacement of the center column. The fraction of the horizontal reaction was measured using the load cells designated as TL-LC, TR-LC, BL-LC positioned on the rod that connects the column to the steel brace. As the vertical displacement of the center column reached the value of about 21 in., the horizontal reaction fraction started to increase until reaching 12 kip. In the plot, positive values of the horizontal reaction represent inward restraint in the top of the south column. Inward restraint generated tension force in the diagonal brace.

Figure 5.29 shows the deformed shapes constructed using displacement measurements taken along the beams at maximum force, after the critical diagonal tension crack widened, and at the end of the test. Cracks that widened in the beams near the exterior columns and center column after the maximum force caused the beam rotation to concentrate at these sections with an increase in vertical displacement in the center column. The linear displacement transducer designated as SS-LDT malfunctioned so this point is not included in the plot.

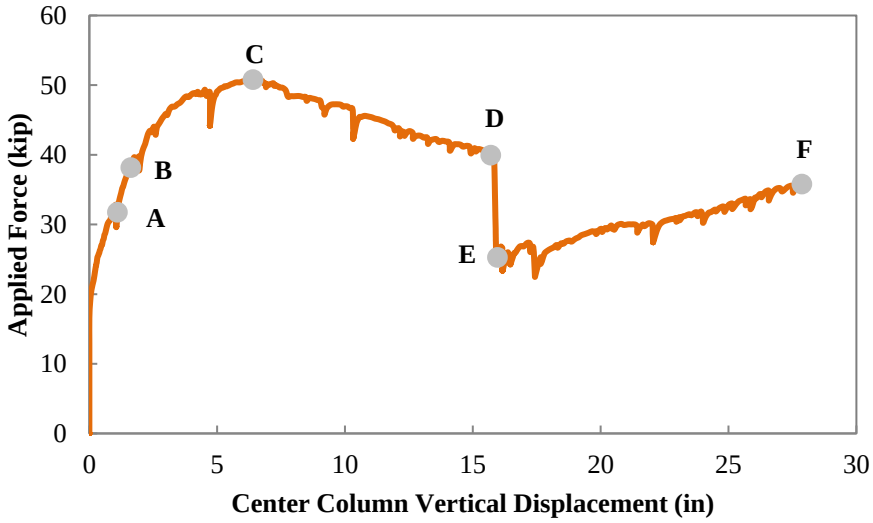

Figure 5.27: Force versus displacement of the center column (Specimen 2)

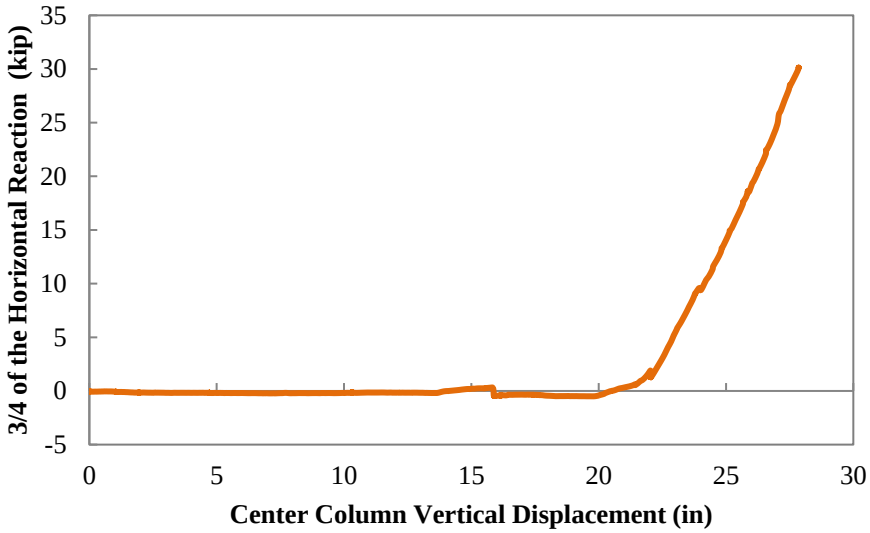

Figure 5.28: Horizontal force measured in three of four rods at the top of the south column versus vertical displacement of the center column (Specimen 2)

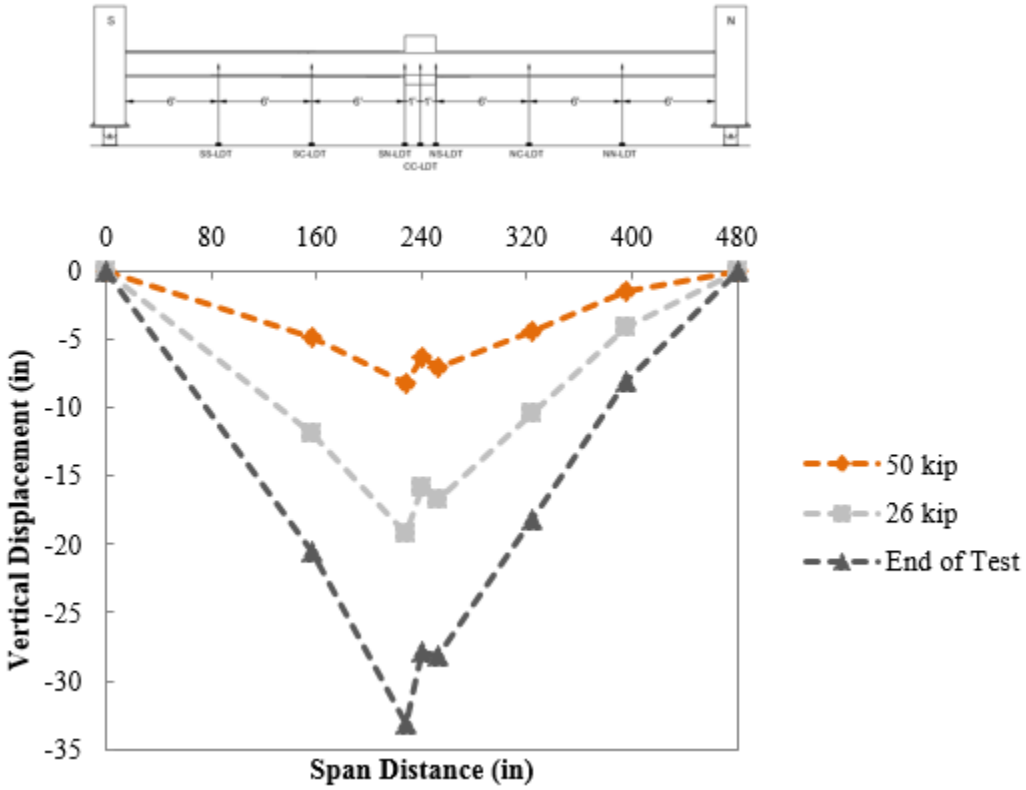

Figure 5.29: Deformed shape of the beams at peak, after widening of the critical diagonal tension crack and at the end of the test (Specimen 2)

5.3.3 Measured Rotation Response

Figure 5.30 shows the applied force versus the rotations measured at both ends of the beam in the south span. Rotations were measured using the inclinometers designated as SS-INC and SN-INC. These instruments were positioned at beam mid-height and centered at a distance of 10 in. from the face of the column. These locations were selected because they are approximately at the center of plastic hinges that were expected to form at ends of beam-column connections. The SS-INC inclinometer was used to measure the rotation in the beam end near the south column, and the SN-INC inclinometer was used to measure the rotation in the beam end near the center column. Similar to Specimen 1, the measured rotations near both beam ends were similar until the load reached approximately 32 kip. At this force level, one flexural crack near the center column widened to approximately 0.060 in., resulting in a significant reduction in section flexural stiffness. Rotations concentrated near the center column stub instead of the south end of the beam. The measured rotations just prior to widening of the critical diagonal tension crack were 0.118 rad for the beam end near the center column, and 0.018 rad for the beam end near the south column. As shown in Figure 5.31, the north span exhibits the same condition than the south span concentrating the rotations near the center column stub. The measured rotations just prior to widening of the critical diagonal tension crack were 0.067 rad for the beam end near the center column, and 0.008 rad for the beam end near the north column.

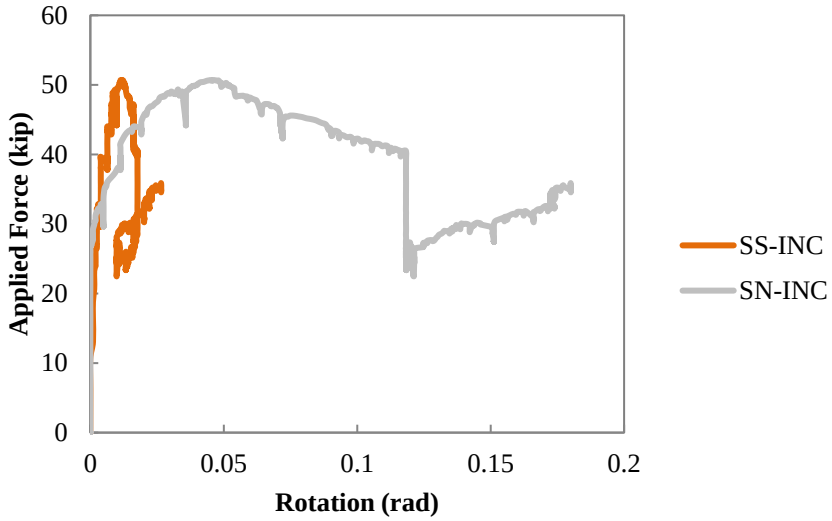

Figure 5.30: Force versus rotations at the beam end for the beam on the south span (Specimen 2)

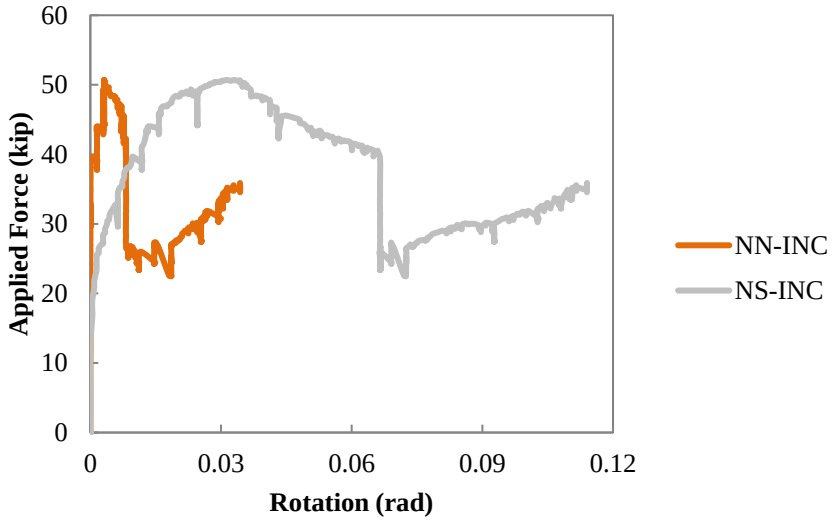

Figure 5.31: Force versus rotations at the beam end for the beam on the north span (Specimen 2)

5.3.4 Measured Strain Response

Figure 5.32 shows the location of strain gauges placed on the bottom reinforcing bars splice zone near the end of the beam-column stub connection, and on the top reinforcing bars in the splice zone near the beam midspan. The bottom splice zone is

located 16 ft. from the centerline of south end column, and the top splice zone is located at midspan (10 ft. from the centerline of south end column). Thirteen strain gauges were used in the bottom splice and seven were used in the top splice. The layouts of strain gauges in the bottom splice and top splice zones are presented in Figure 4.14.

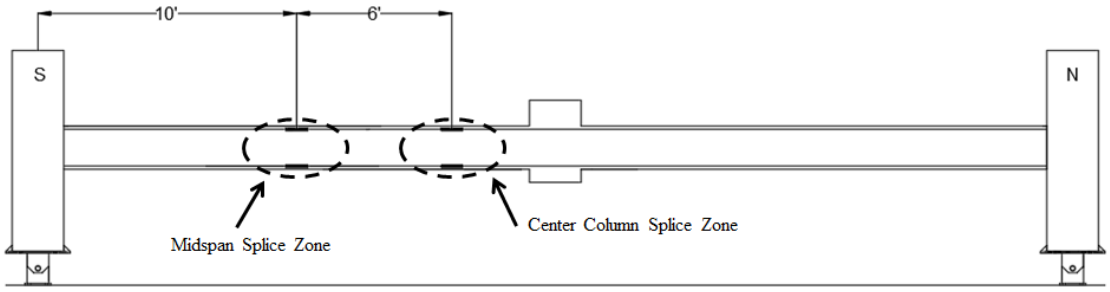

Figure 5.32: Location of sections instrumented using strain gauges (Specimen 2)

Figure 5.33 shows a plot of applied force versus strain for the bottom reinforcing bars B3' and B3 at the center column splice zone. In section CS, tensile strains in both reinforcing bars were similar during the test. Because the instrumented section was outside the location of critical flexural cracks near the center column, strains were smaller than measured in Specimen 1. Yielding of the reinforcing bars in the section CS was not observed. Tensile strains in both reinforcing bars were similar until the force reached approximately 40 kip in section CC. At this force level, reinforcing bar B3 developed strains larger than those for reinforcing bar B3'. This difference occurred because reinforcing bar B3' starts at the south column so the bar may slip and high strains did not develop after the critical diagonal tension crack widened near the south column at 40 kip. The yielding of the reinforcing bars in the section CC was not observed. In section CN, tensile strain in both reinforcing bars were similar until the force reached approximately 16 kip. Due the section is close to the critical flexural cracks, reinforcing bar B3 developed higher strains than reinforcing bar B3' in section CS. The measured strain in

reinforcing bar B3 exceeded the expected yield strain (0.0025) in section CN at applied force of about 44 kip. The maximum measured strain at the splice was 0.023 in the bar B3 in section CN which is less than the maximum strain in Specimen 1. Similar strain variation was observed in bars B4 and B4' and is presented in Appendix D.

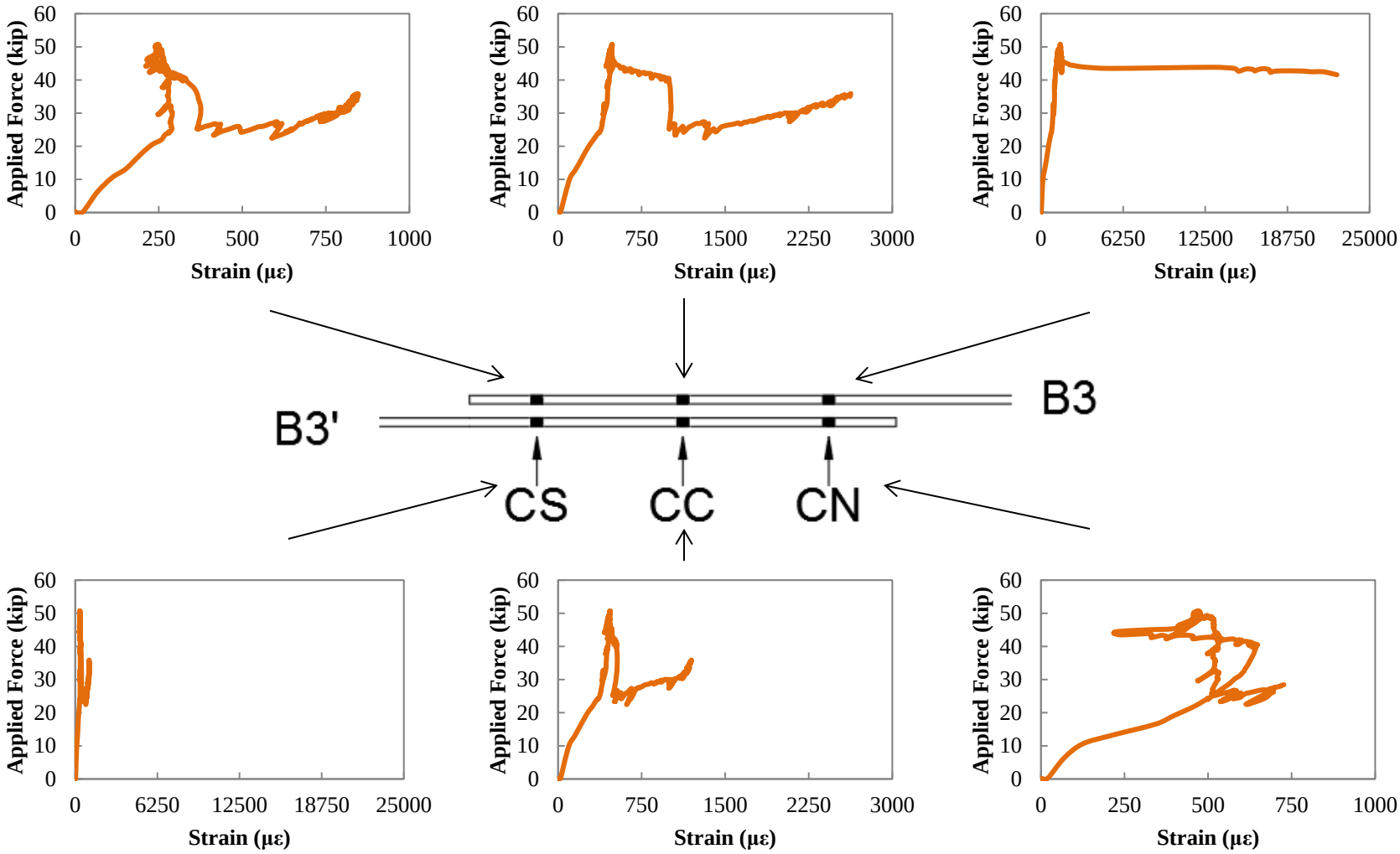

Figure 5.33: Force-strain response of bottom reinforcing bars at center column splice zone (Specimen 2)

Figure 5.34 shows a plot of applied force versus strain for the top reinforcing bars T4’ and T4 at the midspan splice zone. In section MS, tensile strains in both reinforcing bars were similar until the load reached approximately 30 kip. Section MC is located halfway along the splice at beam midspan, so similar tensile strains in both reinforcing bars were measured. Similar to Specimen 1, the strains in this section were in tension initially and gradually changed to compression after the applied peak force. In section MN, strains were in compression initially and gradually changed to tension after the sudden decrease of the applied force, which indicates that a tension axial force developed in the beams. The maximum measured strain at the splice was 0.001 in the bar T4’ in section MS which is similar than the maximum strain in Specimen 1. Yielding of the reinforcing bars in the splice was not observed.

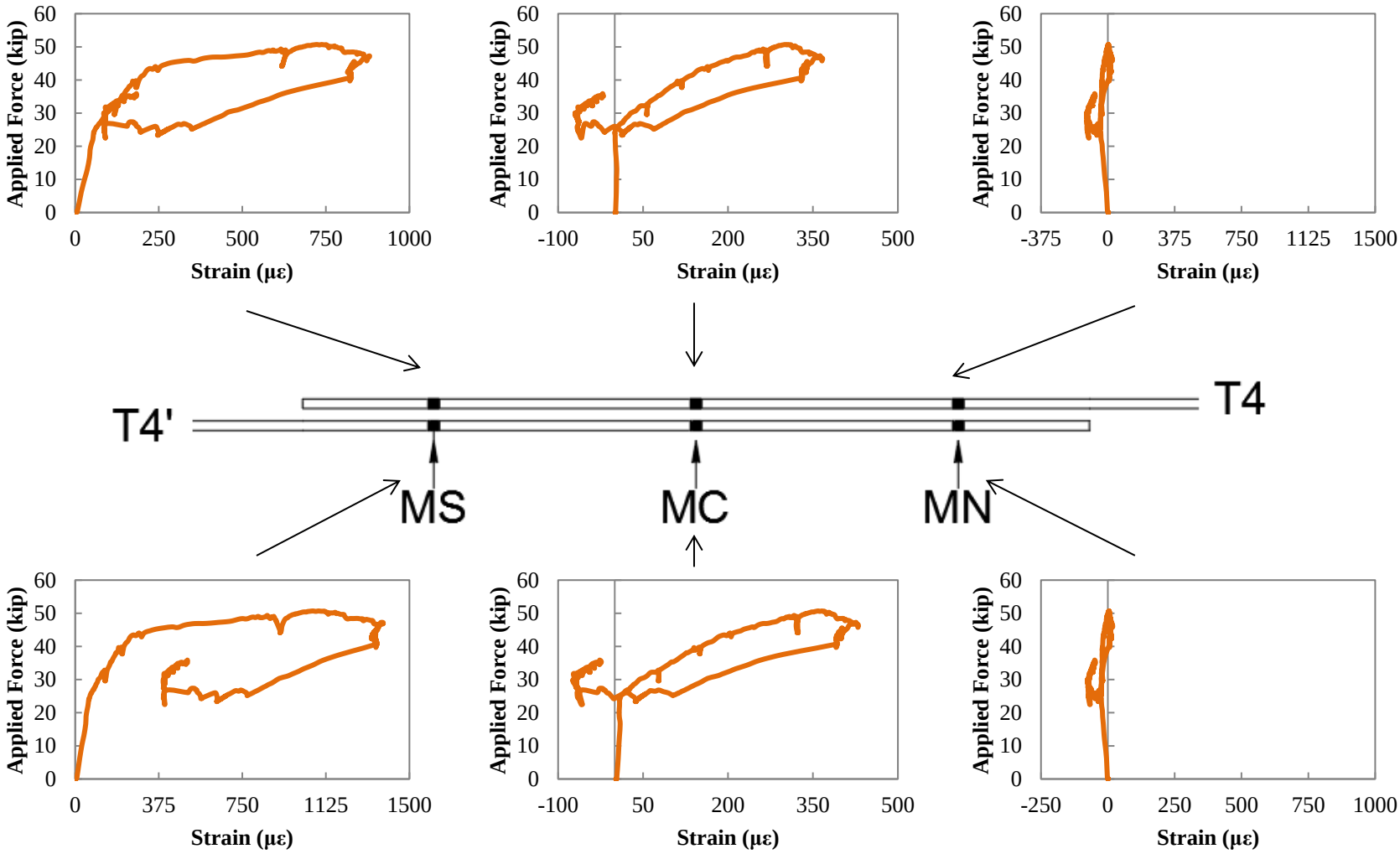

Figure 5.34: Force-strain response of bottom reinforcing bars at midspan splice zone (Specimen 2)

Figure 5.35 shows the strain variation at 52 kip of the bottom reinforcing bars B3’ and B3 in the bottom splice. Similarly, Figure 5.36 shows the strain variation of the bottom reinforcing bars B4’ and B4. In the plots, section CS represents bar cutoff section for reinforcing bars B3 and B4; and section CN represents bar cutoff section for reinforcing bars B3’ and B4’. As shown in Figure 5.35, strains in section CS for the reinforcing bar B3 and CN for the reinforcing bar B3’ are smaller than those in section CN and CS for the reinforcing bars B3 and B3’ respectively, due to the proximity of the instruments to the end of the splice region. In contrast to those bars, strains in reinforcing bar B4 and B4’ are similar in section CS and CN as shown in Figure 5.36. All strains recorded in these bars remained below the yield strain.

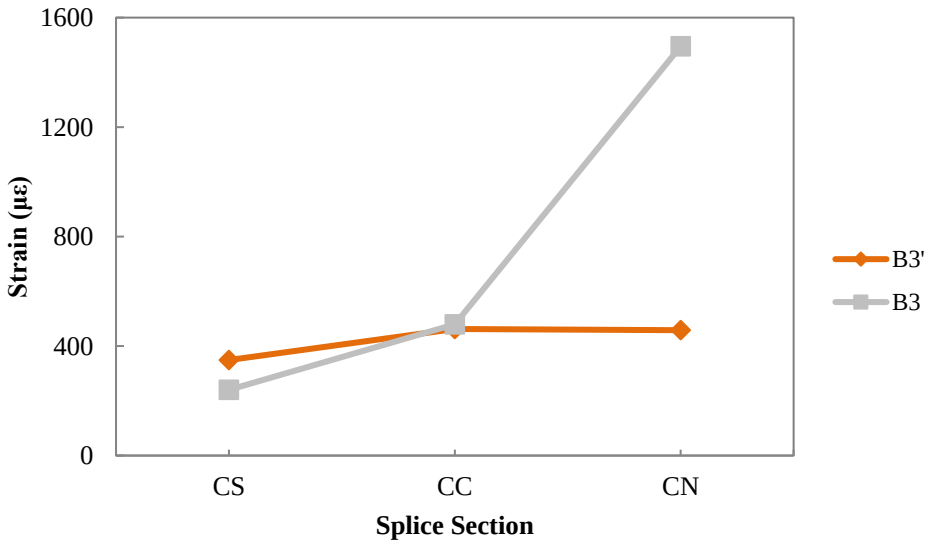

Figure 5.35: Strain variation of bottom reinforcing bars B3’ and B3 in the bottom splice at 50 kip (Specimen 2)

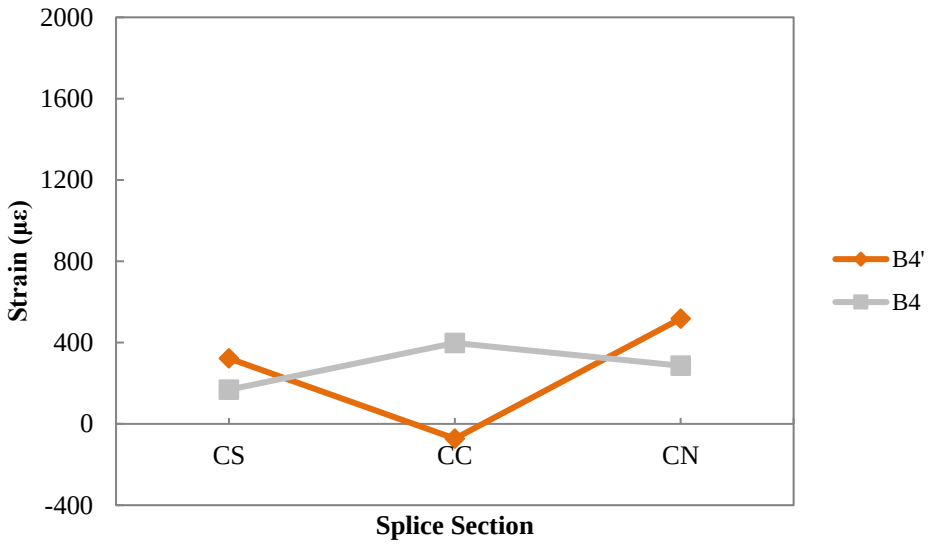

Figure 5.36: Strain variation of bottom reinforcing bars B4' and B4 in the bottom splice at 50 kip (Specimen 2)

5.4 Specimen 3

5.4.1 Observed Response

Due self-weight, narrow flexural cracks developed in the bottom part of the beams near the center column stub. The maximum width of the cracks measured after positioning the specimen in the test setup was 0.005 in. The weight of the double-channel beam used to transfer the force to the specimen increased the width of the cracks near the center column to 0.008 in. The measured deflection caused by self-weight of the concrete beam and the weight of the double-channel loading beam was 0.875 in. Figure 5.37 shows the crack pattern that formed after placement of Specimen 3 in the test apparatus.

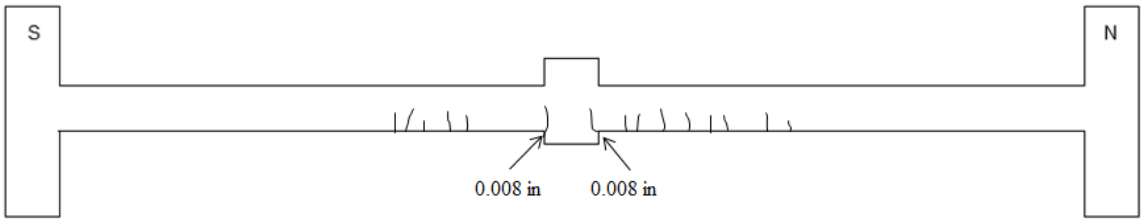

Figure 5.37: Crack pattern of Specimen 3 formed by the self-weight of the specimen during handling and positioning, and by weight of loading beam (Crack widths not indicated are smaller than 0.008 in.)

At 32 kip of applied force and a 1.3 in. vertical displacement of the center column, flexural cracks developed at the top of the beams near the exterior columns, and at the bottom of the beams near the center column. The maximum width of these new cracks was 0.005 in. Two existing dead load cracks near the center column widened to 0.060 in., as shown in Figure 5.38. Figure 5.39 illustrates the crack pattern that the specimen exhibited at this force level.

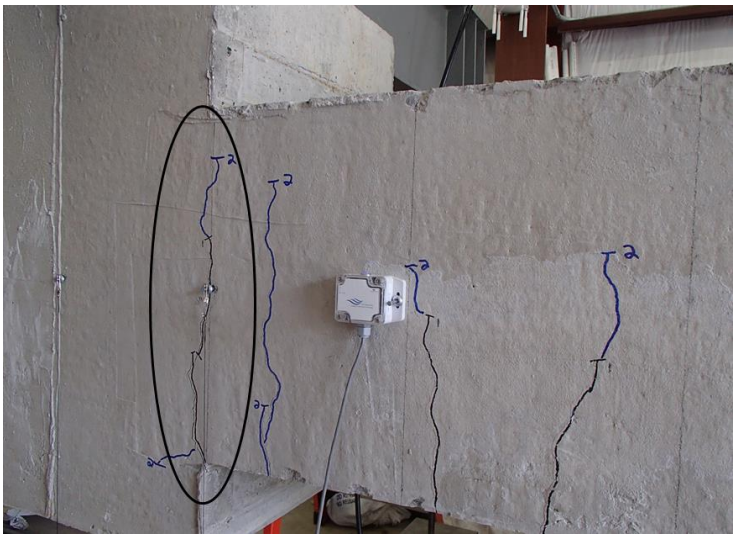

Figure 5.38: Critical flexural crack near the center column (Specimen 3)

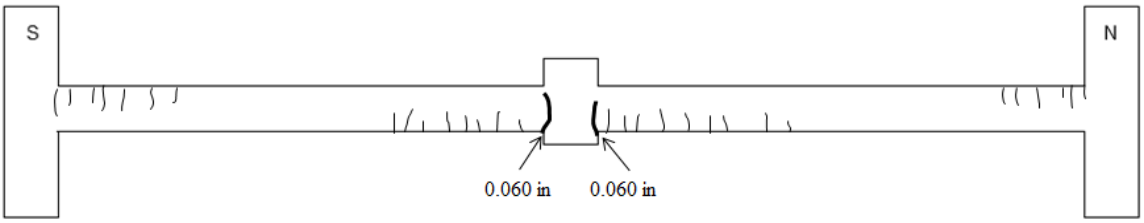

Figure 5.39: Crack pattern of Specimen 3: Force = 32 kip; center displacement = 1.3 in.

As the applied force reached an applied value of 49 kip (center column vertical displacement of 3.9 in.), diagonal tension cracks appeared at the beam ends at near the exterior columns. The maximum width of theses observed cracks was 0.080 in. The critical flexural crack near the center column increased to a width of 0.25 in. Also, initiation of concrete crushing was observed at the top of the beams meeting at the center column. Shear and flexural cracks appeared at the joint and the exterior face of the exterior columns respectively. Figure 5.40 shows the cracks near the north column. Also, Figure 5.41 shows the crack pattern for this force level.

Figure 5.40: Cracks near the north column (Specimen 3)

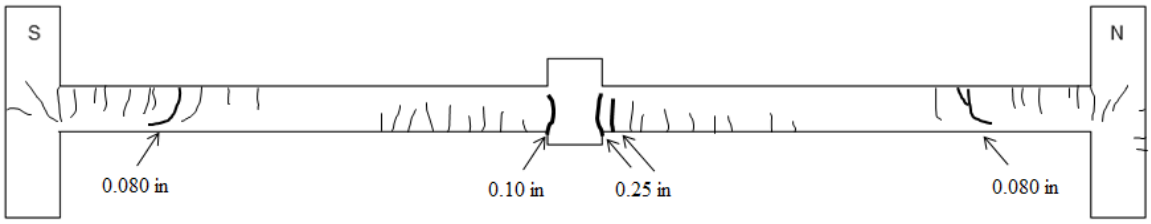

Figure 5.41: Crack pattern of Specimen 3: Force = 49 kip; center displacement = 3.9 in.

The applied force reached the maximum applied value of 53 kip (center column vertical displacement of 8.5 in.). At this point in the testing, loading proceeded without an increase in the applied force. Instead, the force in the specimen dropped at increased center displacement. Widening of the critical diagonal tension crack in the beam near the south column occurred at an applied force equal to 51 kip of (10.8 in. center column vertical displacement). The widening of the diagonal tension crack may have caused loss of aggregate interlock causing the applied force decrease suddenly to 18 kip. With further increase in the center column displacement, the applied force started to increase again until it reached 34 kip (13.8 in. center column vertical displacement). At this applied force, one stirrup fractured at the critical diagonal tension crack at the beam near the south column. Full depth diagonal cracks were observed at the beam near the south column with a maximum width of 4 in. and accompanied by concrete spalling. Crushing of the concrete at the bottom of the beams occurred near the exterior columns. One flexural crack near the center column increased in width to 0.50 in. Figures 5.42 and 5.43 show the condition of Specimen 3 at the end of the test after the loading beam was removed. Also, Figure 5.44 shows the final crack pattern.

Figure 5.42: Specimen 3 condition at the end of the test

a)

b)

c)

Figure 5.43: Specimen 3 condition at the end of the test a) near the south column, b) near the north column and c) at the center column

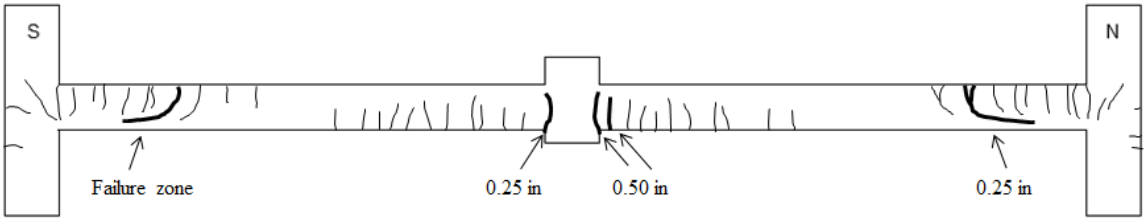

Figure 5.44: Crack pattern of Specimen 3 at failure: Force = 34 kip; center displacement = 13.8 in.

5.4.2 Measured Force-Displacement Response

Figure 5.45 shows the applied force versus the vertical displacement measured at the center column. The applied force was measured using the load cells designated as W-LC and E-LC. The vertical displacement of the center column was measured using a linear displacement transducer referenced to the beam axis at the column stub (CC-LDT). As shown in Figure 5.45, the specimen was slightly unloaded a few times to measure cracks and take pictures.

The longitudinal reinforcement reached the yield strength on both sides of the center column at 33 kip corresponding to a 1.2 in. center column vertical displacement (point A in Figure 5.45). Similarly, the longitudinal reinforcement reached the yield strength near the exterior column at 40 kip corresponding to a 1.8 in. center column vertical displacement (point B in Figure 5.45)

The peak applied force was 53 kip (point C in Figure 5.45). At an applied force equal to 51 kip (point D in Figure 5.45), widening of the critical diagonal tension crack in the beam near the south column occurred causing the applied force decrease suddenly to 18 kip (point E in Figure 5.45). With further increase in the center column displacement, the applied force started to increase again until it reached 34 kip. At this applied force,

one stirrup fractured at the critical diagonal tension crack at the beam near the south column (point F in Figure 5.45). Subsequent to this stage the specimen was fully unloaded.

Figure 5.46 shows the horizontal force measured in three of the four rods located near the top of the south column plotted against the vertical displacement of the center column. The fraction of the horizontal reaction was measured using the load cells designated as TL-LC, TR-LC, BL-LC positioned on the rod that connects the column to the steel brace. The horizontal reaction fraction increased until it reached the maximum value of 0.6 kip corresponding to 11.2 in. center column vertical displacement. With further increase in the center column displacement, horizontal reaction fraction remained constant until one stirrup fractured at the critical diagonal tension crack at the beam near the south column at 13.8 in. center column vertical displacement. In the plot, positive values of the horizontal reaction represent inward restraint in the top of the south column. Inward restraint generated tension force in the diagonal brace.

Figure 5.47 shows the deformed shapes constructed using displacement measurements taken along the beams at maximum force, after the critical diagonal tension crack widened and at the end of the test. Due the formation of plastic hinges in the beams near the exterior columns and center column after the maximum force, the vertical displacement increased and concentrated in the center column.

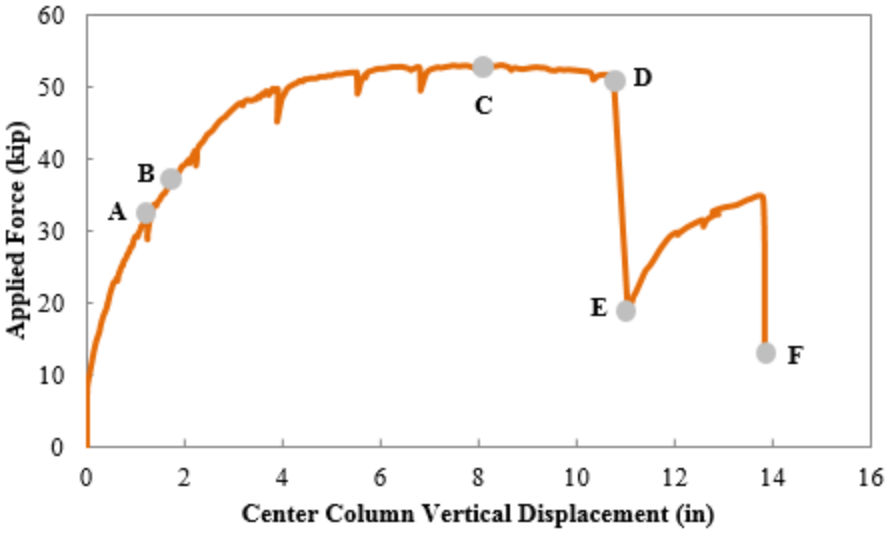

Figure 5.45: Force versus displacement of the center column (Specimen 3)

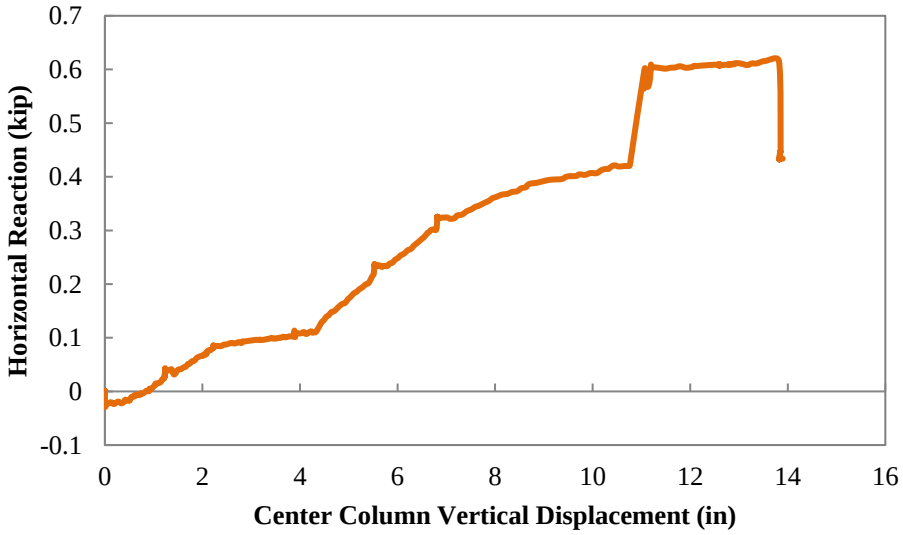

Figure 5.46: Horizontal force measured in three of four rods at the top of the south column versus vertical displacement of the center column (Specimen 3)

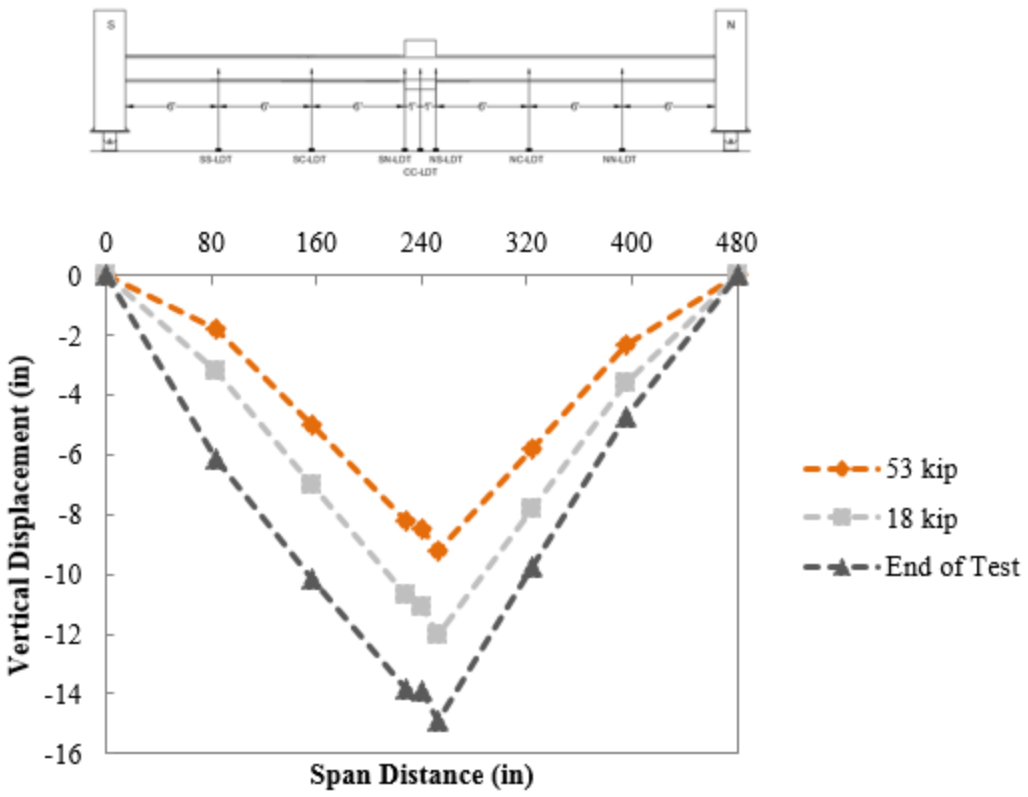

Figure 5.47: Deformed shape of the beams at peak, after the critical diagonal tension crack widened and at the end of the test (Specimen 3)

5.4.3 Measured Rotation Response

Figure 5.48 shows the applied force versus the rotations measured at both ends of the beam in the south span. Rotations were measured using the inclinometers designated as SS-INC and SN-INC. The SS-INC inclinometer was used to measure the rotation in the beam end near the south column, and the SN-INC inclinometer was used to measure the rotation in the beam end near the center column. Similar to Specimen 1 and 2, the measured rotations near both beam ends were similar until the force reached approximately 32 kip. At this force level, one flexural crack near the center column widened to approximately 0.060 in., resulting in a significant reduction section flexural stiffness. Rotations concentrated near the center column stub instead of the south end of

the beam. The measured rotations just prior to widening of the critical diagonal tension crack were 0.047 rad for the beam end near the center column, and 0.017 rad for the beam end near the south column. As shown in Figure 5.49, the north span exhibited similar behavior with the south span, where the rotation near the center column stub are larger than those measured at the end of the span. The measured rotations just prior to widening of the critical diagonal tension crack were 0.052 rad for the beam end near the center column, and 0.019 rad for the beam end near the north column.

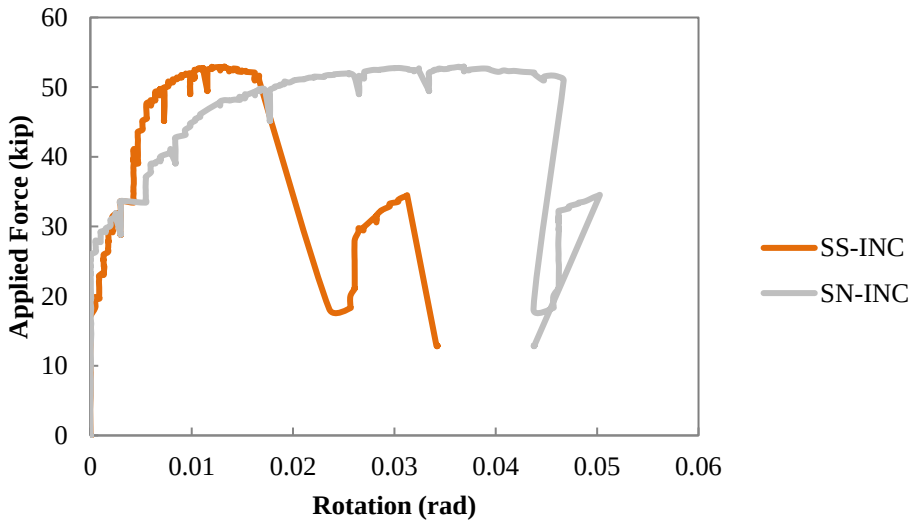

Figure 5.48: Force versus rotations at the beam end for the beam on the south span (Specimen 3)

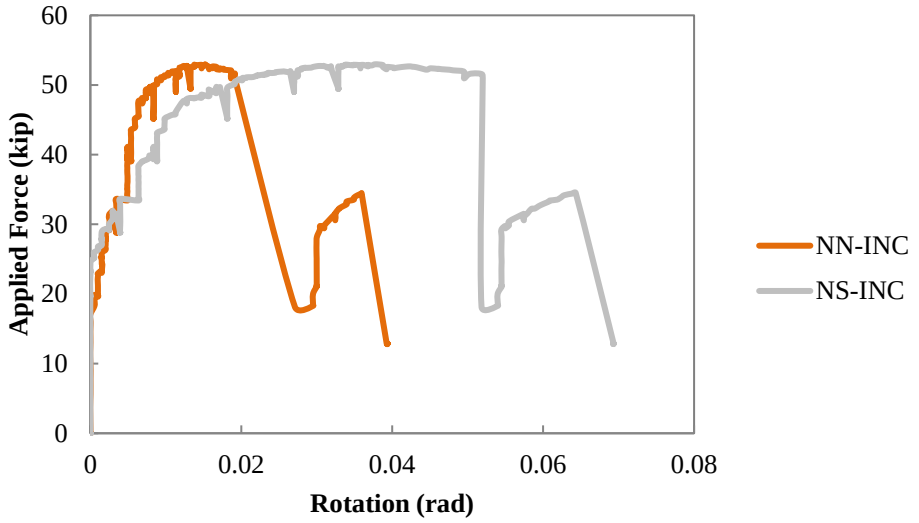

Figure 5.49: Force versus rotations at the beam end for the beam on the north span (Specimen 3)

5.4.4 Measured Strain Response

Figure 5.50 shows the location of strain gauges placed on the bottom reinforcing bars splice zone near the end of the beam-column stub connection, and on the top reinforcing bars in the splice zone near the beam midspan. The bottom splice zone is located near the center column stub 17 ft. 6 in. from the centerline of south end column, and the top splice zone is located at midspan 10 ft. from the centerline of south end column. Thirteen strain gauges were used in the bottom splice and seven were used in the top splice.

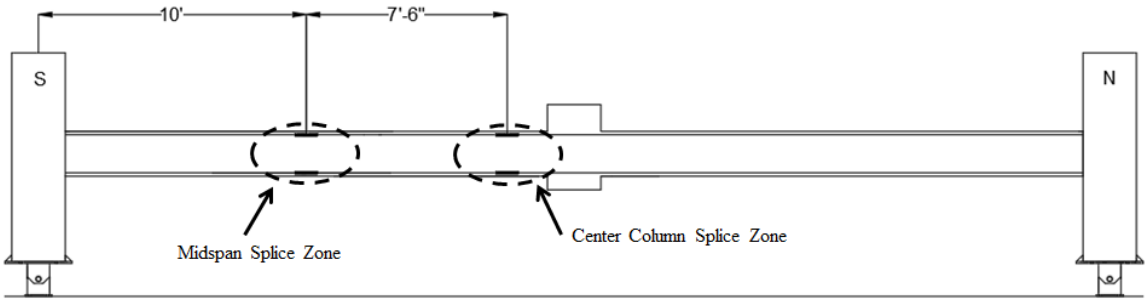

Figure 5.50: Location of sections instrumented using strain gauges (Specimen 3)

Figure 5.51 shows a plot of applied force versus strain for the bottom reinforcing bars B3’ and B3 in the section CS. Tensile strains in both reinforcing bars were similar until the force reached the peak value of 53 kip. Due the sudden decrease of the applied force after the peak, a reduction of the slope in the load-strain curve was observed. This slope reduction occurred in all sections. At the end of the test, reinforcing bar B3 developed strains larger than those for reinforcing bar B3’ and, yielding of the reinforcing bars in the section CS was not observed. Section CC is located halfway along the splice at center column stub, so similar tensile strains in both reinforcing bars was measured. The yielding of the reinforcing bars in the section CC was not registered, which is not surprising given that this section is in the middle of the splice region. In section CN, tensile strains in both reinforcing bars were similar until the force reached approximately 10 kip. After this force step, reinforcing bar B3 developed strains larger than those for reinforcing bar B3’. In contrast to Specimen 2, yielding of the reinforcing bar B3 in the section CN was not measured. The maximum measured strain at the splice was 0.002 in bar B3 in section CN, which is less than the maximum strain in Specimen 1 and 2. Similar strain variation was observed in bars B4 and B4’ and is presented in Appendix D.

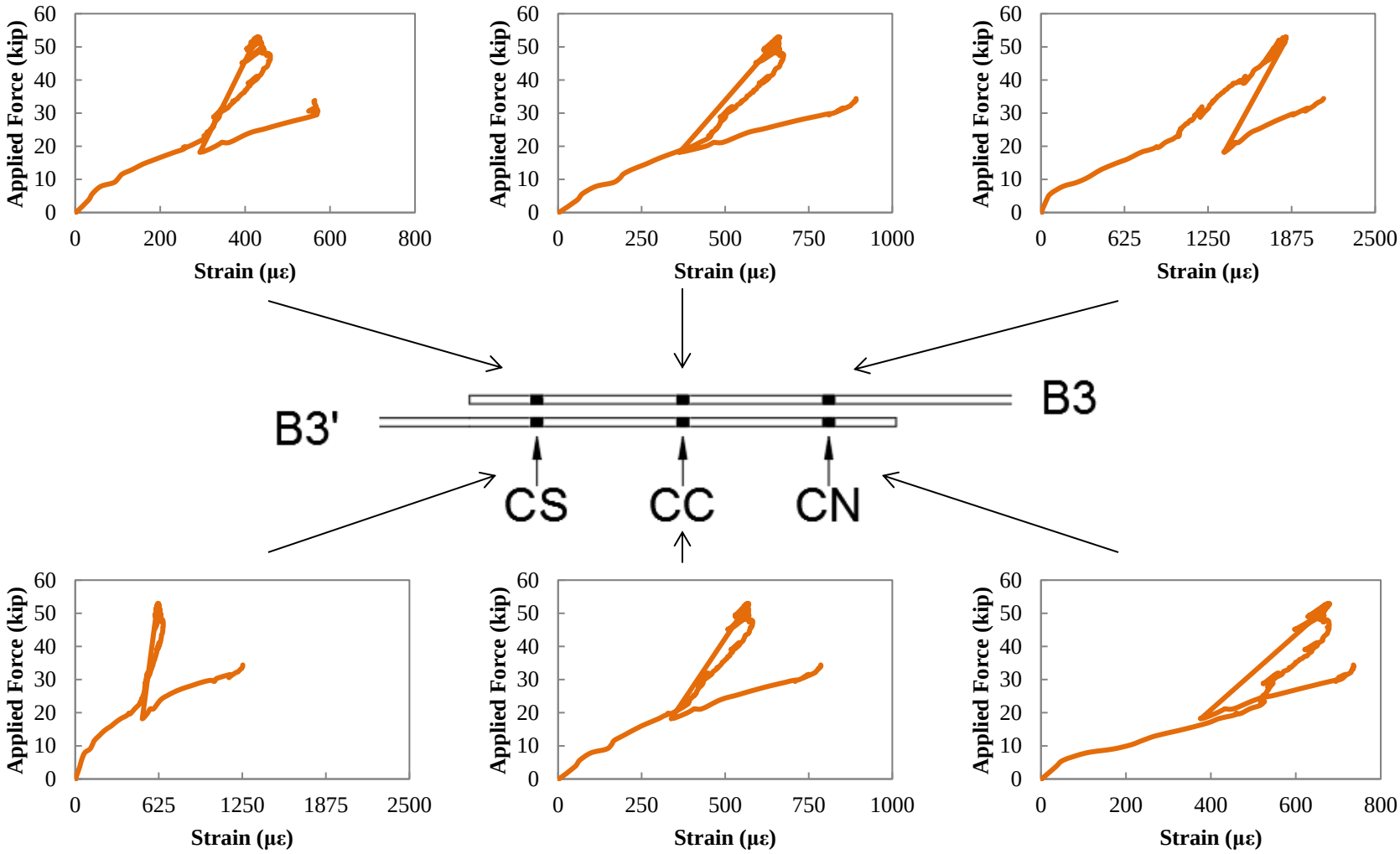

Figure 5.51: Force-strain response of bottom reinforcing bars at center column splice zone (Specimen 3)

Figure 5.52 shows a plot of applied force versus strain for the top reinforcing bars T4’ and T4 at the midspan splice zone. In section MS, tensile strains in both reinforcing bars were similar during the test. At the sudden drop in the applied force (51 kip), the strains decreased significantly at 51 kip. This strain reduction occurred in all sections. Section MC is located halfway along the splice at beam midspan, so similar tensile strains in both reinforcing bars were measured. Similar to Specimen 1 and 2, strains in this section were in tension initially and gradually changed to compression after the applied peak force decreased suddenly. The measured strains in section MN were low (less than 0.0001), so strain values in both reinforcing bars were not significantly different throughout the test. The maximum measured strain at the end of the splice was 0.001 in the bar T4’ in section MS which is similar to the maximum strain in Specimen 1 and 2. This section is in a region of low moment given the shift moment diagram from the applied force. Yielding of the reinforcing bars in the splice was not observed.

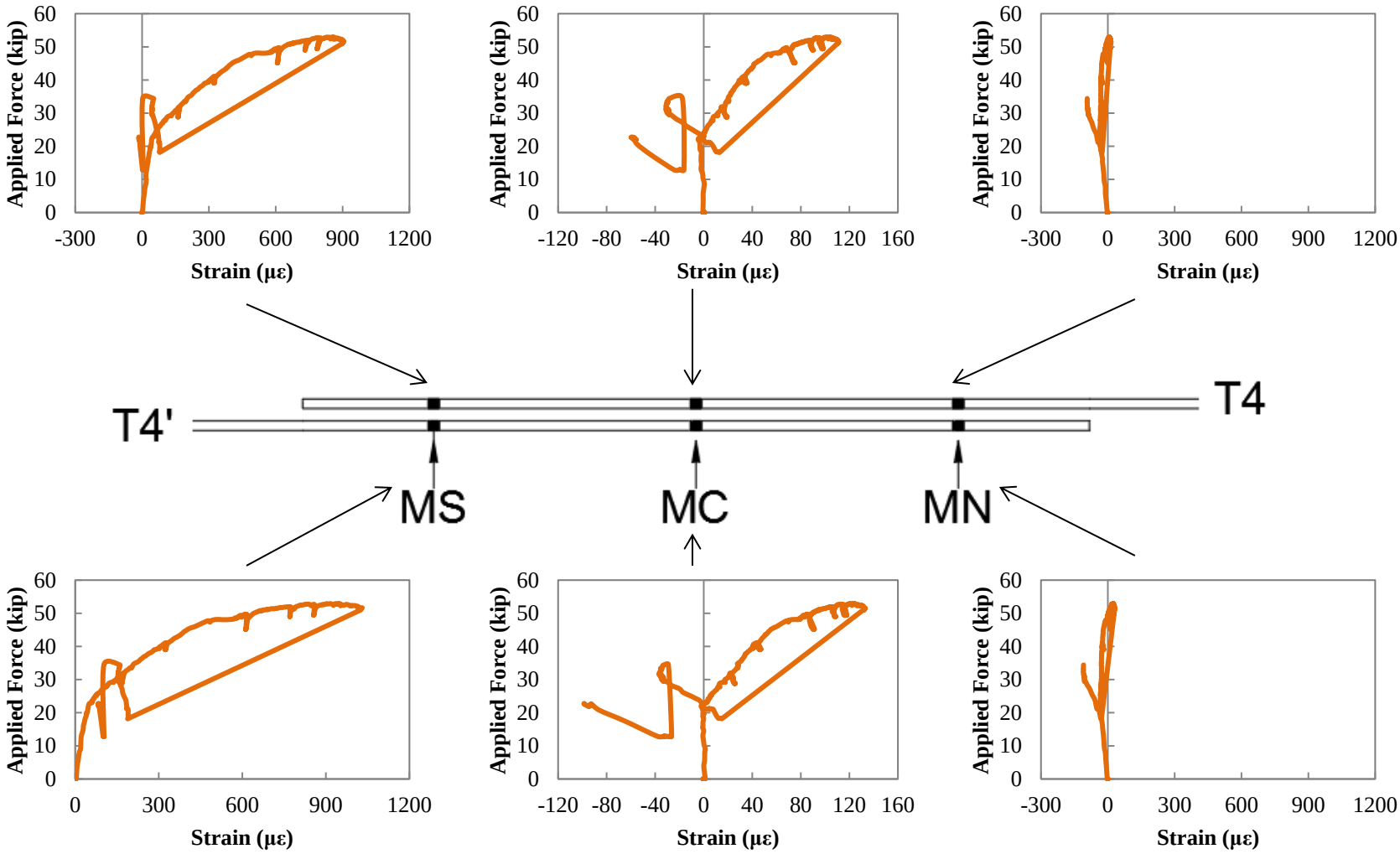

Figure 5.52: Force-strain response of top reinforcing bars at midspan splice zone (Specimen 3)

Figure 5.53 shows the developed strain variation of the bottom reinforcing bars B3’ and B3 in the bottom splice and summarizes the effect of the development length in the strains. Similarly, Figure 5.54 shows the developed strain variation of the bottom reinforcing bars B4’ and B4. In the plots, section CS represents bar cutoff section for reinforcing bars B3 and B4; and section CN represents bar cutoff section for reinforcing bars B3’ and B4’.

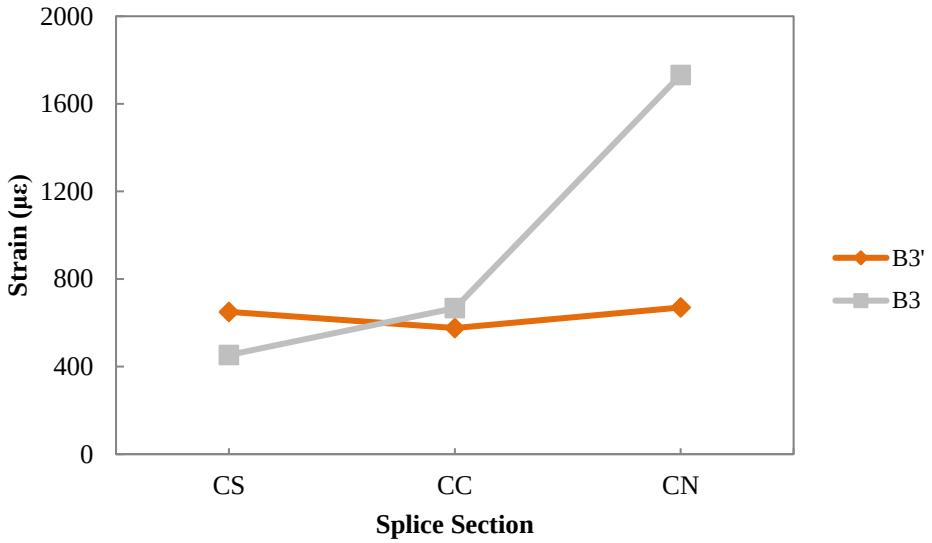

Figure 5.53: Strain variation of bottom reinforcing bars B3’ and B3 in the bottom splice at 53 kip (Specimen 3)

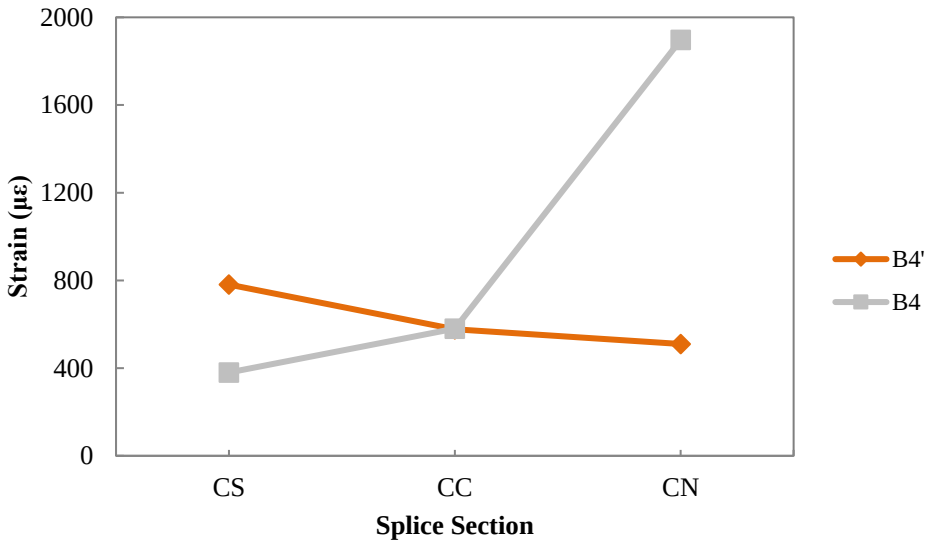

Figure 5.54: Strain variation of bottom reinforcing bars B4' and B4 in the bottom splice at 53 kip (Specimen 3)

5.5 Summary

The observed behavior and test results of the laboratory specimens subjected to vertical load on the center column using the force control method were presented in this chapter. The test results include crack patterns at representative load steps and measurements taken by the internal and external array of instruments described in Chapter 4. For Specimen 1, widening of the critical diagonal tension crack in the beam near the north column occurred at 13.9 in. center column vertical displacement causing the applied force to decrease suddenly from 43 kip to 28 kip. Similarly for Specimen 2, widening of the critical diagonal tension crack in the beam near the south column occurred at 15.8 in. center column vertical displacement causing the applied force to drop from 40 kip to 26 kip. Specimen 3 failed due to fracture of a stirrup at the diagonal tension crack in the beam near the south column at an applied force of 34 kip corresponding to a 13.8 in. center column vertical displacement. The test results of the

laboratory specimens presented in this chapter are discussed in Chapter 6. Table 5.1 summarizes the specimen force-displacement response at different stages.

Table 5.1: Summary of the applied force-center column vertical displacement results for the specimens

Stage[a]	Specimen 1		Specimen 2		Specimen 3	
	Force (kip)	Displacement (in.)	Force (kip)	Displacement (in.)	Force (kip)	Displacement (in.)
A	33	1.5	33	1.0	33	1.2
B	38	1.8	39	1.5	40	1.8
C	52	4.9	50	6.4	53	8.5
D	43	13.9	40	15.8	51	10.8
E	28	14.1	26	15.9	18	11.1
F	28	16.3	35	27.9	34	13.8

[a]Stages are identified in Figures 5.9, 5.27 and 5.45

CHAPTER 6

DISCUSSION OF RESULTS

6.1 Introduction

This chapter discusses the test results of the laboratory specimens presented in Chapter 5. The discussion includes comparison among the specimens by a presentation of the measured response from the instrumentation. First, the sequence in the formation of hinges is discussed as a result of changes in the moment diagram because of removal of the center column. A discussion of the concrete shear strength degradation and the contribution of the stirrup to the shear strength at the critical crack section is presented in this chapter. Also, a comparison is made of the observed behavior of the specimens with tests conducted of similar specimens by previous research groups.

6.2 Observed Formation of Hinges

Design of the specimens was conducted following the moment diagrams associated with the prototype building prior to removal of an interior column. The beams in the specimen followed the design of the perimeter frame of the prototype building. After removal of an interior column, the moment diagrams change significantly placing high tensile demands on bottom reinforcement at the connection with the center column. Furthermore, negative moments at the far connections also change (larger negative moments) because of an increase in span. These changes in the moment diagram pattern affect the sequence in which plastic hinges form in the specimen and placed high tensile demands in reinforcement in places where the bars were originally in compression.

For the three specimens, the first flexural cracks appeared in the bottom of the beam near the center column followed by flexural cracks in the top of the beam near the exterior columns. These cracks grew and widened at increasing applied forces as discussed in Chapter 5. The critical diagonal tension cracks appeared near the beam ends at exterior columns at or before the peak forces was applied to each specimen. The applied force reached similar maximum values for all the specimens; 52 kip, 50 kip and 53 kip for Specimen 1, 2 and 3, respectively. After this point, loading proceeded without an increase in the applied force and widening of the critical diagonal tension crack in the beam near the north column for Specimen 1 and near the south column for Specimen 2 and 3 occurred, causing the applied force to decrease suddenly. A summary of the maximum applied force and key values of the measured response just prior to widening of the critical diagonal crack widening for the specimens is listed in Table 6.1.

Table 6.1: Summary of the maximum applied force and the measured response just prior to widening of the critical diagonal tension crack for the specimens

Specimen	1	2	3
maximum applied force (kip)	52	50	53
applied force just prior to widening of the crack (kip)	43	40	51
displacement just prior to widening of the crack (in.)	13.9	15.8	10.8
NN rotation (rad)	0.029	0.008	0.019
NS rotation (rad)	0.112	0.066	0.052
SN rotation (rad)	0.130	0.118	0.047
SS rotation (rad)	malfunctioned	0.018	0.017

Plastic deformation (yielding) of the longitudinal reinforcement was expected in regions of maximum moment (plastic hinge zones) in all three specimens. In the test specimens, regions of maximum moment are located at the ends of the beams adjacent to the faces of exterior and interior columns corresponding to peak negative and positive moments, respectively. The rotation capacity of the beam in the plastic hinge region is critical for flexural members as it may govern the load carrying and deformation capacities of the member (Zhao et al. 2011). Detailing of reinforcement in plastic hinge zones is critical to avoid premature shear failures or loss of flexural strength at limited rotations. The observed cracking pattern of the specimens during the tests helped to identify the location of plastic hinge zones. The center of the flexural and flexure-shear cracks that formed near the ends of the beams was approximately located by observing the occurrence of cracking in relation with the face of the columns. Figures 6.1 to 6.6 show cracking observed in the plastic hinge zone regions for Specimen 1, 2 and 3. Dashed lines represent the approximate location where most of the rotation of the specimens concentrated just prior to opening (failure) of the critical diagonal tension crack. Table 6.2 summarizes the position with respect to the face of the closest column and the approximate length of the plastic hinge zones for each specimen determined by observing the area where most of the rotations occurred. It should be noted that there were four plastic hinge zone regions in each specimen, two near the ends of each beam span.

a)

b)

c)

Figure 6.1: Plastic hinge zones at the end of the test a) near the south column, b) near the north column and c) at the center column for the Specimen 1

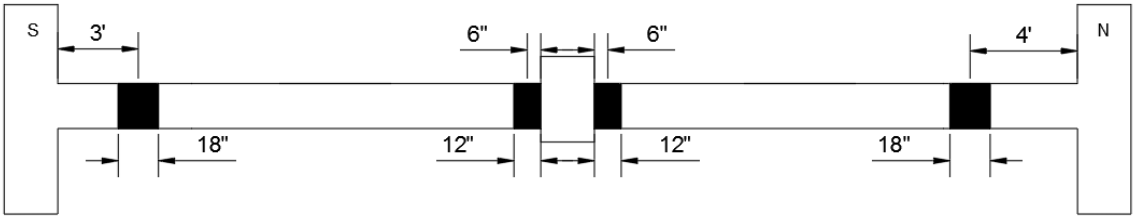

Figure 6.2: Plastic hinge locations and approximate lengths in Specimen 1

a)

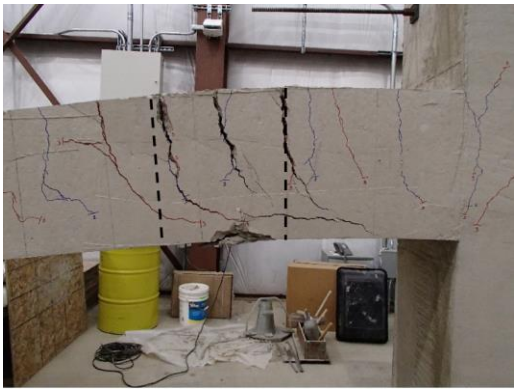

b)

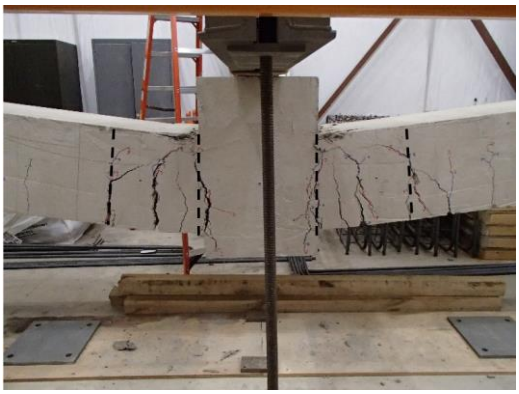

c)

Figure 6.3: Plastic hinge zones at the end of the test a) near the south column, b) near the north column and c) at the center column for the Specimen 2

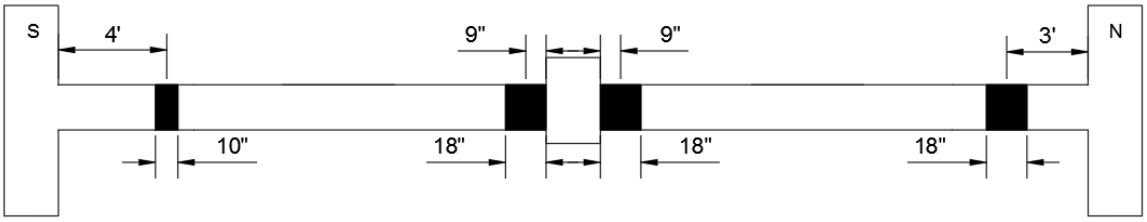

Figure 6.4: Plastic hinge locations and approximate lengths in Specimen 2

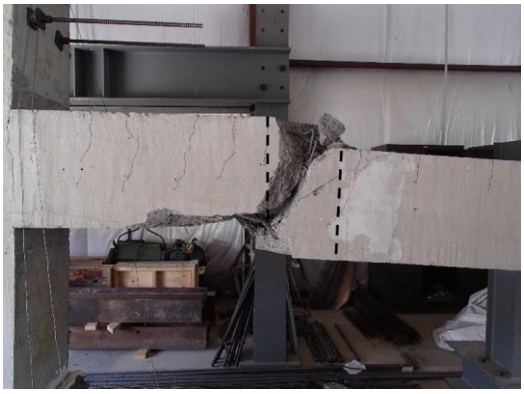

a)

b)

c)

Figure 6.5: Plastic hinge zones at the end of the test a) near the south column, b) near the north column and c) at the center column for the Specimen 3

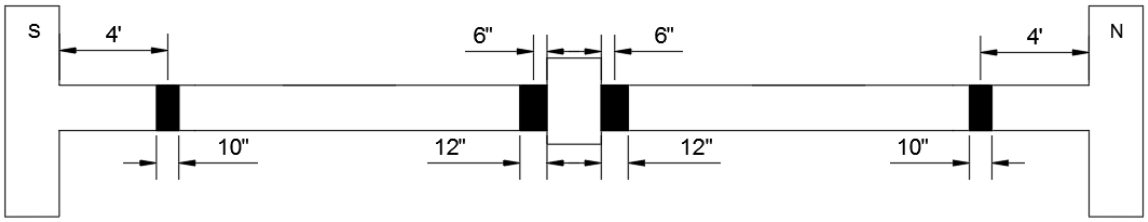

Figure 6.6: Plastic hinge locations and approximate lengths in Specimen 3

Table 6.2: Summary of the plastic hinge details for the specimens

Specimen	1	2	3
south plastic hinge location[a] (ft)	3	4	4
south plastic hinge length[b] (in.)	18	10	10
center plastic hinge location[a] (ft)	6	9	6
center plastic hinge length[b] (in.)	12	18	12
north plastic hinge location[a] (ft)	4	3	4
north plastic hinge length[b] (in)	18	18	10

[a]Distance measured from the face of the closest column to the center of the plastic hinge
[b]Length determined approximately through observation of the concentration of beam rotations (dashed area in pictures above)

The specimens were designed to simulate the condition of the frame after center column removal. Therefore, the reinforcement in the beam at the connection with the center column stub was governed by negative moments generated by gravity loads. After considering removal of the column, the moments in the center connection changed sign from negative to positive; the applied force in the specimens reproduces this condition.

Figure 6.7a shows bending moment diagrams for a typical interior beam on the prototype building before and after column removal. The moment diagrams correspond to $1.2D + 1.6L$ (*ASCE 7-10*) before the column removal, and $1.2D + 0.5L$ (*GSA 2016 Guidelines*) after column removal. In these combinations D and L are dead and live load effects in accordance with *ASCE 7-10.* As shown, the interior column removal generates a decrease in negative moment at the connections where columns still remain, and moment sign reversal from negative to positive at the connection where column removal took place. The laboratory test setup was therefore designed to generate positive moments at the center beam-column connection and large negative moments at exterior beam-column connections.

Figure 6.7b shows the bending moment diagram in the laboratory specimens subjected to the *GSA 2016 Guidelines* load combination (1.2*D* + 0.5*L*), assuming the gravity load distribution found in the prototype building. Figure 6.7c shows two bending moment diagrams in Specimen 1 corresponding to applied forces of 33 kip and 38 kip. It can be observed that the moment diagram corresponding to the applied force resembles the moment diagram constructed using the gravity load distribution of the prototype building, so formation of plastic hinges in the laboratory specimens was be expected to be similar to those in the prototype building. The yield moment capacity diagram of the beam constructed using measured material properties of Specimen 1 is also shown in Figure 6.7c to determine the sequence in which plastic hinges would form in this specimen. Although not presented here, the moment diagrams of Specimens 2 and 3 (demand and capacity diagrams) were similar to those of Specimen 1 (Figure 6.7).

Plastic hinge formation was evaluated using a moment-curvature analysis (Appendix F) based on measured material properties of each specimen. The first sections to reach the hinging moment (M_y) were located near the center column at an applied force of 33 kip in all specimens. The expected ultimate moments of the sections were 1.30M_y, 1.34M_y and 1.33M_y for Specimen 1, 2 and 3 respectively. In Specimens 1 and 3, center hinges formed in the beams at approximately 6 in. from the face of the center column on both sides. In Specimen 2, hinges formed at approximately 9 in. from the face of the center column on both beam spans. The length over which plasticity spread in the center hinging regions of the three specimens, as evidenced from observed crack patterns and crack widths, were 12 in., 18 in. and 12 in. in Specimens 1, 2 and 3 respectively, which correspond approximately to 0.5h and h (h is the depth of the beam, 20 in.). These

lengths are within the range of plastic hinge lengths that have been reported in the literature, for example those summarized by Zhao et al. (2011).

Following formation of hinges at the center column stub, flexural cracking occurred in the negative moment regions at the exterior ends of the two beam spans. Subsequent cracking in these regions revealed that hinging near the exterior ends of the beams initiated at an applied force of 38 kip, 39 kip, and 40 kip in Specimens 1, 2, and 3, respectively. The concentration of plastic deformations as evidenced from the cracking patterns and crack widths was centered at approximately 3 ft, 4 ft and 4 ft from the face of south column for Specimens 1, 2 and 3, respectively. The locations where plastic deformations concentrated in the north end of the beams were 4 ft, 3 ft and 4 ft from the face north column for Specimens 1, 2 and 3 respectively. The estimated lengths where these plastic deformations occurred (plastic hinges) are listed in Figures 6.2, 6.4, and 6.6 for Specimens 1, 2, and 3, respectively.

In contrast with past experiments conducted by Lew et al (2014) where plastic deformations in beams typically initiated close to the face of beam-column connections, hinging in the specimens tested in this research occurred near the section where two of the top reinforcing bars of the beams are terminated. As illustrated for Specimen 1 in Figure 6.7c, the moment demand diagram for an applied force of 38 kip shows that the applied moment reached the expected yield strength of the section at the bar cutoff section prior to reaching the yield strength at the face of the columns (similar results are observed in Specimens 2 and 3). Elastic-perfectly plastic simplified moment–curvature relationships of a beam section corresponding to the center plastic hinges was used to calculate the load at which the yield moments in the exterior hinges were reached, as

shown in Figure 6.7c. Formation of plastic hinges away from the beam-column connection was the result of a reduction in negative flexural strength but, perhaps more importantly, the change in point of inflection resulting from elimination of the center column. The loss of a center column clearly increases the region of the beam subjected to negative moment and triggered yielding at sections that were not designed for this demand. Furthermore, as hinging moves into the span, the plastic collapse mechanism that forms places higher rotation demands on exterior and interior hinges, highlighting the importance of providing closely spaced transverse reinforcement in these regions to prevent premature shear failures. These detailing requirements are not currently required by the ACI code for frames in low seismic regions.

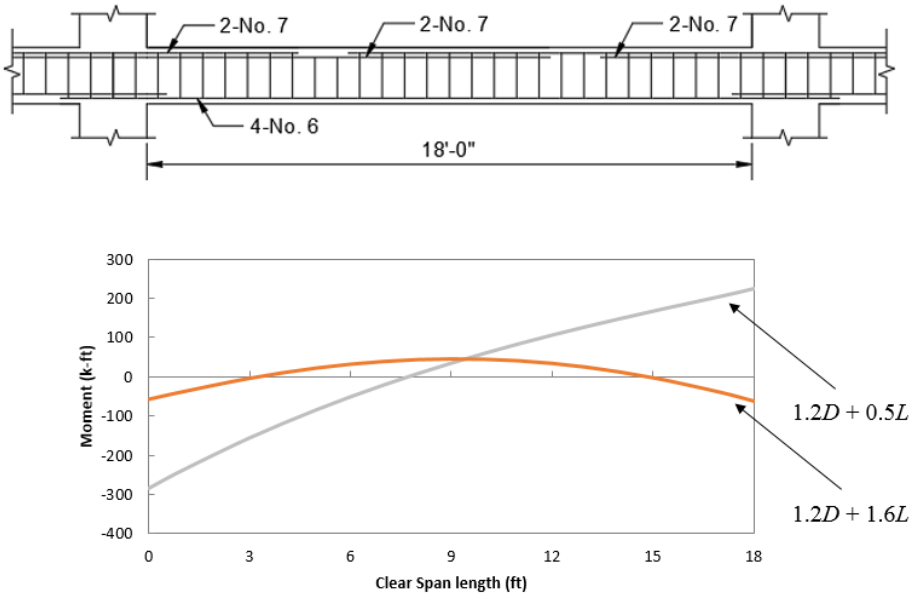

a)

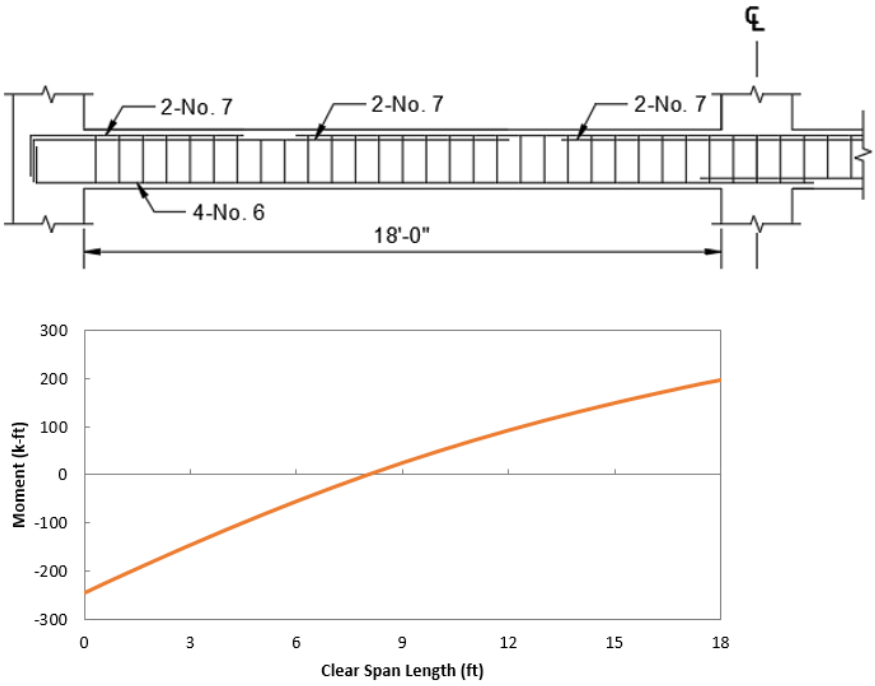

b)

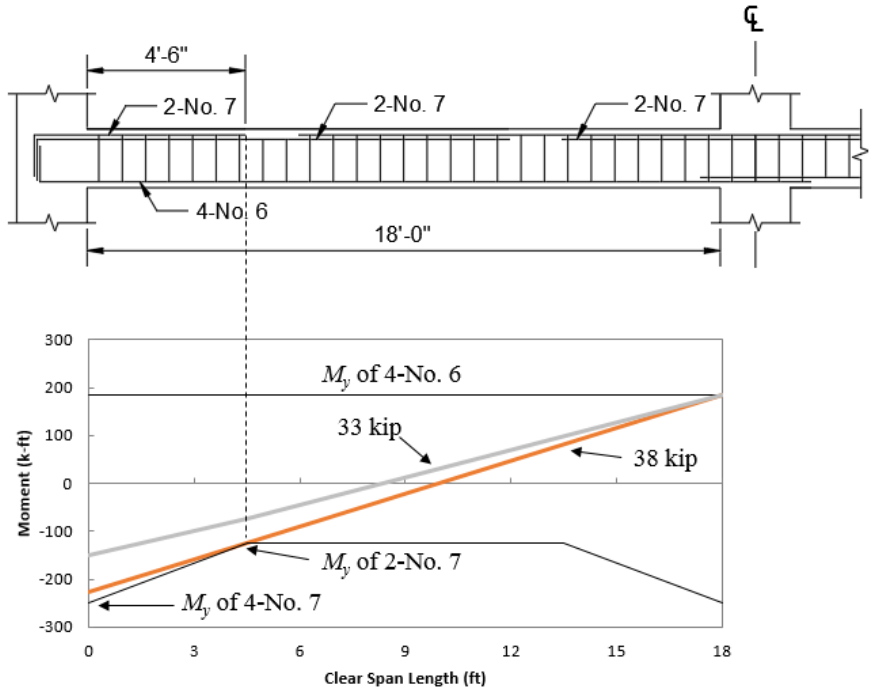

c)

Figure 6.7: Bending moment diagram subjected to the *GSA 2016 Guidelines* load combination for a) typical beam span in the prototype, b) Specimen 1and; c) Specimen 1 due an applied force of 33 kip and 38 kip

6.3 Simplified Plastic Collapse Mechanism of Laboratory Specimens

Specimens were instrumented with inclinometers placed on the surface of the beams at 10 in. from the face of the column. This position was selected to be approximately at a location corresponding to the anticipated position of plastic hinges near beam ends. During testing it was observed that the plastic rotations at beam exterior ends occurred farther into the span than anticipated, so a new plastic collapse mechanism was developed to evaluate the performance of the specimen. A simplified plastic collapse model of the specimens was developed to calculate the rotation in the plastic hinges prior to widening of the critical diagonal tension crack as shown in Figure 6.8. In this model each beam span is considered rigid between exterior and interior plastic hinges. The exterior column and portion of the beam up to the location of exterior plastic hinge is also considered to rotate as a rigid body. The displacement δ_1 was calculated using measured rotations (θ_{SS} or θ_{NN}) of the rigid column and exterior portion of beams at the south and north ends of the specimens. The displacement δ_2 was obtained by subtracting the displacement measured at the center column (δ_{tot}) using the displacement transducer at that location minus δ_1. The angle θ_2 was calculated dividing δ_2 by the beam length within plastic hinges. Finally, the rotation at the plastic hinge prior to specimen failure (θ_{cal}) was obtained by subtracting θ_2 minus measured rotations (θ_{SS} or θ_{NN}) depending on span. Table 6.3 summarizes rotations θ_{cal} that are estimates of the rotation demands placed on each exterior plastic hinge. As listed in this table, the rotations just prior to failure of the specimens were similar for the exterior plastic hinges on the two spans. For Specimen 1, the rotation at the north plastic hinge was 0.047 rad. The inclinometer used to measure the rotation near the south column malfunctioned in this specimen so the rotation at the

south plastic hinge could not be calculated. For Specimen 2, the rotations at the south plastic and north plastic hinge were 0.072 rad and 0.078, respectively. The calculated rotations were 0.044 rad for both plastic hinges in Specimen 3.

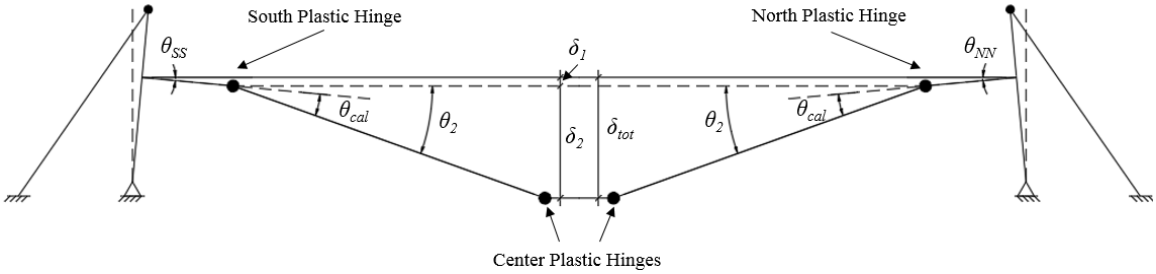

Figure 6.8: Simplified model of the specimen used to calculate the rotation at the plastic hinge just prior to widening of the critical diagonal tension crack

Table 6.3: Summary of the calculated rotations prior to crack widening for the specimens

Specimen	1	2	3
applied force (kip)	43	40	51
south plastic hinge rotation (rad)	---	0.072	0.044
north plastic hinge rotation (rad)	0.047	0.078	0.044

6.4 Shear Strength Degradation

Failure of all specimens occurred after a diagonal crack widened within the exterior plastic hinges that formed in the beams. Widening of the critical tension crack occurred in the north plastic hinge for Specimen 1, and in the south plastic hinge for Specimen 2 and 3. Widening of these diagonal tension cracks triggered loss of aggregate interlock and significant reduction in shear strength eventually leading to failure of the specimens.

The shear force that triggered diagonal tension crack widening was calculated for comparison with the shear strength of the beams. The calculated shear force prior to diagonal tension crack widening included the applied force measured at that stage in the tests and specimen self-weight. The total shear force at the exterior plastic hinge location was 30 kip, 28 kip and 34 kip for Specimen 1, 2 and 3 respectively. These shear forces are smaller than the shear strength of the beam calculated using ACI 318 procedures as described in Chapter 3. The reason for diagonal crack failure had to be investigated further.

After failure of the specimens, it was observed that the critical diagonal tension crack that triggered failure was steeper than the design truss model angle (45 degrees) assumes for design based on *ACI 318-14* (Figures 6.9-6.11). Therefore, it was possible that only one stirrup would be effective by crossing the failure crack on the compression side of the beam, so most of the shear demand needed to be supported by the concrete. Loss of aggregate interlock occurred after the diagonal tension crack widened and the concrete contribution to shear strength decreased significantly with respect to the design strength.

a)

b)

Figure 6.9: Critical diagonal tension crack a) measured angle and b) stirrups location (red lines) near the north column for Specimen 1

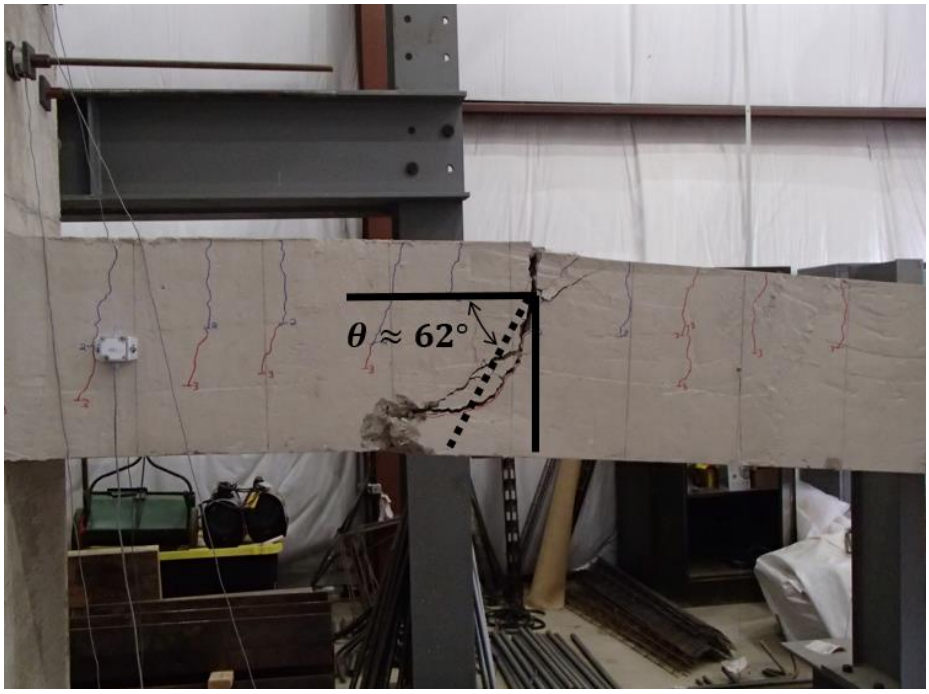

a)

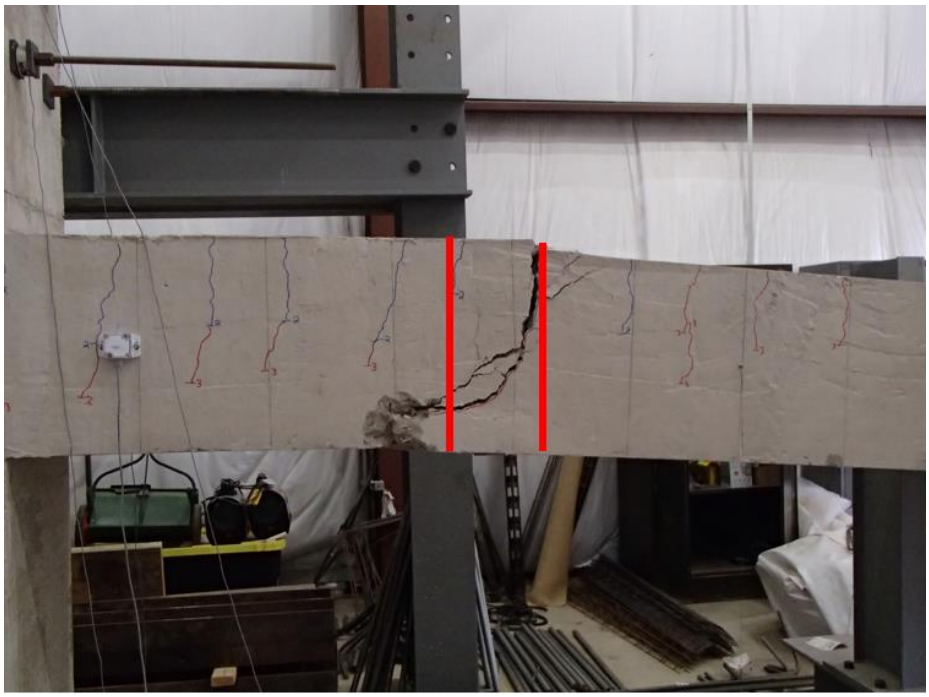

b)

Figure 6.10: Critical diagonal tension crack a) measured angle and b) stirrups location (red lines) near the south column for Specimen 2

a)

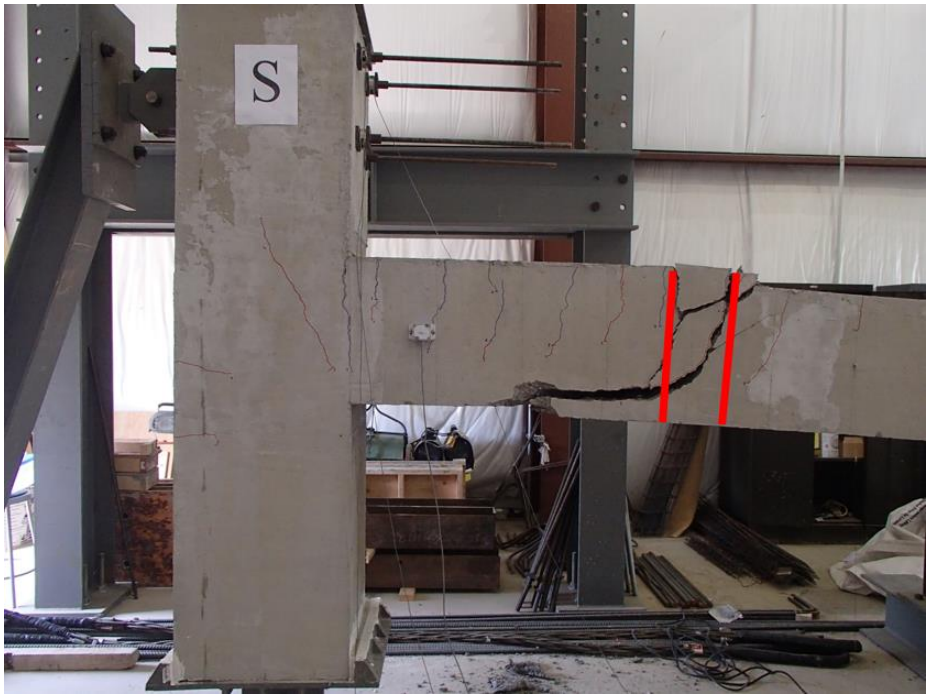

b)

Figure 6.11: Critical diagonal tension crack a) measured angle and b) stirrups location (red lines) near the south column for Specimen 3

To predict the shear strength in the critical section, the model developed by Priestley et al. (1994) was used. This model takes into account the shear strength degradation of the concrete due to widening of cracks and deterioration of other shear transfer mechanisms at increasing deformation demands., In this model, the concrete contribution to shear strength is calculated using Equation 6.1:

$$V_c = k\sqrt{f_c'}A_e \qquad 6.1$$

where:

V_c = contribution of concrete to shear strength,

k = factor that depends on curvature ductility demand (maximum curvature divided by curvature at yield) as shown in Figure 6.12,

f'_c = measured compressive concrete strength (psi), and

A_e = effective shear area, taken as 80% of the section gross area.

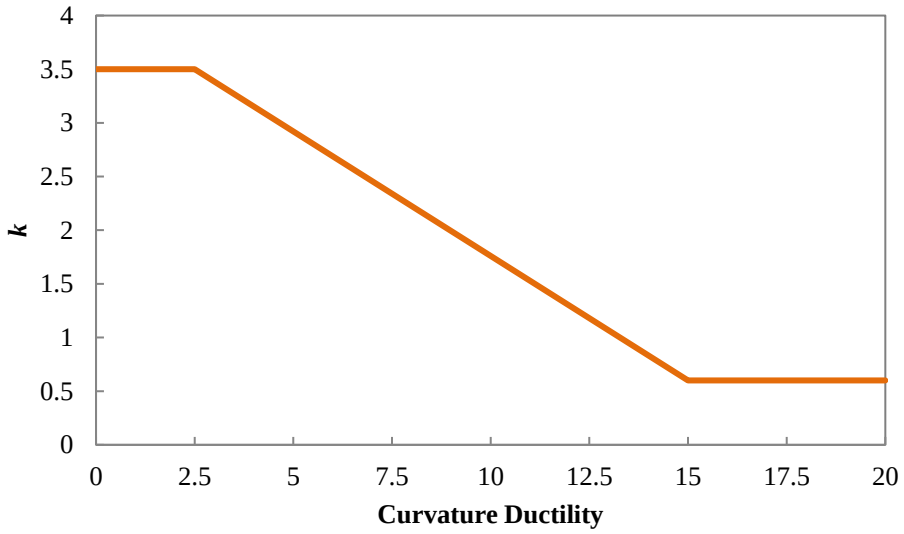

Figure 6.12: k factor based on Priestley et al. (1994)

Figure 6.14 to 6.16 show the shear strength of the specimens computed using three different methods. The dashed horizontal line labeled ACI 318 corresponds to the shear strength using *ACI 318-14* (Equation 6.2). The tri-linear curve labeled Priestley et al. corresponds to the shear strength of the section determined using the Priestley et al. model using the properties of the critical failure section and measured material properties.

$$V_c = 2\sqrt{f_c'}bd \qquad 6.2$$

where:

V_c = contribution of concrete to shear strength,

f'_c = measured compressive concrete strength (psi),

b = width of the beam, and

d= effective depth of the beam.

The curve labeled plastic shear demand corresponds to the shear forces associated to development of yield and plastic moments at the critical plastic hinges (exterior) for various applied force levels. Yield and plastic moments are determined using a moment-curvature analysis of the corresponding beam sections (interior or exterior) using measured material properties for each specimen (see Appendix F for details). A plastic analysis was conducted to relate shears at locations where hinges formed in the tests to applied force as shown in Figure 6.13. The shear that correspond to yield moment at interior and exterior hinges, and plastic bending moment at all four hinge locations was calculated using step by step plastic analysis. Because the plastic moment is less than 1.3 times the yield moment, and elastic-perfectly plastic simplified moment–curvature relationship of a beam section at center plastic hinge was used to calculate the yield shear in the exterior hinge. Table 6.4 summarizes the results of this analysis. Failure of the

critical section was determined by comparing the shear demand determined at exterior hinges (plastic shear) with the corresponding shear strength curve including shear strength degradation. The intersection of the plastic shear demand and the shear strength curves provides an estimate of potential shear failure after large curvature occurs. To determine shear strength, transverse reinforcement contribution was neglected since in some cases only one stirrup (or none) cross the critical diagonal crack at loss of aggregate interlock. Based on this, at low curvatures the shear strength is high enough to avoid shear failure of the section prior to developing the flexural capacity as shown in Figure 6.14a. In contrast, at high curvature shear failure occurs before the development of the maximum flexural capacity as shown in Figure 6.14b. The predicted shear strength at the critical (failure) section for each specimen was 31 kip, 32 kip and 31 kip for Specimen 1, 2 and 3, respectively, which is similar to the shear generated by the applied force during the tests. Also, the curvatures at the critical sections corresponding to the predicted shear strength were 0.0018 1/in., 0.0019 1/in. and 0.0018 1/in. for Specimen 1, 2 and 3, respectively. Plastic hinge lengths are difficult to determine with certainty and various empirical equations have been proposed for prediction of plastic hinge length. Using the equations provided by Zhao et al. (2011), lower and upper bound curvatures were calculated based on two estimates of plastic hinge length. Rotations just prior to failure of the specimens for the exterior plastic hinges presented in Section 6.2 were used to estimate curvatures at those sections by dividing the rotation by lower bound and upper bound plastic hinge lengths of 0.5h and 1.5h. These lengths resulted in upper bound and lower bounds of curvature, respectively, by dividing the rotation by the plastic hinge length. Table 6.5 summarizes the curvature and predicted shear strength for the three

specimens. As the table indicates, predicted curvatures were between the bounding values for Specimen 1 and 3. For Specimen 2, the predicted curvature was close to the lower bound value. Moreover, the concrete shear strength degradation prevented the critical sections from reaching their maximum flexural strength and maximum curvature as show in Figure 6.15 to 6.17.

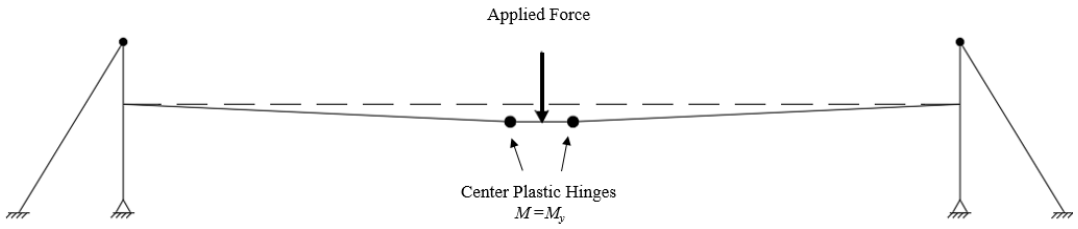

a)

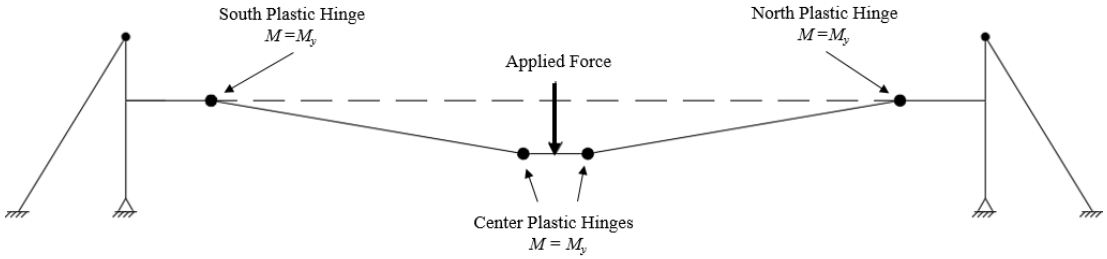

b)

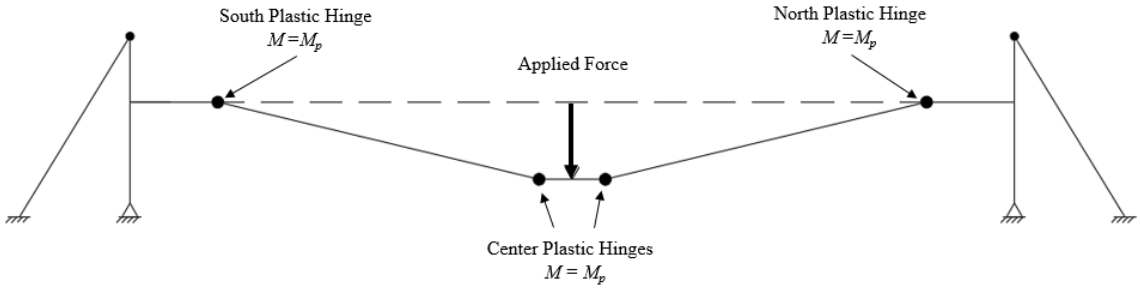

c)

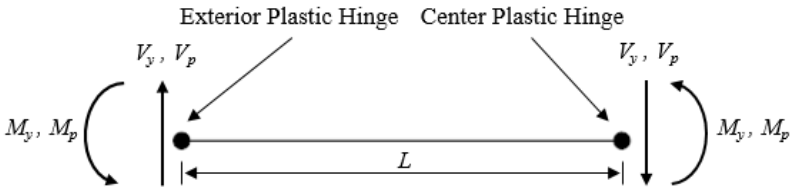

d)

Figure 6.13: Plastic analysis steps to calculate the theoretical shear values a) for yielding of the interior hinges (step I), b) yielding of the exterior hinges (step II), c) plastic formation of at all four hinge locations (step III); and the internal shear and moment for plastic hinge sections

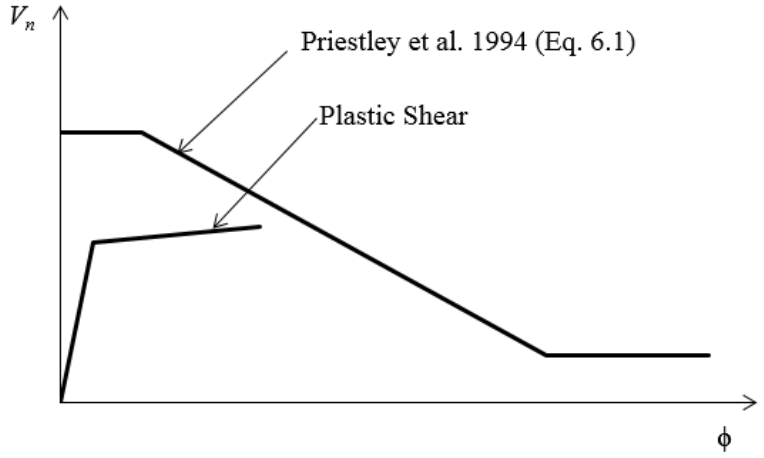

a)

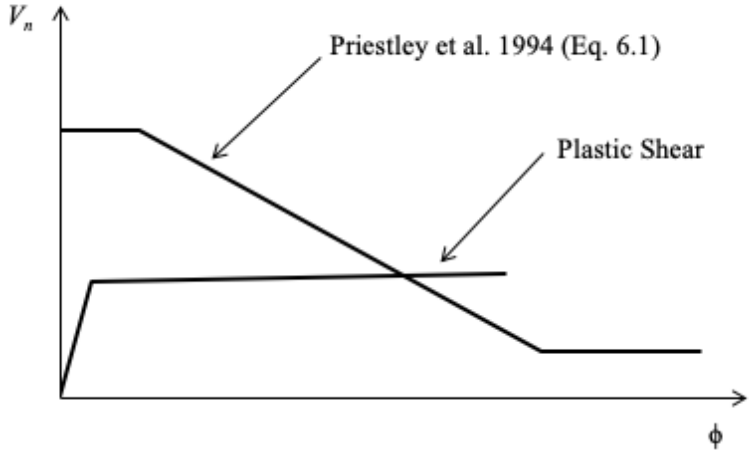

b)

Figure 6.14: Comparison of calculated plastic shear strength at a) low curvature and at b) high curvature based on the Priestley et al. (1994) strength model

Table 6.4: Summary of the step by step plastic hinge analysis for the specimens

Step	Specimen 1			Specimen 2			Specimen 3		
	Force (kip)	Moment (k-ft)	Shear (kip)	Force (kip)	Moment (k-ft)	Shear (kip)	Force (kip)	Moment (k-ft)	Shear (kip)
I	33.8	73.8	25.0	32.5	71.0	24.4	32.7	71.4	24.5
II	38.4	125.0	27.3	36.8	119.8	26.5	36.9	120.1	26.6
III	52.7	171.7	34.5	52.2	171.6	34.2	52.3	173.4	34.3

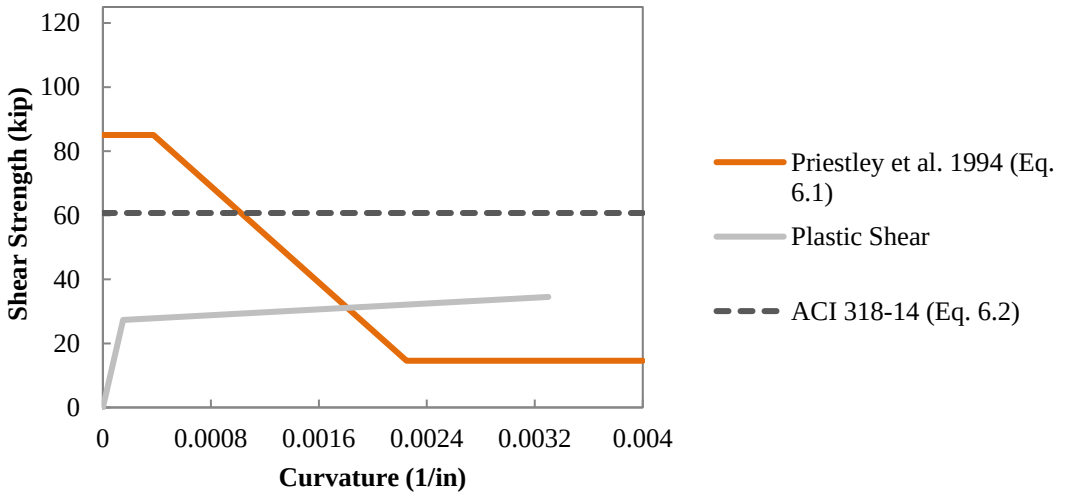

Figure 6.15: Comparison of calculated shear strength for Specimen 1 based on different strength models

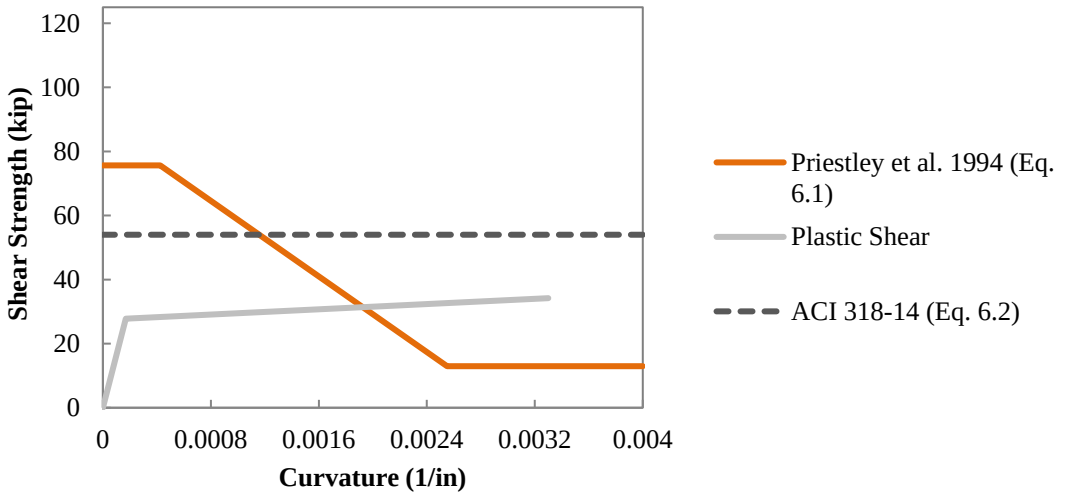

Figure 6.16: Comparison of calculated shear strength for Specimen 2 based on different strength models

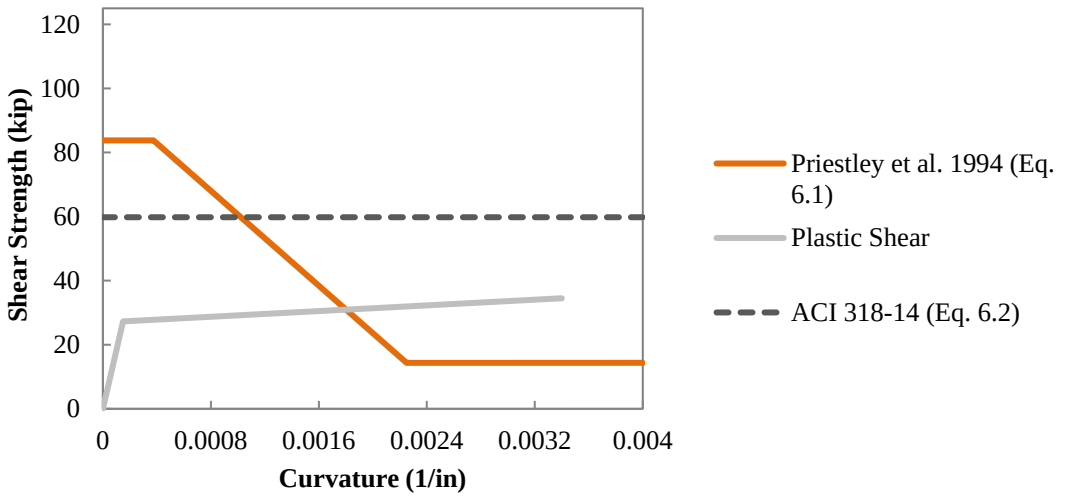

Figure 6.17: Comparison of calculated shear strength for Specimen 3 based on different strength models

Table 6.5: Curvature and predicted shear strength for laboratory specimens

Specimen	1	2	3
predicted shear strength (kip)	31	32	31
shear at the crack widening (kip)	30	28	33
predicted curvature (1/in.)	0.0018	0.0019	0.0018
lower bound curvature at the crack widening[a] (1/in.)	0.0016	0.0024	0.0015
upper bound curvature at the crack widening[b] (1/in.)	0.0047	0.0072	0.0044

[a]plastic hinge length = 1.5h
[b]plastic hinge length = 1.0h

6.5 Post-peak Strength

The first significant drop in applied force in occurred at 43 kip, 40 kip, and 51 kip for Specimens 1, 2, and 3, respectively. At these forces, the critical diagonal crack widened with a subsequent loss in capacity of the specimens triggered by of loss of aggregate interlock. Aggregate interlock is one of the primary shear transfer mechanisms that are included in the concrete contribution to shear strength of the section. Transverse reinforcement remained as the primary mechanism to transfer shear across the critical

diagonal crack. It was considered important to determine the approximate contribution to shear strength of transverse reinforcement given the inclination of diagonal cracks observed in the tests.

Based on *ACI 318-14*, the contribution of transverse reinforcement to shear strength follows a truss model with an assumed inclination of web members of 45 degrees (constant crack angle of 45 degrees). Diagonal tension cracks that form at angles steeper than 45 degrees reduce the number of stirrups that cross cracks generating a decrease in the contribution of transverse reinforcement to shear strength. Equation 6.3 is based on a truss model to account for transverse reinforcement contribution to shear strength considering an inclination of diagonal cracks different from 45 degrees:

$$V_s = \frac{A_v f_y d}{s} \cot\theta \qquad 6.3$$

where:

V_s = contribution of transverse reinforcement to shear strength,

A_v = total area of the transverse reinforcement at a spacing s,

f_y = nominal yield stress of the transverse reinforcement,

d = effective depth of the beam,

s = stirrup spacing, and

θ = diagonal crack angle relative to the beam axis.

The observed shear crack angles in Specimens 1, 2 and 3 were approximately 55 degrees, 62 degrees and 63 degrees, respectively. The contribution to shear strength by transverse reinforcement calculated from Equation 6.3 for the specimens is presented in Table 6.6. As the table indicates, the contribution to shear strength by transverse

reinforcement in Specimen 3 is similar to the shear generated by the applied force that generated the fracture of a stirrup plus calculated self-weight for at the critical crack location. Also, Table 6.6 summarize the predicted concrete shear strength at the critical section presented in Section 6.4 and the shear just prior the crack widening. Figures 6.9 to 6.11 show the critical diagonal tension crack details for the specimens.

Table 6.6: Summary of concrete and transverse reinforcement contribution to shear strength and shear at the critical section

Specimen	1	2	3
predicted concrete shear strength (kip)	31	32	31
shear just prior the crack widening (kip)	30	28	34
transverse reinforcement shear strength (kip)	37	28	27
shear just after the crack widening (kip)	22	21	17
shear at fracture of a stirrup (kip)	---	---	25

6.6 Comparison in Behavior with Past Tests

Lew et al. (2014) tested two similar sub-assemblages as the specimens in this research project but designed for high seismic regions (Seismic Design Category C and Seismic Design Category D). In contrast with those tests, the specimens tested in this research project failed by widening of the critical diagonal tension crack that caused the decrease in applied force followed by fracture of a stirrups in one of the three specimens. This behavior limited the deformation capacity of the beams and prevented them from developing catenary action that is relied upon for collapse resistance. Lew et al. (2014) concluded that the catenary action generated in the beams after the formation of diagonal tension cracks near beam ends was associated with the failure mechanisms. The seismic details provided in the specimens tested by Lew et al. included closer stirrup spacing,

which prevented widening of the critical diagonal tension crack in the beams near the columns and allowed the development of the catenary action at larger displacements. In that study, failure occurred with fracture of the bottom reinforcing bars near a main crack opening close to the center column. Jian and Zheng (2014) developed a simplified model for static analysis of progressive collapse response of reinforced beam-column substructures under column removal. The model calculates the force-deflection response using equations taking into account: the span length, the section dimension, material properties and the reinforcement of the beam. Jian and Zheng concluded that according to the mechanism of progressive collapse resistance to applied forces, the entire collapse progression consists of three stages: beam mechanism stage, transient stage and catenary stage as shown in Figure 6.18. The simplified model was validated with the experiment results presented by Lew et al. (2014) as shown in Figure 6.19. Based on this model, Figure 6.20 shows a comparison between the experimental results of the specimens and the simplified model on the applied force versus center column vertical displacement column. As shown in the figure, widening of the diagonal tension crack decreased the force preventing the beam from developing the maximum value of catenary action that the model by Jian and Zheng predicts. The specimens in the research project failed well before development of catenary action, in some cases early within the transient stage as defined by Jian and Zheng.

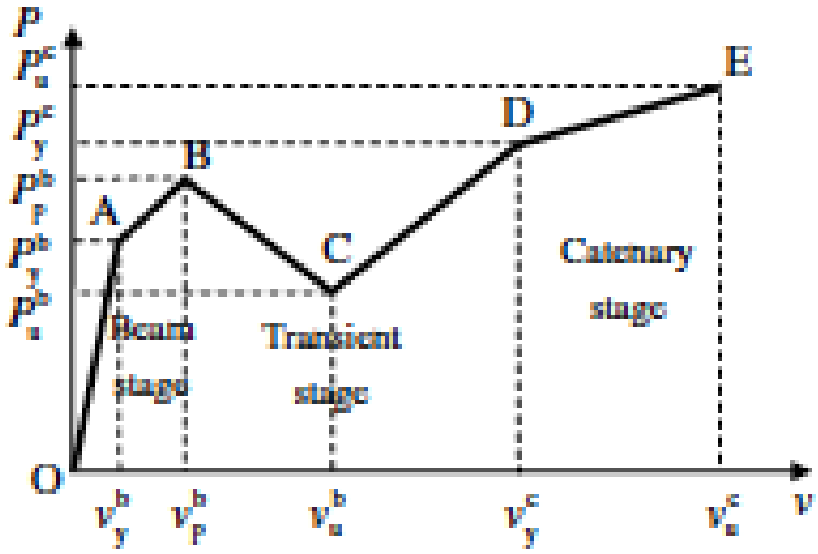

Figure 6.18: Simplified progressive collapse response curve developed by Jian and Zheng (2014)

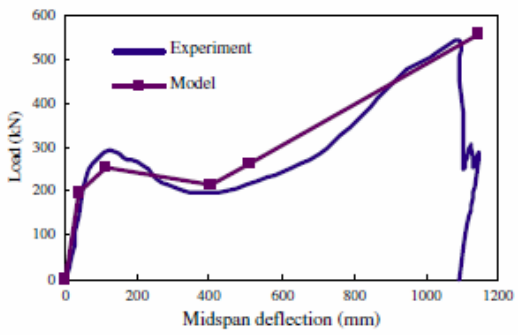

a)

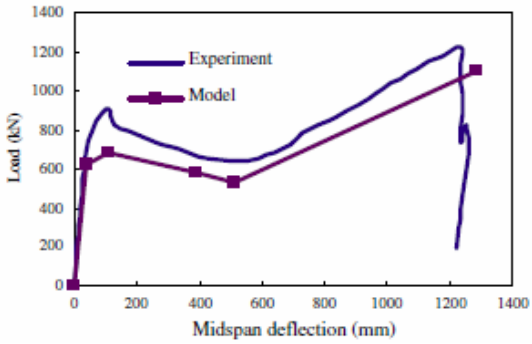

b)

Figure 6.19: Comparisons between the model results and the Lew et al. experimental results on the applied force versus center column vertical displacement column for a) the sub-assemblages designed for SDC C and b) SDC D

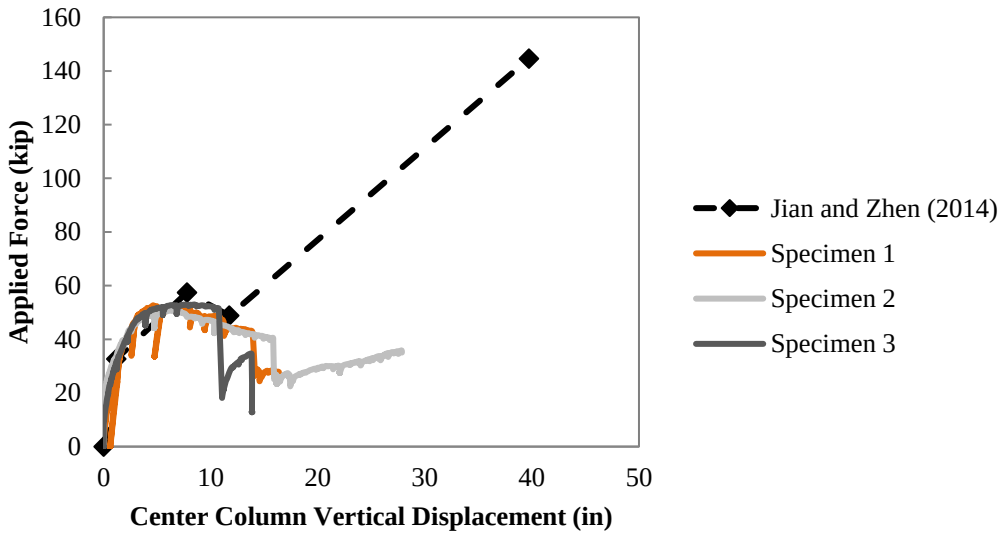

Figure 6.20: Comparisons between the model results and the experimental results of the specimen on the applied force versus center column vertical displacement column

6.7 Summary

The test results of the laboratory specimens presented in Chapter 5 were discussed in this chapter. For the three specimens, the cracks pattern started with flexural cracks in the bottom of the beam near the center column followed by flexural cracks in the top of the beam near the exterior columns. Finally, diagonal tension cracks appeared at the beam ends at near the exterior columns. Plastic hinges formed in the beam near the exterior columns and center column. The applied force reached similar maximum value for all the specimens. After this point, loading proceeded without an increase in the applied force and widening of the critical diagonal tension crack in the beam near the exterior column occurred causing the applied force to decrease suddenly. Rotations just prior to the widening of the crack were similar for the north and south plastic hinges for all specimens. Loss of the aggregate interlock occurred after the diagonal tension crack widened and the concrete contribution to shear strength decreased significantly. Also, the

concrete shear strength degradation did not allow the development of the maximum flexural strength of the section. The observed shear cracks angle was steeper than the truss model angle (45 degrees) assumed in design based on *ACI 318-14*, so the spacing of transverse reinforcement at that section precluded fewer stirrups from crossing the diagonal crack and contribute to the shear strength after the loss of the aggregate interlock. The diagonal tension cracks widened significantly preventing the beam from developing an alternate load path that would presumably allow an increase in the applied force as has been reported by past researchers.

CHAPTER 7

COLLAPSE ANALYSIS OF PROTOTYPE BUILDING

7.1 Introduction

This chapter describes the analytical procedure that was followed to investigate the progressive collapse behavior after elimination of an interior and a corner column in the first story of the ten-story prototype reinforced concrete frame building described in Chapter 3. Furthermore, analytical simulations of one of the laboratory specimens (Specimen 3) were also conducted using SAP2000 (SAP2000 Version 17.0) to calibrate the moment-curvature response of the beam based on the laboratory results. For consistency, the same software (SAP 2000) was used in the analysis of the 10-story prototype building. The analytical model constructed to simulate the experimental results was used to get a reliable nonlinear model for plastic hinges that formed at beam ends that could be validated for use in the prototype building model. The calibrated plastic hinge model was used in the 10-story prototype model to account for the nonlinear frame behavior by assigning plastic hinges at sections along beams and columns. A description of the procedure employed, and key results are discussed in this chapter.

7.2 Plastic Hinge Model

Nonlinear material behavior of the beams was modeled using a lumped plasticity approach by assigning plastic hinges at selected locations along the beam length. By using a lumped plasticity approach, the nonlinear behavior was assumed to concentrate only at locations where plastic deformations were anticipated and effectively concentrates

all the nonlinear action at a point along the beam. The force-deformation properties of plastic hinges along the beam were defined using the moment-curvature relationship at the sections where plastic hinges were placed. The moment-curvature response curves for beam hinges were constructed using measured material properties to construct the nonlinear stress-strain response of reinforcement and concrete. Column hinge properties were constructed using values taken from Table 10-8 (modeling parameters a,b and c in Figure 7.1) on the American Society of Civil Engineers *Seismic Evaluation and Retrofit of Existing Buildings* (ASCE 41-13). Figure 7.1 shows the moment–curvature relationship for columns defined in the *ASCE 41-13* Standard; where yield moment and curvature are defined as M_y and ϕ_y respectively, and ultimate moment and ultimate curvature are defined as $M_{u,}$ and $\phi_{u.}$ Also, the curvature at the tensile reinforcement fracture is defined as ϕ_f. The modeling parameters a, b and c in the figure depend of the section properties and axial load in the column as shown in Table 10-8 of the *ASCE 41-13*. Based on this and the section properties of the column, coupled axial-force and uniaxial-moment hinges were assigned to the column critical sections.

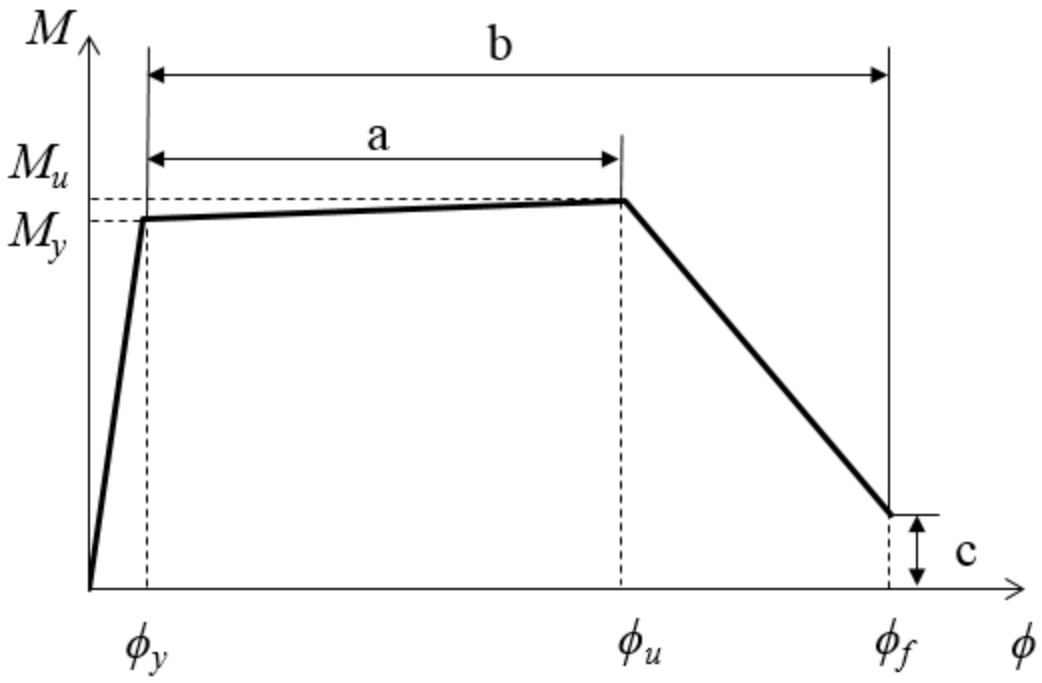

Figure 7.1: Backbone moment–curvature relationship for columns defined in *ASCE 41-13*

7.2.1 Material Properties

The nonlinear material properties used to construct the moment-curvature response of beam hinges are discussed in this section. Two material models were used to represent the uniaxial stress-strain behavior of steel and concrete. Measured parameters needed to define the uniaxial material models are presented in Appendix E.

7.2.1.1 Concrete

The uniaxial stress-strain behavior of concrete in compression was modeled using a curve proposed by Mander et al. (1984). In this model, the compression portion of the unconfined stress-strain curve consists of an exponential function. The maximum compressive stress and the corresponding strain are defined as $f'c$, and ε_{co}, respectively. The ultimate concrete strain capacity is defined as $\varepsilon_{cu.}$ Also, modulus of elasticity of the

concrete is defined as E_c. The secant modulus of elasticity of the concrete defined as the slope of the line drawn from a stress of zero to a compressive stress of 0.45 f'_c is estimated as $57000\sqrt{f'_c}$ (psi), in accordance with *ACI 318-14 §*19.2.2. The tensile stress-strain behavior of concrete consists of a linear relation with slope equal to (E_c). The tensile strength is approximated as $7.5\sqrt{f'_c}$. Figure 7.2 shows the uniaxial stress-strain diagram for concrete and the equations used to describe the behavior of unconfined concrete in compression and tension.

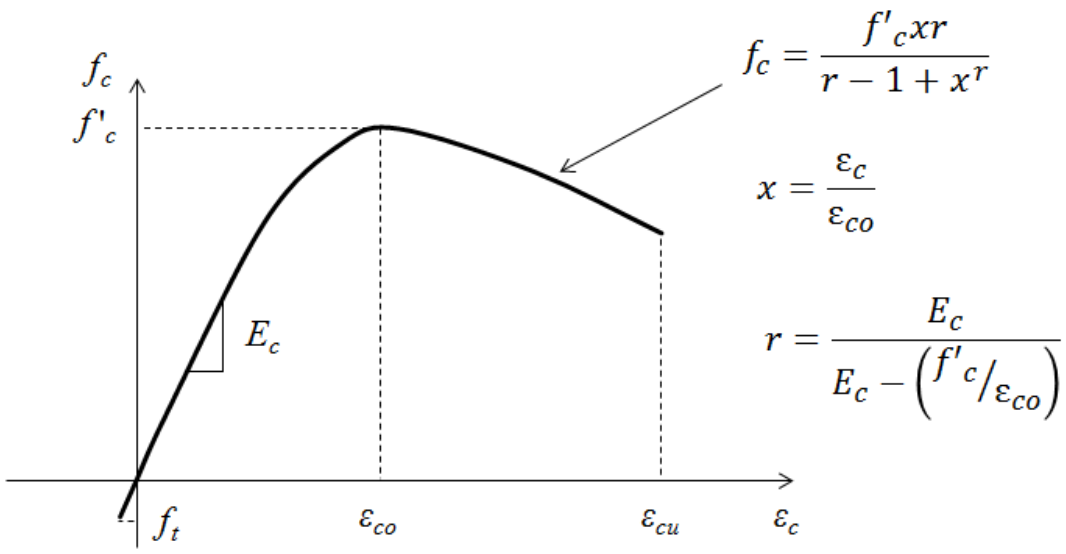

Figure 7.2: Mander et al. (1984) unconfined concrete stress-strain model

Compressive tests of cylinders and split-cylinder tests were conducted to define the concrete tensile and compressive strength for Specimen 1, 2 and 3. Because Specimen 3 exhibited the smallest rotation for the beam end near the failure crack, the concrete test results from Specimen 3 were used in the analysis. The analyses would therefore represent a lower bound on the deformation capacity determined from the models. The average compressive strength ($f'c$) of the concrete measured at the time of testing was

equal to 4137 psi, obtained from testing four 4 in. by 8 in. cylinders and one 6 in. by 12 in. cylinder. Strain at peak stress, ε_{co}, and maximum compressive strain ε_{cu}, were assumed to be equal to 0.002 and 0.004, respectively, because these values were not obtained experimentally. Results from individual cylinder tests for each specimen are summarized in Appendix E.

7.2.1.2 Reinforcing Steel

The stress-strain relationship of the reinforcing steel was based on the measured mechanical properties of the reinforcing bars used to fabricate the specimens. Coupons taken from bars fabricated from the same heat of steel were tested in tension for several sizes used as longitudinal reinforcing bars in the beams. The bar coupons consisted in two no. 6 deformed bars (bottom reinforcing bars) and two no. 7 deformed bars (top reinforcing bars). Figures 7.3 and 7.4 show the average stress-strain curves for the two longitudinal reinforcing bars sizes used in the beams, no. 6 and no. 7, respectively. Table 7.1 shows average values of the measured mechanical properties of reinforcing bars. Results from individual bar coupon tests are summarized in Appendix E.

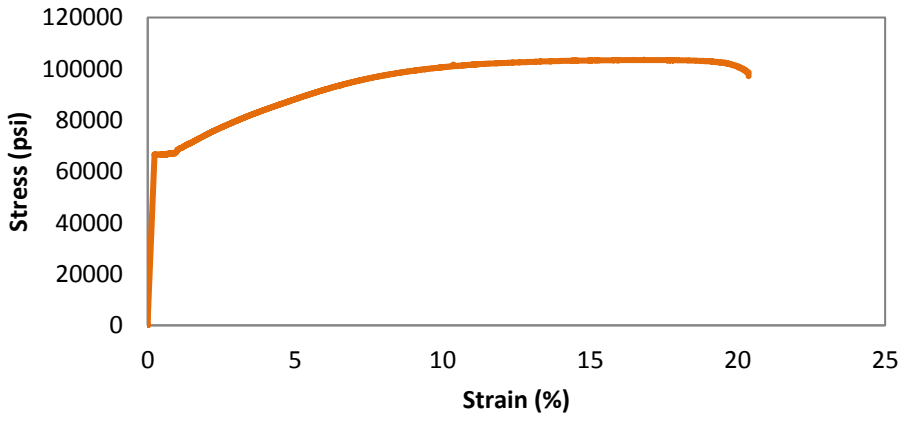

Figure 7.3: Average stress-strain curve for no. 6 longitudinal reinforcing bars

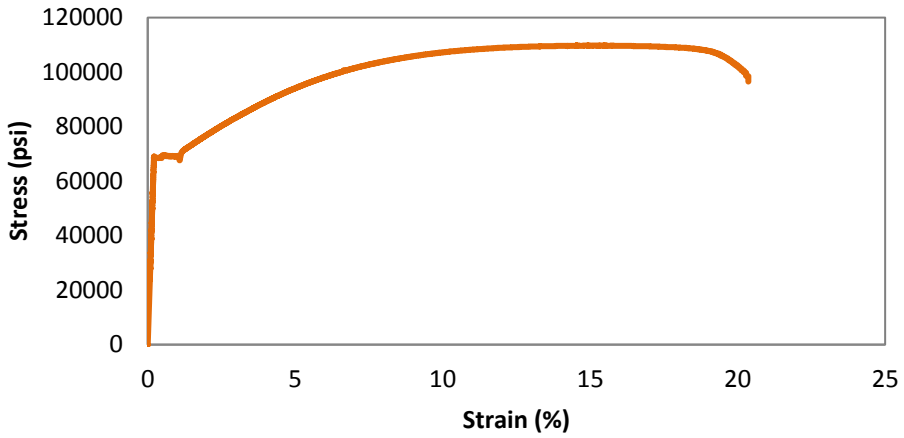

Figure 7.4: Average stress-strain curve for no. 7 longitudinal reinforcing bars

Table 7.1: Average properties of longitudinal reinforcing bars

Bar Size	f_y (ksi)	f_u (ksi)	Rupture Strain (%)
6	65	104	21
7	69	110	21

7.2.2 Moment-Curvature Relationship of Beam Sections

Moment-curvature relationships of reinforced concrete beam sections were calculated based on the section dimensions, reinforcement and material properties based on measured stress-strain curves for steel and concrete compressive strength for concrete. A generic moment–curvature relationship of a section corresponding to a potential plastic hinge location is presented in Figure 7.5. In the curve, yield moment and curvature are denoted as M_y and ϕ_y respectively. Ultimate moment is defined as M_u, and ultimate curvature as ϕ_u. The ultimate condition was defined at crushing of the concrete at a strain equal to 0.004. The shape of this generic curve was modified for input into Sap2000 (SAP2000 Version 17.0) by using an elastic-perfectly plastic simplified moment–curvature relationship of a beam section (Figure 7.6). The modification also included a gradual reduction in strength rather than a sudden drop after reaching the ultimate

curvature. This model take account the reduction in the flexural strength and curvature capacity due the concrete shear strength degradation in the critical section discussed in Section 6.4. Also, the modified model accounts for the gradual reduction in strength until reaching the residual flexural capacity beyond reaching ultimate curvature provided. This reduction reflects the ability of the tensile reinforcement to deform until fracture at a section curvature defined as ϕ_f. An estimate of the fracture curvature was taken from the *GSA 2016* Guidelines. In order to estimate hinge rotation using the relationship between curvature and rotation, a plastic hinge length of 10 in. was used. The plastic hinge lengths were measured directly at the Specimen 3.

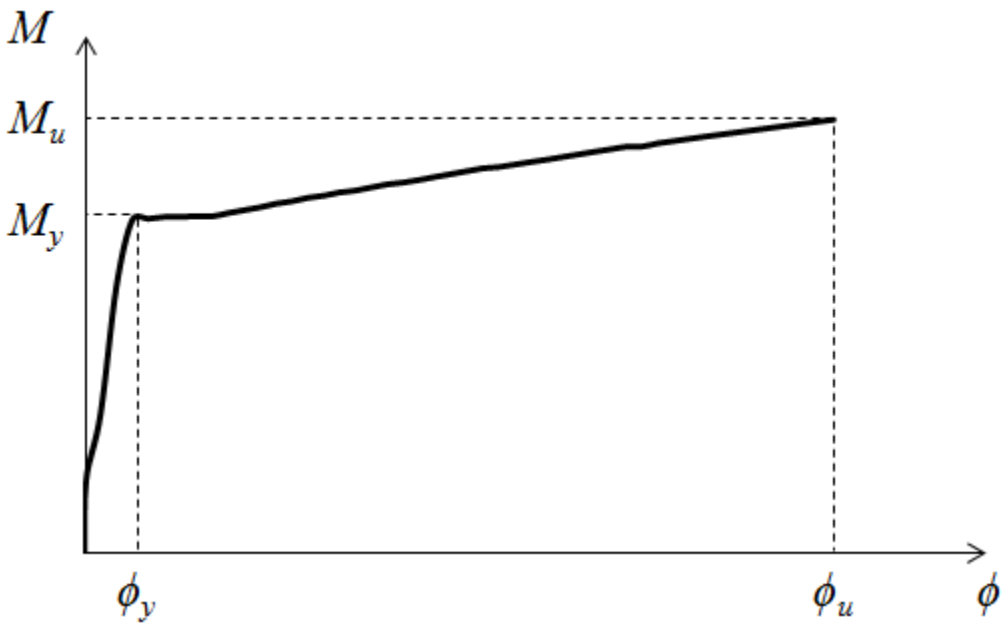

Figure 7.5: Typical shape of the moment–curvature relationship of a beam section

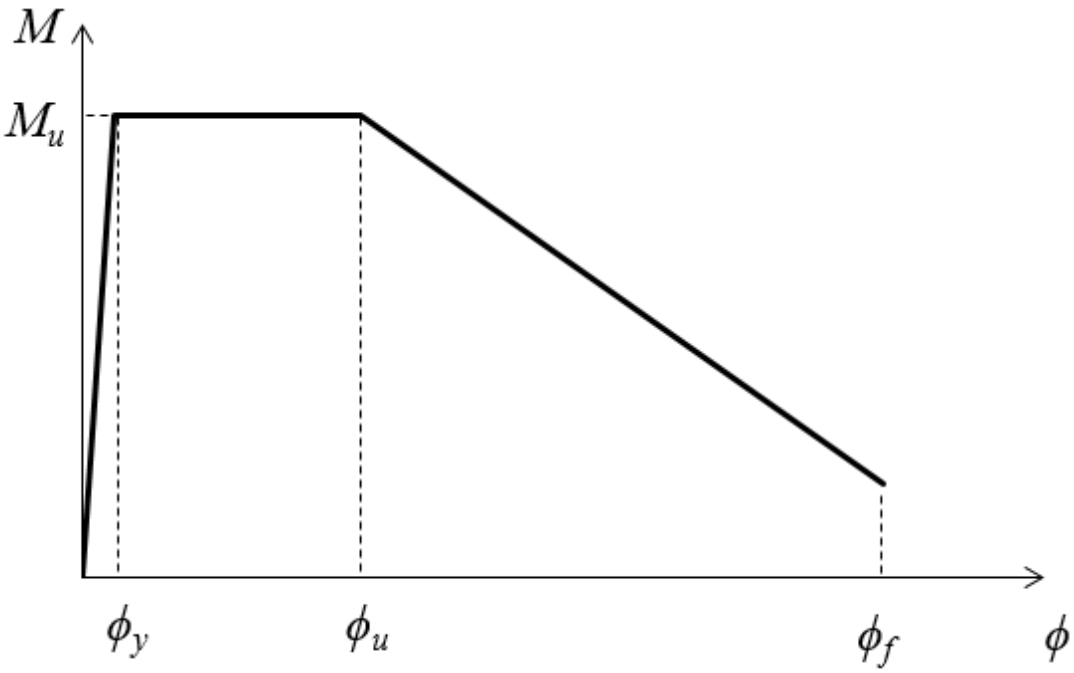

Figure 7.6: Simplified moment–curvature relationship of the plastic hinge

7.3 Verification of Plastic Hinge Behavior

The moment–curvature relationship for a section located at potential plastic hinge regions at the beam ends presented in Section 7.2 was evaluated using the obtained experimental results. Due the Specimen 3 results show the smallest rotation for the beam end near the widened crack, these results presented in Chapter 5 were used to validate the plastic hinges.

A model with the dimensions and reinforcement of Specimen 3 described in Chapter 4 was constructed using SAP2000 (SAP2000 Version 17.0) to execute a push-down nonlinear static analysis. Frame elements were used to model reinforced concrete beams and columns. The longitudinal support system (steel diagonal braces) used for the experiments was also modeled using frame elements. Plastic hinges were modeled at 4 ft. and 6 in. from the face of each column for the exterior and interior column, respectively,

to simulate the concentration of plastic action at the end of beams. The location of the plastic hinges was determined in Specimen 3 from observation of the cracking pattern that formed after the test. To account for concrete cracking along the beam length, a reduced moment of inertia was used by reducing the gross moment of inertia of the elements to 0.20 of the uncracked value. This value was chosen to approximately match the initial two branches in load-displacement response of Specimen 3 that was measured in the laboratory as shown in Figure 7.9. Properties of the plastic hinges placed at ends of beams are presented in Appendix F. The boundary conditions used during the test were included in the SAP 2000 model. The top of the end columns were attached using pins to longitudinal steel braces to restrain the in-plane movement at the top of the column to try to simulate a point of inflection at story midheight. A concentrated force was applied to the middle removed column to simulate the load from upper floors of the prototype structure. Figures 7.7 and 7.8 show the dimensions of Specimen 3 and the two-dimensional (2D) analysis model, respectively.

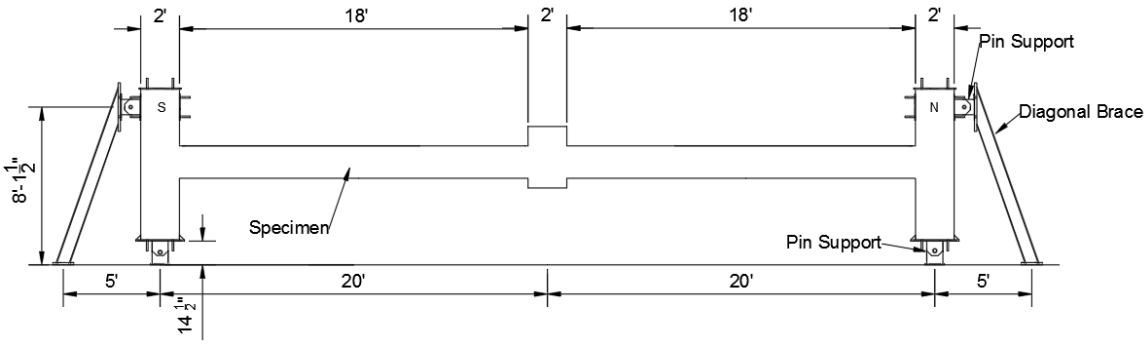

Figure 7.7: Details of the Specimen 3

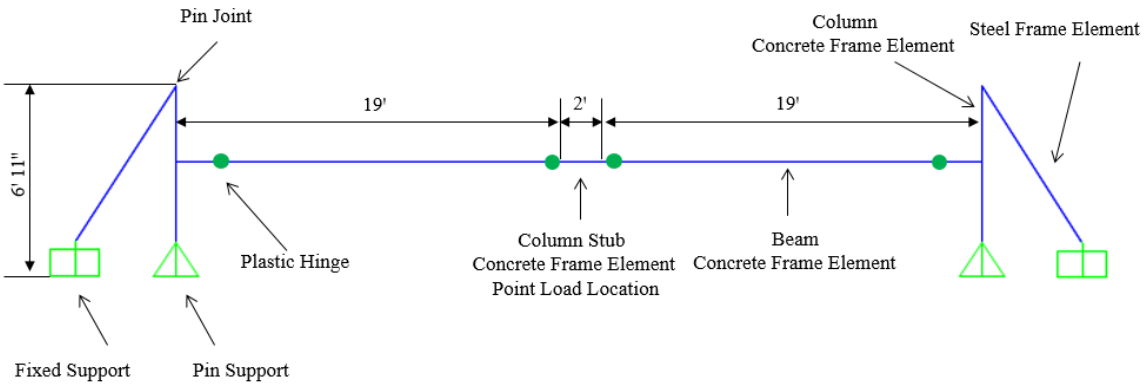

Figure 7.8: Analysis model of Specimen 3

Figure 7.9 shows the applied vertical load versus the vertical displacement measured at the center column of Specimen 3. Push-down nonlinear static analysis from the detailed model of Specimen 3 is also shown in the figure (grey dashed line). The model compared well with the load-displacement response measured in the laboratory as shown in Figure 7.8. Similar to the experimental observations, the maximum applied load was 53 kip at an 8.0 in. center column vertical displacement. The analysis of the model was ended at an applied load of 51 kip with 11.0 in. of center column vertical displacement, after which convergence was not achieved. Approximately at this point, the specimen exhibited a significant drop in resistance caused by opening of the critical diagonal tension crack in the beam near the north column as discussed in Chapter 6. Given the favorable results obtained for Specimen 3, the properties of the sections corresponding to plastic hinge locations used in the analysis were used to analyze the prototype building as discussed in the following section.

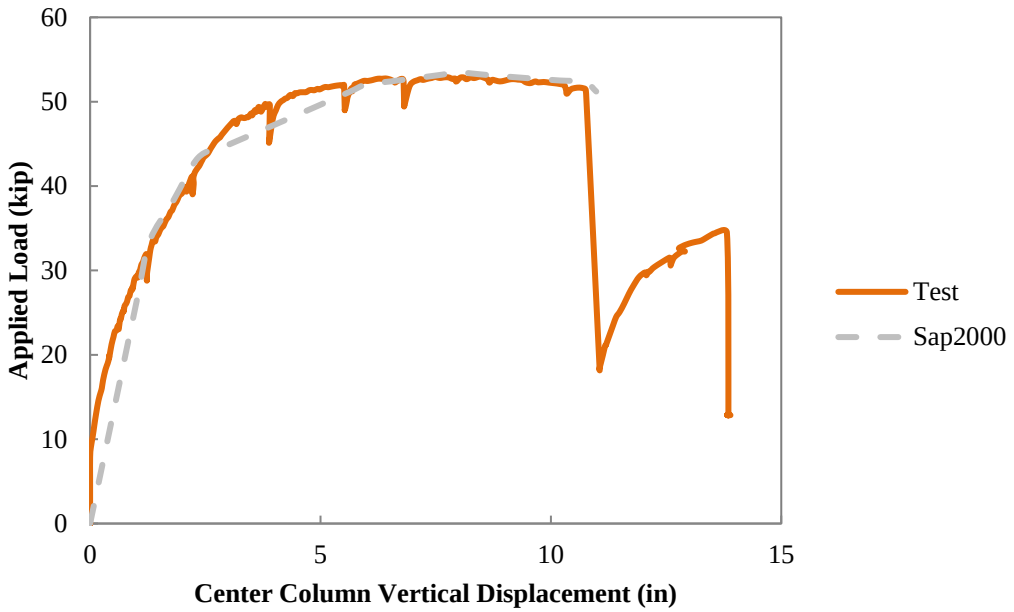

Figure 7.9: Comparison of measured and calculated load-displacement Response of Specimen 3

7.4 Prototype Model

A 3D model using the dimensions and reinforcement of the ten-story prototype reinforced concrete building described in Chapter 3 was constructed using SAP2000 (SAP2000 Version 17.0) to perform the nonlinear static analysis required to capture the response during a first-floor column removal. Two column removal conditions were analyzed, removal of an interior perimeter column and removal of a corner perimeter column. Columns and beams were modeled as frame elements in the model. Six nonlinear hinges were defined along each beam on adjacent spans to the column that was removed throughout the height of the building. Two plastic hinges were inserted at each beam end and four were distributed at equal spaces along the beam span. Two nonlinear hinges were also defined at each end of the columns adjacent and above to the removed column. Plastic hinge properties for the beams and columns are presented in Appendix F.

The moment of inertia of the beams and columns was reduced to 0.20 and 0.70 of the uncracked values, respectively, to simulate cracked section properties as was done in the Specimen 3 calibration model. The self-weight of the slab, the superimposed dead loads and live loads were distributed to the beam elements in each floor in accordance with the tributary areas. Figure 7.10 shows the plan layout of the prototype building model and, Figure 7.11 and 7.12 show the prototype building model with the plastic hinge distribution for the interior and corner perimeter column removal, respectively.

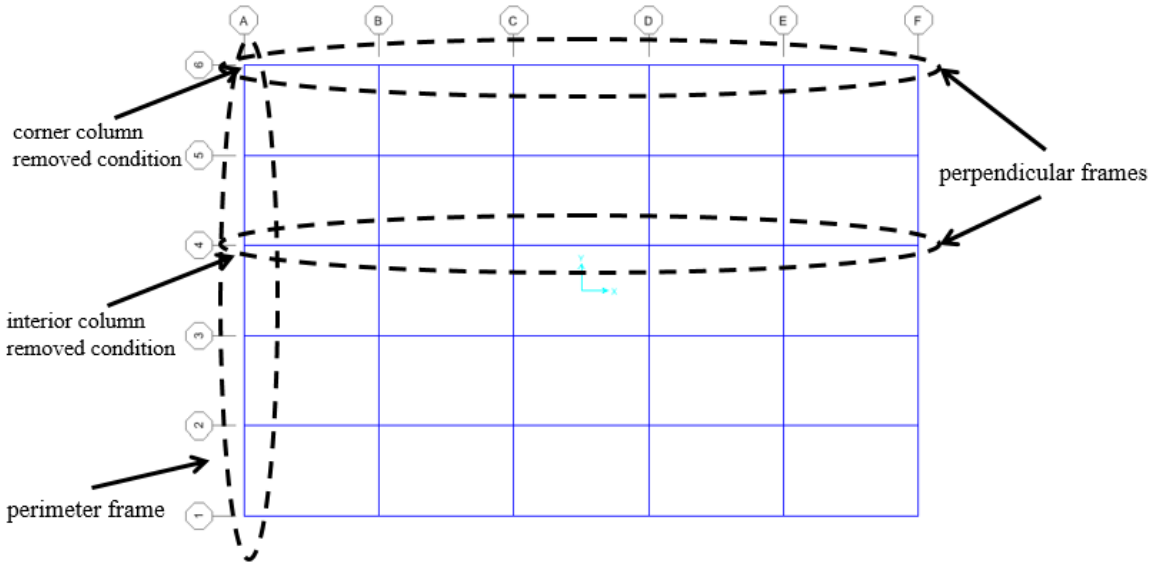

Figure 7.10: Plan layout of the prototype building model

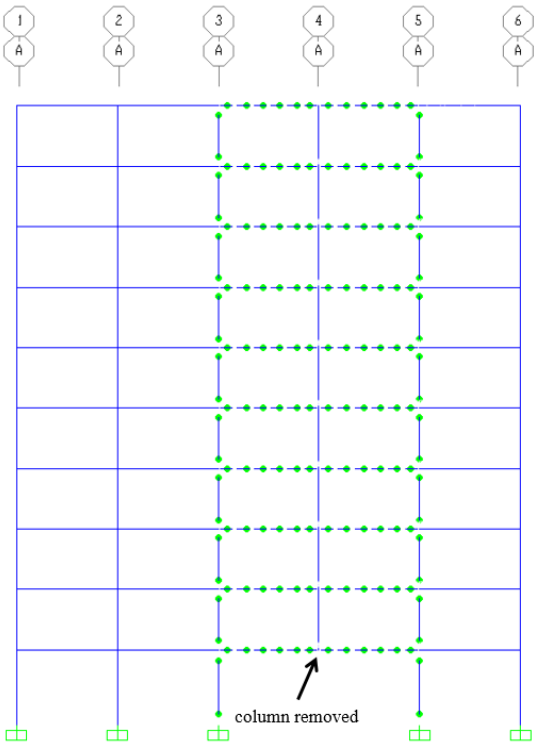

a)

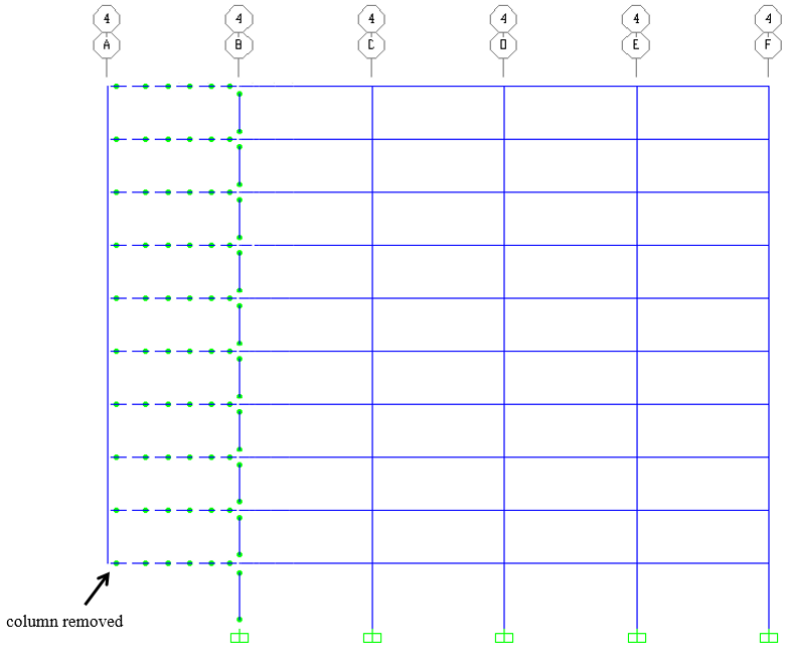

b)

Figure 7.11: Interior perimeter column removal model with plastic hinge distribution in the a) perimeter frame along column line A and b) perpendicular frame along column line 4 (green dots represent plastic hinges)

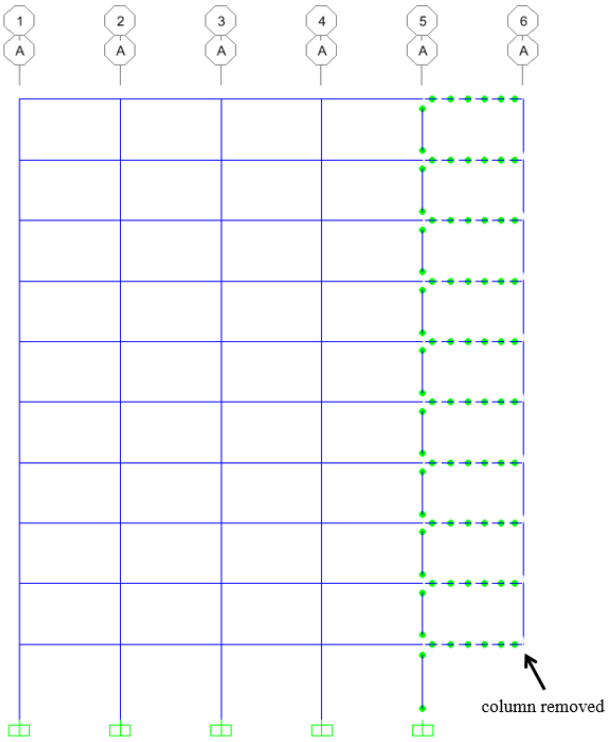

a)

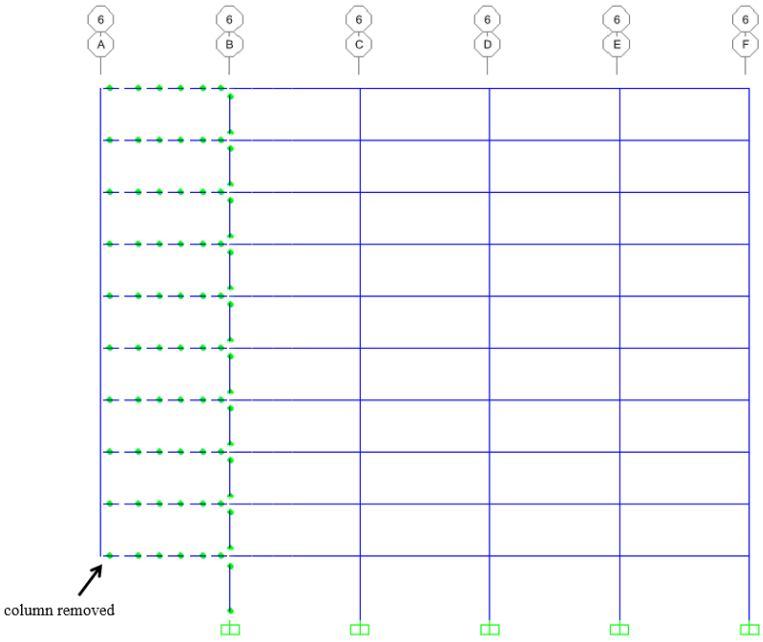

b)

Figure 7.12: Corner perimeter column removal model with plastic hinge distribution in the a) perimeter frame along column line A and b) perpendicular frame along column line 6 (green dots represent plastic hinges)

Following *GSA 2016 Guidelines*, the prototype model was analyzed and evaluated of the potential for progressive collapse after the column was removed using Equations 7.1 and 7.2. The beam spans immediately adjacent to the removed column and on all floors above the removed column were subjected to the gravity load combination given Eq. 7.1, where the factor Ω_N corresponds to a dynamic increase factor specified in the *GSA Guidelines*. The bays located away from the removed column were analyzed using the gravity load combination given in Eq. 7.2 that does not include the amplification factor Ω:

$$G_N = \Omega_N(1.2D + 0.5L) \quad 7.1$$

$$G = 1.2D + 0.5L \quad 7224$$

where, *D* is the dead load effect, and *L* is the live load effect. Following Table 5 in the *GSA 2016 Guidelines*, the dynamic increase factor was equal to 1.13. This value is defined as the smallest ratio of plastic rotation angle and the yield rotation angle for any beam section. Figures 7.13 and 7.14 show the applied gravity load location for the interior and corner perimeter column removal, respectively.

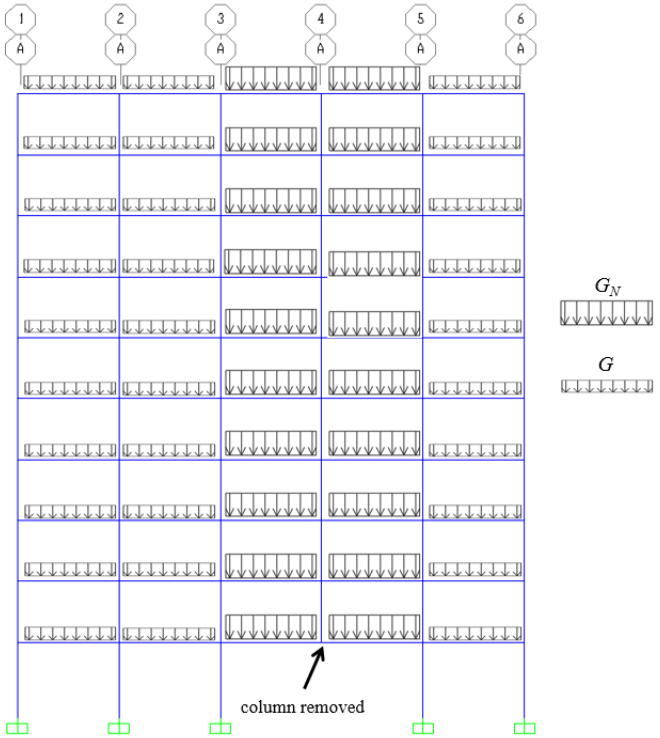

a)

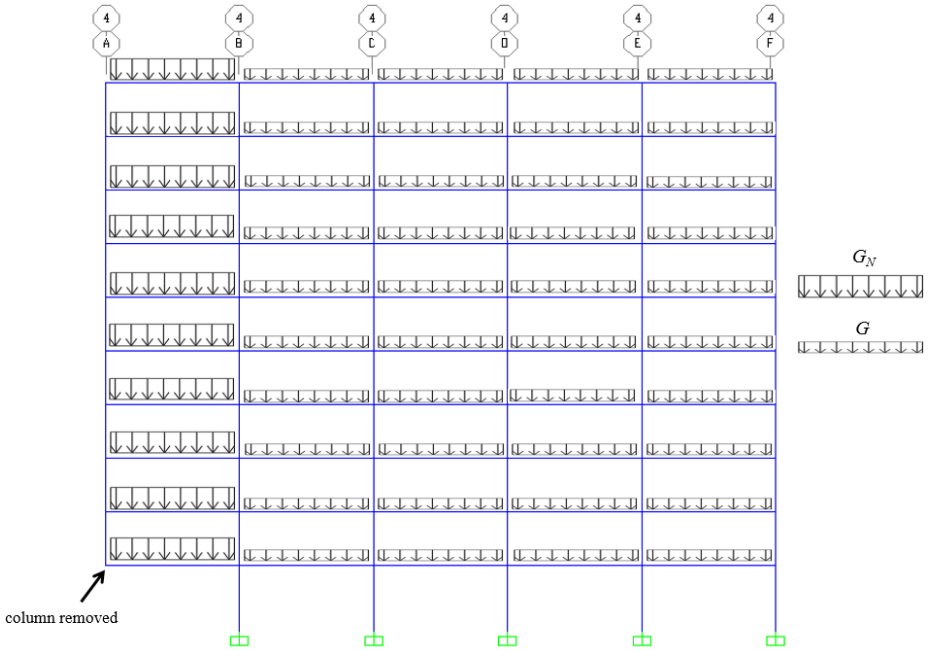

b)

Figure 7.13: Interior perimeter column removal model with the applied gravity load location in the a) perimeter frame along column line A and b) perpendicular frame along column line 4

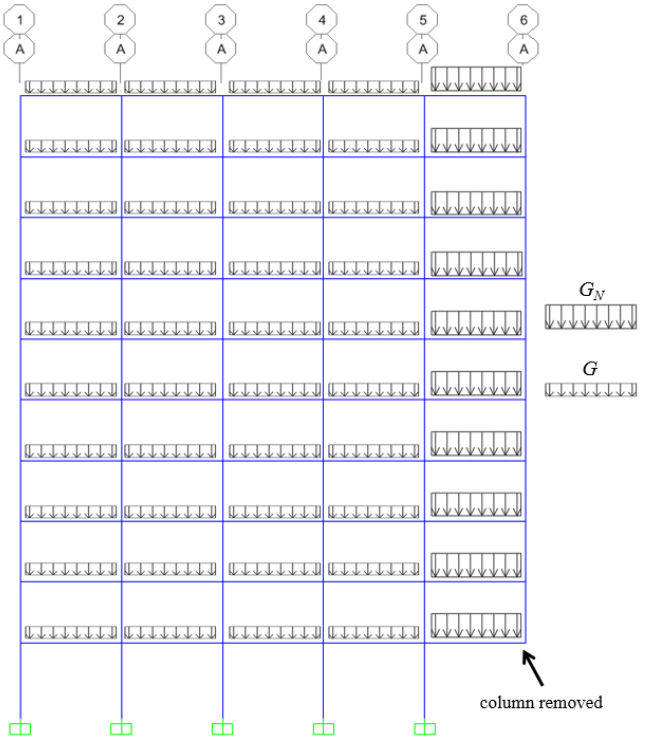

a)

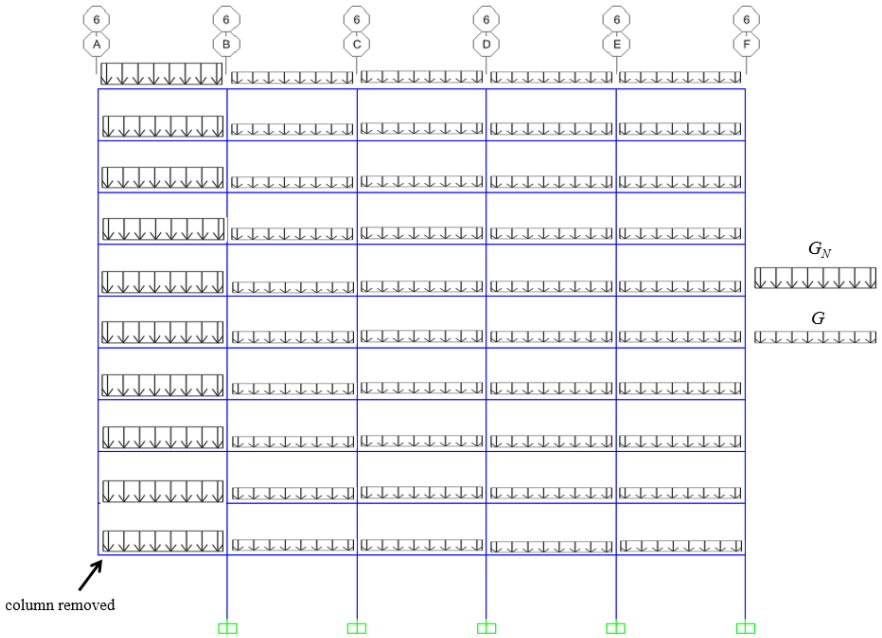

b)

Figure 7.14: Corner perimeter column removal model with the applied gravity load location in the a) perimeter frame along column line A and b) perpendicular frame along column line 6

7.5 Prototype Model Results

A push-down analysis was carried out to investigate the progressive collapse behavior after the two column removal scenarios (interior and corner column removal) of the prototype building. The load application procedure in SAP2000 (SAP2000 Version 17.0) consisted of incremental load application in steps until approximately reaching a target displacement of the node above the removed column.

7.5.1 Interior Perimeter Column Removed Condition

Figure 7.15 shows the load-displacement response for the interior perimeter column removed condition. In this figure, load is plotted as percentage of the load determined from Eq. 7.1 and the displacement represents the vertical deflection at the node above the column removed. A load corresponding to 100% G_N corresponds to the maximum load determined from Eq. 7.1 with an Ω_N factor equal to 1.13, applied in the three beam spans adjacent to the removed column throughout the height of the building (two in the plane of the perimeter frame and one perpendicular to the perimeter frame). The maximum load applied to the model was equal to $1.1G_N$ which meet the criterion stipulated in the *GSA 2016 Guidelines* to assess the likelihood of progressive collapse. If a structure is able to support the loading calculated using Eq. 7.1, then it is deemed that progressive collapse does not occur.

The collapse mechanism developed at a vertical displacement equal to 14.9 in. determined in the node above the interior column that was removed. At this displacement, the curvature in plastic hinges located at the ends of the beams in the perimeter frame reached the fracture curvature. Hinges in the beam framing to the

perimeter frame in the perpendicular direction reached curvature values that were lower to the curvature corresponding to bar fracture. Figure 7.16 shows the formation of plastic hinges during the analysis as a series of dots. In the figure, purple dots represent hinges reached the yielding curvature value and red dots represent hinges reached the fracture curvature value. Formation of a plastic hinge corresponds to the condition where moments exceed the yield moment of the cross section. As illustrated, hinges did not form along the columns, therefore indicating that the yield moment was not exceeded in these elements. After hinges formed in the beams of the perimeter frame, moments were redistributed to beams in the perpendicular direction. Figure 7.17 shows the moment diagrams at the collapse mechanism for the in-plane direction and the perpendicular direction. In the figure point A corresponds to the section at the end of the beams in the perimeter frame adjacent to the removed column, point B represents the moment at the face of the column for the beam adjacent to the removed column in the frame perpendicular to the perimeter frame, and point C represents the section at the bottom end of the second story column directly above the removed column. Table 7.2 summarizes the moment values for sections corresponding to points A, B and C illustrated in the figure throughout the analysis. As the table indicates, moment at point A was redistributed to point B and C after step 16.

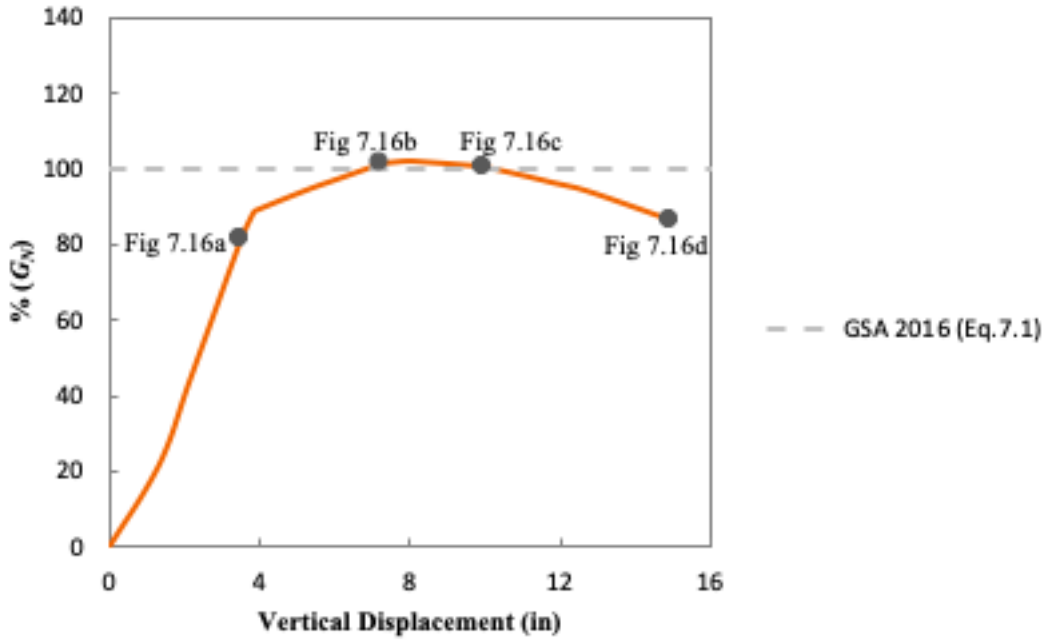

Figure 7.15: Load-displacement response for the interior perimeter column removed condition

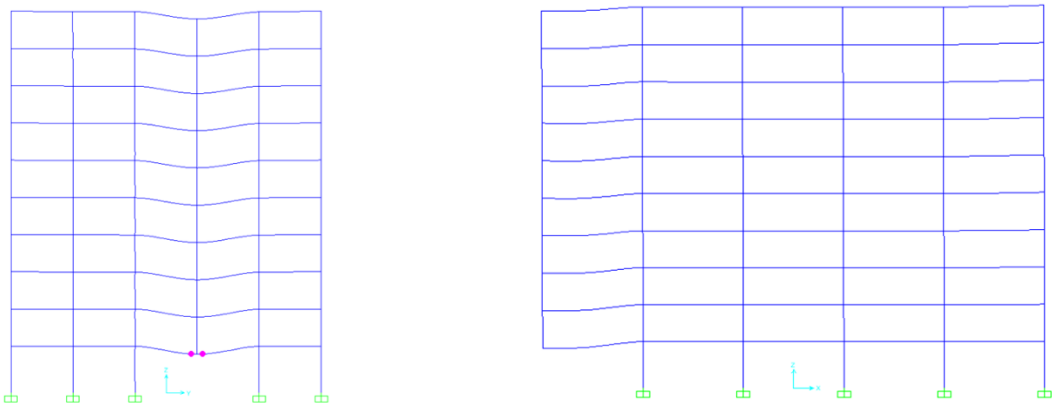

a)

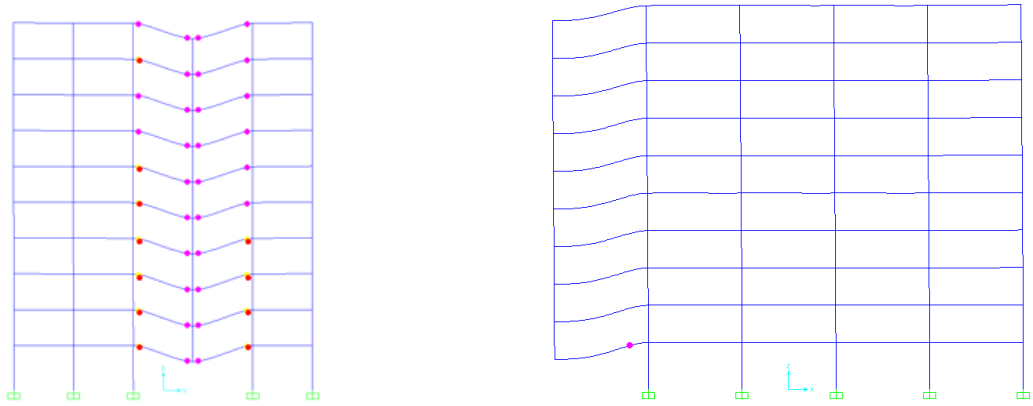

b)

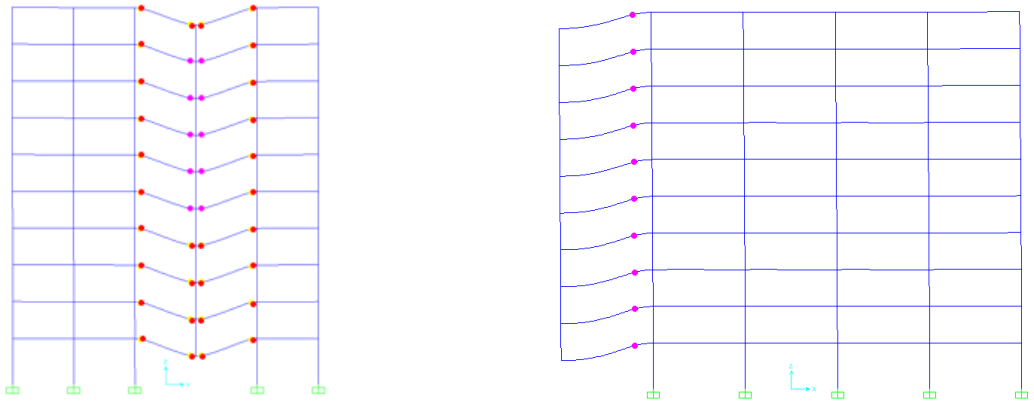

c)

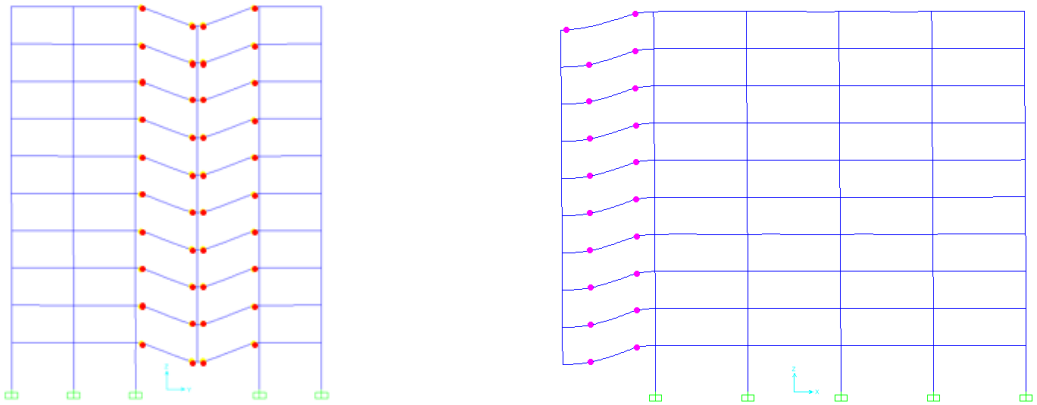

d)

Figure 7.16: Plastic hinge formation at a) vertical displacement = 3.5 in., b) vertical displacement = 7.3 in., c) vertical displacement = 9.9 in., d) vertical displacement = 14.9 in. The left figures represent the in-plane direction and the right figures represent the perpendicular direction.

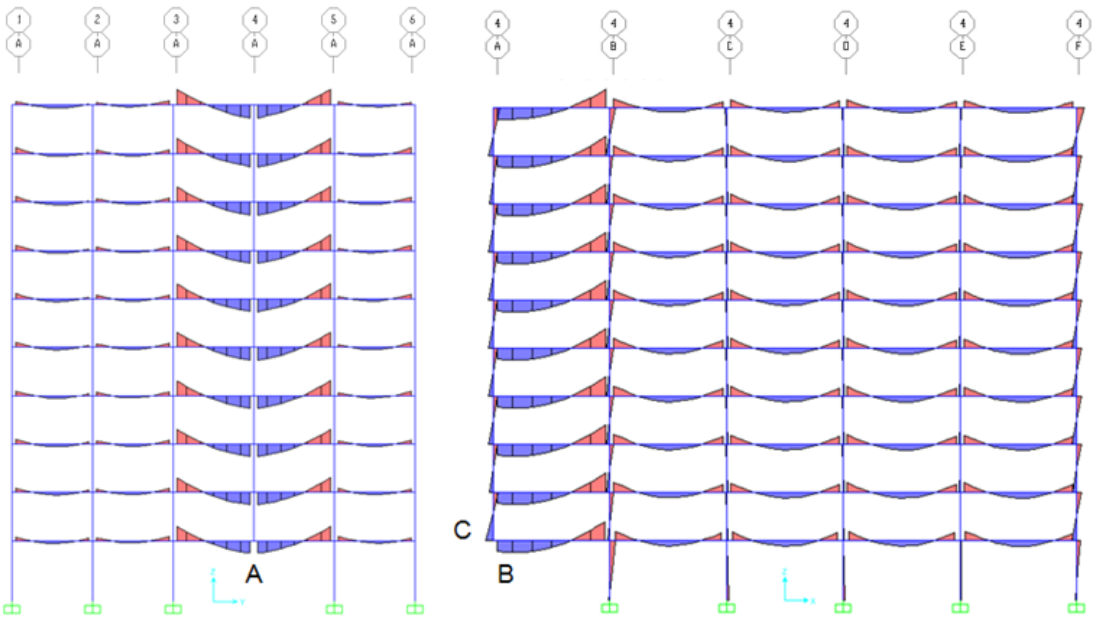

a) b)

Figure 7.17: Moment diagrams at formation of collapse mechanism for the a) in-plane direction and the b) perpendicular direction.

Table 7.2: Moment variation at sections A, B and C

Step	Vertical Displacement (in.)	Moment (k-ft)		
		Point A	Point B	Point C
0	0.0	0	0	0
2	2.1	160.8	-10.9	-58.4
4	3.5	261.1	-39.8	-92.8
6	3.9	260.8	-41.9	-96.7
8	6.1	259.8	22.3	-44.0
10	7.3	259.2	58.3	-14.3
12	7.8	258.7	71.6	-3.4
14	7.9	258.6	76.4	0.7
16	9.5	257.4	125.9	42.2
18	11.0	242.2	178.2	86.8
20	12.6	222.4	234.8	135.3
22	14.9	193.7	264.3	162.3

7.5.2 Corner Perimeter Column Removed Condition

Figure 7.18 shows the load-displacement response for the corner perimeter column removed condition. In the figure, load is plotted as percentage of the load determined from Eq. 7.1 and the displacement represents the vertical deflection at the node above the column-removed. A load corresponding to 100% G_N corresponds to the maximum load determined from Eq. 7.1 with an Ω_N factor equal to 1.13, applied in the two beam spans adjacent to the removed column throughout the height of the building (one in the plane of the perimeter frame and one perpendicular to the perimeter frame). The maximum load applied to the model was equal to $0.95G_N$ which does not meet the criterion stipulated in the *GSA 2016 Guidelines* to assess the likelihood of progressive collapse.

The collapse mechanism developed at a vertical displacement equal to 15.9 in. determined in the node above the corner column that was removed. At this displacement, the curvature in plastic hinges located at the ends of the beams in the perimeter frame reached the fracture curvature. Also, some plastic hinges in the beam framing into the perimeter frame in the perpendicular direction reached the fracture curvature. Figure 7.19 shows the formation of plastic hinges during the analysis as a series of dots. Columns were remained elastic during the push-down analysis. Similar to the interior column removal condition, hinges did not form along the columns and moment redistribution occurred from the beams in the in-plane direction to beams in the perpendicular direction. Figure 7.20 shows the moment diagrams at the collapse mechanism for the in-plane direction and the perpendicular direction. In the figure, point A corresponds to the section at the end of the beam in the perimeter frame adjacent to the removed column, point B

represents the moment at the end of the beam adjacent to the removed column in the frame perpendicular to the perimeter frame, and point C represents the section at the bottom end of the second story column directly above the removed column. Table 7.3 summarizes the moment values for at sections corresponding to points A, B and C illustrated in the figure throughout the analysis.

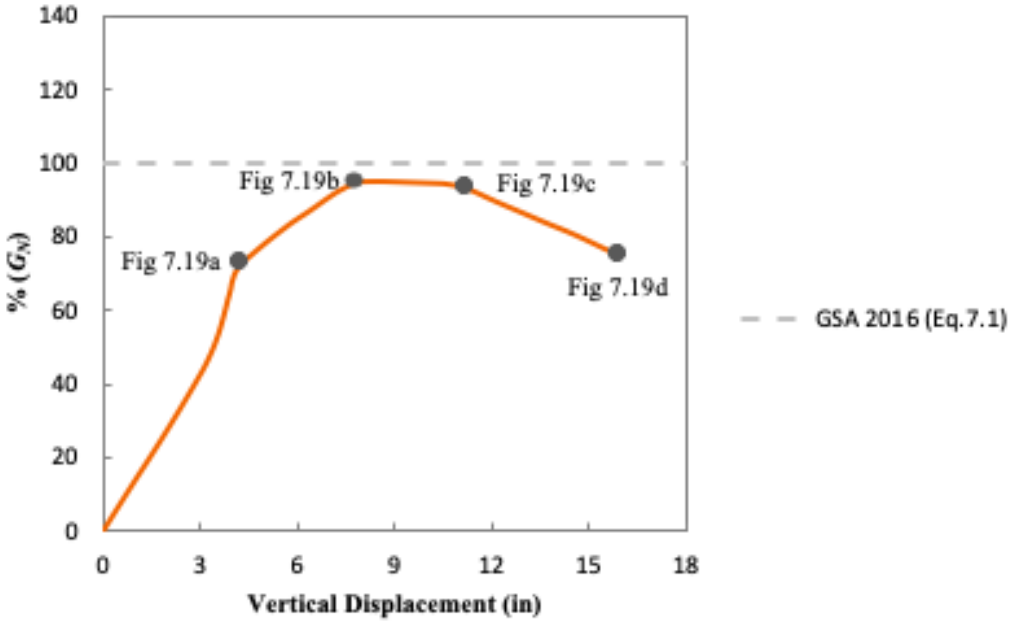

Figure 7.18: Load-displacement response for the corner perimeter column removed condition

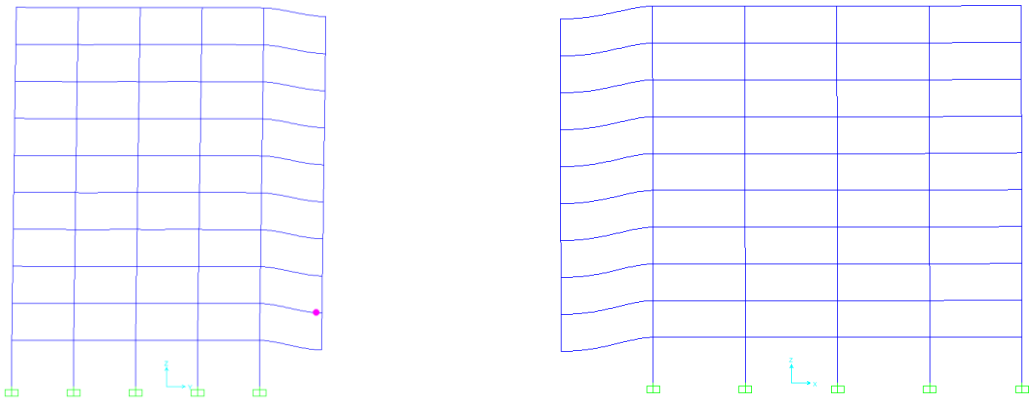

a)

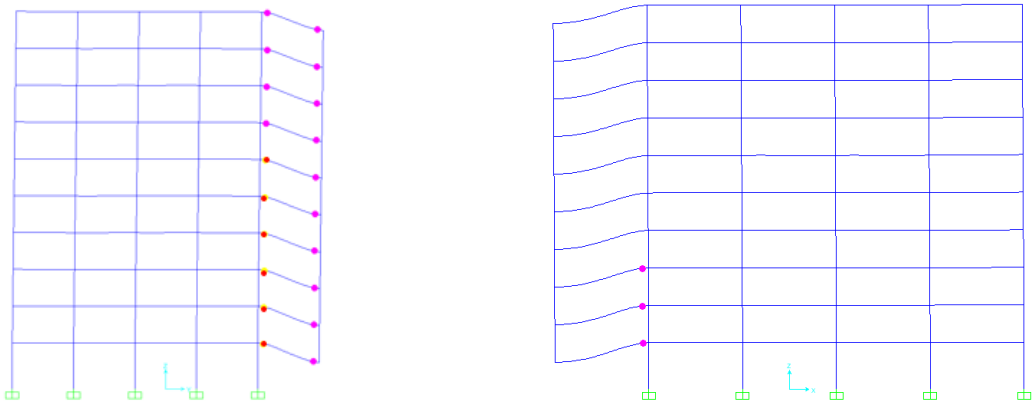

b)

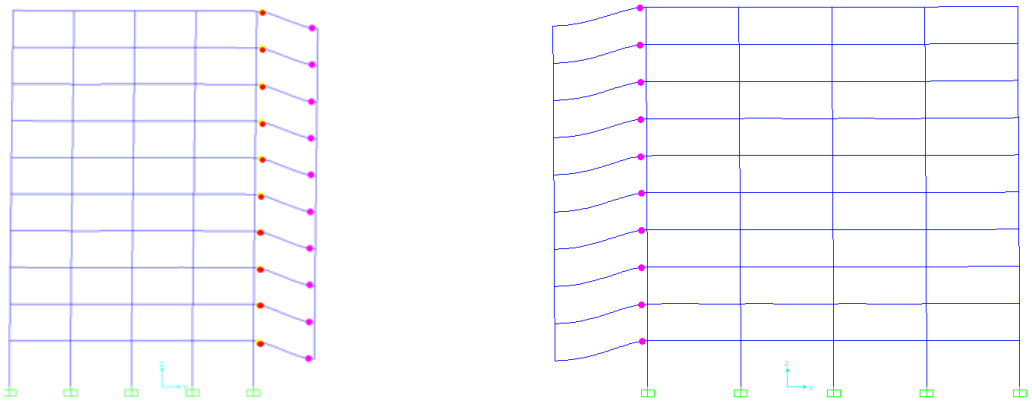

c)

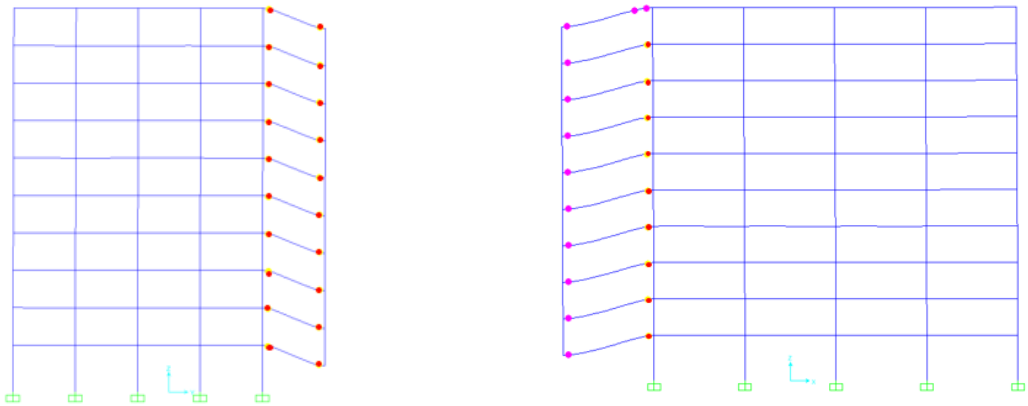

d)

Figure 7.19: Plastic hinges formation at a) center displacement = 3.9 in., b) center displacement = 7.7 in., c) center displacement = 8.7 in., d) center displacement = 15.9 in. The left figures represent the in-plane direction and the right figures represent the perpendicular direction.

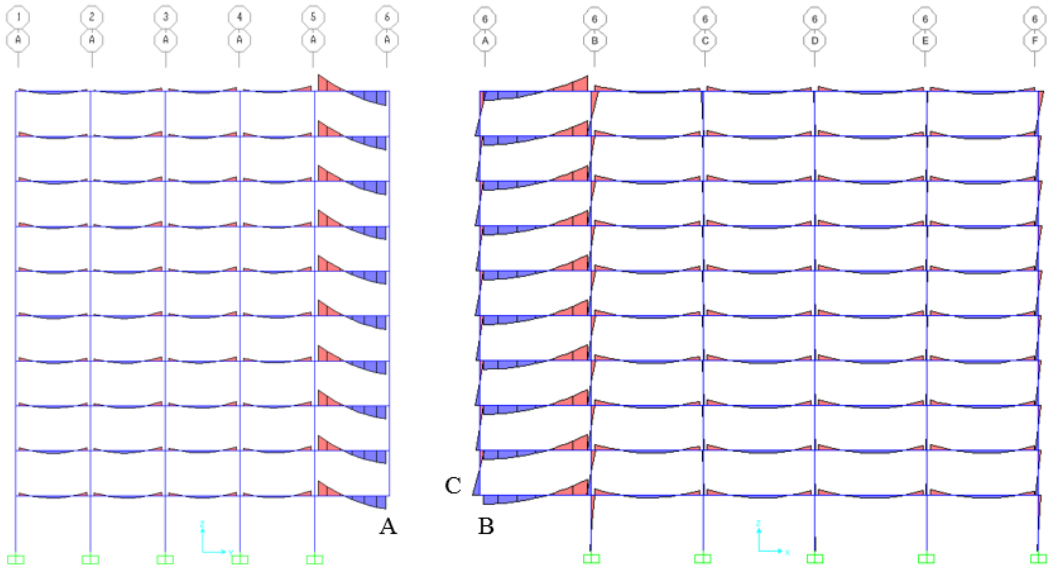

a) b)

Figure 7.20: Moment diagrams at formation of collapse mechanism for the a) in-plane direction and the b) perpendicular direction.

Table 7.3: Moment variation for point A, B and C

Step	Vertical Displacement (in.)	Moment (k-ft)		
		Point A	Point B	Point C
0	0	0	0	0
2	3.9	251.7	63.3	23.2
4	4.3	261.3	67.4	25.6
6	6.4	259.6	127.1	79.1
8	7.7	258.4	160.6	109.2
10	7.9	258.2	164.5	112.6
12	8.2	257.9	171.1	118.6
14	9.5	256.8	202.3	147.1
16	10.6	253.8	226.8	169.4
18	12.1	233.9	237.5	179.9
20	13.7	213.4	238.9	182.3
22	15.9	185.6	240.6	185.4

7.6 Design Modifications to Improve Progressive Collapse Resistance

In order to satisfy requirements of the *GSA 2016 Guidelines* of prevention for progressive collapse for the corner perimeter column removed condition, moment-curvature response curves for beam hinges were constructed using confined concrete stress-strain curve for concrete. For this curve, the stirrups spacing was d/4 instead of d/2 used in the prototype design where d is the effective depth of the section, and the maximum compressive strain ε_{cu} was assumed to be equal to 0.009 (Mander et al. 1984) instead of 0.004 used in the unconfined model. In this model, the confinement steel provides additional capacity of moment and curvature in the beam. Details of the confined concrete model and properties of the plastic hinges placed at ends of beams are presented in Appendix G.

Figure 7.21 shows the load-displacement response for the corner perimeter column removed condition. Load is represented in terms of the percentage of the Eq. 7.1 and the displacement represents the deflection at the column-removed point. The maximum load applied to the model was equal to $1.3G_N$, which satisfies the criterion stipulated in the *GSA 2016 Guidelines* to assess the likelihood of progressive collapse. The collapse mechanism developed at 25.7 in. of column-removed point displacement. The results show an increment in the load-carrying capacity and the displacement response of prototype in resisting progressive collapse.

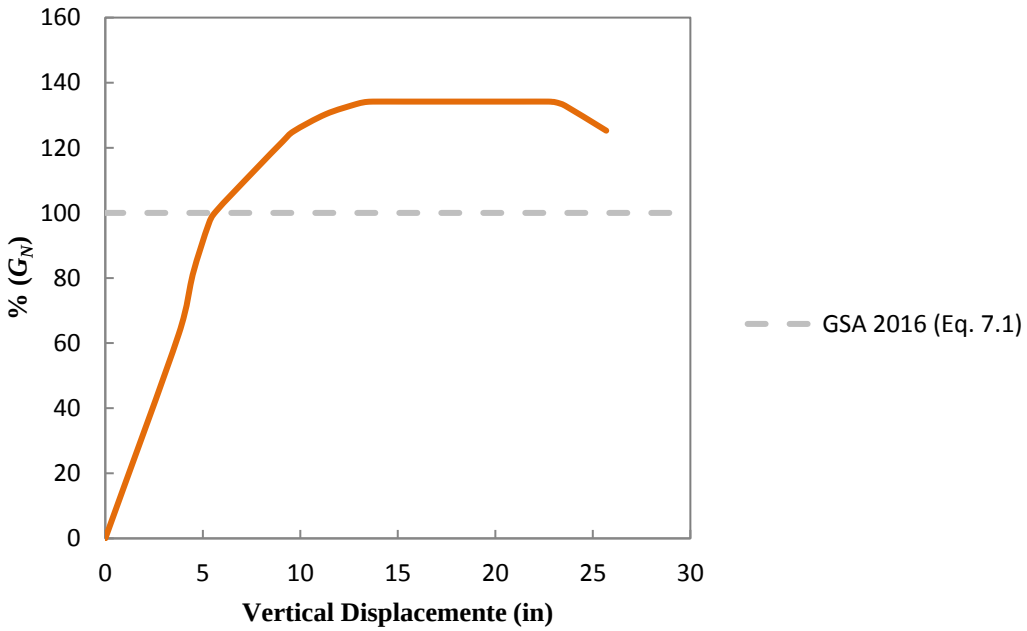

Figure 7.21: Load-displacement response for the corner perimeter column removed condition

7.7 Summary

Analytical models to investigate the progressive collapse behavior after removal of an interior and a corner column of the ten-story prototype reinforced concrete frame building described in Chapter 3 was presented in this chapter. To account for the nonlinear behavior after yielding of beams, plastic hinges were defined at sections along the beams and at the ends of columns using a lumped plasticity approach. The moment–curvature relationship of the beam plastic hinges used were calibrated using the experimental results of Specimen 3 presented in Chapter 5. Based on the *GSA 2016 Guidelines* and the performance on the plastic hinges, the interior perimeter column removed condition met the requirements of prevention for progressive collapse. In contrast, the corner perimeter column removal scenario did not meet the criterion that is defined for prevention for progressive collapse in the guidelines. In order to satisfy

requirements of the *GSA 2016 Guidelines* for this condition, moment-curvature response curves for beam hinges were constructed decreasing the stirrup spacing of beams in the prototype design. This approach was followed to provide a way that the original design could be modified that would then result in a structure where progressive collapse is avoided. The results showed that the structure with the modified design met the requirements of the *GSA 2016 Guidelines* of prevention for progressive collapse. The improved performance of the modified design highlights the importance of providing a closer stirrup spacing than required by the *ACI 318-14* Code for perimeter frames in non-seismic regions.

CHAPTER 8

SUMMARY AND CONCLUSIONS

8.1 Summary

The objective of this study was to evaluate the effect of splice location of structural integrity reinforcement on the performance of beams in perimeter frames after loss of an interior support. Analytical and experimental phases were carried out to provide information on splice location and detailing practices necessary that promote adequate structural integrity performance.

Analysis and design of a ten-story prototype reinforced concrete frame building located in a non-seismic zone was conducted following current design standards. The laboratory specimens were modeled based on this prototype structure. The structural analysis of the prototype building was based on the *IBC 2015* which refers to *ASCE 7-10* to define loading in the prototype building. Design of the structure followed the non-seismic provisions in *ACI 318-14*.

The specimens tested in the experimental phase of the research project represent full-scale beam-column sub-assemblages of a first story frame in the perimeter of the prototype. These laboratory specimens represent two interior spans of a beam in the perimeter of the first story where an intermediate column has been lost. Three specimens were designed and tested by simply varying the splice location of bottom longitudinal reinforcing bars.

A model with the dimensions and reinforcement of the ten-story prototype reinforced concrete building described in Chapter 3 was constructed using SAP2000

(SAP2000 Version 17.0) to perform the nonlinear static analysis required to capture the response during a first-floor column removal. Two column removal conditions, interior perimeter column and corner perimeter column, are considered in the analysis. To account for nonlinear material effects, plastic hinges were assigned at sections along beams and columns adjacent to the removed element.

8.2 Laboratory Test Results

For the three specimens, the crack patterns started with flexural cracks in the bottom of the beam near the center column followed by flexural cracks in the top of the beam near the exterior columns. Finally, diagonal tension cracks appeared at the beam ends at near the exterior columns. Plastic hinges formed in the beam near the exterior columns and center column. The applied force reached similar maximum value for all the specimens. After this point, loading proceeded without an increase in the applied force and widening of the critical diagonal tension crack in the beam near the exterior column occurred causing the applied force to decrease suddenly. Rotations just prior to the widening of the crack were similar for the north and south plastic hinges for all specimens. From these results the following conclusions and recommendations were made:

1. The critical shear crack that formed during the tests was steeper than the truss model angle (45 degrees) assumed in design based on *ACI 318-14*, only one stirrup crossed the crack on the compression side of the beam and a significant portion of the shear was carried by the concrete before the loss of aggregate interlock.

2. Loss of aggregate interlock occurred after the diagonal tension crack widened and the concrete contribution to shear strength decreased significantly.
3. The observed shear crack angle in all specimens were approximately 60 degrees, so the spacing of transverse reinforcement at that section prevented more than one stirrup from crossing the diagonal crack on the compression side of the beam and to contribute to the shear strength after the loss of aggregate interlock.
4. The diagonal tension crack widened significantly preventing the beam from developing an alternate load path that would presumably allow an increase in the applied load through catenary action as has been reported by past researchers.
5. The formation of plastic hinges away from the face of the beam-column connection was the result of a reduction in negative flexural strength where bars were cut following design of the prototype. Perhaps more importantly, the change in location of the point of inflection resulting from elimination of the center column created higher moments at the section where top bars were cut, compared with the location of the point of inflection used in design.
6. A closer stirrup spacing than required for non-seismic zones may prevent widening of the diagonal tension cracks in the beams and would promote development of catenary action as an alternate load path after diagonal cracking. These detailing requirements are not currently required by the ACI Code for frames in low seismic regions, and could provide an effective and simple approach to mitigate progressive collapse.

7. The load carrying capacity and rotation demand in the beams were not affected by the bottom bar splice location, so relocating the splice location outside of the joint may be a good practice to improve constructability.

8.3 Collapse Analysis of Prototype Building

Chapter 7 described the analytical procedure to investigate the progressive collapse behavior after an interior and corner column removal of the ten-story prototype reinforced concrete frame building. Based on the *GSA 2016 Guidelines* and the performance on the plastic hinges determined experimentally, the interior perimeter column removed condition met the requirements of prevention for progressive collapse. Moreover, the corner perimeter column removed condition did not meet the requirements of prevention for progressive collapse.

In order to satisfy requirements of the *GSA 2016 Guidelines* for this condition, moment-curvature response curves for beam hinges were constructed reducing the stirrups spacing in the prototype design to a spacing consistent with seismic detailing of the prototype structure. The results showed that the modified design resulted in a response that satisfied the requirements of the *GSA 2016 Guidelines* for prevention of progressive collapse. The reduction of stirrup spacing increased the load-carrying capacity and the displacement of the prototype in resisting progressive collapse.

APPENDIX A

WIND AND EARTHQUAKE LOADS ANALYSIS

This appendix describes the details of the wind and earthquake analysis procedure used in the ten-story prototype reinforced concrete frame building from which the laboratory specimens were modeled. The structural analysis of the prototype building was based on the *IBC 2015* which refers to *ASCE 7-10* to define loading in the prototype building.

A.1 Wind Loads

Wind load analysis was based on specifications found in the *ASCE 7-10*. The building met all requirements for use the Directional Procedure described in Chapter 27 of the *ASCE 7-10*. The procedure is listed below.

- **Occupancy Category for Building Loads**

The structure met requirements for Occupancy Category II (All buildings and other structures except those listed in Occupancy Categories I, III, and IV) (*ASCE 7-10* Table 1.5-1).

- **Basic Wind Speed (*V*)**

For Houston area (*ASCE 7-10* Figure 26.5-1A),

$$V = 136\ mph$$

- **Wind Directionality Factor (K_d)**

For a main wind force resisting structure (*ASCE 7-10* Table 26.6-1),

$$K_d = 0.85$$

- **Exposure Category**

Exposure B means that the structure is located at an urban and suburban area and terrain with numerous closely spaced obstructions having the size of single-family dwellings or larger. This structure can be considered exposure B (*ASCE 7-10* Section 26.7.3).

- **Topographic Factor (K_{zt})**

For homogenous topography (*ASCE 7-10* Section 26.8.2),

$$K_{zt} = 1.0$$

- **Gust Effect Factor (G)**

Since the building is considered as a rigid structure (*ASCE 7-10* Section 26.9.1),

$$G = 0.85$$

- **Internal Pressure Coefficient (GC_{pi})**

Internal pressures will not be considered it will not make any effect on the net lateral force.

- **Velocity Pressure Exposure Coefficient (K_z)**

Using *ASCE 7-10* Table 27.3-1,

Table A.1: Velocity pressure exposure coefficient

Height (ft)	K_z
123	1.05
111	1.02
99	0.99
87	0.95
75	0.91
63	0.86
51	0.81
39	0.75
27	0.68
15	0.57

- **Velocity Pressure (q_z)**

$$q_z = 0.00256 \times K_z \times K_{zt} \times K_d \times V^2 \ (psf) \ (ASCE\ 7-10\ Equation\ 27.3-1)$$

Table A.2: Velocity pressure

Floor	q_z (psf)
Roof	42.26
9	40.95
8	39.72
7	38.28
6	36.63
5	34.69
4	32.76
3	30.35
2	27.21
1	22.94

- **Wind Direction**

Table A.3: Dimensions of the structure

Direction	E-W	N-S
*B (*ft*)*	100	150
*L (*ft*)*	150	100
*h (*ft*)*	123	123
h/L	0.82	1.23
L/B	1.5	0.67

- **External Pressure Coefficient (C_p)**

Using *ASCE 7-10* Figure 27.4.1,

Table A.4: External pressure coefficient

Wind Direction	E-W	N-S
windward	0.8	0.8
leeward	-0.4	-0.5
sideward	-0.7	-0.7
roof (0 to *h*/2)	-0.99	-1.04
	-0.18	-0.18
roof (*h*/2 to *h*)	-0.77	-0.70
	-0.18	-0.18
roof (*h* to 2*h*)	-0.63	N/A
	-0.18	N/A

- **Wind Force**

Table A.5: Wind loads values

Floor	Concentrated Force	
	E-W	N-S
	(kip)	(kip)
roof	26	42
9	51	83
8	50	82
7	49	80
6	48	78
5	46	76
4	45	74
3	43	71
2	41	68
1	42	71
∑	441	725

A.2 Seismic Loads

Seismic load analysis was also based on specifications found in the *ASCE 7-10*. The analysis was done using the Equivalent Lateral Force Procedure described in Chapter 12 of the *ASCE 7-10*. The procedure is listed below.

- **Occupancy Category for Building Loads**

The structure met requirements for Occupancy Category II (All buildings and other structures except those listed in Occupancy Categories I, III, and IV) (*ASCE 7-10* Table 1.5-1).

- **Importance Factor (*I*)**

Because the structure Occupancy Category is II (*ASCE 7-10* Table 1.5-2),

$$I = 1.00$$

- **Mapped Acceleration Parameters (S_S, S_1)**

For Houston Area,

$$S_S = 0.072\ (ASCE\ 7-10\ Figure\ 22-1)$$

$$S_1 = 0.039\ (ASCE\ 7-10\ Figure\ 22-2)$$

- **Site Class**

The type of soil properties are unknown on site, the classification recommended by the ASCE is D unless the soil properties are found (*ASCE 7-10* Section 11.4.2).

- **Site Coefficient (S_{MS}, S_{M1})**

$$F_a = 1.6\ (ASCE\ 7-10\ Table\ 11.4-1)$$

$$F_v = 2.4\ (ASCE\ 7-10\ Table\ 11.4-2)$$

$$S_{MS} = F_a\ S_S (ASCE\ 7-10\ Equation\ 11.4-1)$$

$$S_{MS} = 1.6 \times 0.072 = 0.115$$

$$S_{M1} = F_v\ S_1\ (ASCE\ 7-10\ Equation\ 11.4-2)$$

$$S_{M1} = 2.4 \times 0.039 = 0.094$$

- **Design Spectral Acceleration Parameter (S_{DS}, S_{D1})**

$$S_{DS} = \frac{2}{3} \times S_{MS}\ (ASCE\ 7-10\ Equation\ 11.4-3)$$

$$S_{DS} = \frac{2}{3} \times 0.115 = 0.077$$

$$S_{D1} = \frac{2}{3} \times S_{M1}\ (ASCE\ 7-10\ Equation\ 11.4-4)$$

$$S_{D1} = \frac{2}{3} \times 0.094 = 0.063$$

- **Seismic Design Category**

Using Category II, S_{DS} = 0.077 and S_{D1} = 0.063; the structure met requirements for Category A (*ASCE 7-10* Table 11.6-1).

- **Seismic Design Requirement for Building Structure (*R*)**

For ordinary reinforced concrete moment frames (*ASCE 7-10* Table 12.2-1),

$$R = 3$$

- **Approximate Fundamental Period (T_A)**

$$T_A = C_t \times h_n^x\ (s)\ (ASCE\ 7-10\ Equation\ 12.8-7)$$

where:

C_t = 0.016 (*ASCE 7-10* Table 12.8-2),

x = 0.9 (*ASCE 7-10* Table 12.8-2), and

h_n = the height of the building (ft).

$$T_A = 0.016 \times 123^{0.9} = 1.22\ s$$

- **Long Period Transition Period (T_L)**

For Houston area (*ASCE 7-10* Figure 22-12),

$$T_L = 12\ s$$

- **Seismic Response Coefficient (C_S)**

$$C_S = \frac{S_{DS}}{(\frac{R}{I})} (ASCE\ 7-10\ Equation\ 12.8-2)$$

$$C_S = \frac{0.077}{(\frac{3}{1})} = 0.026$$

$$C_{Smax} = \frac{S_{D1}}{T \times (\frac{R}{I})}\ (ASCE\ 7-10\ Equation\ 12.8-3)$$

$$C_{Smax} = \frac{0.063}{1.22 \times (\frac{3}{1})} = 0.017$$

$$C_{Smin} = 0.044 \times S_{DS} \times I_e \geq 0.01 (ASCE\ 7-10\ Equation\ 12.8-5)$$

$$C_{Smin} = 0.044 \times 0.077 \times 1 = 0.003 (ASCE\ 7-10\ Equation\ 12.8-5)$$

$$Use\ C_{Smax}\ =\ 0.017$$

- **Seismic Base Shear (*V*)**

$$V = C_S \; W \; (ASCE\ 7-10\ Equation\ 12.8-1)$$

where:

W = weight of the structure (kip).

$$V = 0.017 \times 25540 = 434\ kip$$

- **Seismic Base Shear (*V*) for Seismic Design Category A (Section 11.7)**

$$V = F = 0.01 \times W \; (ASCE\ 7-10\ Equation\ 1.4-1)$$

where:

W = weight of the structure (kip).

$$V = 0.01 \times 25540 = 255\ kip$$

Table A.6: Seismic loads values

Floor	Concentrated Seismic Force (kip)
10	48
9	47
8	40
7	34
6	28
5	22
4	16
3	11
2	7
1	3
∑ (Seismic Base Shear)	255

APPENDIX B

DESIGN CALCULATIONS

This appendix describes details of the design calculation used in the ten-story prototype reinforced concrete frame building from which the laboratory specimens were modeled. The first story of the exterior frame labeled as 1 in Figure 3.1 was designed for a low seismic design category so that the non-seismic provisions of *ACI 318-14* would apply (*ACI 318-14*, Chapter 18 was not followed for design of the prototype).

B.1 Flexure Design for Beams

This section describes the flexural design for the maximum positive moment in a typical exterior beam of exterior frame 1 on the first story. From predesign the beam size is 24"x20"

- **Steel Reinforcement Required**

$$M_u = 88.6\ k-ft$$

$$R_n = \frac{M_u}{\phi b d^2}$$

$$Assuming\ d = h - 2.5$$

$$d = 20 - 2.5 = 17.5\ in$$

$$R_n = \frac{88.6 \times 12 \times 1000}{0.9 \times 24 \times 17.5^2} = 160.73\ psi$$

$$\rho = \frac{0.85 f_c'}{f_y}\left(1 - \sqrt{1 - \frac{2R_n}{0.85 f_c'}}\right)$$

$$\rho = \frac{0.85 \times 4}{60}\left(1 - \sqrt{1 - \frac{2 \times 160.73}{0.85 \times 4000}}\right) = 0.0027$$

$$A_s = \rho b d$$

$$A_s = 0.0027 \times 24 \times 17.5 = 1.13\ in^2$$

$$A_{s,min} = \frac{3\sqrt{f_c'}}{f_y} bd \geq \frac{200bd}{f_y}$$

$$A_{s,min} = \frac{3\sqrt{4000}}{60000} \times 24 \times 17.5 = 1.33\ in^2$$

$$A_{s,min} = \frac{200 \times 24 \times 17.5}{60000} = 1.40\ in^2$$

$$A_s\ required = 1.40\ in^2$$

$$Use\ 4\#6\ (A_s = 1.76\ in^2)$$

- **Maximum Spacing Allowed**

$$s_{max} = 15\left(\frac{40000}{f_s}\right) - 2.5c_c \leq 12\left(\frac{40000}{f_s}\right)$$

$$Assuming\ c_c = 1.5 + 0.5 = 2\ in$$

$$f_s = \frac{2}{3} f_y$$

$$f_s = \frac{2}{3} \times 60000 = 40000\ ksi$$

$$s_{max} = 15\left(\frac{40000}{40000}\right) - 2.5 \times 2 = 10\ in$$

$$s_{max} = 12\left(\frac{40000}{40000}\right) = 12\ in$$

$$Use\ s_{max} = 10\ in$$

$$s_{provided} = \frac{1}{3}\left[24 - 2 \times \left(1.5 + 0.5 + {}^{6}\!/_{8}\!/_{2}\right)\right] = 6.4\ in$$

$$s_{provided} < s_{max}\ \therefore\ ok$$

- **Top Bars Splices**

$$l_d = \left(\frac{f_y \psi_t \psi_e}{20\lambda\sqrt{f_c'}}\right) d_b$$

$$\psi_t = 1.3$$

$$\psi_e = 1.0$$

$$l_d = \left(\frac{60000 \times 1.3 \times 1}{20 \times 1 \times \sqrt{4000}}\right)\left(\frac{7}{8}\right) = 54\ in = 4'6"$$

$$Class\ B\ splice\ =\ 1.3 l_d$$

$$Class\ B\ splice\ =\ 1.3 \times 54 = 71\ in = 5'11"$$

- **Bottom Bars Splices**

$$l_d = \left(\frac{f_y \psi_t \psi_e}{25\lambda\sqrt{f_c'}}\right) d_b$$

$$\psi_t = 1.0$$

$$\psi_e = 1.0$$

$$l_d = \left(\frac{60000 \times 1 \times 1}{25 \times 1 \times \sqrt{4000}}\right)\left(\frac{6}{8}\right) = 29\ in = 2'5"$$

$$Class\ B\ splice\ =\ 1.3 \times = 38\ in = 3'2"$$

B.2 Shear and Torsion Design for Beams

This section describes the shear and torsion design for the critical section in a typical exterior beam of exterior frame 1 on the first story. From predesign the beam size is 24”x20”

$$V_u = 25.3\ kip$$

$$T_u = 81.2\ k - ft$$

- **Torsion**

The area used in the torsion analysis has included the slab portion as shown in Figure B.1. Note that the maximum effective width of slab used is 4 times its thickness.

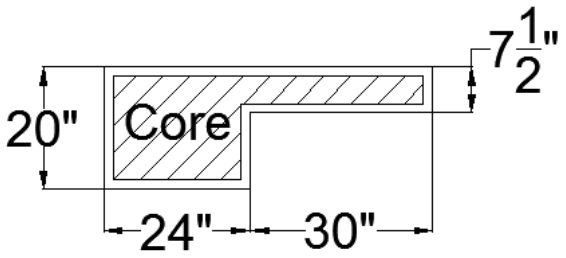

Figure B.1: Area used in the torsion analysis

$$T_c = \phi\lambda\sqrt{f_c'}\left(\frac{A_{cp}^2}{P_{cp}}\right)$$

$$T_c = \frac{0.75 \times 1 \times \sqrt{4000}\left[\frac{(24 \times 20 + 30 \times 7.5)^2}{(24+20)\times 2 + 30 \times 2}\right]}{12 \times 1000} = 13.3\ k-ft$$

$$T_c < T_u \ \therefore \ Torsion\ must\ be\ considered$$

$$\frac{A_t}{s} = \frac{T_u}{\phi 2 A_o f_y cot\theta}$$

$$A_o = 0.85 A_{oh}$$

$$A_o = 0.85(21 \times 17 + 30 \times 4.5) = 418.2\ in^2$$

$$\frac{A_t}{s} = \frac{81.2 \times 12 \times 1000}{2 \times 0.75 \times 418.2 \times 60000 \times \cot(45)} = 0.025\ in^2/in/leg$$

- **Shear**

$$\phi V_c = \phi 2\lambda\sqrt{f_c'} bd$$

$$\phi V_c = \frac{0.75 \times 2 \times 1 \times \sqrt{4000} \times 24 \times 17.5}{1000} = 39.84\ kip$$

$$\phi V_c > V_u \ \therefore \ No\ strength\ requirement$$

- **Combined shear and torsion stirrup requirement**

$$\frac{A_t}{s} + \frac{A_v}{2s} = 0.025 + 0 = 0.025\ in^2/in/leg$$

$$s = \frac{A_t}{0.025}$$

$$Use\ stirrup\ \#4\ (A_t = 0.20\ in^2)$$

$$s = \frac{0.20}{0.025} = 8\ in$$

- **Maximum spacing for torsion**

$$s_{max} = \frac{P_h}{8}$$

$$s_{max} = \frac{(21 + 17) \times 2 + 30 \times 2}{8} = 17\ in$$

$$s_{max} = 12\ in$$

- **Maximum spacing for shear**

$$s_{max} = \frac{d}{2}$$

$$s_{max} = \frac{17.5}{2} = 8.75\ in$$

$$s_{max} = 24\ in$$

$$Use\ s_{max} = 8.75\ in$$

$$s < s_{max} \therefore\ Use\ s = 8\ in$$

$$Use\ \#4\ @\ 8\ in$$

$$min(A_t + 2A_v) = \frac{0.75\sqrt{f_c'}bs}{f_{yt}} \geq \frac{50bs}{f_{yt}}$$

$$min(A_t + 2A_v) = \frac{0.75 \times \sqrt{4000} \times 24 \times 8}{60000} = 0.15\ in^2$$

$$min(A_t + 2A_v) = \frac{50 \times 24 \times 8}{60000} = 0.16\ in^2$$

$$Required\ (A_t + 2A_v) = 0.16\ in^2$$

$$A_{provided} = 0.20 \times 2 = 0.40\ in^2$$

$$A_{provided} > Required\ \left(\frac{A_t}{s} + \frac{A_v}{2s}\right)\ \therefore\ ok$$

B.3 Column Design

This section describes the design for a typical interior column of exterior frame 1 on the first story. Figure B.2 shows the interaction diagrams with the factored loads for typical interior column of exterior frame 1 on the first story. Further on, shear design calculations are presented. From predesign the column size is 24”x24”

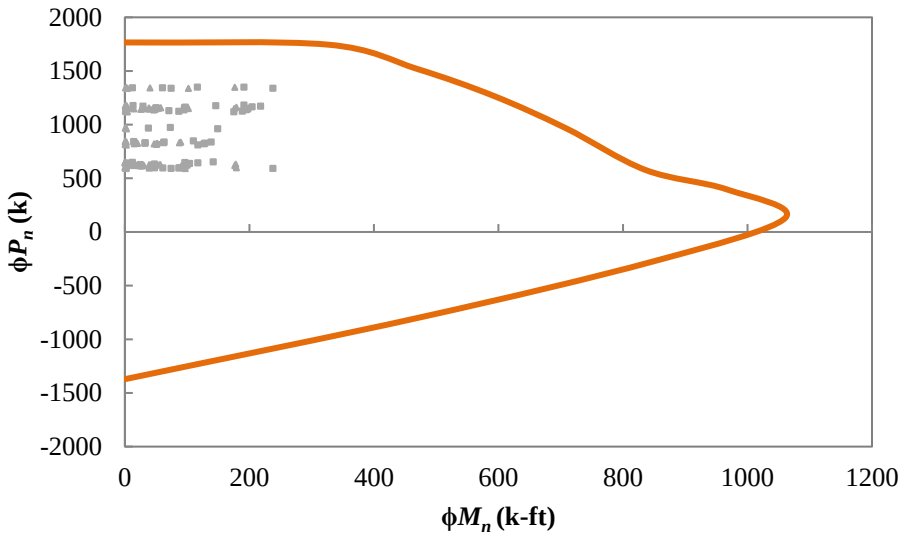

Figure B.2: Interaction diagram for an interior column of exterior frame 1 on the first story (grey triangles and squares represent values from different load combinations)

- **Shear Design**

$$V_u = 29.9\ kip$$

$$\phi V_c = \phi 2(1 + \frac{N_U}{2000 \times A_g})\lambda\sqrt{f_c'}bd$$

$$\phi V_c = \frac{0.75 \times 2 \times (1 + \frac{613.16 \times 1000}{2000 \times 24 \times 24}) \times 1 \times \sqrt{4000} \times 24 \times 21.5}{1000} = 75.0\ kip$$

$$\frac{\phi V_c}{2} > V_u \therefore No\ shear\ design\ required$$

- **Ties**

$$s_{max} = 16d_b$$

$$s_{max} = 16 \times \left(\frac{10}{8}\right) = 20\ in$$

$$s_{max} = 48d_t$$

$$s_{max} = 48 \times \left(\frac{3}{8}\right) = 18\ in$$

$$s_{max} = h$$

$$s_{max} = 24\ in$$

$$Use\ s_{max} = 18\ in$$

$$Use\ \#3\ @\ 18\ in$$

APPENDIX C

TEST SETUP DETAILS

This appendix presents the details of the steel elements used in the laboratory setup. Figure C.1 shows the schematic drawing of the test setup described in Chapter 4. The details of the steel elements used in the laboratory setup also are presented in Figure to C.2 to C.11 Steel A-992 Grade 50 was used for the w-shape elements and Steel A-36 Grade 36 was used in the other elements. Also, the tolerance of the pin holes was 1/16 in to provide relative movement between connected parts.

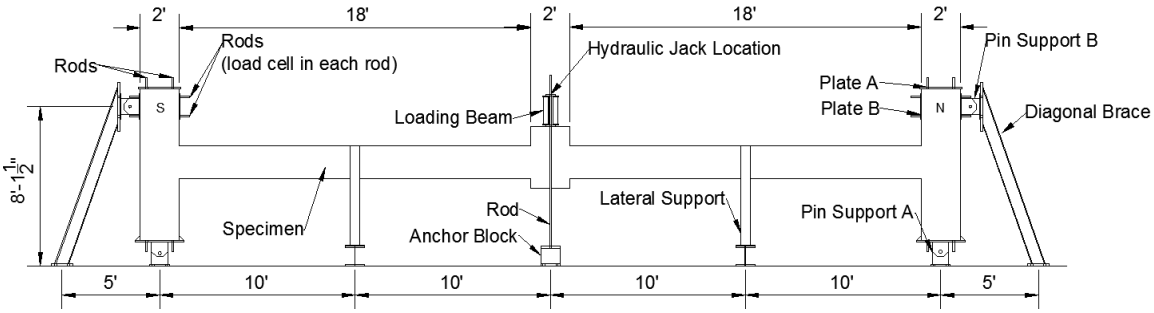

Figure C.1: Test setup details

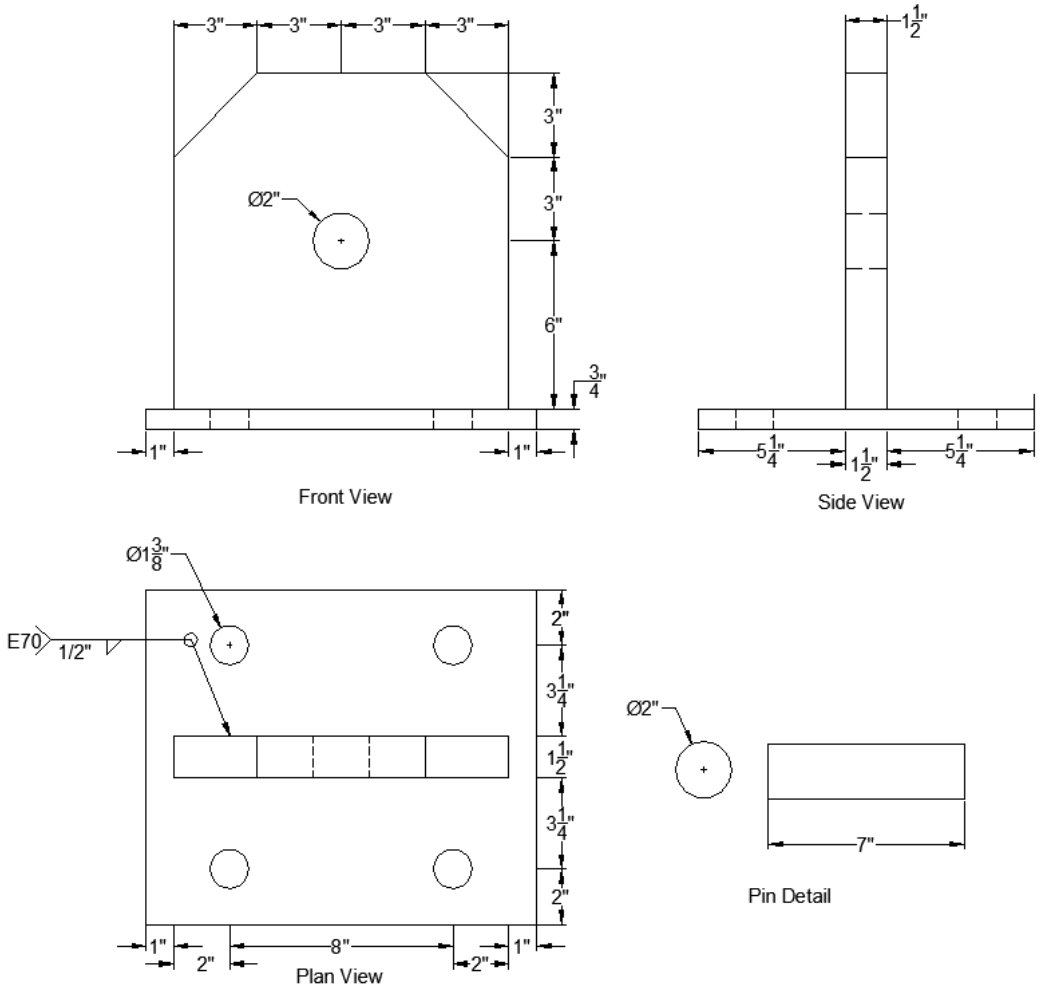

Figure C.2: Pin Support A bottom part details

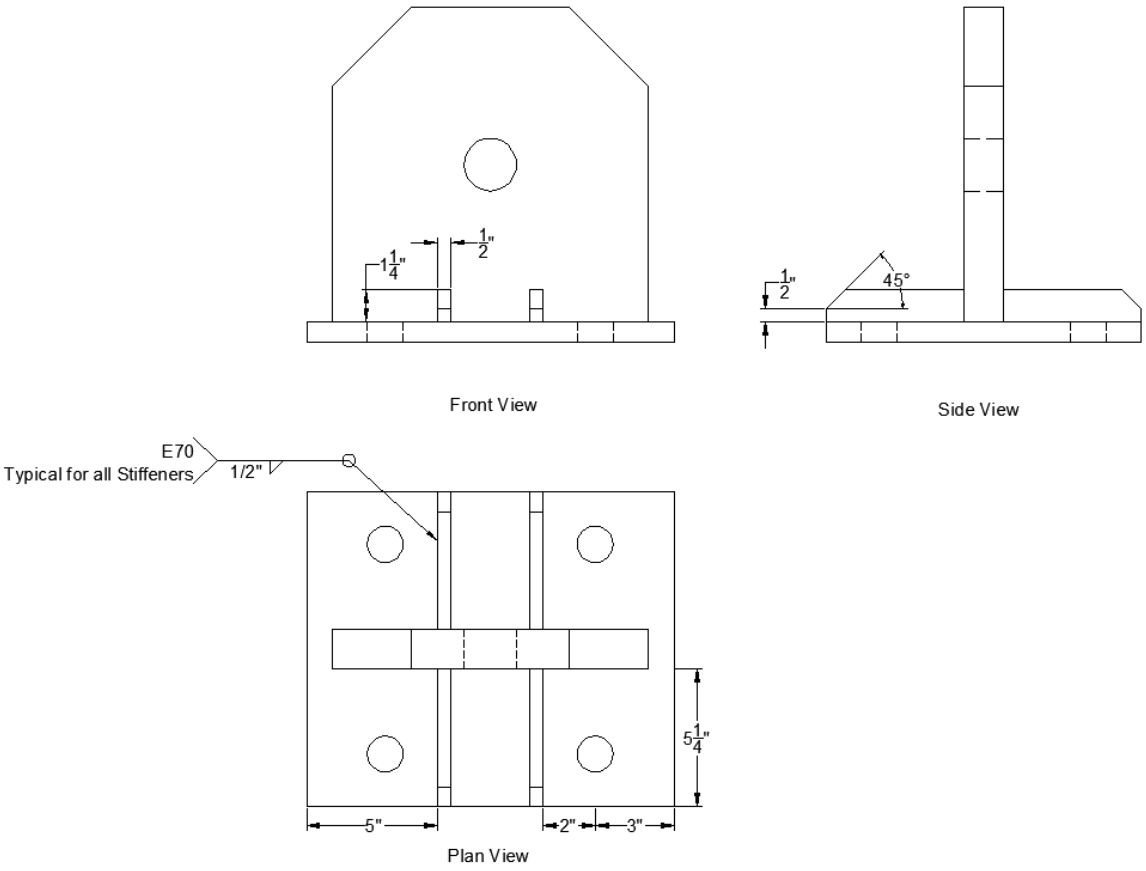

b)

Figure C.3: Stiffeners details of Pin Support A bottom part

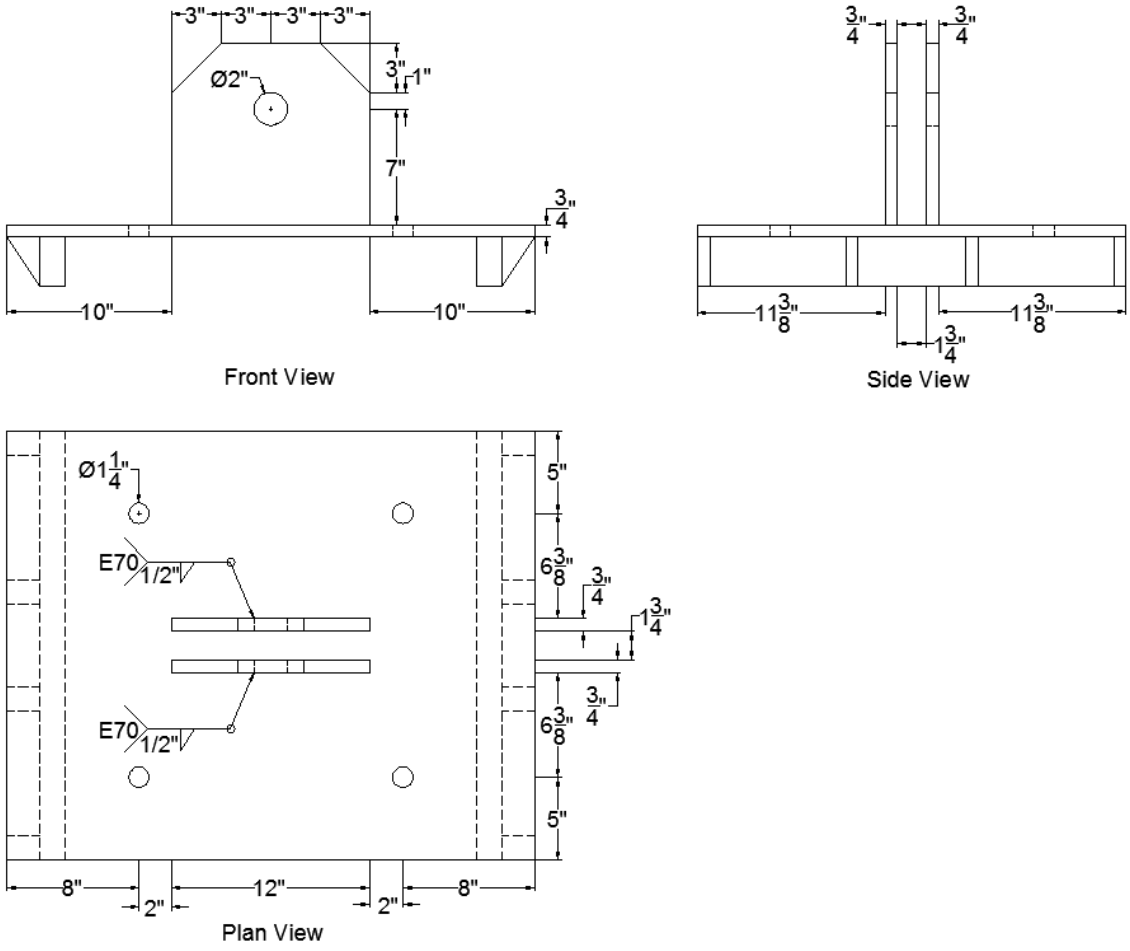
3"
3"
3"
3"
Ø2"
3"
1"
7"
3/4"
10"
10"
Front View
3/4"
3/4"
11 3/8"
11 3/8"
1 3/4"
Side View
Ø1 1/4"
E70 1/2"
E70 1/2"
5"
6 3/8"
3/4"
1 3/4"
3/4"
6 3/8"
5"
8"
2"
12"
2"
8"
Plan View

a)

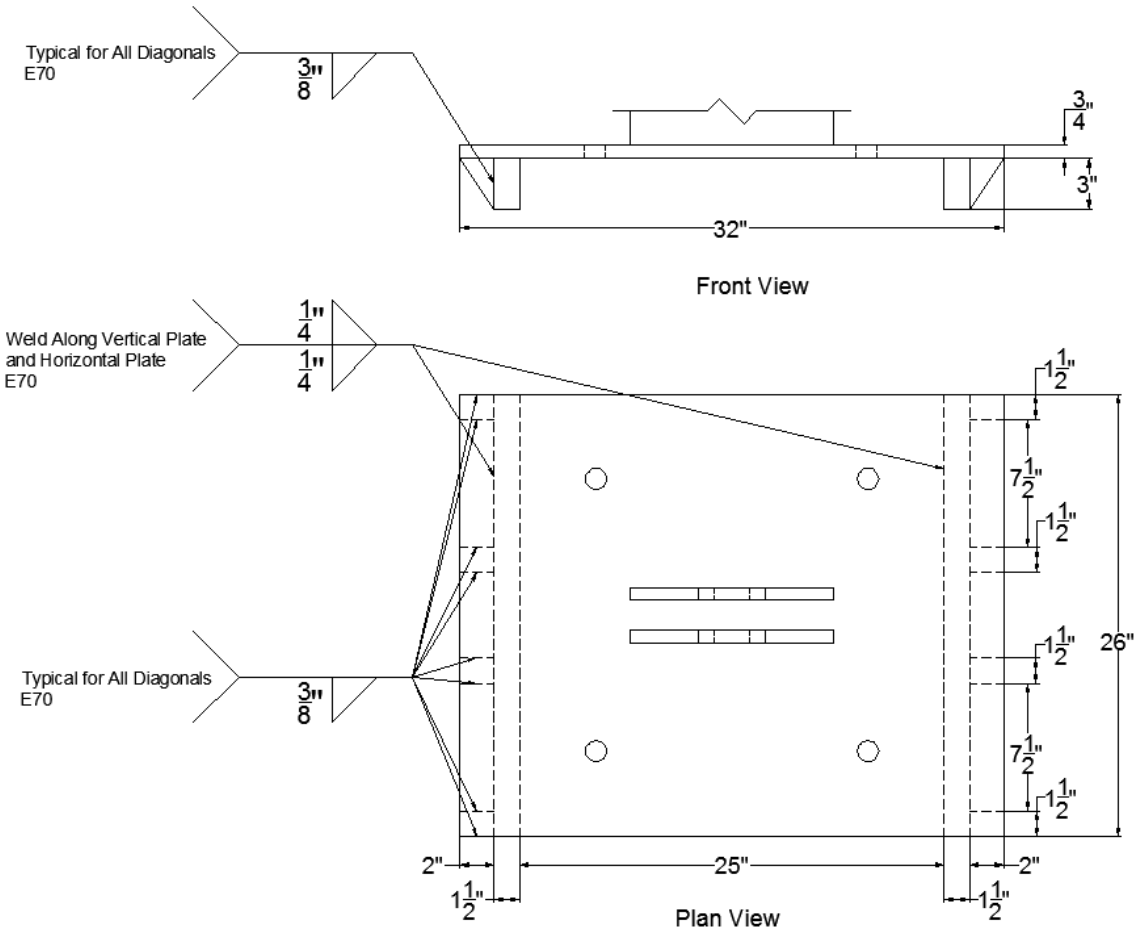

b)

Figure C.4: Pin Support A top part details

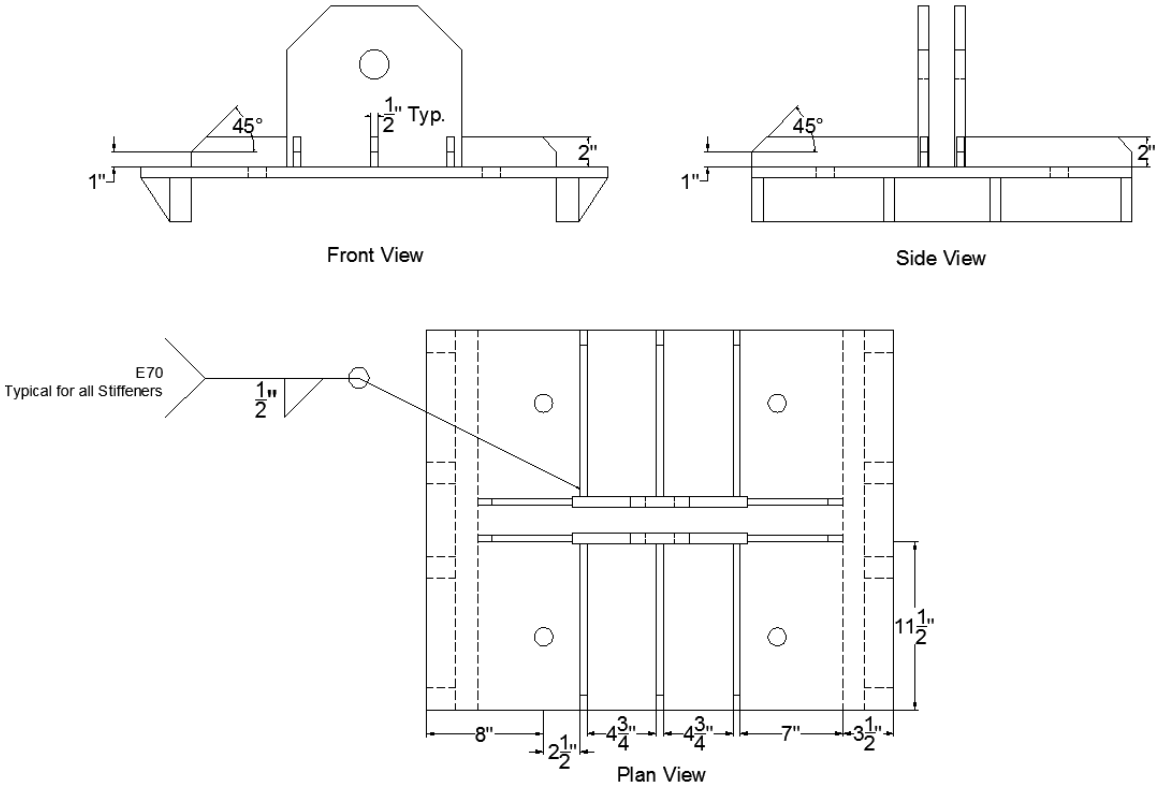

Figure C.5: Stiffeners details of Pin Support A top part

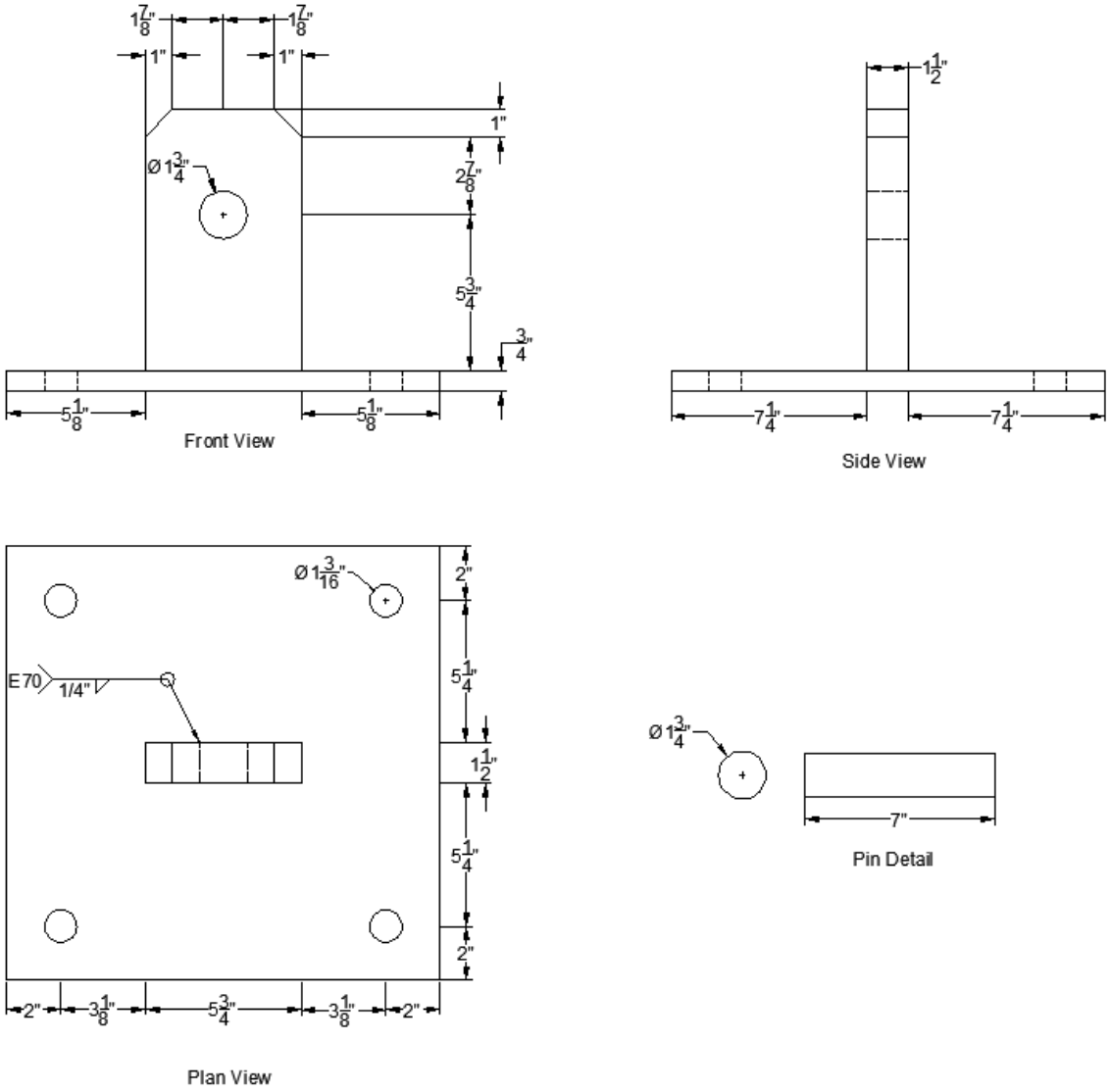

Figure C.6: Pin Support B exterior part details

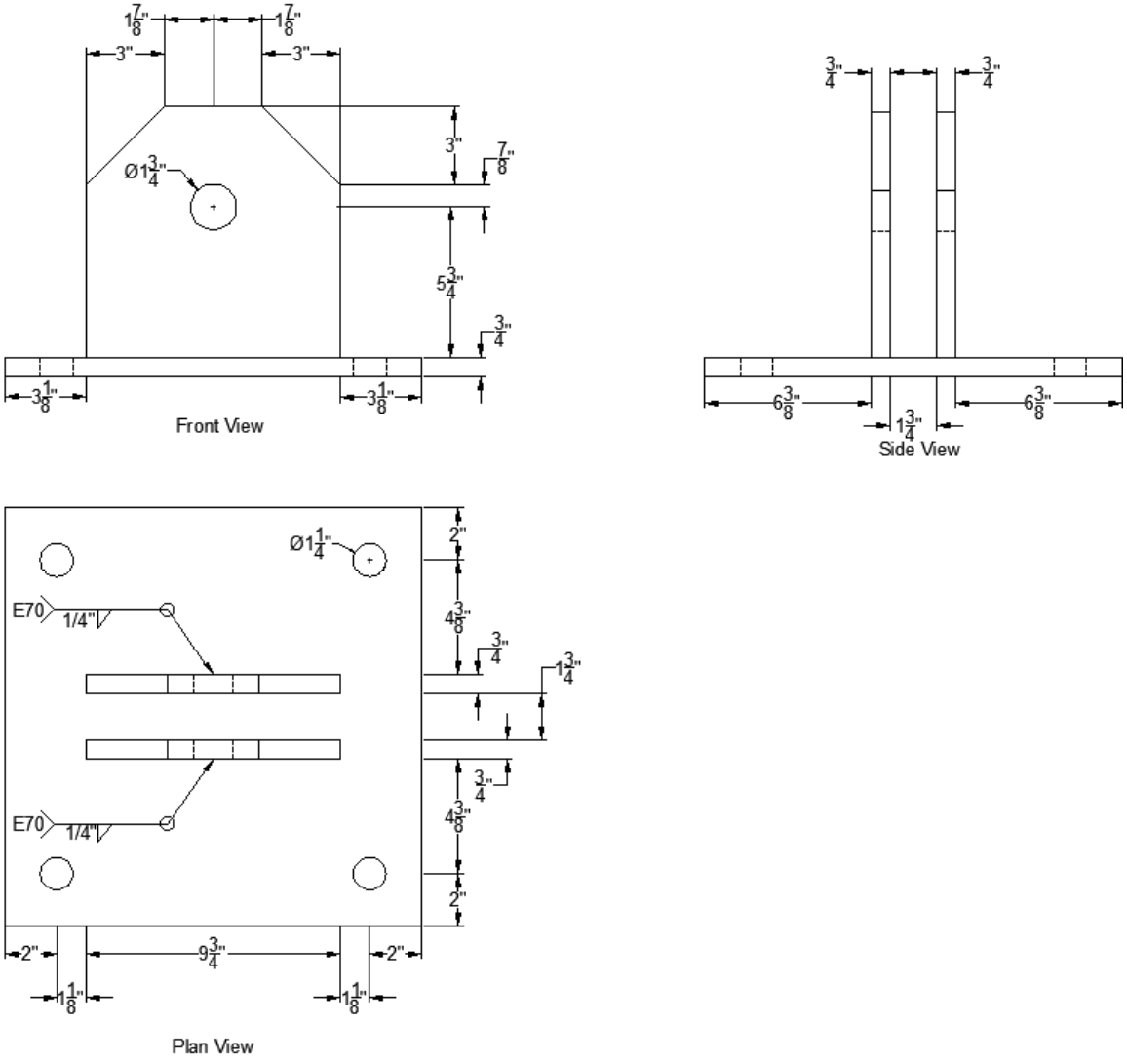

Figure C.7: Pin Support B interior part details

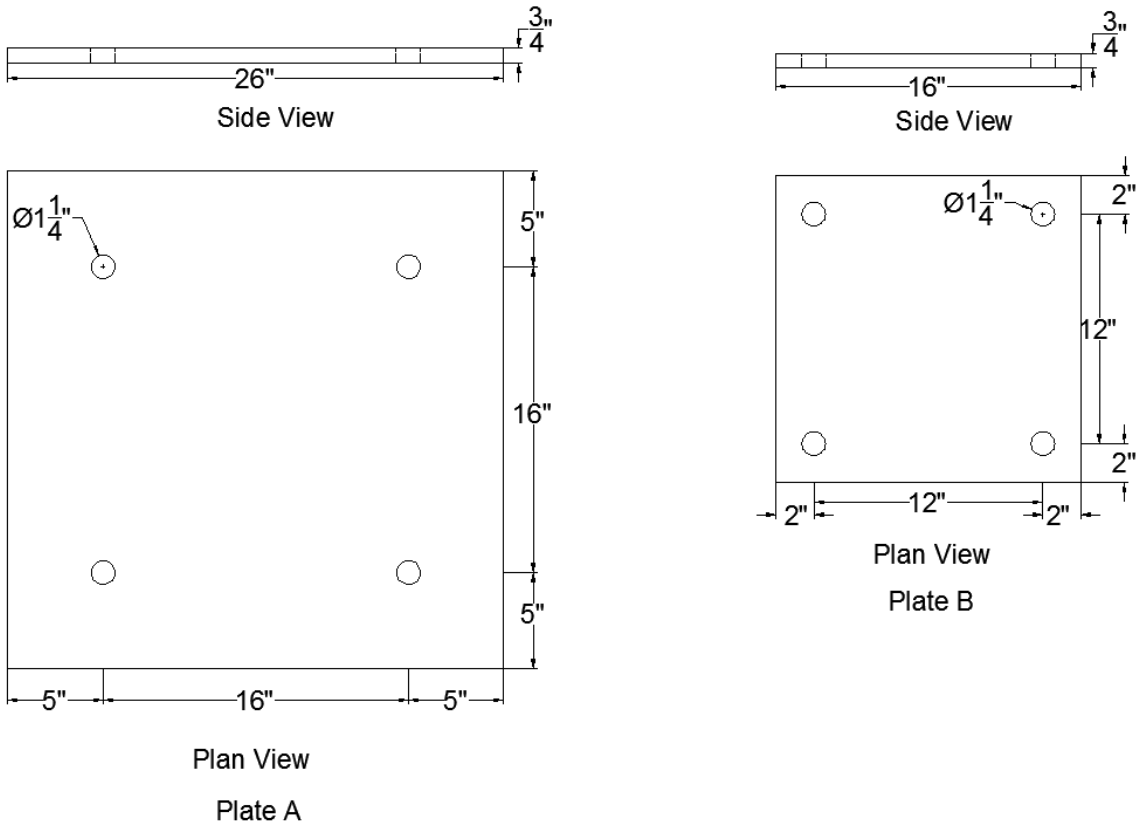

Figure C.8: Plate A and B details

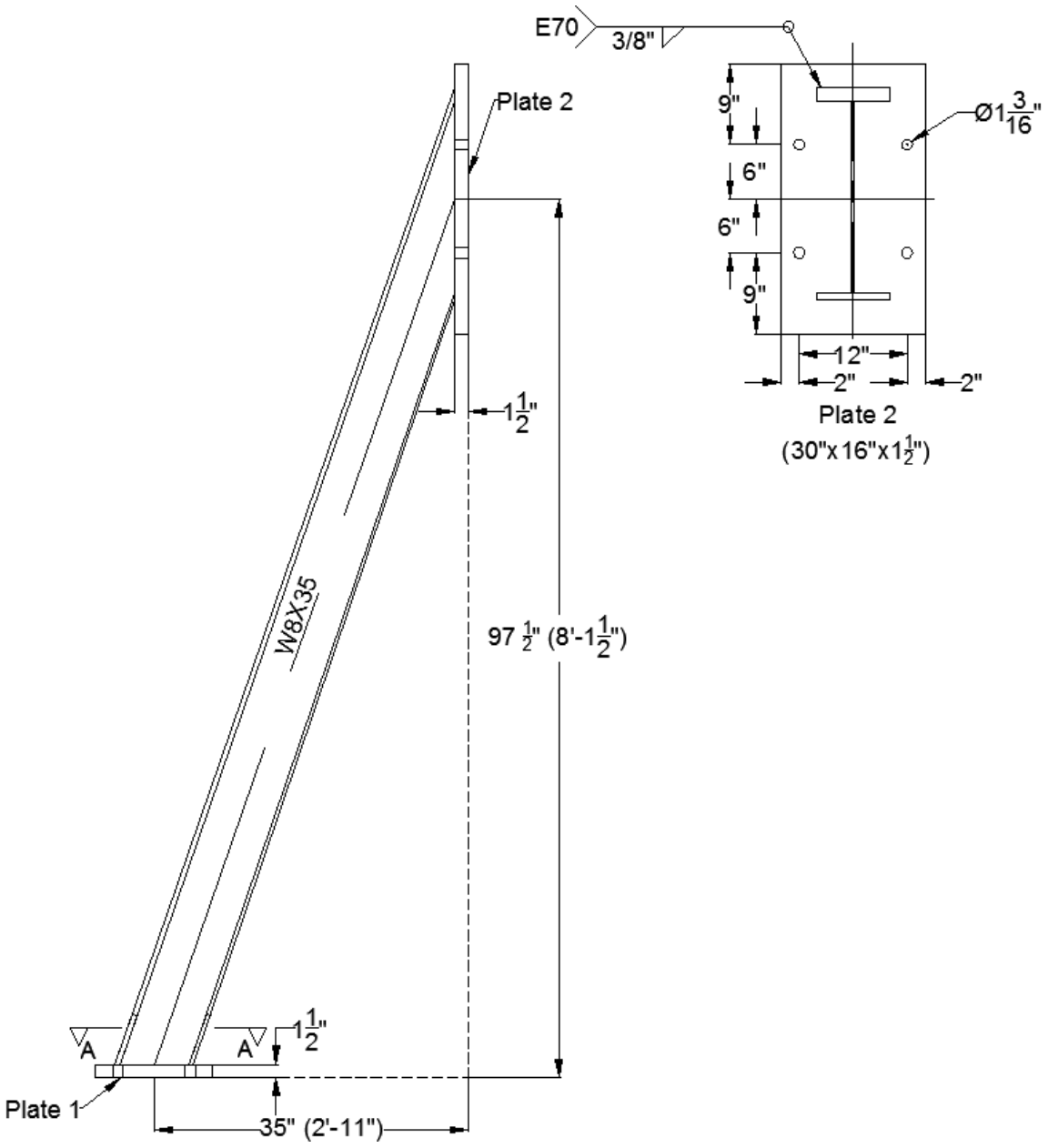
E70
3/8"
Plate 2
9"
6"
6"
9"
Ø1 3/16"
12"
2"
2"
Plate 2
(30"x16"x1½")
1½"
W8X35
97 ½" (8'-1½")
A
A
1½"
Plate 1
35" (2'-11")

a)

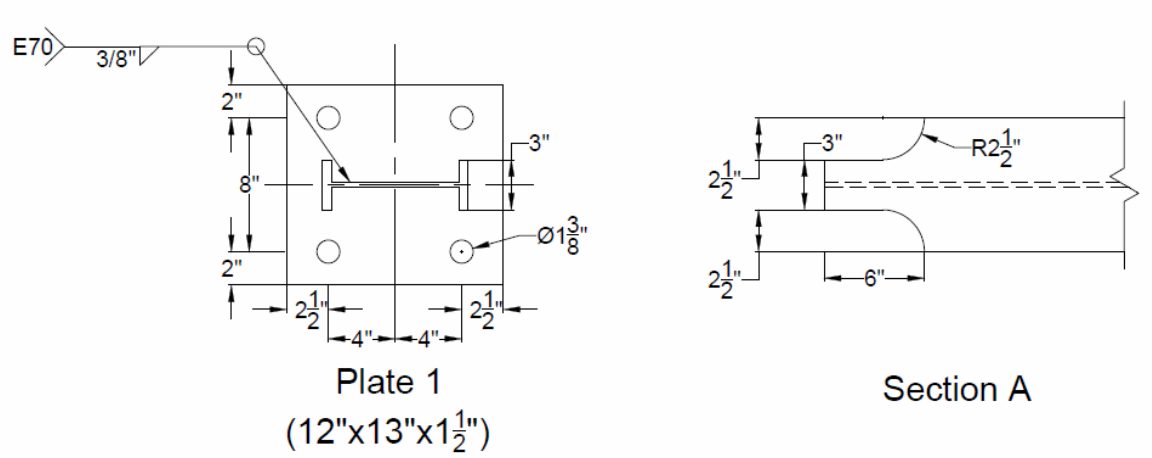

b)

Figure C.9: Diagonal brace details

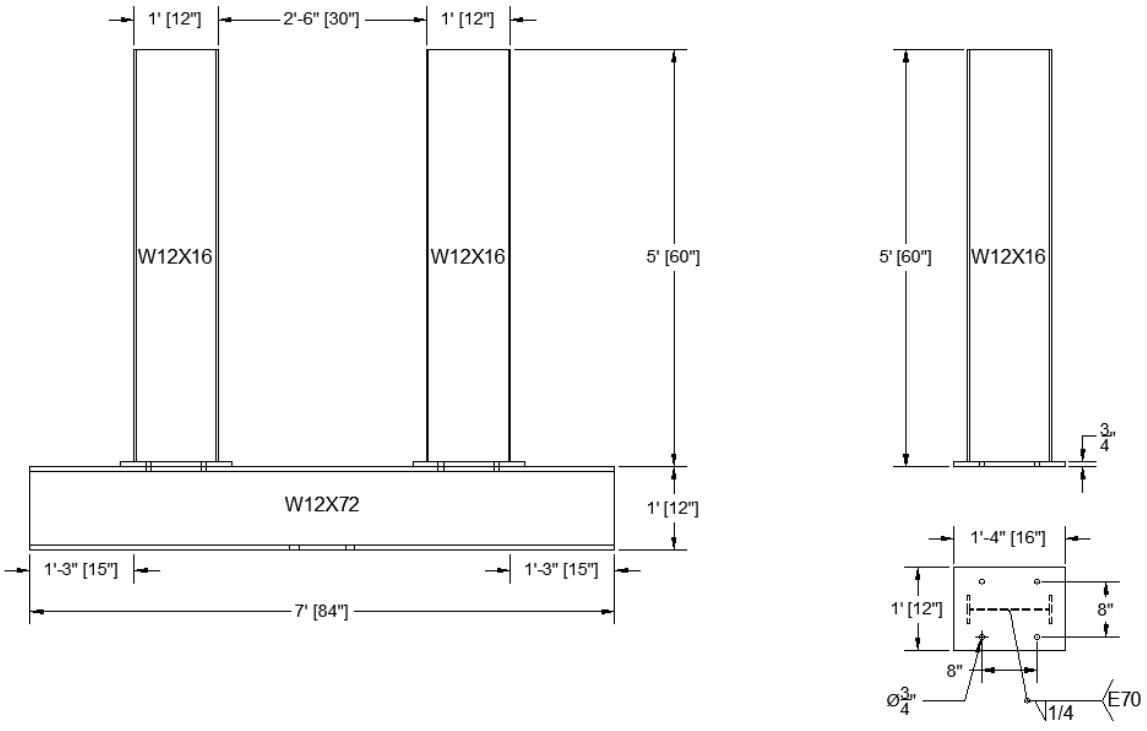

a)

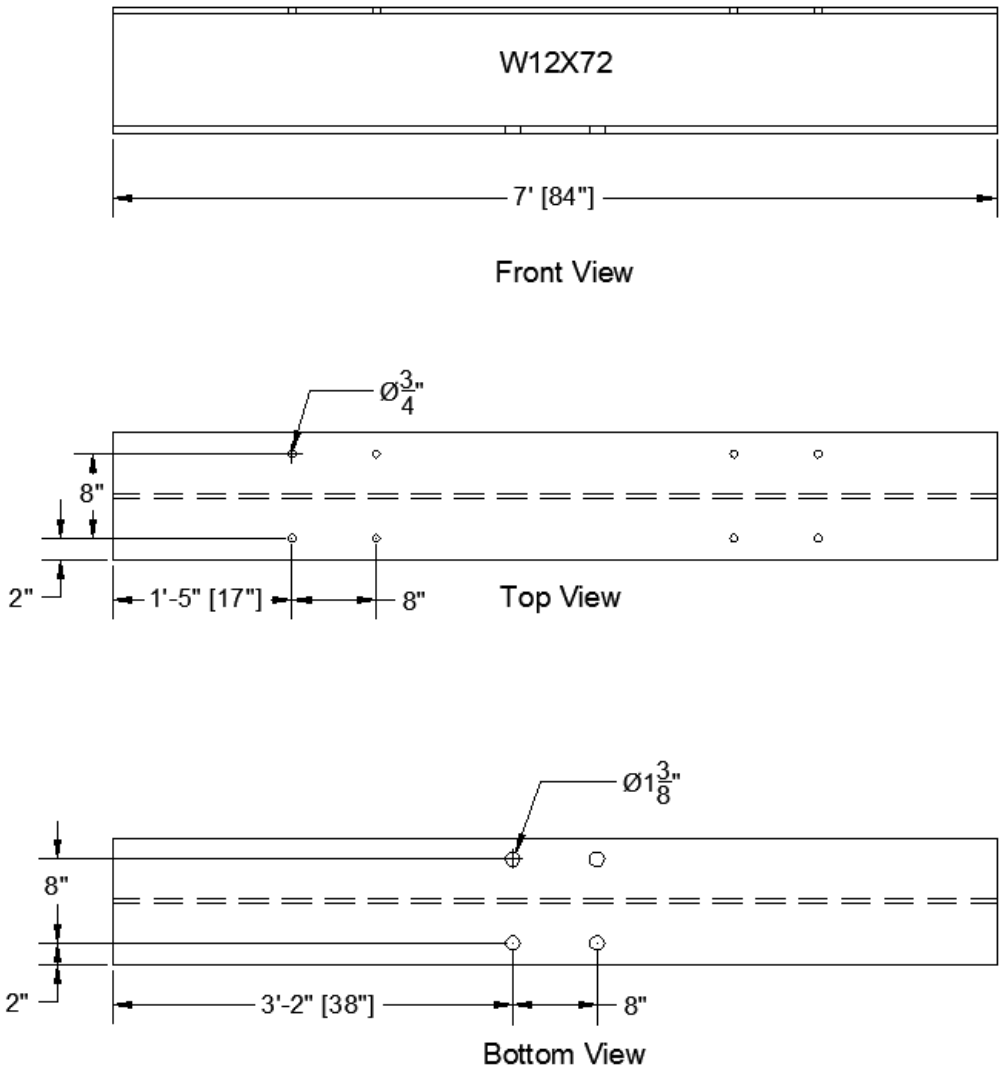

b)

Figure C.10: Lateral Support details

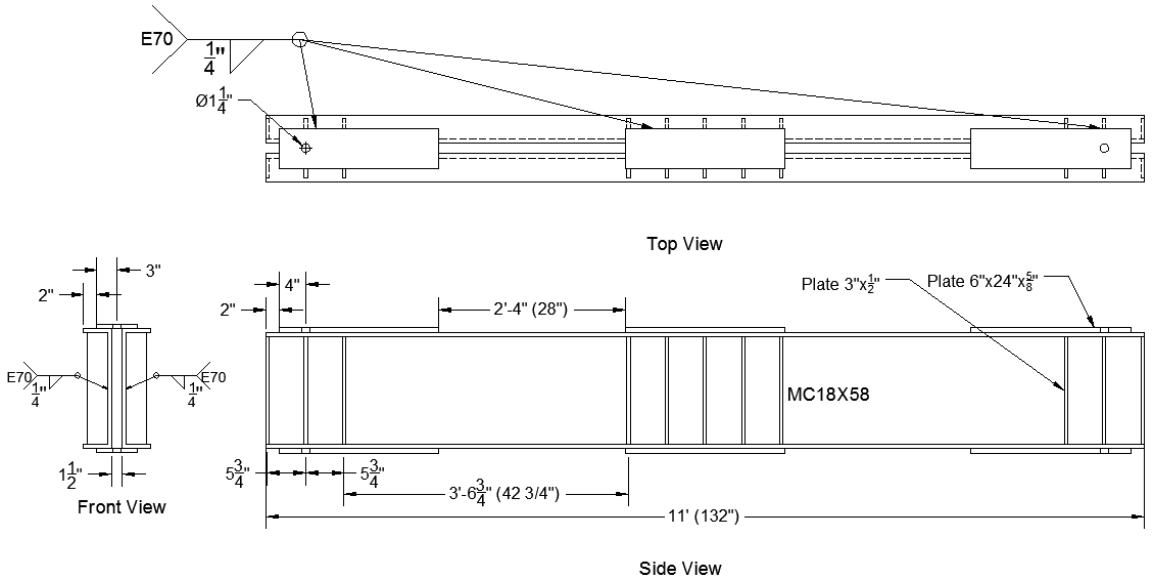

Figure C.11: Loading Beam details

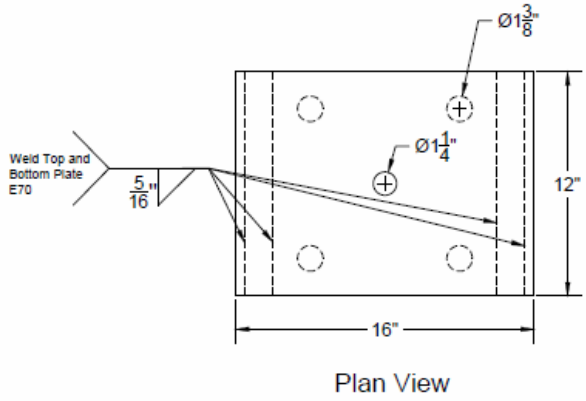

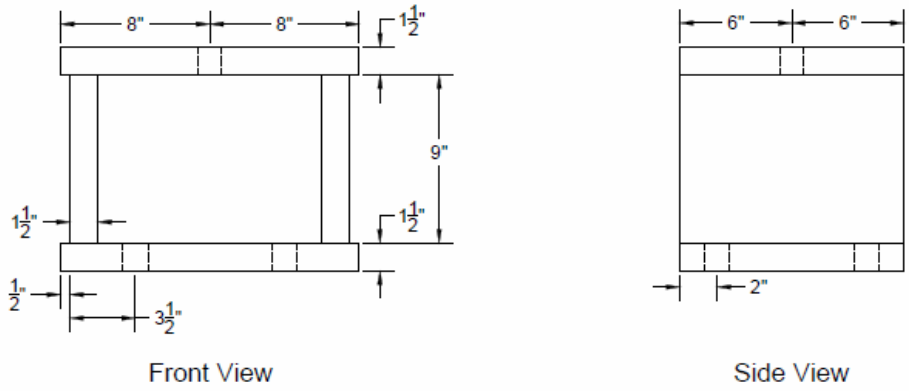

Figure C.12: Anchors Block details

APPENDIX D

SPECIMEN RESULTS

The measurements taken by the internal and external array of instruments from Specimen 1, 2 and 3 that did not discuss in Chapter 5 are presented in this appendix. The results include measured force-displacement and strain gauge response. The internal and external array of instruments is described in Chapter 4.

D.1 Specimen 1 Results

D.1.1 Measured Force-Displacement Response

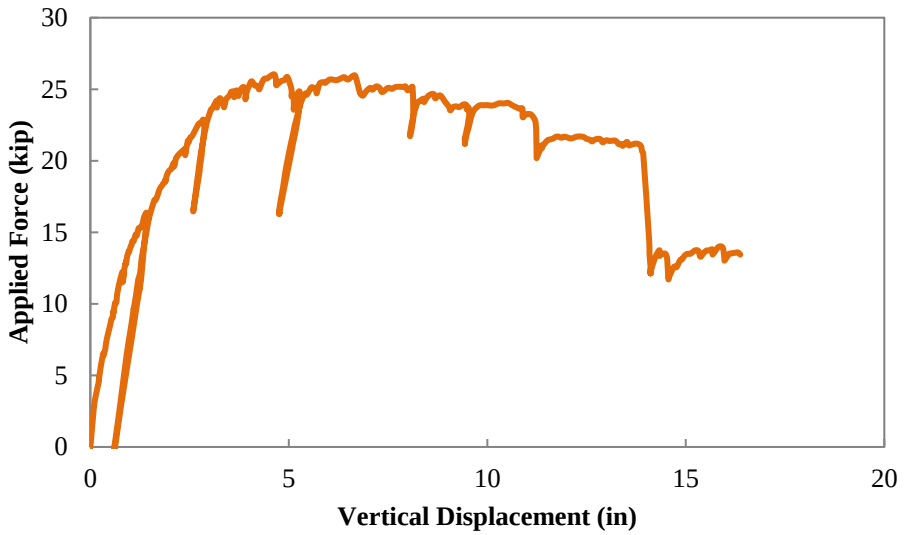

Figure D.1: E-LC force versus NS-PT vertical displacement (Specimen 1)

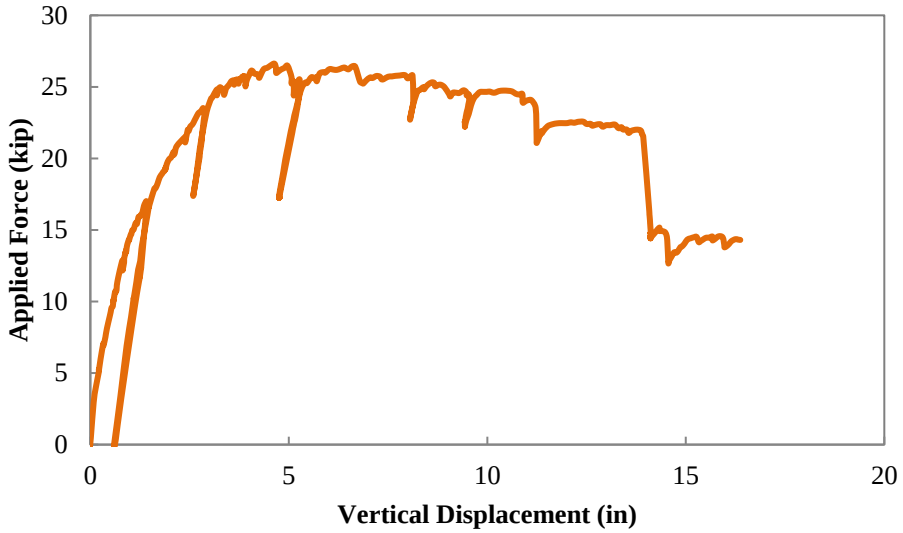

Figure D.2: W-LC force versus NS-PT vertical displacement (Specimen 1)

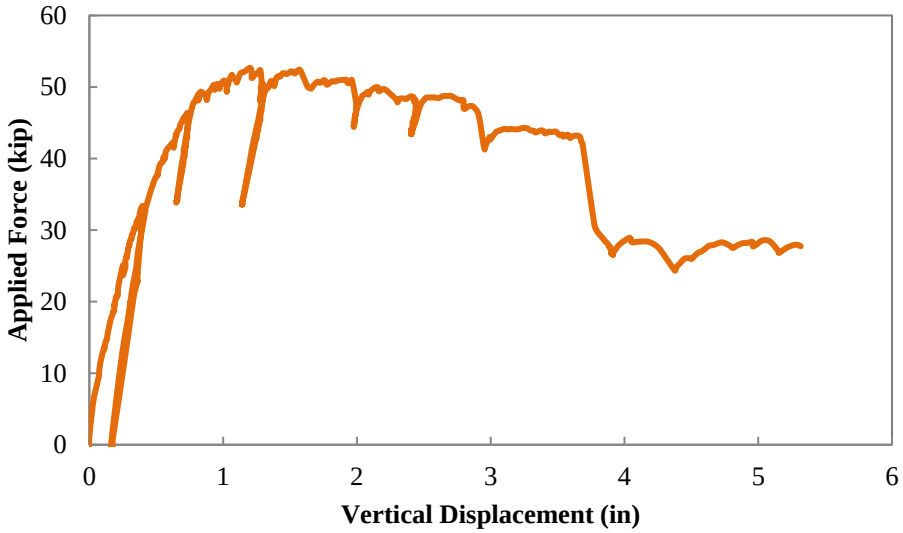

Figure D.3: Force versus NN-PT vertical displacement (Specimen 1)

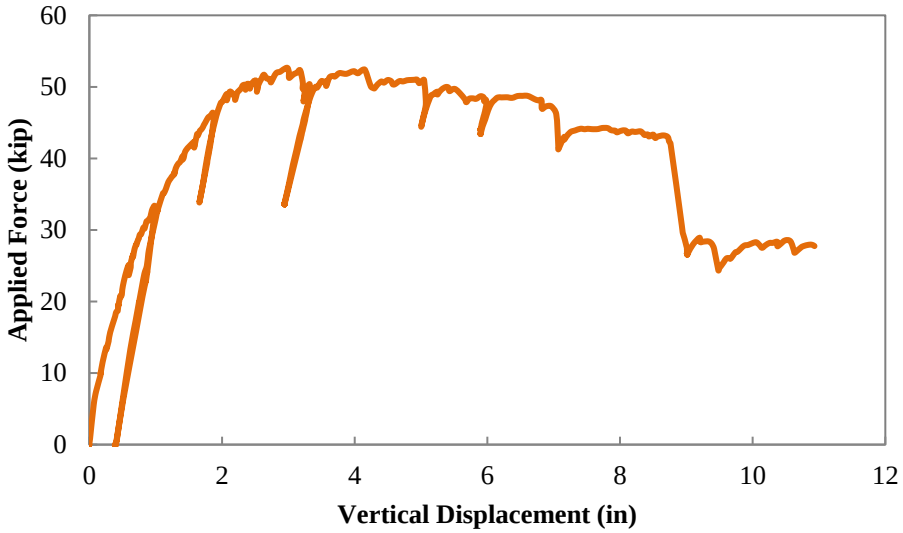

Figure D.4: Force versus NC-PT vertical displacement (Specimen 1)

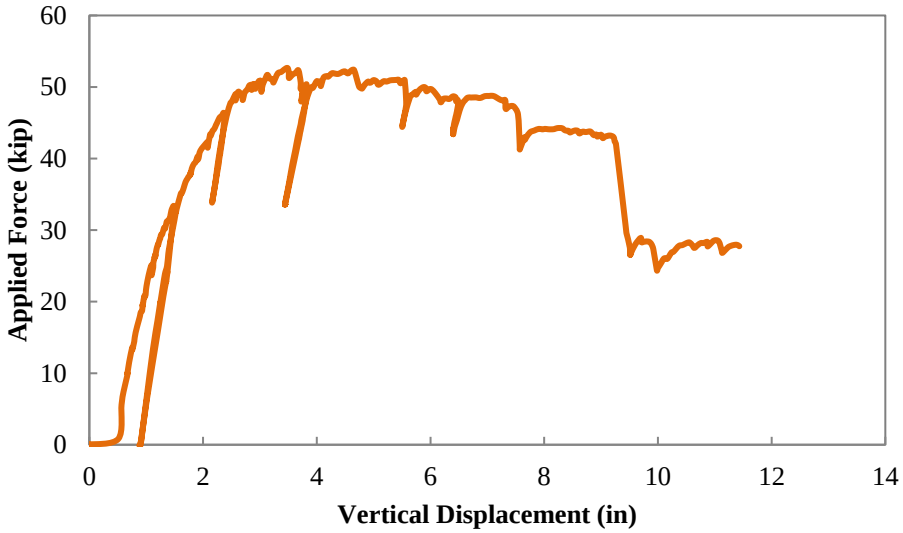

Figure D.5: Force versus SC-PT vertical displacement (Specimen 1)

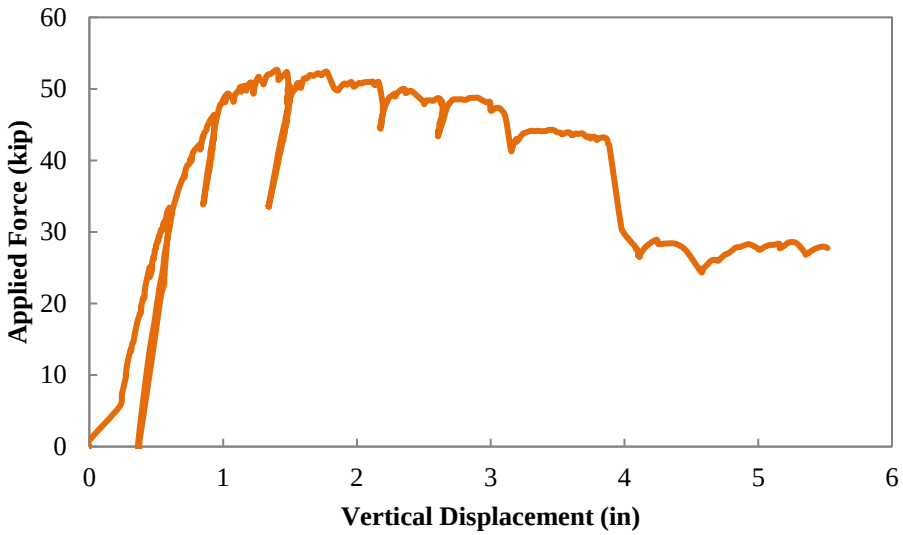

Figure D.6: Force versus SS-PT vertical displacement (Specimen 1)

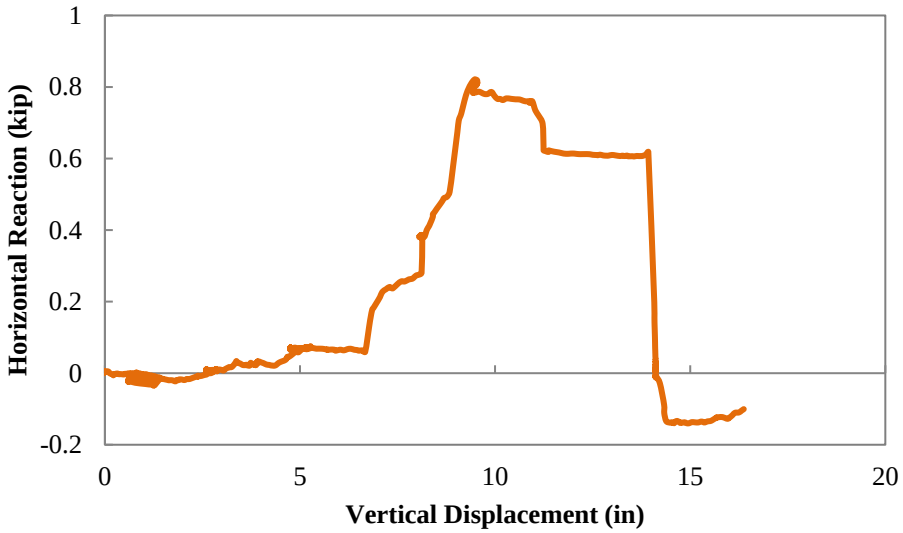

Figure D.7: TL-LC horizontal reaction versus NS-PT vertical displacement (Specimen 1)

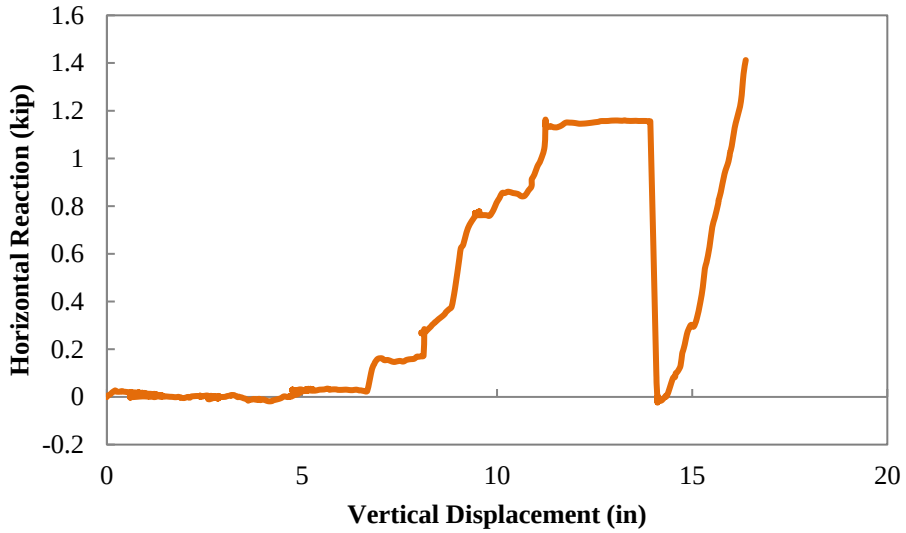

Figure D.8: TR-LC horizontal reaction versus NS-PT vertical displacement (Specimen 1)

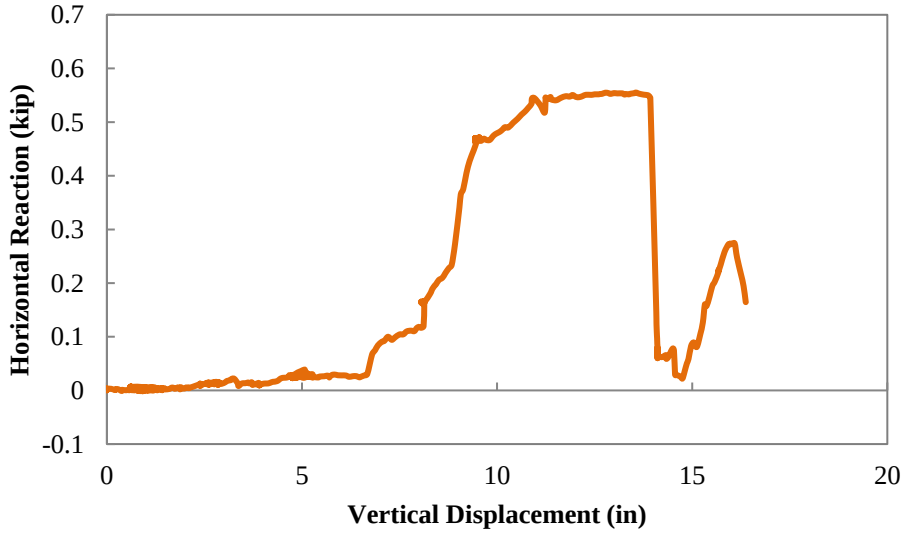

Figure D.9: BL-LC horizontal reaction versus NS-PT vertical displacement (Specimen 1)

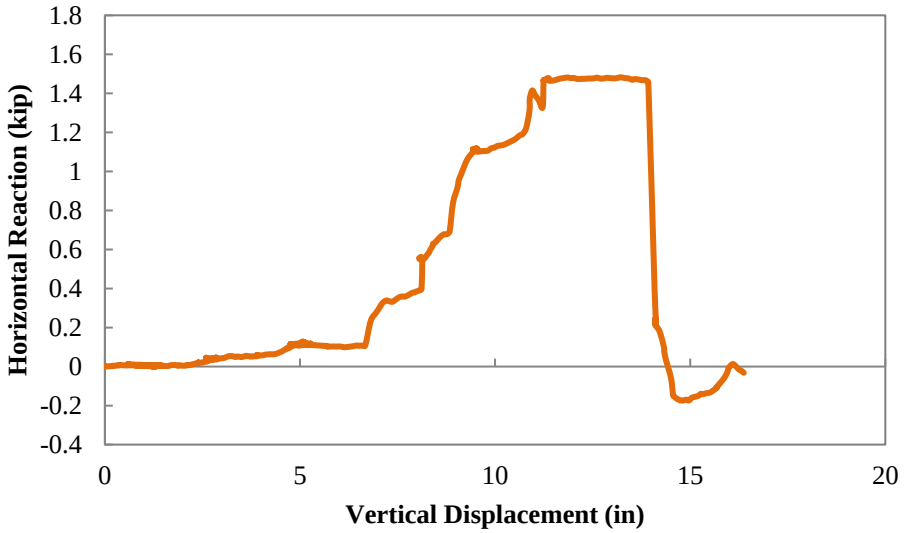

Figure D.10: BR-LC horizontal reaction versus NS-PT vertical displacement (Specimen 1)

D.1.2 Measured Strain Response

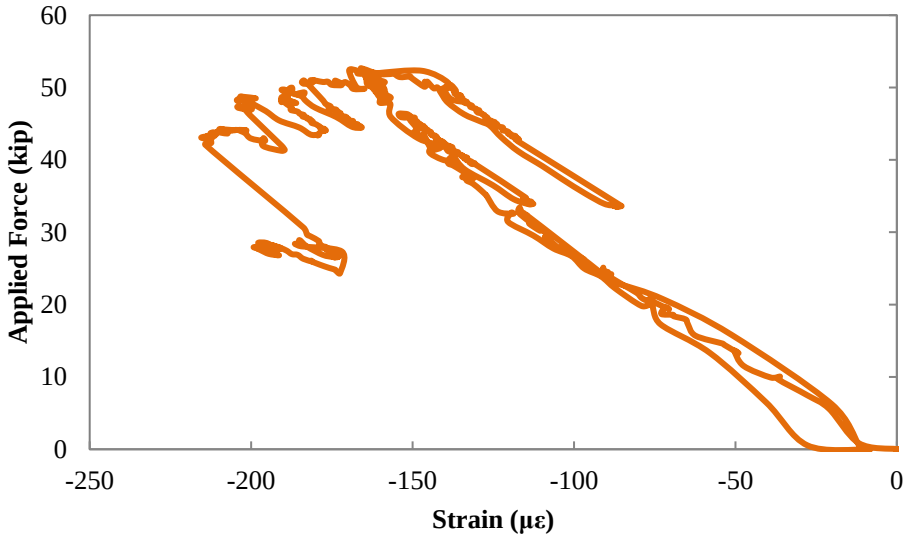

Figure D.11: Force-strain response of top reinforcing bar T3 at section CC (Specimen 1)

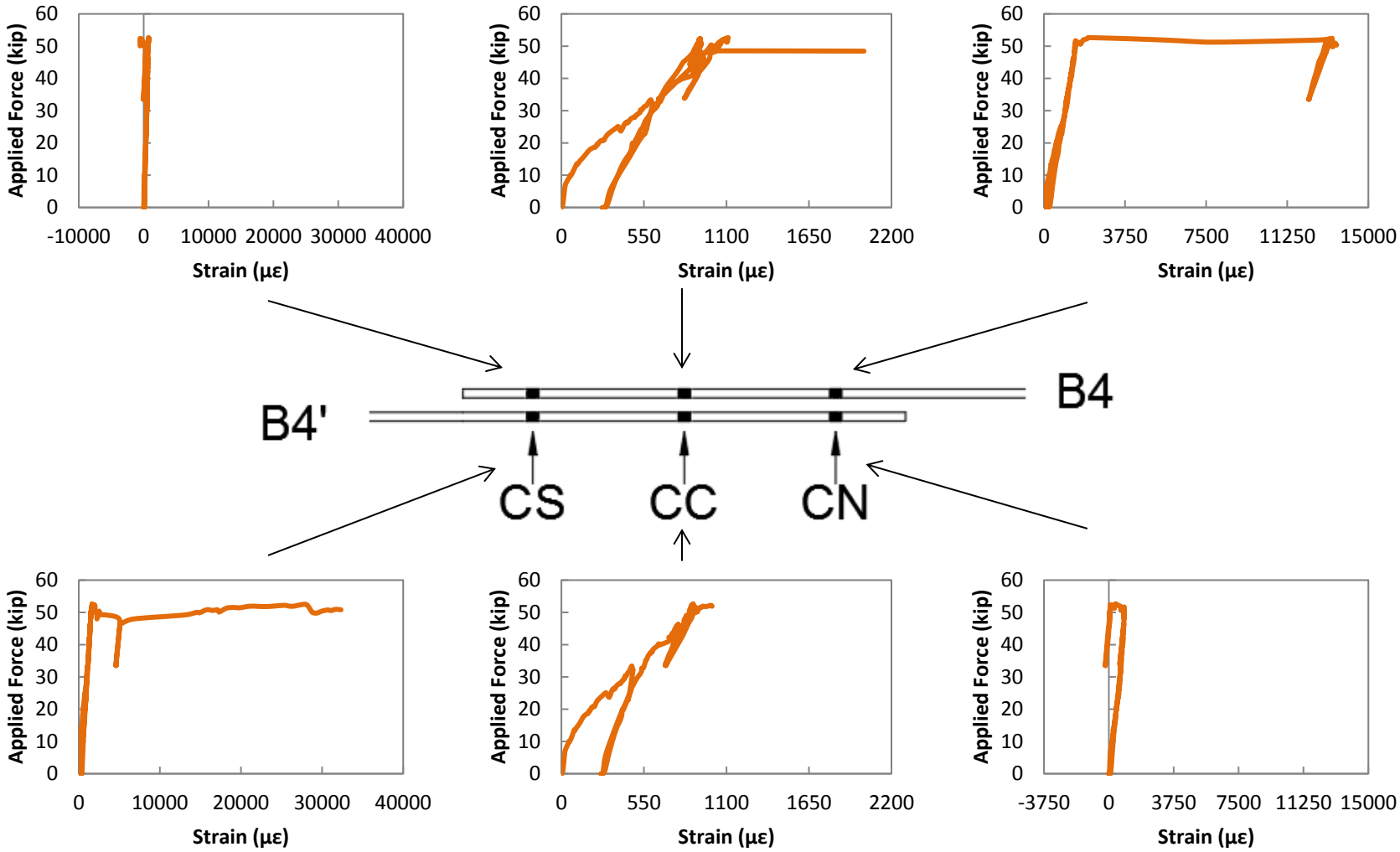

Figure D.12: Force-strain response of bottom reinforcing bars at center column splice zone (Specimen 1)

D.2 Specimen 2 Results

D.2.1 Measured Force-Displacement Response

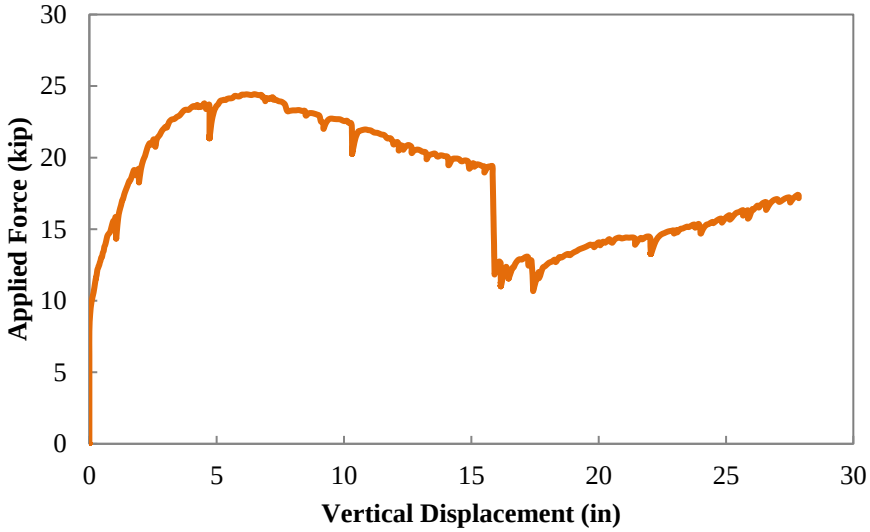

Figure D.13: E-LC force versus CC-PT vertical displacement (Specimen 2)

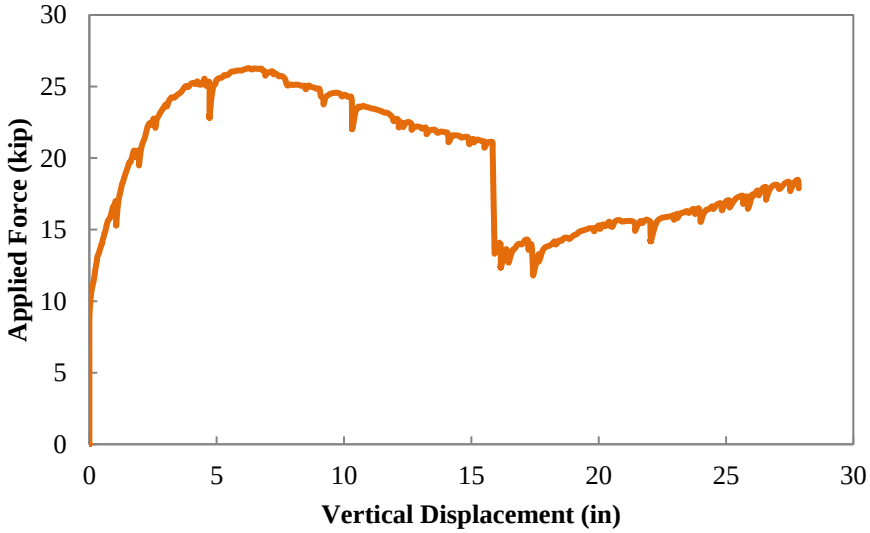

Figure D.14: W-LC force versus CC-PT vertical displacement (Specimen 2)

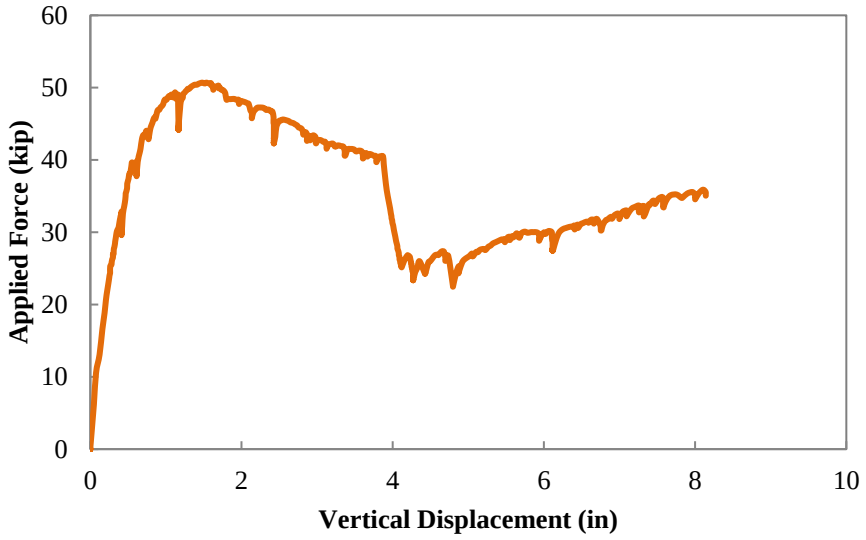

Figure D.15: Force versus NN-PT vertical displacement (Specimen 2)

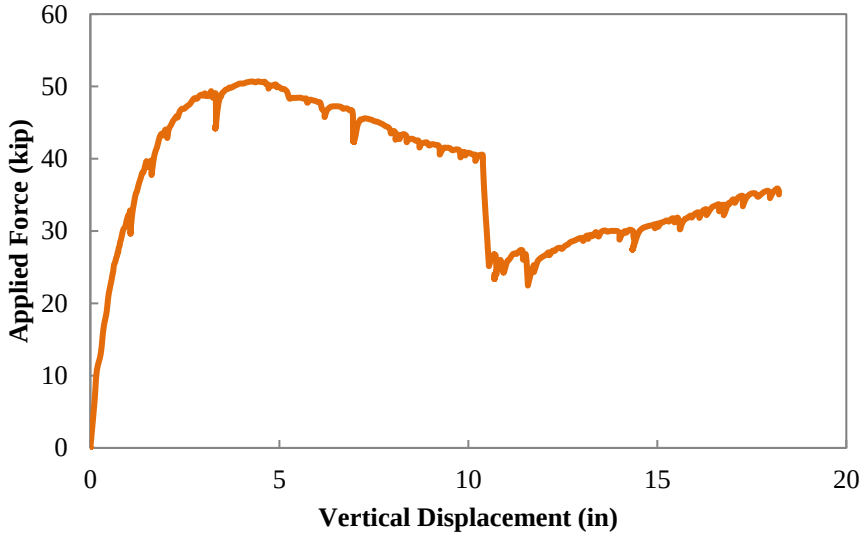

Figure D.16: Force versus NC-PT vertical displacement (Specimen 2)

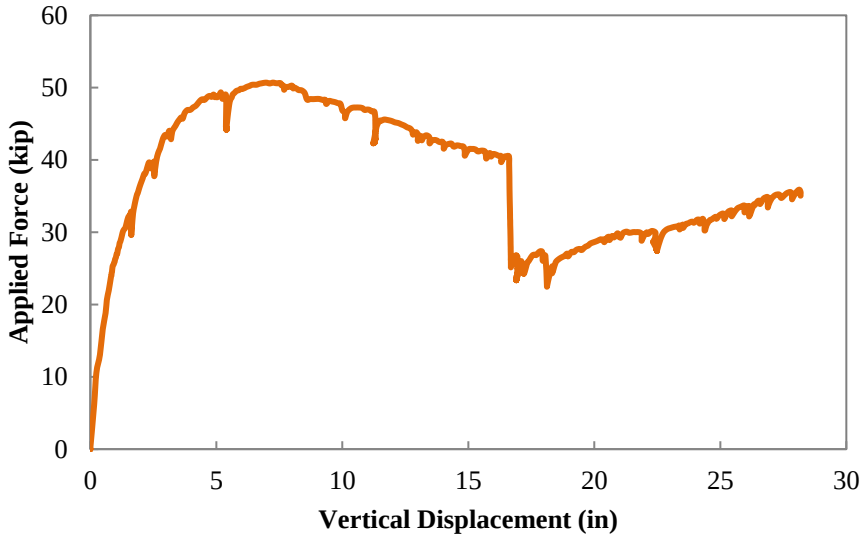

Figure D.17: Force versus NS-PT vertical displacement (Specimen 2)

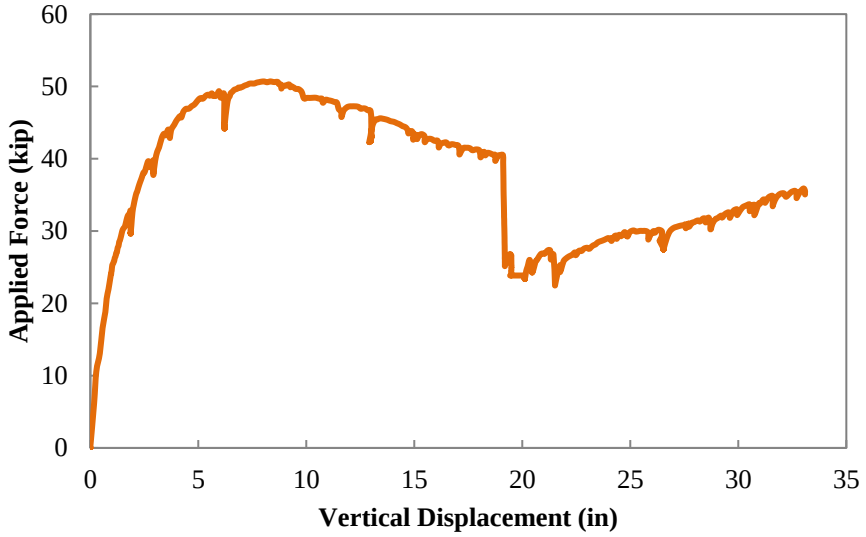

Figure D.18: Force versus SN-PT vertical displacement (Specimen 2)

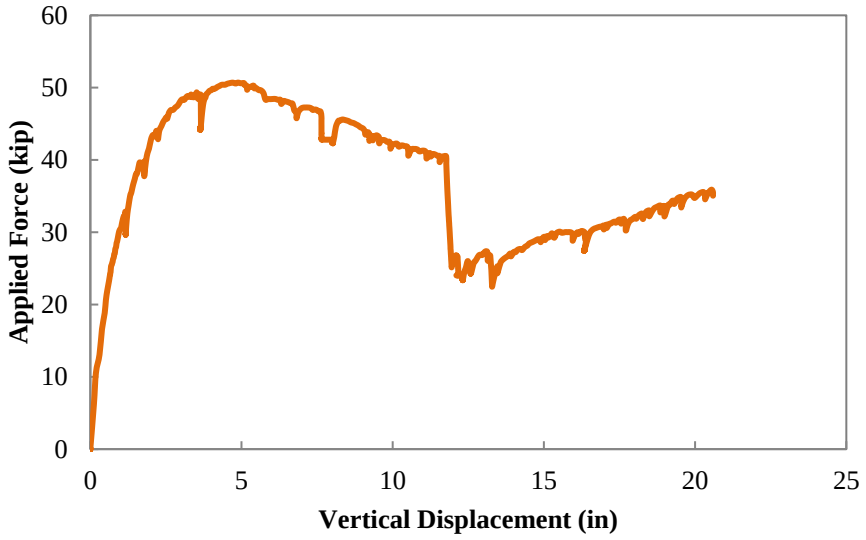

Figure D.19: Force versus SC-PT vertical displacement (Specimen 2)

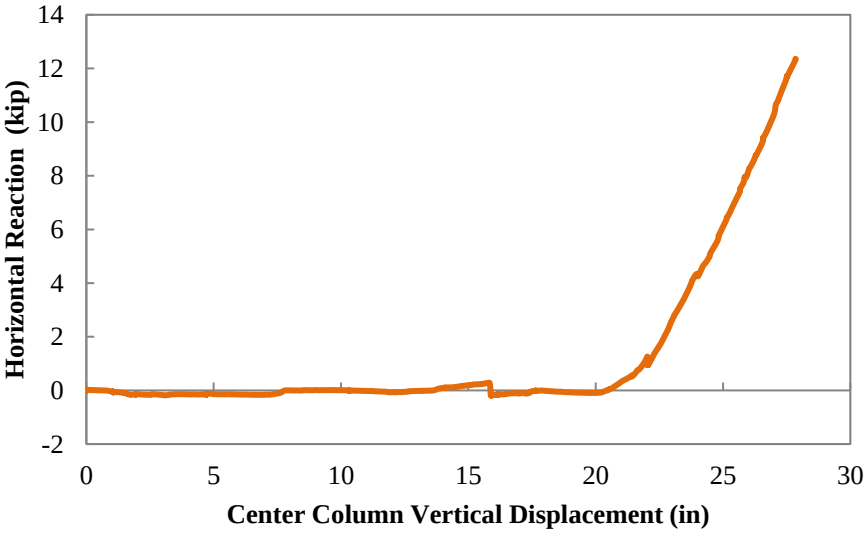

Figure D.20: TL-LC horizontal reaction versus CC-PT vertical displacement (Specimen 2)

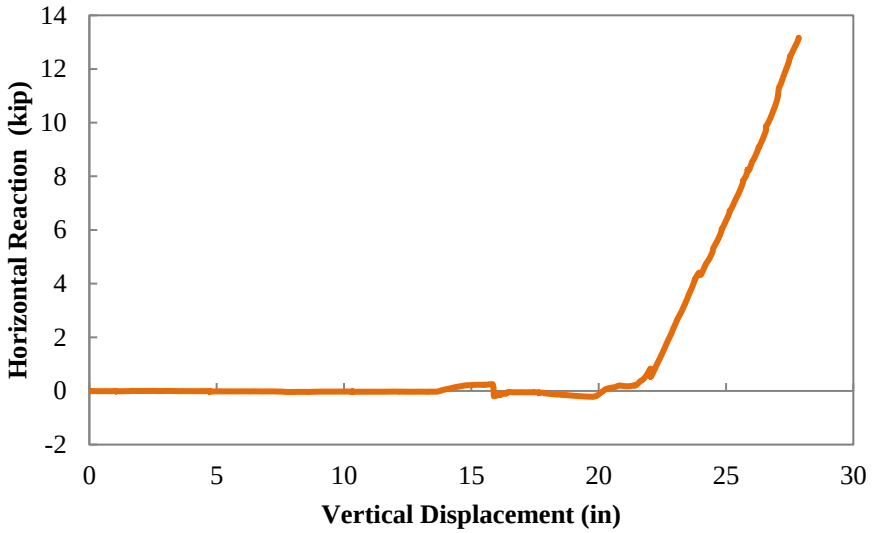

Figure D.21: TR-LC horizontal reaction versus CC-PT vertical displacement (Specimen 2)

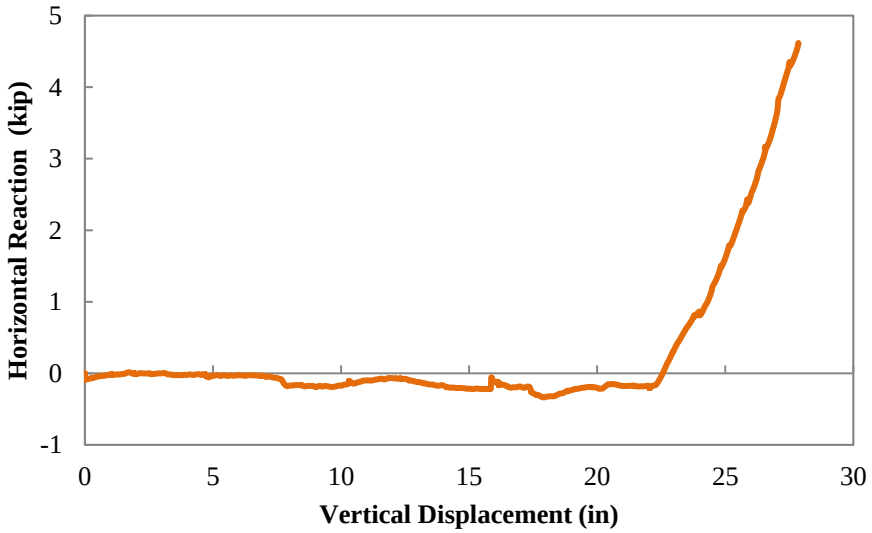

Figure D.22: BL-LC horizontal reaction versus CC-PT vertical displacement (Specimen 2)

D.2.2 Measured Strain Response

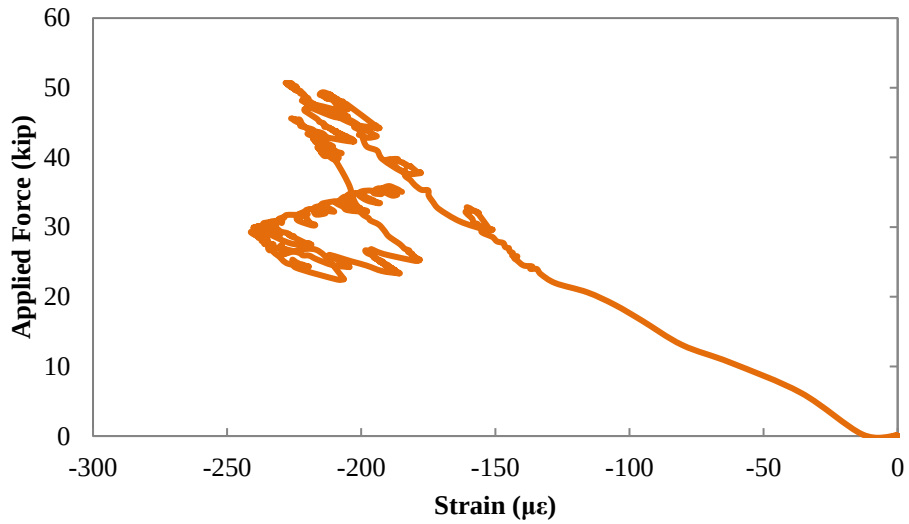

Figure D.23: Force-strain response of top reinforcing bar T3 at section CC (Specimen 2)

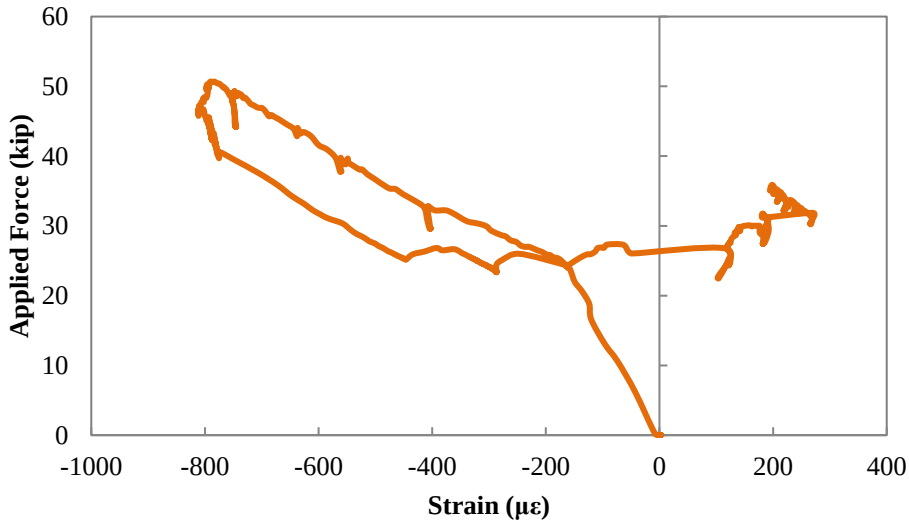

Figure D.24: Force-strain response of top reinforcing bar B3’ at section MC (Specimen 2)

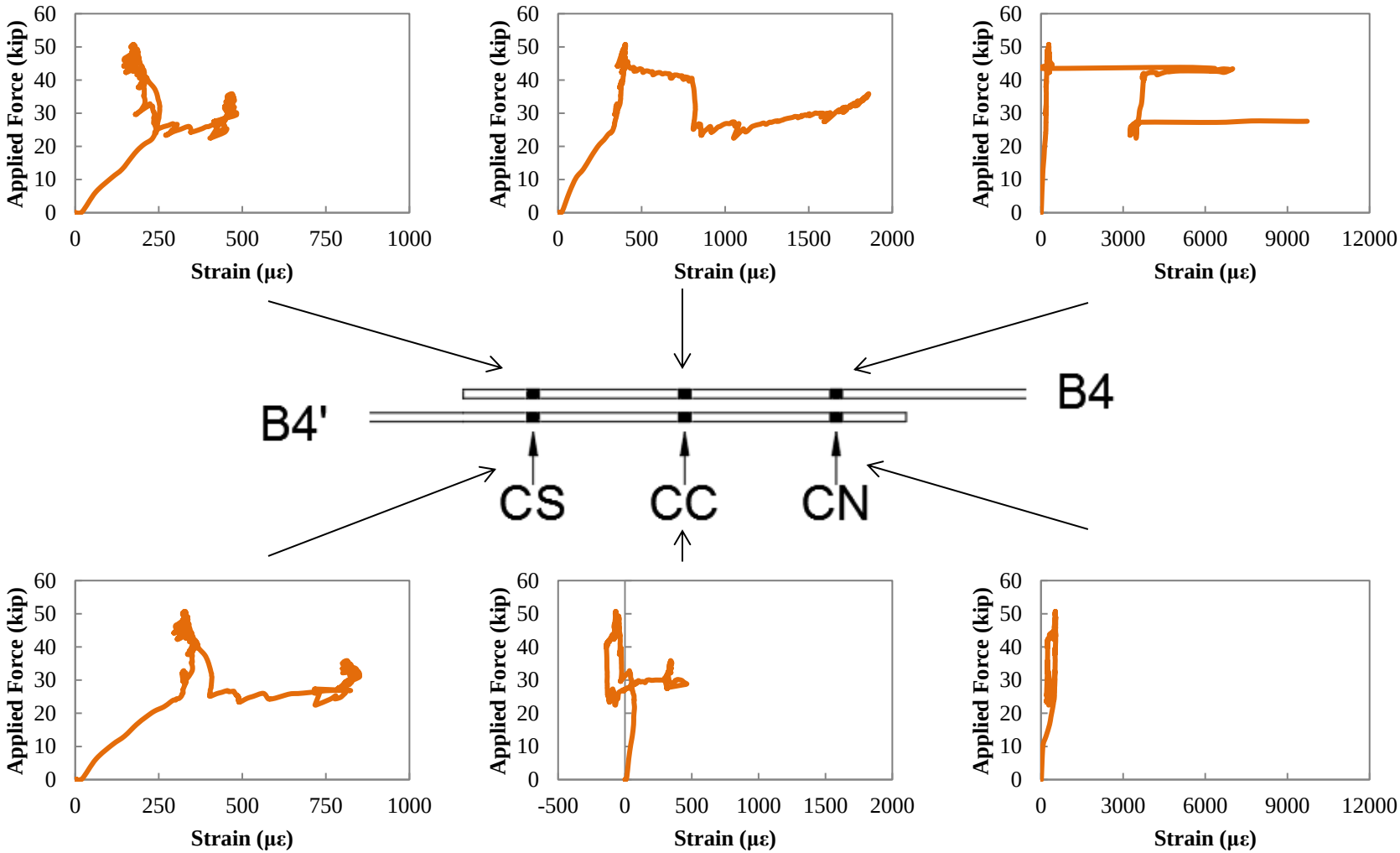

Figure D.25: Force-strain response of bottom reinforcing bars at center column splice zone (Specimen 2)

D.3 Specimen 3 Results

D.3.1 Measured Force-Displacement Response

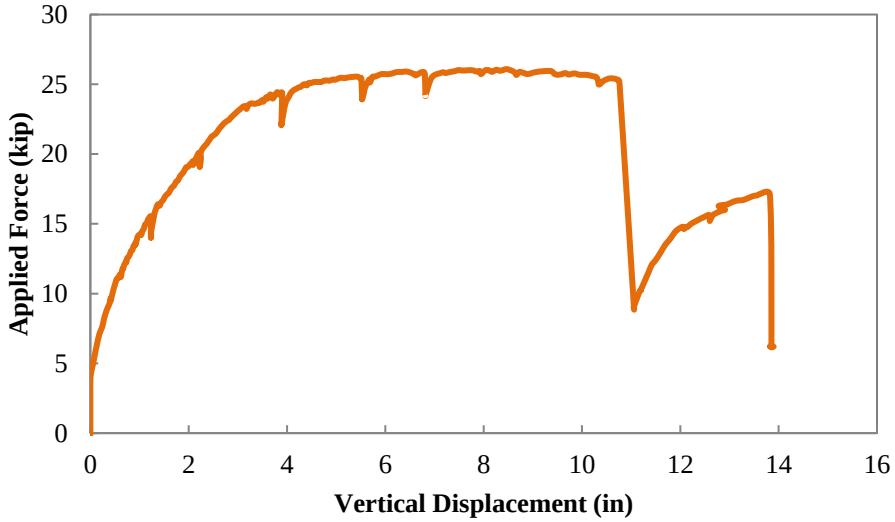

Figure D.26: E-LC force versus CC-PT vertical displacement (Specimen 3)

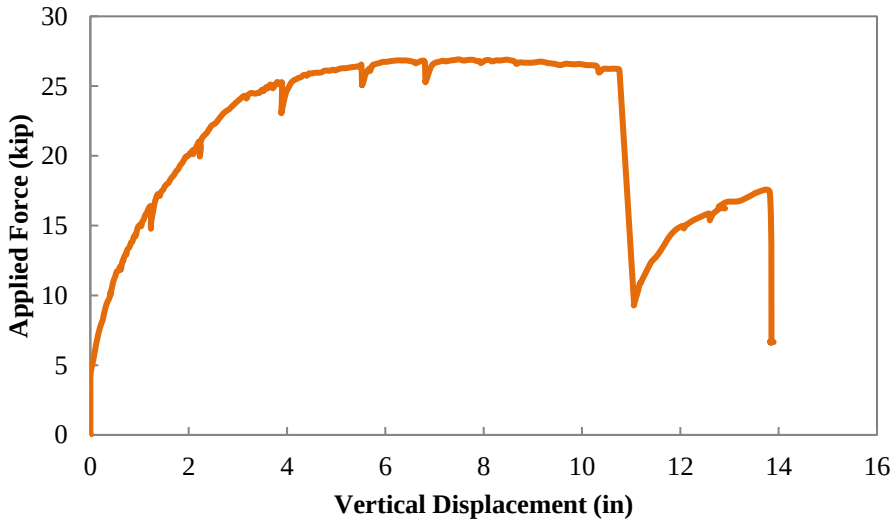

Figure D.27: W-LC force versus CC-PT vertical displacement (Specimen 3)

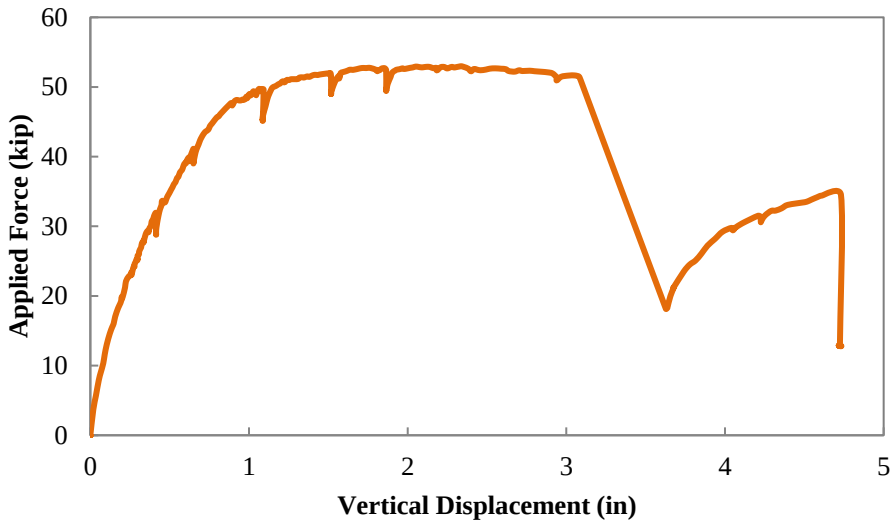

Figure D.28: Force versus NN-PT vertical displacement (Specimen 3)

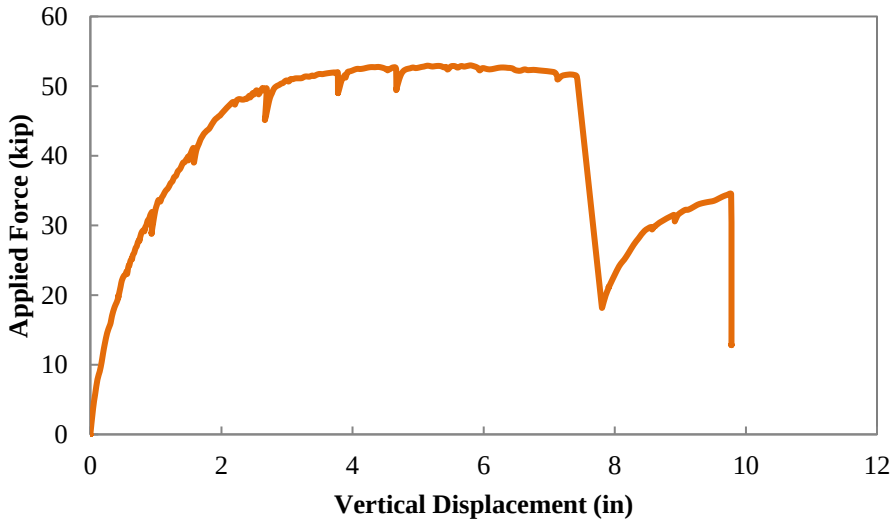

Figure D.29: Force versus NC-PT vertical displacement (Specimen 3)

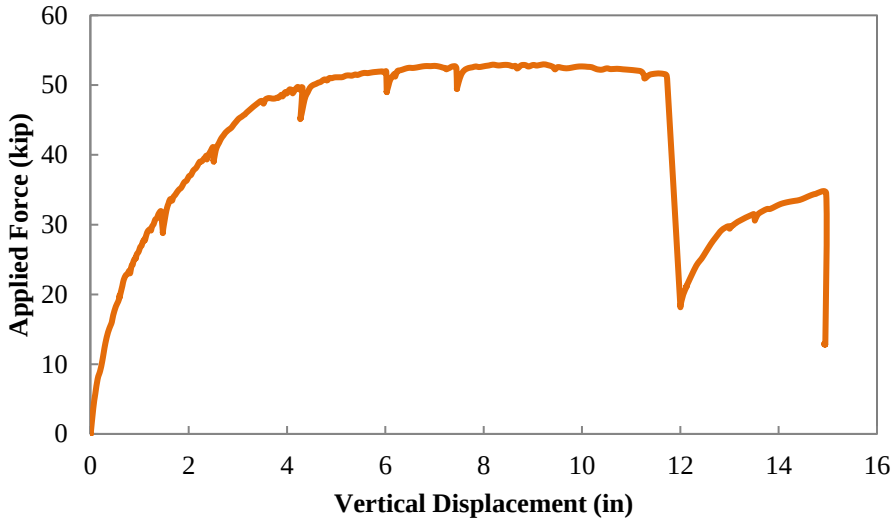

Figure D.30: Force versus NS-PT vertical displacement (Specimen 3)

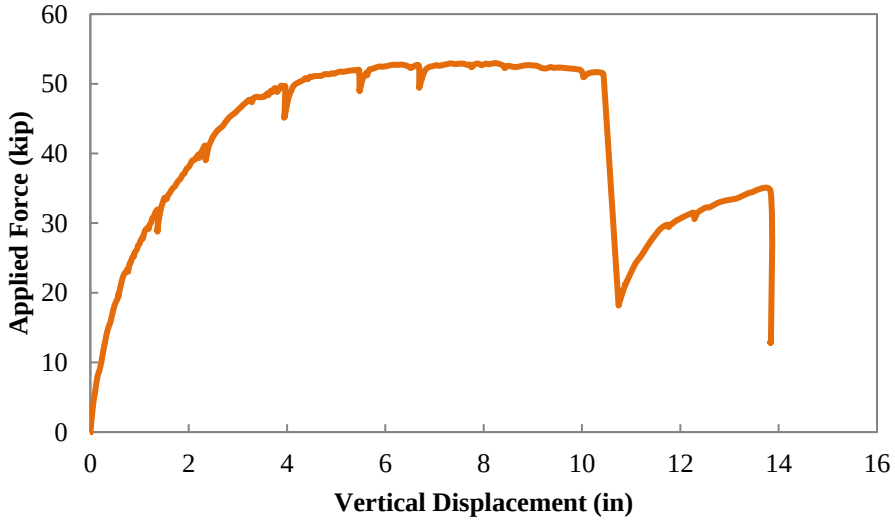

Figure D.31: Force versus SN-PT vertical displacement (Specimen 3)

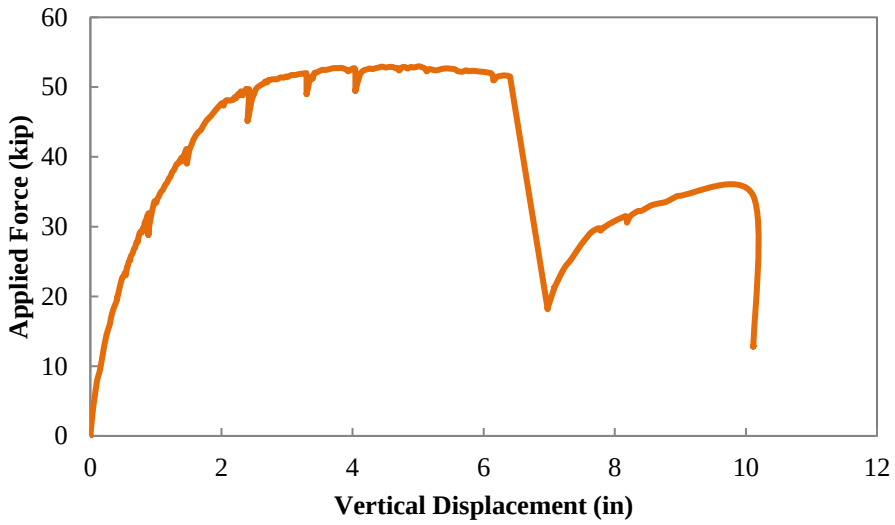

Figure D.32: Force versus SC-PT vertical displacement (Specimen 3)

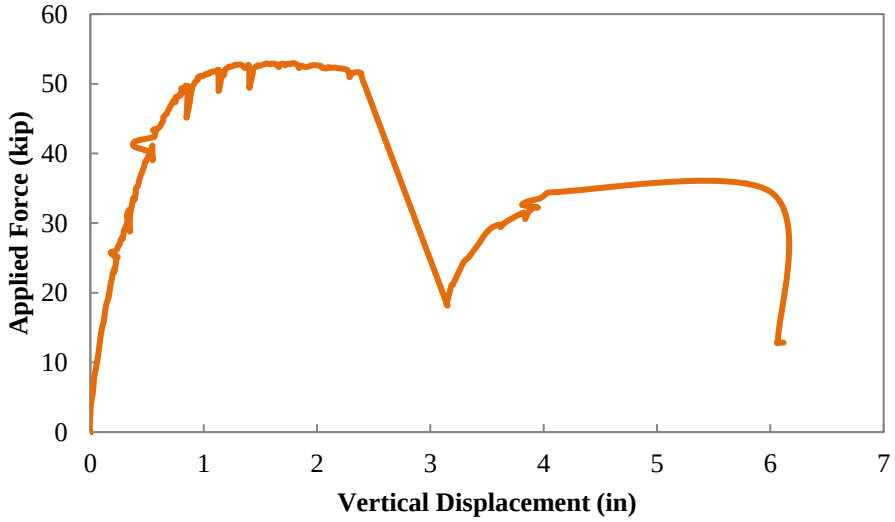

Figure D.33: Force versus SS-PT vertical displacement (Specimen 3)

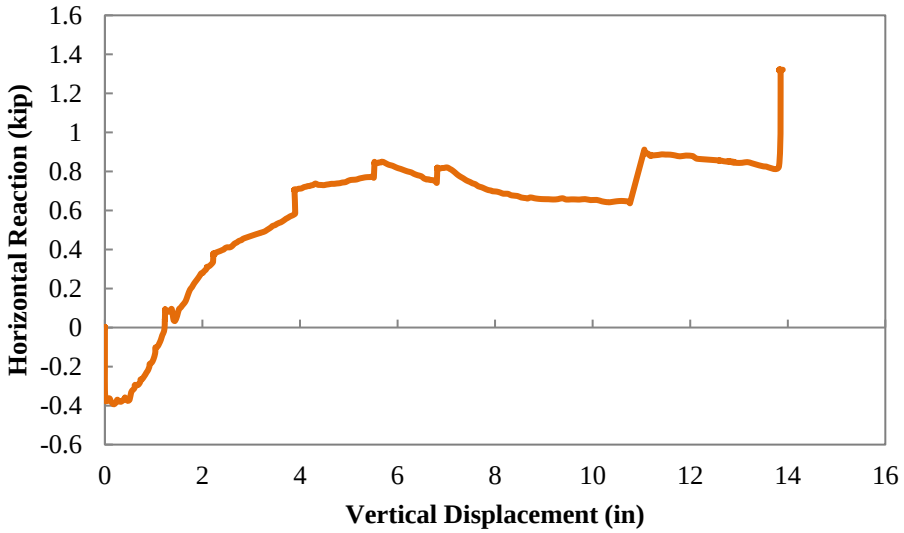

Figure D.34: TL-LC horizontal reaction versus CC-PT vertical displacement (Specimen 3)

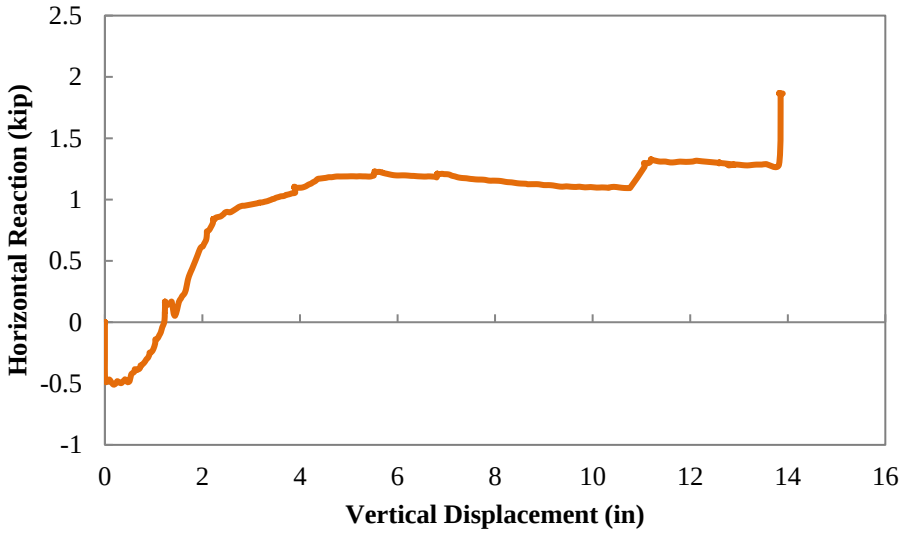

Figure D.35: TR-LC horizontal reaction versus CC-PT vertical displacement (Specimen 3)

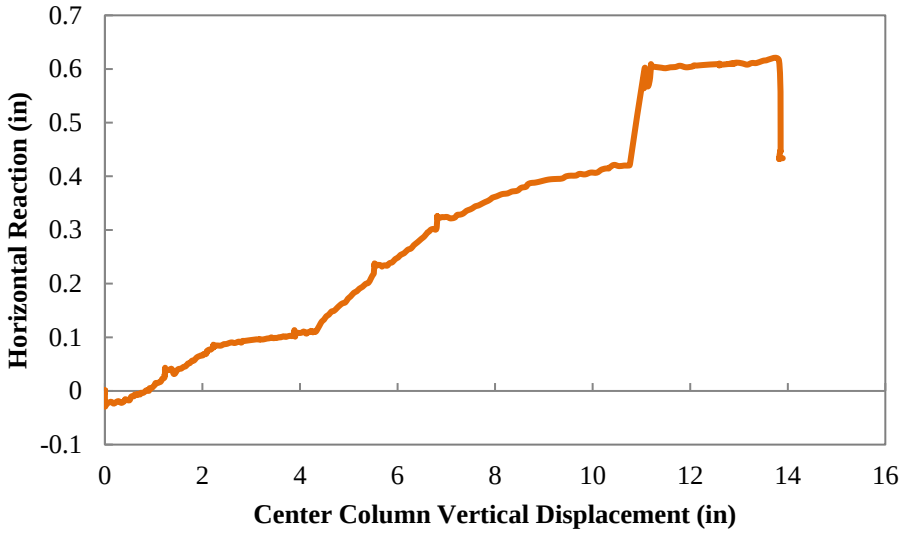

Figure D.36: BL-LC horizontal reaction versus CC-PT vertical displacement (Specimen 3)

D.3.2 Measured Strain Response

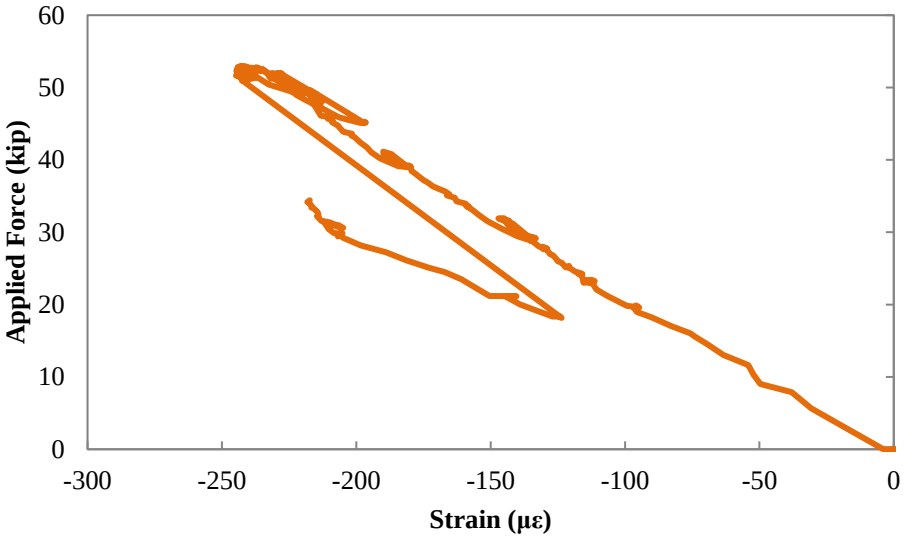

Figure D.37: Force-strain response of top reinforcing bar T3 at section CC (Specimen 3)

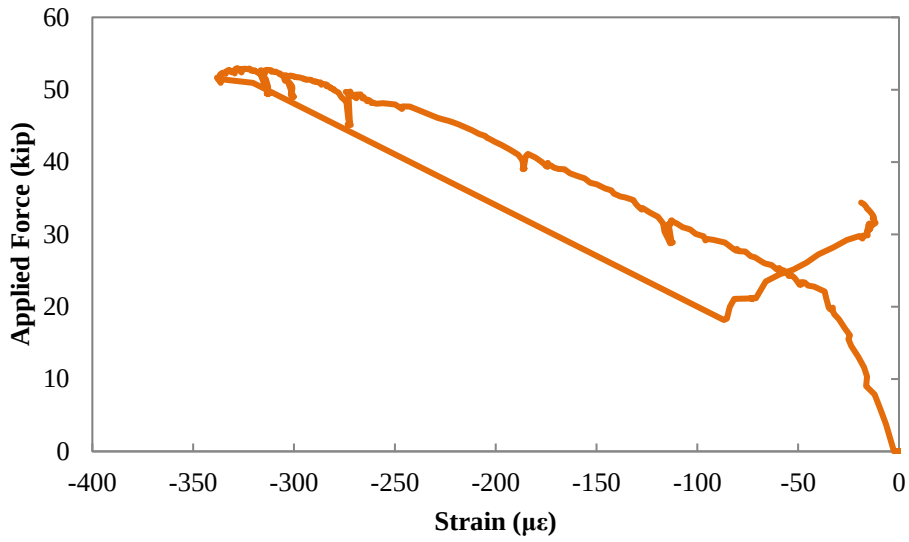

Figure D.38: Force-strain response of top reinforcing bar B3’ at section MC (Specimen 3)

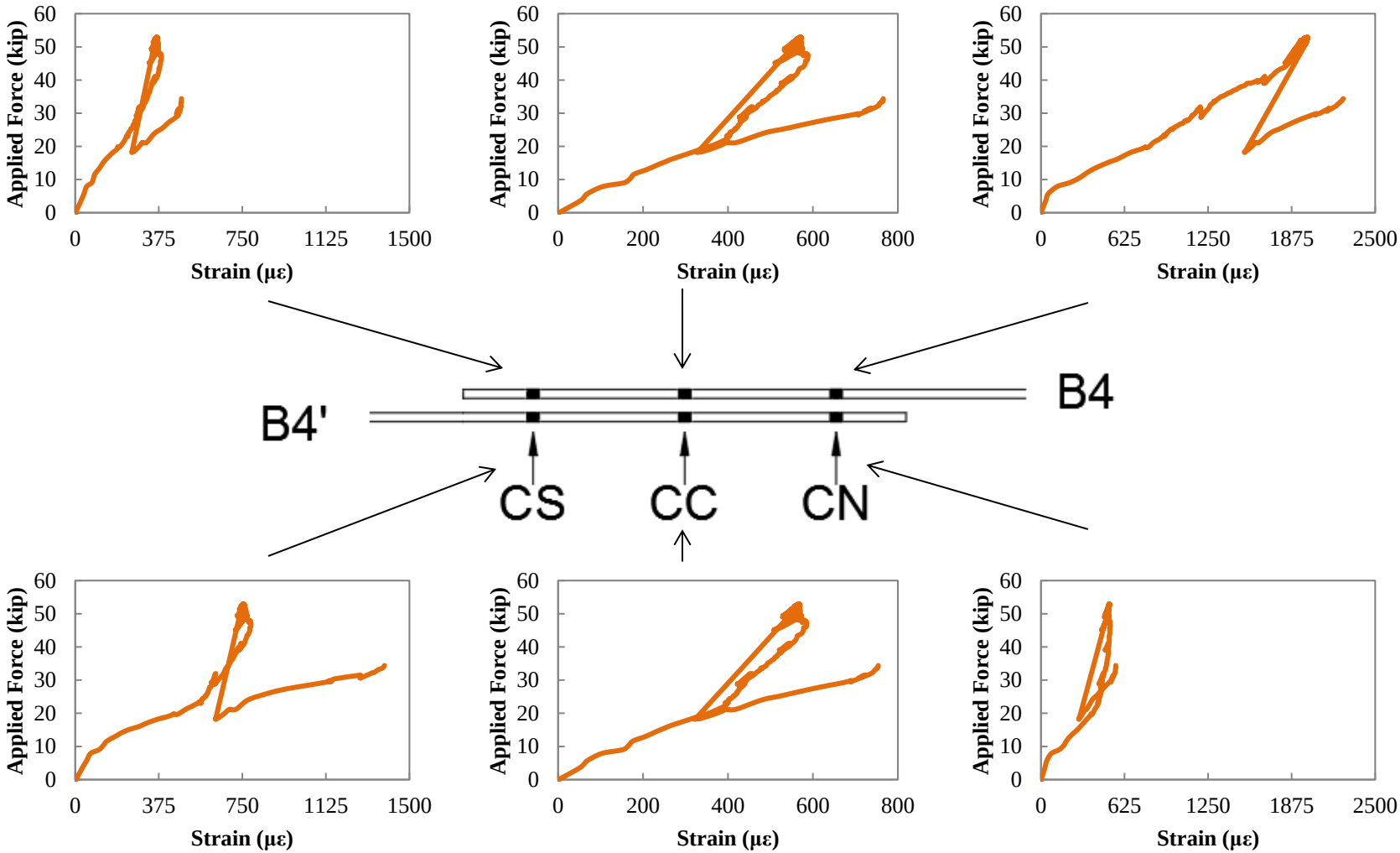

Figure D.39: Force-strain response of bottom reinforcing bars at center column splice zone (Specimen 3)

APPENDIX E

MEASURED MATERIAL PROPERTIES

This appendix presents the properties of the materials used to fabricate the specimens. Concrete cylinders and steel coupons were tested in order to determine the material properties. Measured parameters were used to define the material models described in Chapter 7.

E.1 Concrete

Following standard ASTM procedures as specified in ASTM C-31 (ASTM, 2018), ten concrete cylinders, seven with 4 in. diameter by 8 in. in height, and three with 6 in. diameter by 12 in. in height, were fabricated using the same mix design. The concrete cylinders were removed from their molds at the time the specimen beams were removed from the forms to simulate concrete to similar curing conditions. The concrete cylinders and specimen were cured in the same laboratory under ambient conditions.

E.1.1 Specimen 1

In order to star the lifting process of the specimen, two cylinders were tested in compression 21 days after casting to evaluate strength. Six cylinders were tested in compression the day after the test (108 days after the casting). Also, split-cylinder tests were conducted for two cylinders. The results are summarized in Table E.1 and E.2.

Table E.1: Measured compression properties of concrete for Specimen 1

Test	Age (days)	Cylinder Dim.	f'_c (psi)	Avg. f'_c (psi)
1	21	4" x 8"	5330	5613
2	21	4" x 8"	5895	
1	108	4" x 8"	5150	5230
2	108	4" x 8"	5516	
3	108	6" x 12"	6071	
4	108	4" x 8"	4477	
5	108	4" x 8"	5081	
6	108	4" x 8"	5086	

Table E.2: Measured tensile properties of concrete for Specimen 1

Test	Age (days)	Cylinder Dim.	f_t (psi)	Avg. f_t (psi)
1	108	6" x 12"	351	360
2	108	6" x 12"	368	

E.1.2 Specimen 2

In order to star the lifting process of the specimen, four cylinders were tested in compression, two cylinders 26 days after casting and two cylinders 30 days after casting to evaluate strength. Four cylinders were tested in compression the day after the test (50 days after the casting). Also, split-cylinder tests were conducted for two cylinders the day after the tests. The results are summarized in Table E.3 and E.4.

Table E.3: Measured compression properties of concrete for Specimen 2

Test	Age (days)	Cylinder Dim.	*f'c* (psi)	Avg. *f'c* (psi)
1	26	4" x 8"	3681	3792
2	26	4" x 8"	3903	
1	30	4" x 8"	4027	3930
2	30	6" x 12"	3833	
1	50	4" x 8"	4357	4137
2	50	4" x 8"	3978	
3	50	4" x 8"	3909	
4	50	4" x 8"	4303	

Table E.4: Measured tensile properties of concrete for Specimen 2

Test	Age (days)	Cylinder Dim.	*ft* (psi)	Avg. *ft* (psi)
1	50	6" x 12"	389	361
2	50	6" x 12"	332	

E.1.3 Specimen 3

In order to star the lifting process of the specimen, six cylinders were tested in compression; two cylinders 10 days after casting, two cylinders 14 days after casting and two cylinders 18 days after casting to evaluate strength. Two cylinders were tested in compression the day after the test (22 days after the casting). Also, split-cylinder tests were conducted for two cylinders the day after the tests. The results are summarized in Table E.5 and E.6.

Table E.5: Measured compression properties of concrete for Specimen 3

Test	Age (days)	Cylinder Dim.	*f'c* (psi)	Avg. *f'c* (psi)
1	10	4" x 8"	3828	3915
2	10	4" x 8"	4001	
1	14	4" x 8"	4386	4352
2	14	4" x 8"	4317	
1	18	4" x 8"	4588	4552
2	18	4" x 8"	4516	
1	22	4" x 8"	4992	5076
2	22	6" x 12"	5159	

Table E.6: Measured tensile properties of concrete for Specimen 3

Test	Age (days)	Cylinder Dim.	*ft* (psi)	Avg. *ft* (psi)
1	22	6" x 12"	500	458
2	22	6" x 12"	416	

E.2 Reinforcing Steel

Steel coupons were tested in tension for the longitudinal reinforcing bars used in the beams. Stress-strain curves were determined for the beams longitudinal reinforcing bars because these were the only bars expected to yield during the tests. The specimens were fabricated using reinforcing bars from the same heat.

The steel coupons consisted in two deformed bars #6 (bottom reinforcing bars) and bars and two deformed bars #7 (top reinforcing bars). Figure E.1 and E.2 show the stress-strain curves for the longitudinal reinforcing bars #6 and #7 respectively. The results are summarized in Table E.7.

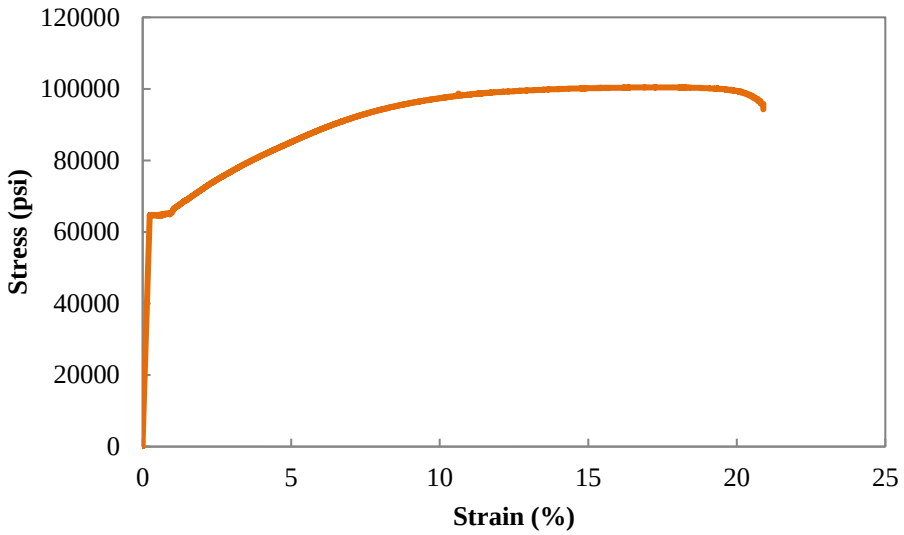

a)

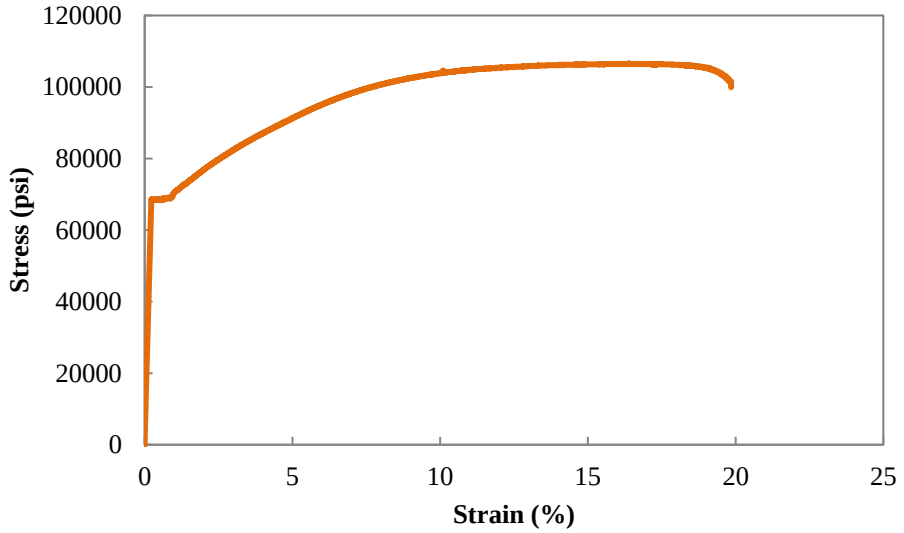

b)

Figure E.1: Stress-strain curves for longitudinal reinforcing bars #6 for a) test 1 and b) test 2

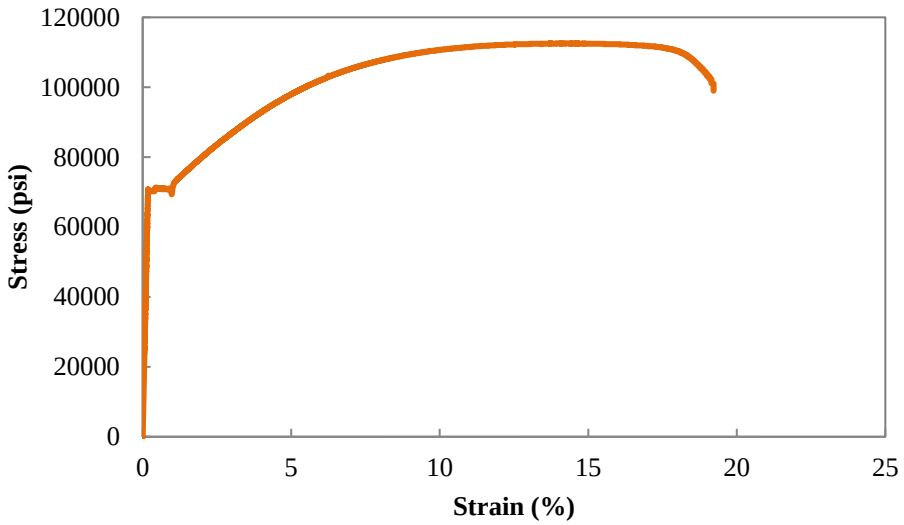

a)

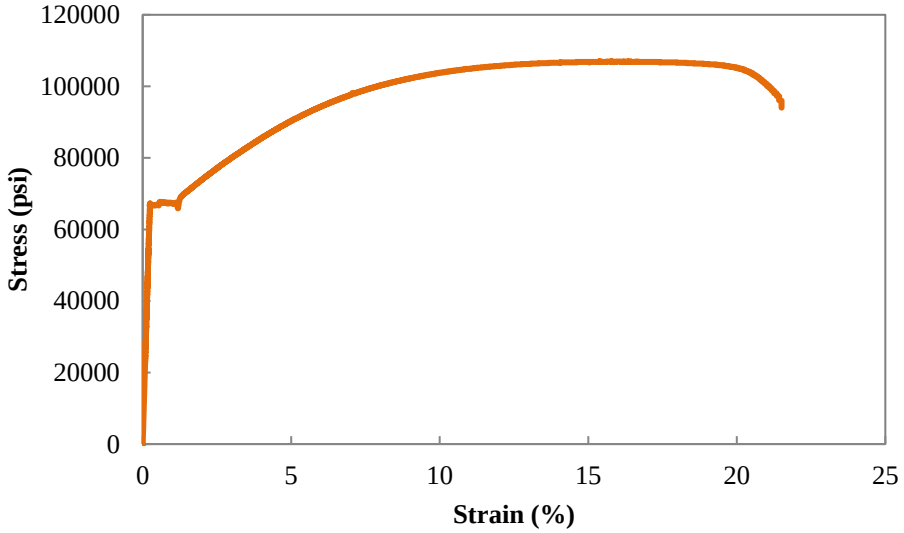

b)

Figure E.2: Stress-strain curves for longitudinal reinforcing bars #7 for a) test 1 and b) test 2

Table E.7: Measured tensile properties of reinforcing bars

Bar Size	f_y (ksi)	Yield Strain (%)	f_u (ksi)	Rupture Strain (%)
6	67	0.25	104	21
7	69	0.21	110	21

APPENDIX F

PLASTIC HINGES

This appendix describes the properties and location of the plastic hinges used to find the applied force and the theoretical shear values corresponding to yield and plastic bending moment for the Specimen 1, 2 and 3 presented in Chapter 6. Also, this appendix describes the properties and location of the plastic hinges modeled in the Specimen 3 and prototype building model presented in chapter 7. The moment–curvature relationship for plastic hinges at the beam in critical sections for the Specimen 3 and the prototype building are presented.

For the specimen model, plastic hinges were defined as the zones with cracks concentration and measured directly on the specimens. Also, center of the crack concentration zones was localized in relation with the face of the columns as shown in Chapter 6. In the prototype building model, six plastic hinges were inserted at each beam adjacent and above to the removed column. Two plastic hinges were inserted at each beam end and four along the beam. Figure F.1 shows the location of the plastic hinges in the Specimen and Figure F.2 and F.3 show the location of the plastic hinges for the interior and corner perimeter column condition of the prototype building model respectively. Also, Figure F.4 to F.13 show the moment–curvature relationship for each section.

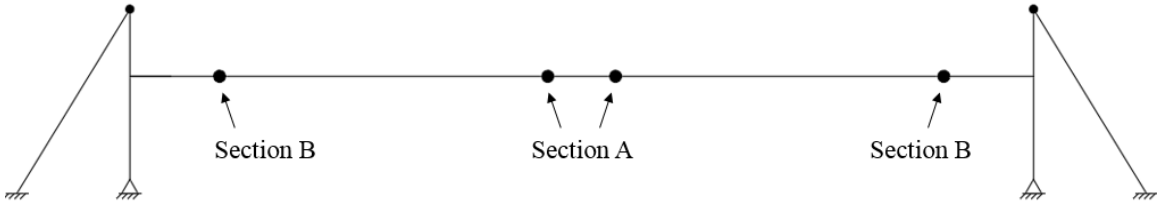

a)

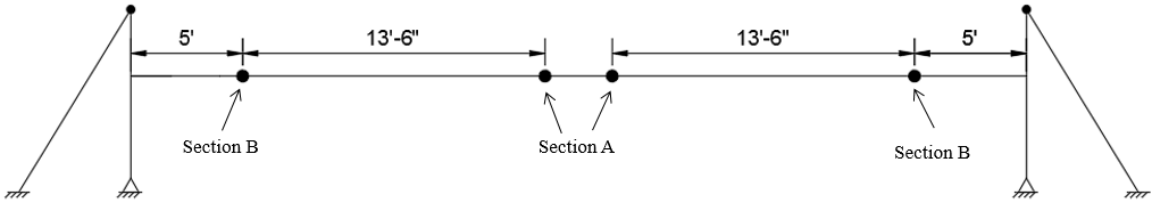

b)

Figure F.1: Plastic hinge details of a) the model presented in Chapter 6 and b) Chapter 7

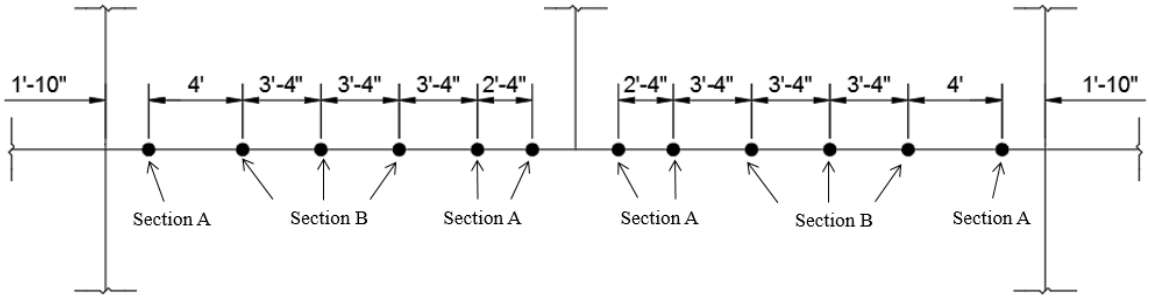

a)

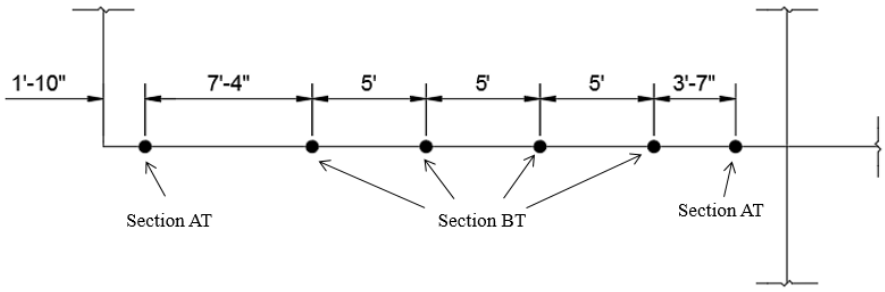

b)

Figure F.2: Plastic hinges location of the beam adjacent to the removed interior perimeter column in the a) in-plane direction and, b) perpendicular direction in the prototype building model

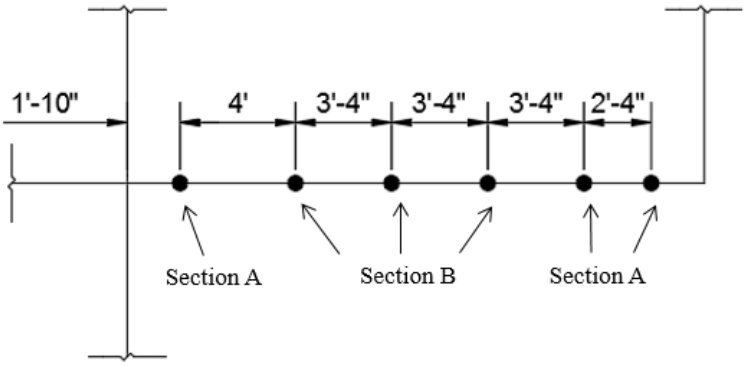

a)

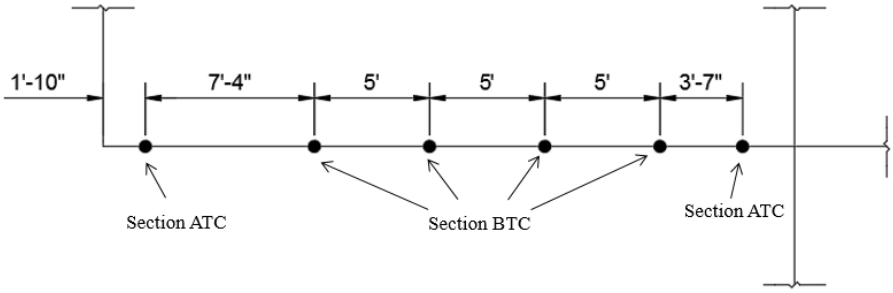

b)

Figure F.3: Plastic hinge location of the beam adjacent to the removed corner perimeter column in the a) in-plane direction and, b) perpendicular direction in the prototype building model

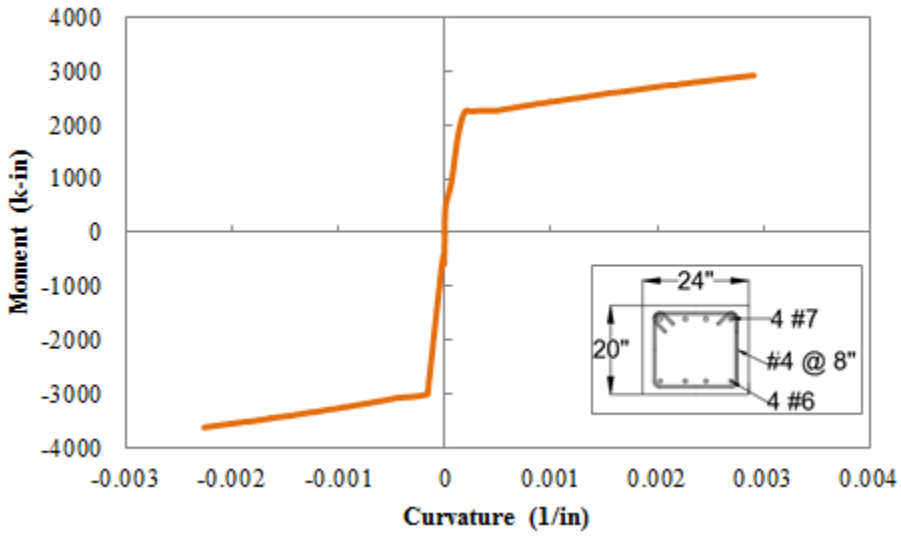

Figure F.4: Moment–curvature relationship of the Specimen 1 Section A

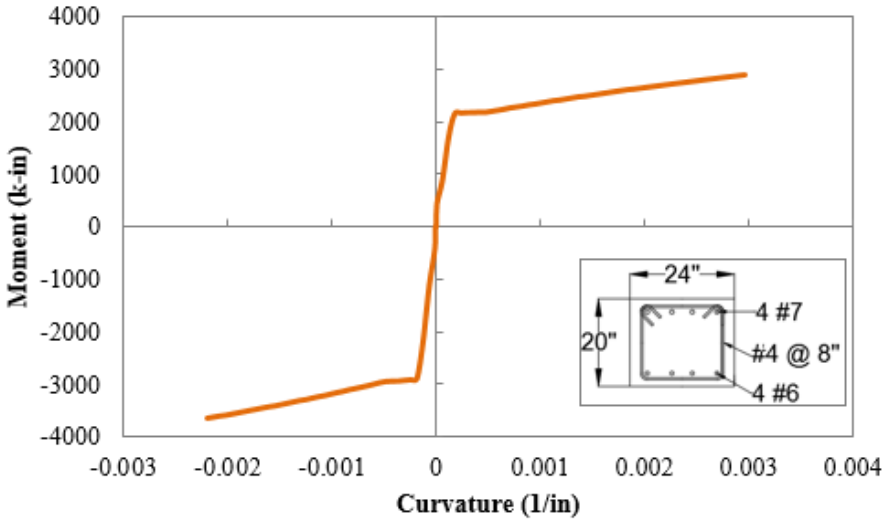

Figure F.5: Moment–curvature relationship of the Specimen 2 Section A

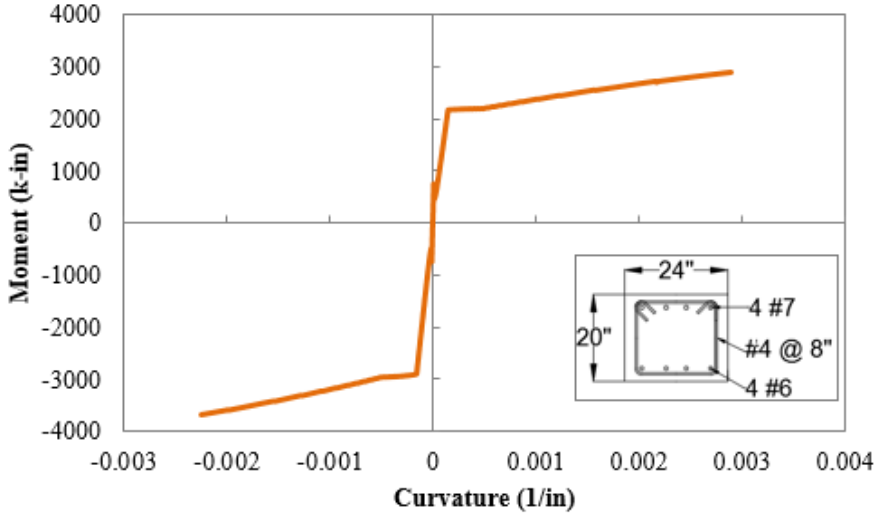

Figure F.6: Moment–curvature relationship of the Specimen 3 Section A

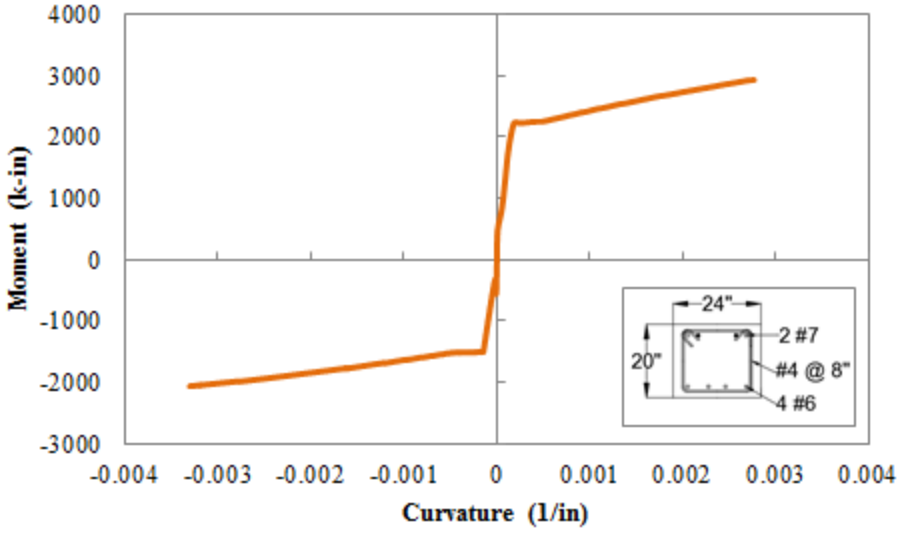

Figure F.7: Moment–curvature relationship of the Specimen 1 Section B

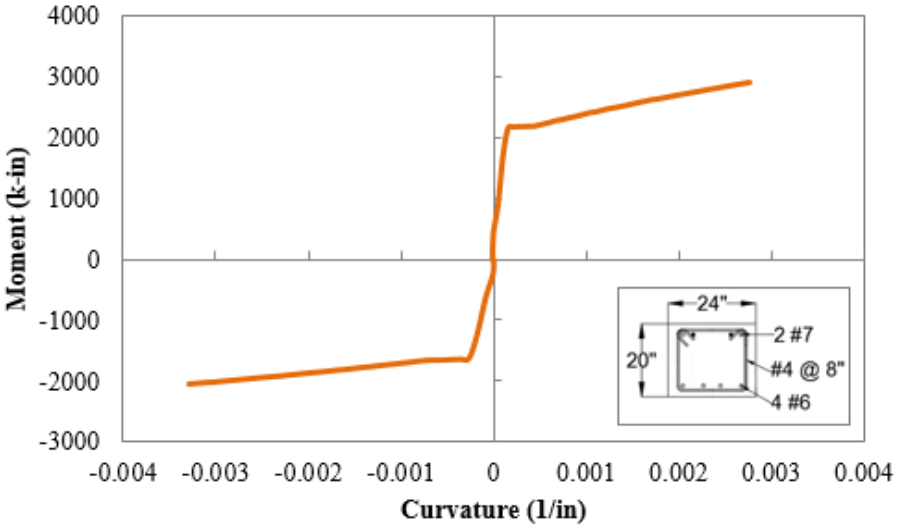

Figure F.8: Moment–curvature relationship of the Specimen 2 Section B

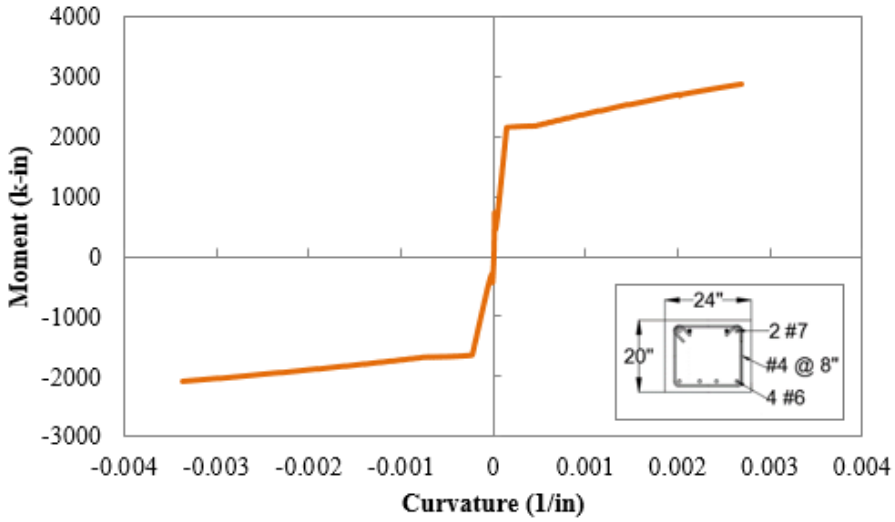

Figure F.9: Moment–curvature relationship of the Specimen 3 Section B

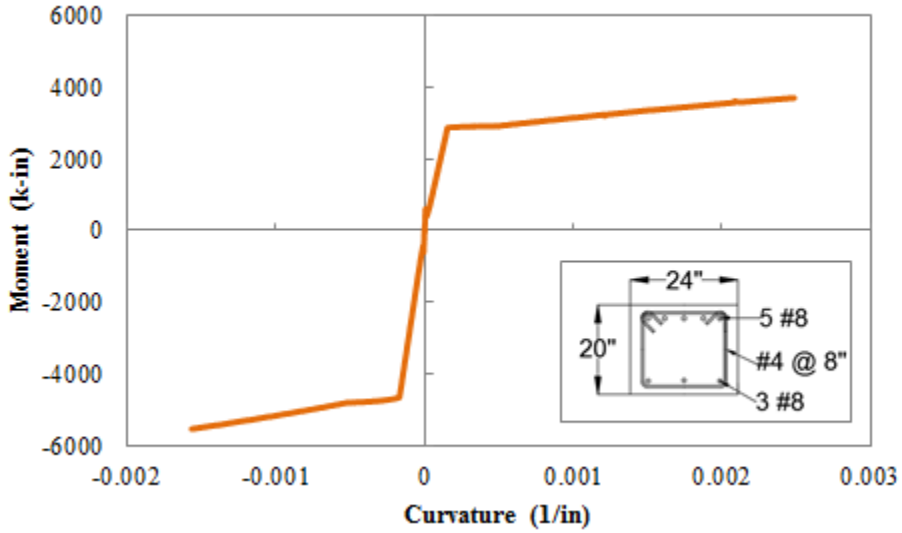

Figure F.10: Moment–curvature relationship of the Section AT

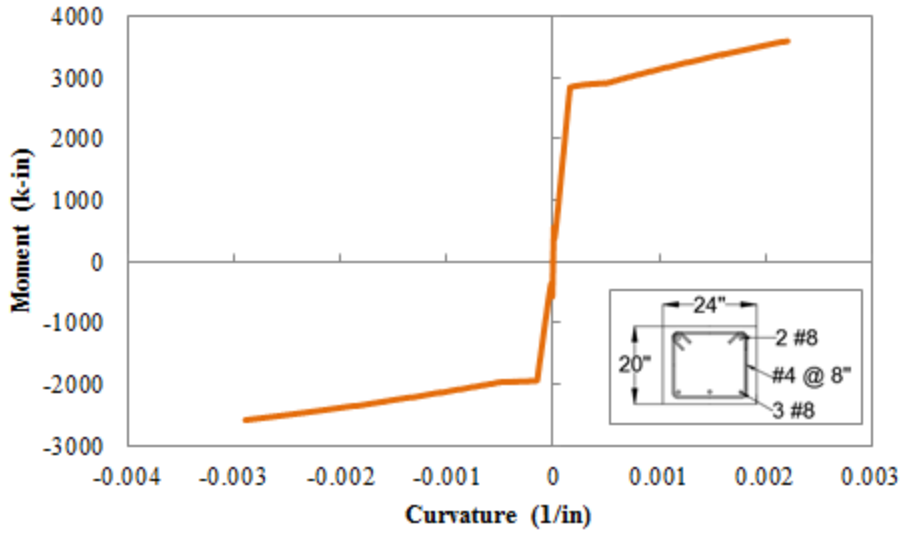

Figure F.11: Moment–curvature relationship of the Section BT

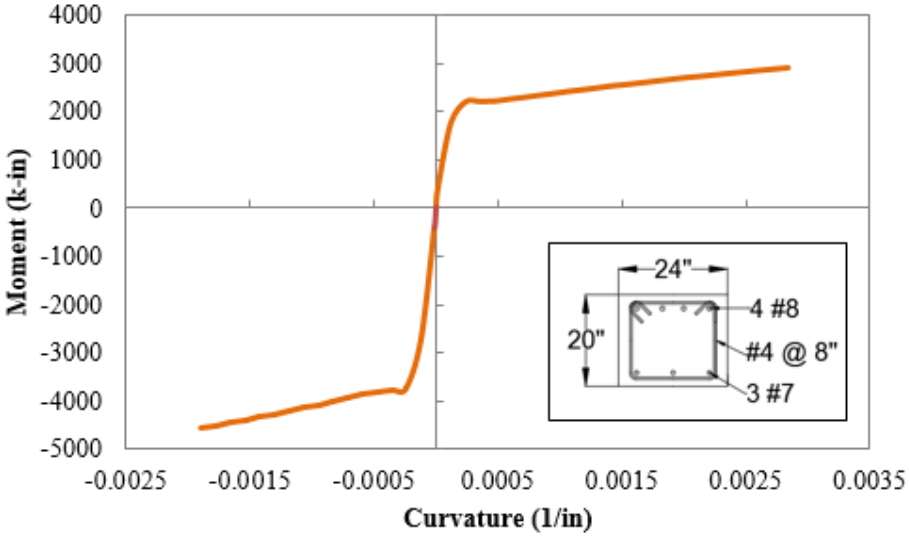

Figure F.12: Moment–curvature relationship of the Section ATC

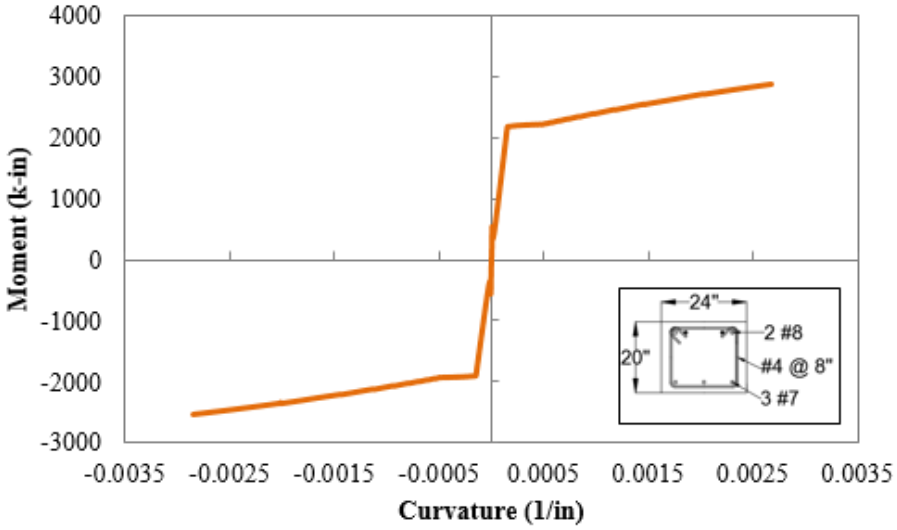

Figure F.13: Moment–curvature relationship of the Section BTC

APPENDIX G

CONFINED MOMENT-CURVATURE RELATIONSHIP DETAILS

This appendix describes the uniaxial stress-strain behavior of the concrete model used in the moment-curvature response curves for beam hinges constructed using confined concrete. Also, the moment–curvature relationship for plastic hinges at the beam in critical sections for the corner perimeter column removal condition of the prototype building are presented.

G.1 Concrete

The uniaxial stress-strain behavior of concrete in compression was modeled using a curve proposed by Mander et al. (1984). In this model, the compression portion of the confined stress-strain curve consists of an exponential function. The compressive strength and the ultimate strain of the confined concrete are based on the confinement of the concrete. The maximum compressive stress and the corresponding strain are defined as f'_{cc}, and ε_{cc}, respectively. Based on the first stirrup fracture, the ultimate concrete strain capacity is defined as $\varepsilon_{cu.}$ Also, modulus of elasticity of the concrete is defined as E_c. The tangent modulus of elasticity of the concrete is estimated to 57000√f 'c (psi). The tensile stress-strain behavior consists of a linear relation with slope equal to (E_c). The tensile strength is taken as $7.5\sqrt{f'_c}$. Figure G.1 shows stress-strain diagram and the equations used to describe the behavior of confined concrete in compression and tension.

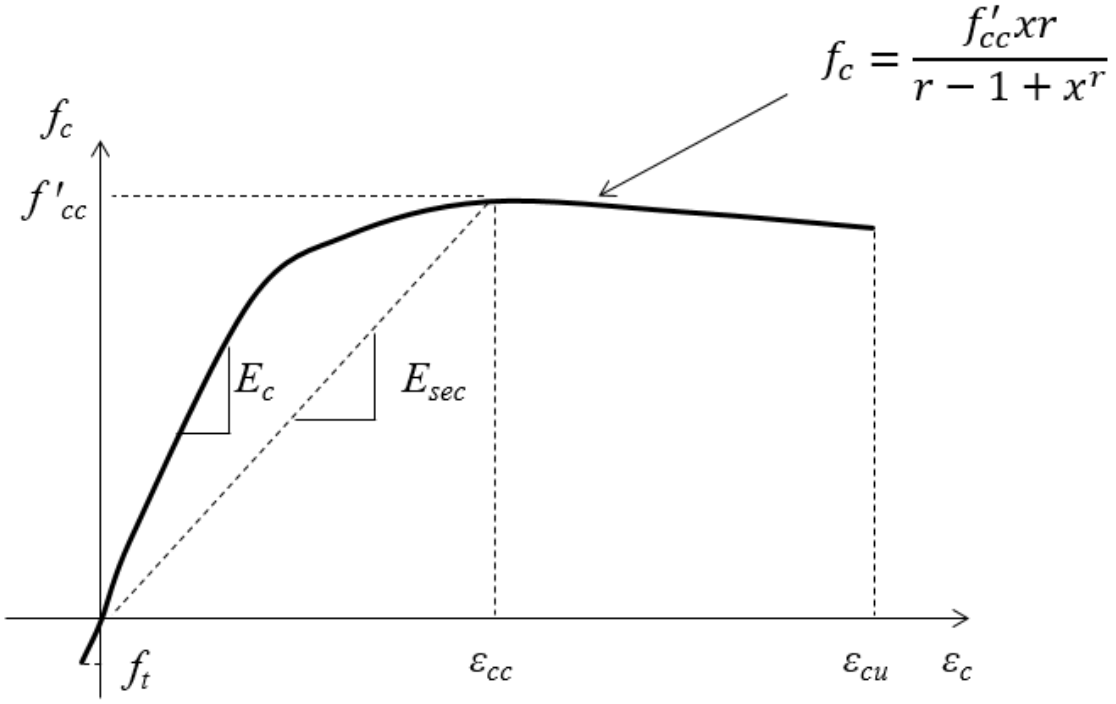

Figure G.1: Mander et al. (1984) confined concrete stress-strain curve

$$\varepsilon_{cc} = \left\{5\left(\frac{f'_{cc}}{f'_c} - 1\right) + 1\right\}\varepsilon_{co} \quad \text{G.1}$$

$$f'_{cc} = f'_c\left(2.254\sqrt{1 + \frac{7.94f'_L}{f'_c}} - 2\frac{f'_L}{f'_c} - 1.254\right) \quad \text{G.2}$$

$$f'_L = K_e f_L \quad \text{G.3}$$

$$K_e = A_e / A_{cc} \quad \text{G.4}$$

$$A_e = \left(b_c d_c - \sum_{i-1}^{n}\frac{(w'_i)^2}{6}\right)\left(1 - \frac{s'}{2b_c}\right)\left(1 - \frac{s'}{2d_c}\right) \quad \text{G.5}$$

$$A_{cc} = b_c d_c \quad \text{G.6}$$

$$f_L = \rho f_{yh} \quad \text{G.7}$$

$$\rho = A_s / s d_c \quad \text{G.8}$$

$$r = E/(E - E_{sec}) \quad \text{G.9}$$

$$E_{sec} = f'_{cc}/\varepsilon_{cc} \quad \text{G.10}$$

$$x = \varepsilon_c/\varepsilon_{cc} \quad \text{G.11}$$

where:

A_e = concrete area that is effectively confined,

A_{cc} = concrete core area excluding longitudinal bars,

A_s = area of rectangular hoop legs,

b_c = centerline to centerline distance between rectangular perimeter hoop legs that extend in the y-direction,

d_c = Centerline to centerline distance between rectangular perimeter hoop legs that extend in the x-direction,

E_{sec} = secant modulus of elasticity of the concrete

f_L = lateral pressure on confined concrete provided by the confinement steel,

f'_c = average compressive strength of the concrete,

f'_L = effective lateral pressure on confined concrete provided by the confinement steel,

K_e = coefficient measuring the effectiveness of the confinement steel,

s = centerline to centerline longitudinal distance between hoops or spirals,

s' = clear longitudinal distance between hoops or spirals,

w' = clear transverse distance between adjacent longitudinal bars with cross ties,

ε_{co} = strain corresponding to the maximum compressive stress of the unconfined concrete,

and

ρ = Steel ratio for rectangular hoop legs.

Compressive tests of cylinders and split-cylinder tests were conducted to define the concrete tensile and compressive strength for Specimen 1, 2 and 3. Due the Specimen 3 results show the smallest rotation for the beam end near the widened crack, the Specimen 3 concrete test results were used in the analysis. The average compressive strength ($f'c$) of the concrete measured at the time of testing was equal to 4137 psi obtained from testing four 4 in. by 8 in. cylinder and one 6 in. by 12 in. cylinder. Also, the average tensile strength (f_t) of the concrete measured at the time of testing was equal to 361 psi obtained from testing two 6 in. by 12 in. cylinder. Maximum compressive strain ε_{cu}, were assumed to be equal to 0.009, because these values could not be obtained experimentally. Details of individual cylinder tests for each specimen are summarized in Appendix E.

G.2 Moment–curvature relationship

Moment-curvature response curves for beam hinges constructed using confined concrete stress-strain curve for concrete for the corner perimeter column removal condition of the prototype building are presented in this section. In the curve, ultimate condition represents fracture of the longitudinal bar at strain equal to 0.21. In order to input the moment–curvature relationship into Sap2000 (SAP2000 Version 17.0), an elastic-perfectly plastic simplified moment–curvature relationship of a plastic hinge was used in the analysis as discussed in Section 7.2.2. In order to estimate hinge rotation using the relationship between curvature and rotation, a plastic hinge length of 10 in. was used. The plastic hinge lengths were measured directly at the Specimen 3. Figures G.2 to G.5 show the moment–curvature relationship for each section.

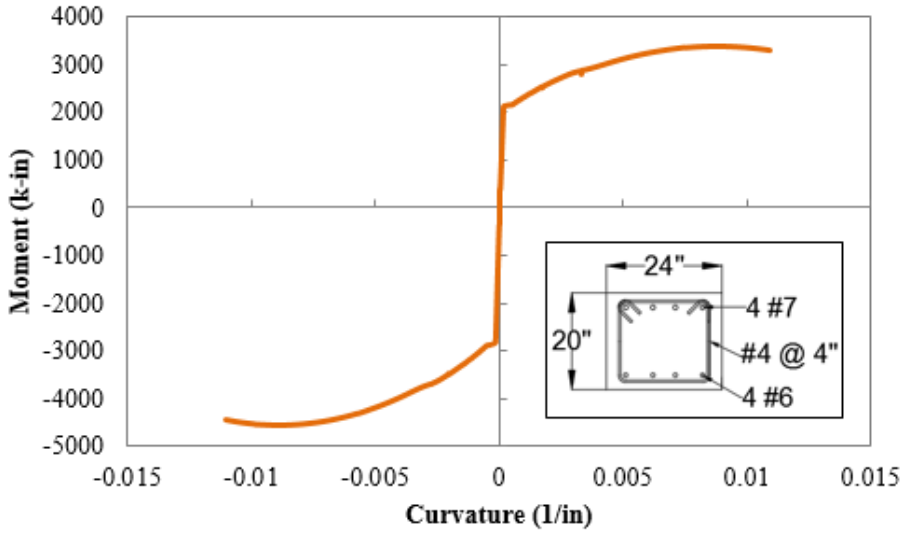

Figure G.2: Moment–curvature relationship of the Section A

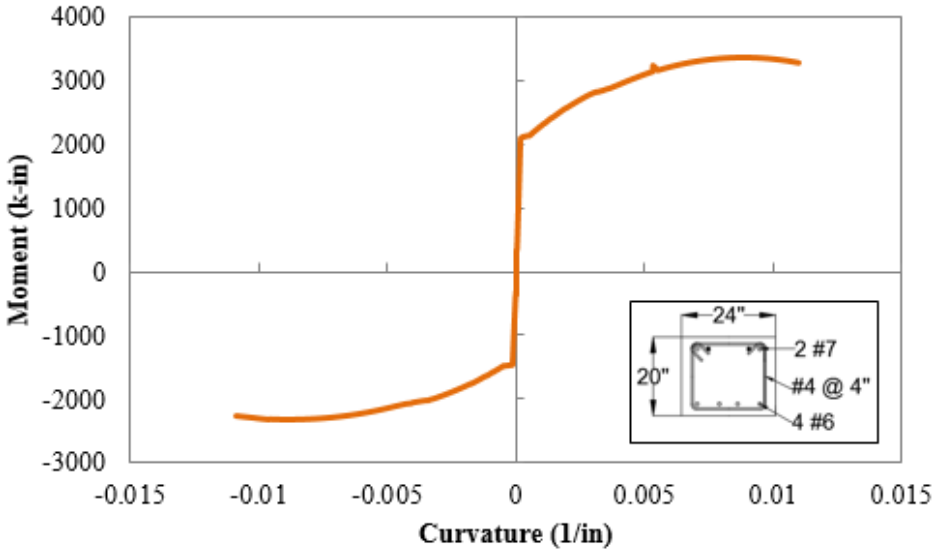

Figure G.3: Moment–curvature relationship of the Section B

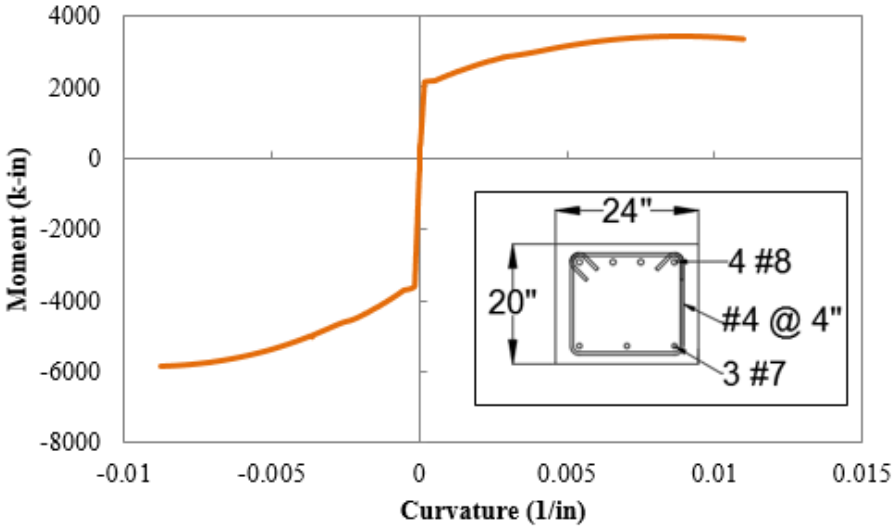

Figure G.4: Moment–curvature relationship of the Section ATC

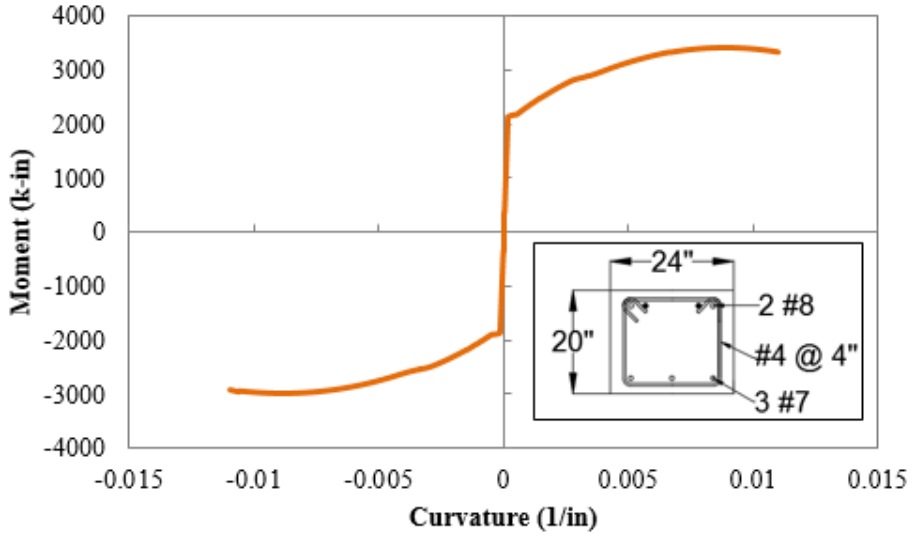

Figure G.5: Moment–curvature relationship of the Section BTC

BIBLIOGRAPHY

Alogla, K., Weekes, L., & Augusthus-Nelson, L. (2016). A new mitigation scheme to resist progressive collapse of RC structures. Construction and Building Materials, 125, 533–545. http://doi.org/10.1016/j.conbuildmat.2016.08.084

American Concrete Institute (ACI). (2014). *Building code requirements for structural concrete* (ACI 318-14), ACI, Farmington Hills, MI.

American Society of Civil Engineers (ASCE). (2010). *Minimum design loads for buildings and other structures* (SEI/ASCE 7-10), ASCE, Reston, Va.

American Society of Civil Engineers (ASCE). (2013). *Seismic Evaluation and Retrofit of Existing Buildings* (SEI/ASCE 41-13), ASCE, Reston, Va.

Dat, P. X., & Hai, T. K. (2013). Membrane actions of RC slabs in mitigating progressive collapse of building structures. *Engineering Structures*, *55*, 107–115. http://doi.org/10.1016/j.engstruct.2011.08.039

Federal Emergency Management Agency (FEMA). (2000). *Prestandard and Commentary for the Seismic Rehabilitation of Buildings* (FEMA-356), Washington, D.C.

General Services Administration (GSA). (2016). *Alternate path analysis and design guidelines for progressive collapse resistance* (GSA 2016), Washington, D.C.

Hinman, E. E., and Hammond, D. J. (1997). Lessons from the Oklahoma City Bombing, Defensive Design Techniques, ASCE Press, New York.

Jian, H., & Zheng, Y. (2014). Simplified Models of Progressive Collapse Response and Progressive Collapse-Resisting Capacity Curve of RC Beam-Column Substructures. *Journal of Performance of Constructed Facilities*, *28*, 1–7. http://doi.org/10.1061/(ASCE)CF.1943-5509.0000492.

Khorsandnia, N., Valipour, H., Foster, S., & Amin, A. (2017). Experimental Study of Progressive Collapse Resistance of RC Framed Structures. *ACI Structural Journal*, *114*(6), 1385–1396. http://doi.org/10.14359/51689496

Kowalsky, M. J., & Priestley, M. J. N. (2000). Improved Analytical Model for Shear Strength of Circular Reinforced Concrete Columns in Seismic Regions. *ACI Structural Journal*, *97*(3), 388–396.

Lew, H. S., Bao, Y., Pujol, S., & Sozen, M. A. (2014). Experimental Study of Reinforced Concrete Assemblies under Column Removal Scenario. *ACI Structural Journal*, *111*(4), 881–892. http://doi.org/10.14359/51686739

Mander, J.B., M.J.N. Priestley, and R. Park. (1984). Theoretical StressStrain Model for Confined Concrete. Journal of Structural Engineering. ASCE. 114(3). 1804-1826.

Mohamed, O. A. (2006). Progressive Collapse of Structures: Annotated Bibliography and Comparison of Codes and Standards. *Journal of Performance of Constructed Facilities*, *20*, 418–425.

Muttoni, A., & Ruiz, M. F. (2008). Shear Strength of Members without Transverse Reinforcement as Function of Critical Shear Crack Width. *ACI Structural Journal*, *105*(2), 163–172.

Nair, R. S. (2006). Preventing Disproportionate Collapse. *Journal of Performance of Constructed Facilities*, *20*, 309–314.

Pearson, C., & Delatte, N. (2005). Ronan Point apartment tower collapse and its effect on building codes. *Journal of Performance of Constructed Facilities*, *19*(2), 172–177. http://doi.org/10.1061/(ASCE)0887-3828(2005)19:2(172)

Priestley, M. J. N., Verma, R., & Xiao, Y. (1994). Seismic Shear Strength of Reinforced Concrete Columns. *Journal of Structural Engineering*, *120*(8), 2310–2329.

Qian, K., & Li, B. (2012). Experimental and Analytical Assessment on RC Interior Beam-Column Subassemblages for Progressive Collapse. *Journal of Performance of Constructed Facilities*, *26*(5), 576–589. http://doi.org/10.1061/(ASCE)CF.1943-5509.0000284

Ren, P., Li, Y., Lu, X., Guan, H., & Zhou, Y. (2016). Experimental investigation of progressive collapse resistance of one-way reinforced concrete beam-slab substructures under a middle-column-removal scenario. *Engineering Structures*, *118*, 28–40. http://doi.org/10.1016/j.engstruct.2016.03.051

SAP2000 Version 17.0. (2014). Linear and nonlinear static and dynamic analysis and design of three-dimensional structures, Computers and Structures Inc., Berkeley CA.

Sasani, M., & Sagiroglu, S. (2008). Progressive Collapse Resistance of Hotel San Diego. *Journal of Structural Engineering*, *134*, 478–488.

Tsai, M. H., & Lin, B. H. (2008). Investigation of progressive collapse resistance and inelastic response for an earthquake-resistant RC building subjected to column failure. *Engineering Structures*, *30*, 3619–3628. http://doi.org/10.1016/j.engstruct.2008.05.031

Wu, Y., & Hu, B. (2017). Shear Strength Components in Reinforced Concrete Members. *Journal of Structural Engineering*, *143*(9), 1–16. http://doi.org/10.1061/(ASCE)ST.1943-541X.0001832.

Yi, W., He, Q., Xiao, Y., & Kunnath, S. K. (2008). Experimental Study on Progressive Collapse-Resistant Behavior of Reinforced Concrete Frame Structures. *ACI Structural Journal*, *105*(4), 433–439.

Yu, J., & Tan, K. H. (2013). Experimental and numerical investigation on progressive collapse resistance of reinforced concrete beam column sub-assemblages. *Engineering Structures*, *55*, 90–106. http://doi.org/10.1016/j.engstruct.2011.08.040

Yu, J., & Tan, K. H. (2014). Special Detailing Techniques to Improve Structural Resistance Against Progressive Collapse. *Journal of Structural Engineering*, *140*, 130531211421001. http://doi.org/10.1061/(asce)st.1943-541x.0000886

Zhao, X., Wu, Y., Leung, A. Y., & Lam, H. F. (2011). Plastic Hinge Length in Reinforced Concrete Flexural Members. *Procedia Engineering*, *14*, 1266–1274. http://doi.org/10.1016/j.proeng.2011.07.159

Zhao, X., Wu, Y., & Leung, A. Y. T. (2012). Analyses of plastic hinge regions in reinforced concrete beams under monotonic loading. *Engineering Structures*, *34*, 466–482. http://doi.org/10.1016/j.engstruct.2011.10.016